COLLINEAR REATION DYNAMICS AND HYDRODYNAMIC ANALYSIS OF THE VIBRATIONALLY EXCITED Cl + HCl → ClH + Cl, Cl + DCl → ClD + Cl AND Cl + TCl → ClT + Cl REACTIONS ON TWO LEPS SURFACES

Carrie Kim Stroud

July 1993

Thesis in partial fulfillment of the degree of Master of Science

California Institute of Technology

For Dave

TABLE OF CONTENTS

ABSTRACT

Quantum dynamical calculations for the collinear Cl + HCl → ClH + Cl, Cl + DCl → ClD + Cl, and Cl + TCl → ClT + Cl reactions on low and high barrier potential energy surfaces are presented and discussed within the framework of the hyperspherical coordinate representation. Vibrational excitation of the reagent diatomic is found to decrease the reaction rate for the low barrier surface and increase the reaction rate for the high barrier surface. Quantum mechanical streamline calculations and tunneling fractions are used for analysis, and discussion of the results is made in terms of the topology of the potential surface, in which the skew angle and barrier height of the system play a leading role in explaining the dynamics of the reaction.

INTRODUCTION

Collinear triatomic light atom exchange reactions of the type Cl + H(D,T)Cl → ClH(D,T) + Cl, in which the first diatomic bond is broken while the second is created, are considered within the framework of quantum reactive scattering. Confinement of the reaction process to a straight line to avoid the complicated mathematics associated with molecular rotations introduces an artificial constraint on the reaction forcing it to react in a fictitious configuration. However, it is hoped that insight concerning the full three-dimensional reaction process can be gained from such a one dimensional analysis, especially in regard to the effects of translational and vibrational energy distributions. In this sense the collinear circumstance serves as a good first step for the testing of methods applicable to the more intense three-dimensional calculations.

The Cl + HCl → ClH + Cl reaction, classified as a heavy-light-heavy (**H-L-H**) reaction, sports a very small skew angle which has made it difficult to efficiently perform calculations on. However, the development of hyperspherical coordinate methods for collinear chemical reactions has permitted accurate quantum calculations on both **H-L-H** and dissociative systems, neither of which were well represented by conventional approaches based on natural collision coordinates.[24-26,54,59] Examination of the hydrogen atom transfer between two heavy atoms has especially benefited from the hyperspherical coordinates ability to accurately represent the large curvature encountered in such systems.[1,3,7-9,15-16,30,33,37-41] As a result of these investigations it has been determined that the collinear light atom transfer reactions typically exhibit characteristics such as oscillating reaction probabilities,[7,16] highly favored vibrational adiabaticity,[12,13] and equivalent reaction probabilities for nonreactive and reactive off-diagonal transitions. The specific reactions of this research also feature sharp resonance spectra.[46] All of these phenomena tend to be quantum in nature.[42,47,50,52]

In order to effectively discuss the title reactions, this document is organized by first presenting a detailed overview of the mathematics and physics of quantum reaction dynamics for a general collinear triatomic system. Each aspect of the

theory is discussed separately and independently of the others in order to focus on the structure of the numerical implementation of the mathematics. Initially the coordinate representation of the Hamiltonian and the separation of the Schrödinger equation are addressed, followed by a discussion of the Renormalized Numerov propagator. The final step in obtaining reactive scattering information is discussed in the asymptotic analysis section where the projection of numerical solutions and the establishment of physically meaningful data is outlined. The final section in the mathematical description of chemical reactions is dedicated to the analysis of quantum streamlines.

Quantum mechanical streamline calculations supply a great deal of valuable information pertaining to the wave function in the interaction region of the potential energy surface. Specifically, they provide otherwise unobtainable information about the reacting system as it goes from its initial to its final configuration by revealing more details of the collision mechanism than can be inferred from the product distribution alone. The streamlines can be thought of as quantum mechanical analogs to the classical trajectories of a single particle of corresponding reduced mass traveling through the potential surface. In addition, through the appearance of vortices and their penetration into classically forbidden regions of configuration space, streamlines provide a pictorial way of gaining information on important quantum effects such as resonances and tunneling which classical trajectory calculations fail to account for. Finally, the will be a crucial component in the analysis of the sensitivity of the reaction rate to the barrier height for vibrationally excited state systems.

The second part of this thesis will present new results for the collinear Cl + H(D,T)Cl reactions, emphasizing the effects of vibrational excitation on the reaction probabilities, for which little attention has been previously directed. It is perceived that the barrier height of the potential energy surface plays a vital role in the final reaction rate upon vibrational excitation of the reagent diatomic molecule. This observation is in itself not surprising, however the outcome is actually the opposite of what one intuitively expects for the lighter two of the three isotopes. That is, that vibrational excitation produces an increased reaction rate for a high

barrier surface and a decreased reaction rate for a low barrier surface. A full streamline analysis of the reacting process is utilized in order to discern the physical reasons for this observance.

COLINEAR REACTIVE SCATTERING FORMALISM

REACTIVE SCATTERING
RENORMALIZED NUMEROV PROPAGATOR
RS ANALYSIS
QUANTUN MECHANICAL STREAMLINES

COLLINEAR REACTIVE SCATTERING

One of the most rudimentary chemically reactive processes occurs in the gas phase when a single atom collides with a diatomic molecule, subsequently dissolving the first chemical bond and forming the second. Triatomic exchange reactions of this type are of the form A + BC → AB + C or A + BC → AC + B, in which the atom A is free to react with either end of the diatomic molecule. The mathematics associated with the rotations in three-dimensional space for such a reaction are complicated and in order to avoid them the reaction can be superficially confined to a straight line. Collinear configurations, although substantially simpler than their three-dimensional counter parts, assist in direct analysis of the effects of the vibrational and translational degrees of freedom available to a chemical reaction and in many cases constitute the dominant geometrical path of the reaction.

The coordinate system for a general collinear reaction is shown in Figure 1.[32] When atom A collides with molecule BC the most convenient coordinates to describe the process are r_α' and R_α' which are the BC internuclear distance and the distance from A to the center of mass of BC respectively. The reverse reaction, in which C collides with BA, is described by the coordinates r_γ' and R_γ'. Neglecting spin interactions and removing the motion of the system's center of mass furnishes the nuclear motion Hamiltonian in either the α or γ coordinate frame

$$H = -\frac{\hbar^2}{2\mu_{A,BC}}\frac{\partial^2}{\partial R_\alpha'^2} - \frac{\hbar^2}{2\mu_{BC}}\frac{\partial^2}{\partial r_\alpha'^2} + V(R_\alpha', r_\alpha'),$$

$$H = -\frac{\hbar^2}{2\mu_{C,BA}}\frac{\partial^2}{\partial R_\gamma'^2} - \frac{\hbar^2}{2\mu_{BA}}\frac{\partial^2}{\partial r_\gamma'^2} + V(R_\gamma', r_\gamma'). \qquad 1$$

There are two reduced masses in each reference frame, one being the reduced mass of the diatomic molecule and the other that of the separate atom and molecule. In α coordinates these reduced masses are explicitly written

$$\mu_{BC} = \frac{m_B m_C}{(m_B + m_C)}, \quad \mu_{A,BC} = \frac{m_A (m_B + m_C)}{m_A + m_B + m_C}. \qquad 2$$

The kinetic energy components of the Hamiltonian describe the vibrational motion of the diatomic molecule and the relative kinetic motion of the atom as it moves with respect to the diatomic center of mass. The potential energy term is obtained from solving the electronic motion in three dimensions and is electronically adiabatic in the cases presented here.

In order to understand the basic mechanism of a three particle chemical reaction the motions and interactions of the particles are needed. Therefore, solutions to the nuclear motion Schrödinger equation,

$$H\Psi = E\Psi \qquad 3$$

subject to the appropriate asymptotic conditions, are sought. The asymptotic conditions are the boundary conditions of this two dimensional partial differential equation and come from the region of configuration space where the physical wave function is specifically known to be a linear combination of diatomic vibrational wavefunctions only depending on the variable r_λ'. Due to the fact that the bound vibrational wavefunctions differ significantly from zero only over a relatively small range of r_λ', and that grouping together both the forward and backwards reactions exhibits no loss of generality, the asymptotic conditions can be written simply as

$$\Psi^{\lambda' n_\lambda'} \sim \sum_{\lambda n_\lambda} \left[\delta_{\lambda n_\lambda}^{\lambda' n_\lambda'} e^{-ik_{\lambda n_\lambda}' R_\lambda'} + f_{\lambda n_\lambda}^{'\lambda' n_\lambda'} e^{ik_{\lambda n_\lambda}' R_\lambda'} \right] \phi_{\lambda n_\lambda}(r_\lambda), \qquad 4$$

where λ is equivalent to either the α or γ representation and $\lambda' n_\lambda'$ denotes the initial state of the reagents. The ~ stands for the asymptotic form of the wavefunction and literally means that either $R_\alpha' \to \infty$ or $R_\gamma' \to \infty$. For the α arrangement, the reaction as $R_\alpha' \to \infty$ is indicative of atom A advancing toward the diatom BC in vibrational state n_α' with relative wavevector $k_{\alpha n_\alpha'}'$, superimposed on a sum of waves describing BC molecules in vibrational state n_α retreating from atom

A with wave vector $k'_{\alpha n_\alpha}$. The behavior at $R'_\gamma \to \infty$ is that of the reactive scattering term consisting of AB molecules in vibrational state n_γ moving away from atom C with relative wave vector $k'_{\gamma n_\gamma}$. Note that in this scenario it is the α channel that contains the term for the incoming wave since it describes the initial state of the reaction. The relation describing the conservation of energy can be written as

$$E = \frac{\hbar^2 k'^2_{\alpha n'_\alpha}}{2\mu_{A,BC}} + E_{\alpha n'_\alpha} = \frac{\hbar^2 k'^2_{\alpha n_\alpha}}{2\mu_{A,BC}} + E_{\alpha n_\alpha} = \frac{\hbar^2 k'^2_{\gamma n_\gamma}}{2\mu_{C,BA}} + E_{\gamma n_\gamma} \qquad 5$$

with $E_{\lambda n_\lambda}$ indicating the internal state energy eigenvalues of the vibrational states $\phi_{\lambda n_\lambda}(r_\lambda)$. The diatomic vibrational motion is quantized but the wave numbers and the total energy, which is a known quantity, are not. Thus the reagents collide with an established relative kinetic energy in a given internal state from which state resolved reaction probabilities can be acquired.

A reactive process with reagents in the state designated by the quantum numbers $\alpha n'_\alpha$ and products in λn_λ has a scattering amplitude $f'^{\alpha n'_\alpha}_{\lambda n_\lambda}$. For open channels, channels for which $E \geq E_{\lambda n_\lambda}$, the corresponding flux is $v'_{\lambda n_\lambda}\left|f'^{\alpha n'_\alpha}_{\lambda n_\lambda}\right|^2$, where $v'_{\lambda n_\lambda}$ is the relative motion velocity of the channel. The collision cross-section of this reaction is the dimensionless probability given by the ratio of the incoming and reactive fluxes:

$$P^{\alpha n'_\alpha}_{\lambda n_\lambda} = \left(\frac{v'_{\lambda n_\lambda}}{v'_{\alpha n'_\alpha}}\right)\left|f'^{\alpha n'_\alpha}_{\lambda n_\lambda}\right|^2. \qquad 6$$

At this point the physical interpretation of the reaction is that of a particle of mass $\mu_{A,BC}$ moving quantum mechanically from the reagent region α to the products region of configuration space denoted by the coordinates (R'_α, r'_α). However, the products region in these coordinates does not correspond to the true diatomic AB well produced in the reaction. Furthermore, the reverse reaction is not characterized by simply reversing the direction of the particle in the same

space, but rather by tracing a particle of mass $\mu_{C,BA}$ in the configuration space defined by the coordinates $\left(R_\gamma^{'}, r_\gamma^{'}\right)$. Neither the reduced masses nor the coordinate axes are interchangeable between the two systems. Consequently, the skew angles of these two potential energy surfaces, the acute angles made between the $R_\lambda^{'}$ and $r_\lambda^{'}$ axes, differ with each a function of the masses of the associated atoms,

$$\theta' = \tan^{-1}\left[1+{}^{m_B}\!/_{m_C}\right]. \qquad 7$$

Thus, the potential surface is apt to change shape under the transformation between α and γ coordinates.

Obviously it is advantageous to be able to work in a coordinate space which satisfies the intuitive meaning of the particle motion and permits an equally convenient description of both the forward and reverse reactions. In order to summarize the entire collision process with the motion of a single reduced mass μ, the coordinate system introduced by Delves is exploited and can be generated by an elementary mass scaling of either the α or γ coordinates in the following manner,

$$\begin{aligned} R_\alpha &= a_\alpha R_\alpha^{'} \quad r_\alpha = a_\alpha^{-1} r_\alpha^{'} \quad a_\alpha = \left(\mu_{A,BC}/\mu_{BC}\right)^{1/4} \\ R_\gamma &= a_\gamma R_\gamma^{'} \quad r_\gamma = a_\gamma^{-1} r_\gamma^{'} \quad a_\gamma = \left(\mu_{C,BA}/\mu_{BA}\right)^{1/4}. \end{aligned} \qquad 8$$

The resulting Hamiltonian encompasses a single reduced mass which is independent of the choice of coordinates and can be written in a general form with λ depicting either α or γ

$$H = -\frac{\hbar^2}{2\mu}\frac{\partial^2}{\partial R_\lambda{}^2} - \frac{\hbar^2}{2\mu}\frac{\partial^2}{\partial r_\lambda{}^2} + V(R,r). \qquad 9$$

The single reduced mass μ is equally weighted in terms of all three atomic masses in this sense and is

$$\mu = \left[m_A m_B m_C / (m_A + m_B + m_C) \right]^{1/2}. \qquad 10$$

Using this mass scaling, the change of coordinates from the α to γ set has a simple form and the two systems reduce to one having a skew angle that equally well represents both the forward and reverse reactions. The concurring transformation $(R_\alpha, r_\alpha) \rightarrow (R_\gamma, r_\gamma)$ corresponds to a rotation in the Delves' mass-scaled configuration space with a clockwise angle of rotation

$$\omega = \tan^{-1}\left(m_A m_C / m_B M \right)^{1/2}. \qquad 11$$

Under this transformation the potential energy surface does not change shape, since now the two axes systems are orthogonal, and thus the motion of the ABC system in one physical dimension is akin to the motion of a particle of reduced mass in a two mathematical dimensional space. The subsequent skew angle of the system is measured between the R_α and R_γ axes

$$\theta = \tan^{-1}\left(m_B M / m_A m_C \right)^{1/2} \qquad 12$$

and consequently has dynamic significance. One peculiarity of the collinear restrictions on the reaction is that in these skewed coordinates the R_α axis transforms into the r_γ axis and R_γ into r_α.

Solving the Schrödinger equation has been assailed from a diversity of angles with the most popular techniques exploiting the coupled channel method. In this approach two variables are used; the first variable, x, is held constant while the second variable, y, surveys the potential with the assumption that the limits of y reside in regions of the potential having very large energies. A one dimensional Hamiltonian in the variable y, at a fixed x, with potential $V(\bar{x}, y)$ yields a set of eigenfunctions in which the wave function can be expanded. In a sense the Hamiltonian is separated into two variable dependencies. From this point, a set of coupled ordinary differential equations with x dependent coefficients is solved. Natural collision coordinates constitute the bulk of traditional choices for x and y.

In this case three regions of configuration space are established, two equivalent to the asymptotic regions of the reactant and product channels and the third corresponding to the interaction region. Unfortunately, reactive processes involving the exchange of a light atom between two heavy atoms or the complete dissociation of the system are inaccessible using these coordinates. The dissociative process is indescribable because natural collision coordinates typically don't sample the dissociative plateau region of configuration space, thus restricting calculations to energies well below those of break up collisions. The light atom exchange reactions are difficult for reasons based on their small skew angles. For such processes the scaled distances are highly compressed in the strong interaction region and the gradient of the potential energy increases rapidly. The symmetric stretch coordinate, which is perpendicular to the reaction coordinate, is very broad and can support a much larger number of bound states than the diatomic wells characterizing the reactant and product channels. This makes for an unusually intense calculation requiring a significantly higher number of basis functions for convergence than would be expected considering the asymptotic channels alone.

More recent advances in reactive scattering exploit the convenience of hyperspherical coordinates to obtain reactive transition probabilities. Hyperspherical coordinates, which are the same as the circular polar coordinates (ρ,α) in collinear scattering, are distinguished by the use of a coordinate measuring the size of the system, namely ρ. Unlike the natural collision coordinates of earlier methods, hyperspherical coordinates have no channel specialization and can therefore be implemented over all areas of configuration space. Consequently, the dissociative plateau is adequately described and calculations for break up collisions are possible. Furthermore, the angular coordinates more accurately represent the saddle point regions of very skewed systems allowing for a thorough description of the rapidly changing gradient of the potential surface in that area. Finally, since the angular coordinate in the strong interaction region does not remain perpendicular to the reaction path, the number of basis functions needed in that area does not increase as it did in the other cases where the symmetric stretch mode was very soft and held many bound states.

In hyperspherical coordinates the one dimensional nuclear motion Hamiltonian in Delves' mass scaled form with the single reduced mass transforms into

$$H(\rho,\alpha)=\frac{-\hbar^2}{2\mu}\left[\frac{\partial^2}{\partial\rho^2}+\frac{1}{\rho}\frac{\partial}{\partial\rho}+\frac{1}{\rho^2}\frac{\partial^2}{\partial\alpha^2}\right]+V(\rho,\alpha), \qquad 13$$

and the Schrödinger equation at a given total energy becomes a function of the polar coordinates ρ and α,

$$H\psi(\rho,\alpha)=E\psi(\rho,\alpha). \qquad 14$$

To avoid the mixed derivative arising from the second order differential equation the wave function is written in the form

$$\psi_j(\rho,\alpha)=\rho^{-½}B_j(\rho,\alpha), \qquad 15$$

and evaluation of the Schrödinger equation yields

$$\frac{-\hbar^2}{2\mu}\left[\frac{\partial^2}{\partial\rho^2}+\frac{1}{\rho^2}\frac{\partial^2}{\partial\alpha^2}\right]B_i(\rho,\alpha)+\left[V(\rho,\alpha)-\frac{\hbar^2}{8\mu\rho^2}-E\right]B_i(\rho,\alpha)=0. \qquad 16$$

The role of x in the coupled channel procedure is played by the variable ρ and thus upon selecting a constant value labeled $\bar{\rho}$, the variable α is allowed to span the full range of the skew angle. At this point a complete orthogonal set of discrete basis functions in the variable α, but which are also parametrically dependent on $\bar{\rho}$, are obtained from solving the relation

$$\left[-\frac{\hbar^2}{2\mu\bar{\rho}^{\,2}}\frac{\partial^2}{\partial\alpha^2}+V(\alpha;\bar{\rho})-\varepsilon_j^{\bar{\rho}}\right]Y_j(\alpha;\bar{\rho})=0 \qquad 17$$

The above equation contains both a kinetic energy term and a potential energy function in the variable α and is the equivalent of a Hamiltonian in α with eigenvalues $\varepsilon_j^{\bar{\rho}}$ and eigenfunctions $Y_j(\alpha;\bar{\rho})$. These functions are called the surface functions in collinear scattering. The total wavefunction is expanded in these functions

$$\psi_i(\rho,\alpha) = \rho^{-1/2} B_i(\rho,\alpha) = \rho^{-1/2} \sum_{j=1} b_{ij}(\rho;\bar{\rho}) Y_j(\alpha;\bar{\rho}), \tag{18}$$

plugged into the Schrödinger equation which is multiplied by $Y_k(\alpha;\bar{\rho})$, integrated over the variable α and rearranged to give

$$\begin{aligned} \frac{\partial^2}{\partial\rho^2} b_{ik}(\rho;\bar{\rho}) = &\left[\frac{2\mu\varepsilon_k^{\bar{\rho}}\bar{\rho}^2}{\hbar^2\rho^2} - \frac{1}{4\rho^2} - \frac{2\mu E}{\hbar^2}\right] b_{ik}(\rho;\bar{\rho}) \\ &+ \sum_j b_{ij}(\rho;\bar{\rho}) \left[-\frac{2\mu\bar{\rho}^2}{\hbar^2\rho^2} V_{jk}(\alpha;\bar{\rho}) + \frac{2\mu}{\hbar^2} V_{jk}(\rho;\bar{\rho})\right]. \end{aligned} \tag{19}$$

Due to the orthogonality of the surface functions at each $\bar{\rho}$, the kinetic energy is diagonalized but the expressions for the potential remain more complex. In this expression the potential matrix elements are defined as

$$\begin{aligned} V_{jk}(\alpha;\bar{\rho}) &= \int_0^{\alpha_{max}} Y_j(\alpha;\bar{\rho})\, V(\alpha;\bar{\rho})\, Y_k(\alpha;\bar{\rho})\, d\alpha, \\ V_{jk}(\rho;\bar{\rho}) &= \int_0^{\alpha_{max}} Y_j(\alpha;\bar{\rho})\, V(\rho;\alpha)\, Y_k(\alpha;\bar{\rho})\, d\alpha, \end{aligned} \tag{20}$$

where the second is referred to as the interaction potential matrix element. Rewriting the expression in matrix form, which makes for simple implementation, gives

$$\mathbf{b}'' = \mathbf{W}\mathbf{b} \tag{21}$$

with the matrix $\mathbf{W}$ defined in terms of the diagonal matrices $\boldsymbol{\varepsilon}$ and $\mathbf{I}$ and the nondiagonal matrices $\mathbf{V}(\alpha;\bar{\rho})$ and $\mathbf{V}(\rho;\bar{\rho})$,

$$\mathbf{W} = \frac{2\mu\bar{\rho}^2}{\hbar^2\rho^2}\boldsymbol{\varepsilon} - \left[\frac{1}{4\rho^2} + \frac{2\mu E}{\hbar^2}\right]\mathbf{I} - \frac{2\mu\bar{\rho}^2}{\hbar^2\rho^2}\mathbf{V}(\alpha;\bar{\rho}) + \frac{2\mu}{\hbar^2}\mathbf{V}(\rho;\bar{\rho}). \qquad 22$$

This is the most convenient form of the coupled channel Schrödinger equation for evaluation of the second derivative expression for the many propagation schemes available.

RENORMALIZED NUMEROV METHOD

Solving the coupled channel Schrödinger equation consists of evaluating the eigenvalue problem of one variable, to get surface functions, while propagating in the other, which the surface functions are parametrically dependent on. Integrating Schrödinger's equation in hyperspherical coordinates is best accomplished with an outward integration procedure that is initiated deep within the strongly repulsive potential region, corresponding to small values of ρ, and completed at a distance sufficiently far out that the reactive channels have separated completely, a region of the potential analogous to large values of ρ. Eigenfunctions of the angular variable can be numerically determined by standard algorithms, but integration in the hyperradius requires one of the many numerical approaches to solving linear second-order differential equations, which are not quite so readily available in computation libraries for multidimensional problems.

The coupled-channel Schrödinger equation is most conveniently written in the form of a matrix differential equation

$$\left[\mathbf{I}\frac{d^2}{d\rho^2} + \mathbf{Q}(\rho;\bar{\rho})\right]\mathbf{b}(\rho;\bar{\rho}) = \mathbf{0} \qquad 1$$

where

$$\mathbf{Q}(\rho;\bar{\rho}) = \left(\frac{2\mu}{\hbar^2}\right)\left[E\,\mathbf{I} - \mathbf{W}(\rho;\bar{\rho})\right]. \qquad 2$$

In this sense, $\mathbf{b}(\rho;\bar{\rho})$ is the 'wavefunction' matrix, $\mathbf{I}$ the identity matrix, and $\mathbf{W}(\rho;\bar{\rho})$ a symmetric potential matrix. In one dimension, when Q is positive and usually written as k^2 the solutions are oscillatory with local wavenumber k, but when k^2 is negative the solutions grow or decay exponentially at a local rate $(-k^2)^{1/2}$. A particularly simple and efficient method for solving these types of differential equations is the renormalized Numerov algorithm.[21,22]

The Numerov method is derived from the Schrödinger equation by first approximating the second derivative by a three point difference relation,

$$\frac{\mathbf{b}_{n+1}-2\mathbf{b}_n+\mathbf{b}_{n-1}}{h^2}=\mathbf{b}_n+\frac{h^2}{12}\mathbf{b}_n''''+O\left(h^4\right) \qquad 3$$

In this expression the symbol $\mathbf{b}_n$ means $\mathbf{b}\left(\rho_n;\bar{\rho}\right)$. The $O\left(h^2\right)$ error term, where h is the distance between an equally spaced set of grid points in the variable ρ, has been written out explicitly and can be derived from the taylor expansion of an arbitrary function,

$$f(x)=f_0+xf'+\frac{x^2}{2!}f''+\frac{x^3}{3!}f'''+\cdots \qquad 4$$

which gives

$$f_{\pm1}\equiv f(x=\pm h)=f_0\pm hf'+\frac{h^2}{2}f''\pm\frac{h^3}{6}f'''+O\left(h^4\right). \qquad 5$$

The differential equation itself yields

$$\begin{aligned}\mathbf{b}_n''''&=\frac{d^2}{d\rho^2}[-\mathbf{Q}\mathbf{b}]_{\rho=\rho_n}\\&=\mathbf{Q}_{n+1}\mathbf{b}_{n+1}-2\mathbf{Q}_n\mathbf{b}_n+\mathbf{Q}_{n-1}\mathbf{b}_{n-1}\end{aligned} \qquad 6$$

again keeping in mind the notation symbolized by the subscripts. Substituting this expression into the three point recursion relation and rearranging terms to simplify the equation gives the three point recurrence formula from which the renormalized Numerov algorithm follows,

$$\left(\mathbf{I}+\frac{h^2}{12}\mathbf{Q}_{n+1}\right)\mathbf{b}_{n+1}-2\left(\mathbf{I}-\frac{5h^2}{12}\mathbf{Q}_n\right)\mathbf{b}_n+\left(\mathbf{I}+\frac{h^2}{12}\mathbf{Q}_{n-1}\right)\mathbf{b}_{n-1}=\mathbf{0}. \qquad 7$$

A convenient substitution is made by defining the matrix

$$\mathbf{T}_n = -\left(\frac{h^2}{12}\right)\mathbf{Q}(\rho_n;\bar{\rho}) \qquad 8$$

to give

$$[\mathbf{I}-\mathbf{T}_{n+1}]\mathbf{b}_{n+1} - [2\mathbf{I}-10\mathbf{T}_n]\mathbf{b}_n + [\mathbf{I}-\mathbf{T}_{n-1}]\mathbf{b}_{n-1} = \mathbf{0}. \qquad 9$$

Solving this equation for either $\mathbf{b}_{n+1}(\rho;\bar{\rho})$ or $\mathbf{b}_{n-1}(\rho;\bar{\rho})$, provides a recursion relation for integrating either forward or backwards in ρ. Two transformations are performed next, the first being

$$\mathbf{F}_n = [\mathbf{I}-\mathbf{T}_n]\mathbf{b}_n \qquad 10$$

which when substituted back into the recurrence relation gives an expression across three points of the grid again denoted by the subscripts

$$\mathbf{F}_{n+1} - \mathbf{U}_n\mathbf{F}_n + \mathbf{F}_{n-1} = \mathbf{0} \qquad 11$$

with the symmetric matrix

$$\mathbf{U}_n = (\mathbf{I}-\mathbf{T}_n)^{-1}(2\mathbf{I}+10\mathbf{T}_n). \qquad 12$$

This transformation is advantageous in that at each step the value of **F** requires one less multiplication to calculate than does the corresponding value of **b**. The determinental relation $|\mathbf{I}-\mathbf{T}_n| > 0$ is assumed true. Failure of this relation is indicative of too large a grid spacing for at least some of the components of the wavefunction. In the limit $h \to 0$ and $|\mathbf{I}-\mathbf{T}_n| \to 1$. If the determinant deviates too far from this limiting value, truncation error arises. In an extreme case the numerical solution will break into an unphysical oscillation with a node at every grid point. The difficulty tends to occur near the origin where the diagonal elements of the potential matrix can become very large and positive in value. A simple solution to

this problem comes from recognizing that the wavefunction is negligibly small since the potential is so large. The potentials can thus be truncated to some high value with out effecting the solution in any significant way.

The second transformation results in defining the ratio matrix

$$\mathbf{R}_n = \mathbf{F}_{n+1}\mathbf{F}_n^{-1} \tag{13}$$

from which the desired two term recurrence relation results,

$$\mathbf{R}_n = \mathbf{U}_n - \mathbf{R}_{n-1}^{-1}. \tag{14}$$

The quantity $\mathbf{R}_n$ is much easier to deal with than the value $\mathbf{F}_n$ because it does not grow exponentially in the classically forbidden regions of the potential as does the latter. This equation can be solved once the value of the initial term $\mathbf{R}_0$ is specified. The initial grid point lies deep in the repulsive potential region at the point ρ_0 where the initial values of the wavefunction are very small and the corresponding value of the inverse of the initial term is 0. Exceptions do occur for this condition, the most immediate being the calculation of the bound states of the hydrogen atom. Once the initial state had been determined, the equation can be iterated from small ρ to large ρ and if the iteration is stopped at any point along the way both the quantities $\mathbf{R}_n$ and $\mathbf{R}_{n-1}$ are available. The wavefunction at the three points ρ_{n-1}, ρ_n, and ρ_{n+1} can then be calculated to within a normalization factor,

$$\begin{aligned} \mathbf{b}_{n+1} &= N\left(\mathbf{I}-\mathbf{T}_{n+1}\right)^{-1}\mathbf{R}_n, \\ \mathbf{b}_n &= N\left(\mathbf{I}-\mathbf{T}_n\right)^{-1}, \\ \mathbf{b}_{n-1} &= N\left(\mathbf{I}-\mathbf{T}_{n-1}\right)^{-1}\mathbf{R}_{n-1}^{-1}. \end{aligned} \tag{15}$$

This is where the designation of the renormalized Numerov method comes in since a renormalized wavefunction is calculated at each step. The method is very stable and converges to the desired solution easily for complicated problems such as this

where the potential has a double minimum separated by a very high barrier. The Numerov algorithm is also free of overflow and linear dependence problems and thus no special programming precautions are needed.

Shore identifies four of the five sources of error possibly found in numerical results.[56] These include round off errors, termination errors, toleration errors and truncation errors. Round off error is inherent to most numerical calculations not utilizing integer arithmetic. If the wavefunction is forced to be zero at an artificial boundary point the introduction of termination error is possible. The truncation error is a function of the grid spacing h and comes from the replacement of the differential equation with the approximate finite difference equation. Numerical calculations determine that this error is given by

$$\Delta E_{trunc} = C_4 h^4 + C_6 h^6 + \cdots \qquad 16$$

which is consistent with the h^4 accuracy of the traditional Numerov method. All of these errors can be adjusted with the appropriate choice of parameters, except the round off error. A fifth source of numerical error comes from cutting an infinite set of coupled differential equations down to the finite set necessary for computation.

Reactive scattering information comes primarily out of the reactance and scattering matrices. These can be established once the propagation has been performed by projecting the wavefunction onto the diatomic basis at the asymptotic value of ρ. To do this the logarithmic derivative of the wavefunction is needed and can be established from the renormalized Numerov formalism using the matrix formula derived by Blatt. The derivative of the wavefunction at a point is given by

$$\mathbf{b}_n' = h^{-1}\left[(0.5\mathbf{I} - \mathbf{T}_{n+1})\mathbf{b}_{n+1} - (0.5\mathbf{I} - \mathbf{T}_{n-1})\mathbf{b}_{n-1}\right]. \qquad 17$$

This expression has an error term on the order of h^5 which is poorer than the order h_6 of the basic Numerov formula. However, it has been shown that the cumulative

error of the Numerov algorithm at a point is of the order h^4. The logarithmic derivative expression is produced when the derivative of the wavefunction is calculated, within the normalization factor, by substituting the equations for $\mathbf{b}_{n-1}$ and $\mathbf{b}_{n+1}$ followed by multiplying on the right by the inverse of $\mathbf{b}$ at the point ρ_n. Cancellation of the normalization factor gives

$$\mathbf{y}(\rho_n;\bar{\rho}) = h^{-1}\left(\mathbf{A}_{n+1}\mathbf{R}_n - \mathbf{A}_{n-1}\mathbf{R}_{n-1}^{-1}\right)\left(\mathbf{I}-\mathbf{T}_n\right) \qquad 18$$

where the matrix $\mathbf{A}$ is defined as

$$\mathbf{A}_n = \left(0.5\mathbf{I}-\mathbf{T}_n\right)\left(\mathbf{I}-\mathbf{T}_n\right)^{-1}. \qquad 19$$

A measure of the quality of the calculation is directly obtainable from an analysis of the symmetry of the logarithmic and reactance matrices. At the inner most value of ρ the inverse of the ratio matrix is inherently symmetric and the iterative procedure subsequently yields a symmetric $\mathbf{U}$ matrix and therefore a symmetric $\mathbf{R}$ matrix at each point. The deviation from symmetry in the reactance matrix is a direct measure of the convergence of the integration and the error accumulated in the calculation.

PROJECTION AND ASYMPTOTIC ANALYSIS

Separating the problem of obtaining arbitrary solutions to the coupled channel Schrödinger equation from the problem of imposing asymptotic boundary conditions appropriate for acquiring solutions of physical relevance, comes about with the determination of the reactance and scattering matrices. From the scattering matrix state-to-state reaction probabilities are evaluated.

The set of mathematical solutions for a collinear reaction have an asymptotic form in the λ arrangement channel given by

$$\psi^{\lambda' n'_{\lambda'}} \sim \sum_{\lambda n_\lambda} g^{\lambda' n'_{\lambda'}}_{\lambda n_\lambda} (R_\lambda)\, \phi_{\lambda n_\lambda}(r_\lambda) \qquad 1$$

where the ϕ are the complete discrete set of diatomic basis functions which satisfy the relation

$$-\frac{\hbar^2}{2\mu}\frac{d^2\phi_{\lambda n_\lambda}(r_\lambda)}{dr_\lambda^2} + V_\lambda(r_\lambda)\phi_{\lambda n_\lambda}(r_\lambda) = E_{\lambda n_\lambda}\phi_{\lambda n_\lambda}(r_\lambda). \qquad 2$$

The solutions to the set of equations

$$-\frac{\hbar^2}{2\mu}\frac{d^2 g^{\lambda' n'_{\lambda'}}_{\lambda n_\lambda}}{dR_\lambda^2} \sim \left(E - E_{\lambda n_\lambda}\right) g^{\lambda' n'_{\lambda'}}_{\lambda n_\lambda} \qquad 3$$

are written in the form

$$g^{\lambda' n'_{\lambda'}}_{\lambda n_\lambda} \sim v^{-1/2}_{\lambda n_\lambda}\left[\vartheta_{\lambda n_\lambda}(R_\lambda)\, A^{\lambda' n'_{\lambda'}}_{\lambda n_\lambda} - \mathcal{O}_{\lambda n_\lambda}(R_\lambda)\, B^{\lambda' n'_{\lambda'}}_{\lambda n_\lambda}\right]. \qquad 4$$

Here the coefficients $A^{\lambda' n'_{\lambda'}}_{\lambda n_\lambda}$ and $B^{\lambda' n'_{\lambda'}}_{\lambda n_\lambda}$ are integration constants, $v^{-1/2}_{\lambda n_\lambda}$ is the channel velocity and $k_{\lambda n_\lambda}$ is the channel wavenumber. $\vartheta_{\lambda n_\lambda}$ and $\mathcal{O}_{\lambda n_\lambda}$ are

diagonal matrix elements describing the relative translational motion of an atom and a diatomic molecule through the incoming and outgoing plane waves as a function of the wavenumber

$$\mathcal{J}_{\lambda n_\lambda}(R_\lambda) = \begin{cases} e^{\left(-ik_{\lambda n_\lambda} R_\lambda\right)} & \textit{open channels} \\ e^{\left(\left|k_{\lambda n_\lambda}\right| R_\lambda\right)} & \textit{closed channels} \end{cases} \qquad 5$$

$$\mathcal{O}_{\lambda n_\lambda}(R_\lambda) = \begin{cases} e^{\left(ik_{\lambda n_\lambda} R_\lambda\right)} & \textit{open channels} \\ e^{\left(-\left|k_{\lambda n_\lambda}\right| R_\lambda\right)} & \textit{closed channels.} \end{cases} \qquad 6$$

In matrix notation this relation for the coefficients becomes

$$\mathbf{g} = \mathbf{v}^{-1/2}\left[\mathcal{J}\mathbf{A} - \mathcal{O}\mathbf{B}\right]. \qquad 7$$

The scattering matrix is defined as the matrix that generates the matrix of outgoing wave coefficients **B** when acting upon the matrix **A** of incoming coefficients,

$$\mathbf{B} = \mathbf{S}\mathbf{A}. \qquad 8$$

When the initial state and flux of collision reagents is known, then the scattering matrix enables the determination of the final states and fluxes of the products. An alternative way of writing the expression for the **g** involkes the more simplistic nature of real rather than complex algebra and has the form

$$\mathbf{g} = \mathbf{v}^{-1/2}\left[\mathcal{J}\mathbf{C} + \mathcal{O}\mathbf{D}\right]. \qquad 9$$

In this instance the new integration constants **C** and **D** are related by the reactance matrix **R** in the same way **A** and **B** are related by the scattering matrix. All the

matrices are now real and are obtainable through real quantities. The $\mathcal{S}$ and $\mathcal{C}$ are diagonal sine and cosine matrices representing standing waves, thus they carry no flux. They can be obtained immediately from the I and O by writting the trigonometric form of the imaginary exponential expressions. Their elements are given by

$$\mathcal{S}_{\lambda n_\lambda}(R_\lambda) = \begin{cases} \sin\left(k_{\lambda n_\lambda} R_\lambda\right) & \textit{open channels} \\ e^{\left(\left|k_{\lambda n_\lambda}\right| R_\lambda\right)} & \textit{closed channels} \end{cases} \qquad 10$$

$$\mathcal{C}_{\lambda n_\lambda}(R_\lambda) = \begin{cases} \cos\left(k_{\lambda n_\lambda} R_\lambda\right) & \textit{open channels} \\ e^{\left(-\left|k_{\lambda n_\lambda}\right| R_\lambda\right)} & \textit{closed channels} \end{cases} . \qquad 11$$

Both the scattering and reactance matrices are unique, in other words for a given set of incoming states, there is only one possible set of outgoing states. It is crucial to note that both matrices are functions of the total energy of the system. The scattering matrix is symmetric, a basic result of quantum mechanical microscopic reversibility, however only the open portion, that subblock spanned by the indices of the open rows and columns, of the reactance matrix is expected to be symmetric. Furthermore, the open part of the scattering matrix is unitary and thus conservation of particle flux is adhered to. Computationally, the reactance matrix is much easier to obtain than the scattering matrix but it is ultimately the latter which is desired. The open parts of the two are related by

$$\mathbf{S}^o = \left(\mathbf{I} + i\mathbf{R}^o\right)\left(\mathbf{I} - i\mathbf{R}^o\right)^{-1} \qquad 12$$

from which the real and imaginary components of the scattering matrix are made functions of the reactance matrix

$$\mathbf{S}^o = \mathrm{Re}\mathbf{S}^o + i\,\mathrm{Im}\mathbf{S}^o \qquad 13$$

$$\mathrm{Re}\mathbf{S}^{o} = \left(\mathbf{I} - \mathbf{R}^{o2}\right)\left(\mathbf{I} + \mathbf{R}^{o2}\right)^{-1} \qquad 14$$

$$\mathrm{Im}\mathbf{S}^{o} = 2\mathbf{R}^{o}\left(\mathbf{I} + \mathbf{R}^{o2}\right)^{-1}. \qquad 15$$

Another quantity of interest is the scaled configuration space scattering amplitude which is directly related to S by

$$f_{\lambda n_\lambda}^{\lambda' n'_{\lambda'}} = \left(\frac{v_{\lambda' n'_{\lambda'}}}{v_{\lambda n_\lambda}}\right)^{1/2} S^{o\,\lambda' n'_{\lambda'}}_{\lambda n_\lambda} \qquad 16$$

As mentioned before, the square of the scattering amplitude is proportional to the state-to-state reaction probability with a proportionality constant determined by the ratio of the scaled channel velocities. Combining these last two expressions provides the relation between the scattering matrix elements and the reactive transition probabilities for collinear collision dynamics,

$$P_{\lambda n_\lambda}^{\lambda' n'_{\lambda'}} = \left| S^{o\,\lambda' n'_{\lambda'}}_{\lambda n_\lambda} \right|^2. \qquad 17$$

All of these equations have been expressed in the distance vectors $\mathbf{r}_\lambda$ and $\mathbf{R}_\lambda$ rather than in the hyperspherical coordinates used in the integration scheme. Thus it becomes necessary to 'project' the solutions in one set of variables onto the other set. The projection itself is a change of basis from the surface functions to the asymptotic solutions.

The asymptotic wavefunctions are functions of the inter atomic distance of the diatomic molecule and thus are independent of the distance between the atom and molecule. However, the surface functions are dependent on both distances subject to the constraints of constant ρ and varying angle. There are two common procedures for accomplishing the desired change of variable. The first is the constant R projection. In this case the hyperspherical surface functions are projected onto the diatomics at a constant value of R. The alternative is the projection of the asymptotic functions onto the surface functions at a constant

value of ρ. It has two major advantages over the constant R approach. The first is that the expression for the reactance matrix is a function of the logarithmic derivative of the wavefunction rather than a function of both the wavefunction and its derivative separately, as is the case for the constant R projection. Secondly, in the constant ρ projection calculation there is no need for an extra projection region, a typical requirement in the constant R formalism.

Expansion of the wavefunction in the hyperspherical basis set and hyperradial coefficients is written as

$$\psi^i(\rho,\alpha) = \rho^{-1/2}\sum_k b_k^i(\rho;\bar{\rho})Y_k(\alpha;\bar{\rho}), \qquad 18$$

while the asymptotic wavefunction expanded in the diatomic basis is written

$$\psi^i(R,r) \sim \sum_l g_l^i(R)\phi_l(r), \qquad 19$$

the full set of quantum numbers represented by *i, j, k* and *l*. In the asymptotic region these two expressions are matched to give

$$\rho^{-1/2}\sum_k b_k^i(\rho;\bar{\rho})Y_k(\alpha;\bar{\rho}) = \sum_l g_l^i(R)\phi_l(r). \qquad 20$$

The coefficients $b_k^i(\rho;\bar{\rho})$ are functions of ρ but are also parametrically dependent on $\bar{\rho}$ as are the surfacefunctions. If both sides of this equation are multiplied by the function $Y_j(\alpha;\bar{\rho})$ and integrated over the angular variable α, we obtain

$$\begin{aligned}&\rho^{-1/2}\sum_k \int_0^{\alpha_{max}} b_k^i(\rho;\bar{\rho})\,Y_k(\alpha;\bar{\rho})\,Y_j(\alpha;\bar{\rho})\,d\alpha \\ &= \sum_l \int_0^{\alpha_{max}} g_l^i(R(\alpha,\rho))\phi_l(r(\alpha,\rho))\,Y_j(\alpha;\bar{\rho})\,d\alpha\end{aligned} \qquad 21$$

and from implementing the orthogonality of the surface functions

$$\rho^{-1/2} b_j^i(\rho;\bar{\rho}) = \sum_l \int_0^{\alpha_{max}} g_l^i(R(\alpha,\rho)) \phi_l(r(\alpha,\rho))\, Y_j(\alpha;\bar{\rho})\, d\alpha. \qquad 22$$

The matrix element F_j^l is defined

$$F_j^l = \phi_l(r(\alpha,\rho))\, Y_j(\alpha,\bar{\rho}), \qquad 23$$

and rewriting the above expression in terms of this value yields

$$\rho^{-1/2} b_j^i(\rho;\bar{\rho}) = \sum_l \int_0^{\alpha_{max}} F_j^l(r(\alpha,\rho),\alpha;\bar{\rho}) g_l^i(R(\alpha,\rho))\, d\alpha. \qquad 24$$

This equation can be written in matrix form if the integral and sum are interchangeable;

$$\rho^{-1/2}\mathbf{b}(\rho;\bar{\rho}) = \int_0^{\alpha_{max}} \mathbf{F}(r(\alpha,\rho),\alpha;\bar{\rho})\ \mathbf{g}(R(\alpha,\rho))\ d\alpha. \qquad 25$$

One must be careful in retaining the meaning of such an expression; the integral indicates that each matrix element of the product matrix of **F** and **g** is integrated over the range defined by the angular variable α.

Recall the definition of **g** as a function of the sine, cosine and coefficient matrices which were related by the reactance matrix,

$$\mathbf{D} = \mathbf{RC} \qquad 26$$

$$\mathbf{g} \sim \mathbf{v}^{-1/2}[\mathcal{S}\mathbf{C} + \mathcal{C}\mathbf{D}] = \mathbf{v}^{-1/2}[\mathcal{S}\mathbf{C} + \mathcal{C}\mathbf{RC}] = \mathbf{v}^{-1/2}[\mathcal{S} + \mathcal{C}\mathbf{R}]\mathbf{C}. \qquad 27$$

Substituting **g** into the integral equation gives

$$\rho^{-1/2}\mathbf{b}(\rho;\bar{\rho}) = \int_0^{\alpha_{max}} \mathbf{F}(r(\alpha,\rho),\alpha;\bar{\rho})\mathbf{v}^{-1/2}\left[\mathcal{A}(R(\alpha,\rho)) + \mathcal{C}(R(\alpha,\rho))\mathbf{R}\right]d\alpha\ \mathbf{C}. \qquad 28$$

At this point it becomes convenient to define the matrices $\underline{\mathbf{A}}$ and $\underline{\mathbf{B}}$ in the following manner,

$$\underline{\mathbf{A}}(\rho;\bar{\rho}) = \int_0^{\alpha_{max}} \mathbf{F}(r(\alpha,\rho),\alpha;\bar{\rho})\ \mathbf{v}^{-1/2}\ \mathcal{A}(R(\alpha,\rho))\ d\alpha \qquad 29$$

$$\underline{\mathbf{B}}(\rho;\bar{\rho}) = \int_0^{\alpha_{max}} \mathbf{F}(r(\alpha,\rho),\alpha;\bar{\rho})\ \mathbf{v}^{-1/2}\ \mathcal{C}(R(\alpha,\rho))\ d\alpha \qquad 30$$

which, when put back into the equation for **b** provide

$$\mathbf{b}(\rho;\bar{\rho}) = \rho^{1/2}\left[\underline{\mathbf{A}} + \underline{\mathbf{B}}\mathbf{R}\right]\mathbf{C}. \qquad 31$$

The **C** matrix can be eliminated by implementing the logarithmic derivative **y**. The inverse of the matrix **b** is

$$\mathbf{b}^{-1}(\rho;\bar{\rho}) = \mathbf{C}^{-1}\left[\underline{\mathbf{A}} + \underline{\mathbf{B}}\mathbf{R}\right]^{-1}\rho^{-1/2} \qquad 32$$

and its derivative is given by

$$\rho^{-1/2}\frac{d\mathbf{b}(\rho;\bar{\rho})}{d\rho} = \frac{\mathbf{b}(\rho;\bar{\rho})}{2\rho^{3/2}} + \left[\frac{d\underline{\mathbf{A}}}{d\rho} + \frac{d\underline{\mathbf{B}}}{d\rho}\mathbf{R}\right]\mathbf{C}. \qquad 33$$

Combining the two to fulfill the definition of the logarithmic derivative yields

$$\mathbf{y} = \frac{1}{2\rho}\mathbf{I} + \left[\frac{d\underline{\mathbf{A}}}{d\rho} + \frac{d\underline{\mathbf{B}}}{d\rho}\mathbf{R}\right]\left[\underline{\mathbf{A}} + \underline{\mathbf{B}}\mathbf{R}\right]^{-1}, \qquad 34$$

which can be rearranged to solve for the reactance matrix

$$\mathbf{R} = \left[\frac{d\underline{\mathbf{B}}}{d\rho} - \mathbf{X}\underline{\mathbf{B}}\overline{\mathbf{B}}\right]^{-1}\left[\mathbf{X}\underline{\mathbf{A}} - \frac{d\underline{\mathbf{A}}}{d\rho}\right], \qquad 35$$

$$\mathbf{X} = \mathbf{y} - \frac{1}{2\rho}\mathbf{I}.$$

So the reactance matrix is determined from the logarithmic derivative matrix obtained in the hyperspherical coordinates and the projection is accomplished through the matrices $\underline{\mathbf{A}}$ and $\underline{\mathbf{B}}$. It is useful to see the actual forms of these matrices in terms of the two basis sets and the derivatives involved.

The matrix $\underline{\mathbf{A}}$ was defined above but it is crucial to remember that it has both open and closed pieces. The matrix elements turn out to be

$$\underline{A}^i_j(\rho;\bar{\rho}) = \int_0^{\alpha_{max}} F^i_j\left(r(\alpha,\rho),\alpha;\bar{\rho}\right)\, v_i^{-1/2}\sin\left(k_i R(\alpha,\rho)\right)d\alpha \quad \textit{open channels}$$

$$\underline{A}^i_j(\rho;\bar{\rho}) = \int_0^{\alpha_{max}} F^i_j\left(r(\alpha,\rho),\alpha;\bar{\rho}\right)\, v_i^{-1/2}\, e^{\left(|k_i|R(\alpha,\rho)\right)}d\alpha \quad \textit{closed channels} \qquad 36$$

$$\underline{B}^i_j(\rho;\bar{\rho}) = \int_0^{\alpha_{max}} F^i_j\left(r(\alpha,\rho),\alpha;\bar{\rho}\right)\, v_i^{-1/2}\cos\left(k_i R(\alpha,\rho)\right)d\alpha \quad \textit{open channels}$$

$$\underline{B}^i_j(\rho;\bar{\rho}) = \int_0^{\alpha_{max}} F^i_j\left(r(\alpha,\rho),\alpha;\bar{\rho}\right)\, v_i^{-1/2}\, e^{\left(-|k_i|R(\alpha,\rho)\right)}d\alpha \quad \textit{closed channels.} \qquad 37$$

The differentials of these matrix elements are more complicated and when F is written out the immediate dependence on the variables R and r of the diatomic basis set becomes obvious. To evaluate the derivatives correctly the following expression is used,

$$\left(\frac{\partial}{\partial\rho}\right)_\alpha = \cos\alpha\left(\frac{\partial}{\partial R}\right)_r + \sin\alpha\left(\frac{\partial}{\partial r}\right)_R. \qquad 38$$

The derivative matrix elements become

$$\frac{\partial \underline{A}^i_j}{\partial \rho} = \int_0^{\alpha_{max}} v_i^{-1/2} \frac{d\phi_i}{dr} Y_j \sin(k_i R) \ \sin\alpha + \phi_i Y_j v_i^{-1/2} k_i \cos(k_i R)\cos\alpha \ d\alpha \quad \textit{open channels}$$

$$\frac{\partial \underline{A}^i_j}{\partial \rho} = \int_0^{\alpha_{max}} v_i^{-1/2} \frac{d\phi_i}{dr} Y_j e^{(|k_i|R)} \sin\alpha + \phi_i Y_j v_i^{-1/2} |k_i| e^{(|k_i|R)} \cos\alpha \ d\alpha \quad \textit{closed channels} \qquad (39)$$

$$\frac{\partial \underline{B}^i_j}{\partial \rho} = \int_0^{\alpha_{max}} v_i^{-1/2} \frac{d\phi_i}{dr} Y_j \cos(k_i R) \ \sin\alpha - \phi_i Y_j v_i^{-1/2} k_i \sin(k_i R)\cos\alpha \ d\alpha \quad \textit{open channels}$$

$$\frac{\partial \underline{B}^i_j}{\partial \rho} = \int_0^{\alpha_{max}} v_i^{-1/2} \frac{d\phi_i}{dr} Y_j e^{(-|k_i|R)} \sin\alpha - \phi_i Y_j v_i^{-1/2} |k_i| e^{(-|k_i|R)} \cos\alpha \ d\alpha \quad \textit{closed channels.} \qquad (40)$$

These are the expressions for the matrix elements which get programmed. Each element is calculated and then placed in its respective matrix. When all four matrices are complete, the **R** matrix is calculated using matrix multiplication and inversion routines. The desired quantity is the upper left hand corner of the scattering matrix corresponding to the energetically accessible states. This submatrix can be calculated using only the open part of the reactance matrix. As a result only the open columns of the reactance matrix are needed which can be obtained using only the open columns of $\underline{\mathbf{A}}$ and its derivative. The exceptionally nice part of this is that the exponentially growing terms, which are functions of R, are not needed in the final calculation of **R** and the computational errors inherent to such functions are completely avoided. The exponentially decreasing functions are still needed though and can cause problems if left unchecked. The best way to deal with these is to multiply the exponential function by another exponential function with a positive argument. It can be shown that this transformation does not change the elements of the open-open corner of the reactance matrix but do tame the elements corresponding to closed channel rows which can poison the other values.

QUANTUM MECHANICAL STREAMLINES

Quantum mechanical streamlines[17-20,34,36,44-45,60] provide a great deal of information pertaining to the wavefunction in the interaction region of the potential. Specifically, they make known how the reacting system goes from its initial to its final configuration by revealing more details of the mechanism of the collision than can be inferred from the product distribution alone. Regions of configuration space where the reaction may or may not be found are visible in probability and flux density contours from which the current density and streamlines are calculated. Streamlines act as the quantum analogs of the classical trajectories of a single particle of corresponding reduced mass traveling through the potential surface. Therefore, streamlines show how the features of the surface effect the flux flow represented by **j** and also aid in explaining how the surface effects change with energy. In addition, through the appearance of vortices and their penetration into classically forbidden regions, streamlines provide a pictorial way of obtaining information on significant quantum effects such as resonances and tunneling.

Vortices arising in a streamline calculation constitute the most curious of features and have been found to have vital influence on the interpretation of dynamic results. They have been found to be associated with the nodes of the wavefunction and the angular momentum found in a vortex is quantized. Derivations of these conclusions only depend on the single-valued nature of the wavefunction and its continuity. The vortices result from interference phenomena of the wavefunction and generally appear in locations which are independent of the features of the potential energy surface.

The solution of problems in classical hydrodynamics is associated with finding suitable expressions for the velocity fields describing the flow of the situation. The velocity field of fluid motion is conveniently expressed in terms of a scalar field function whose gradient is the velocity. A vector field in hydrodynamics describes both the direction and magnitude of the velocity of a fluid particle at any time *t*. In quantum mechanics this corresponds to the current density vector field given by

$$\mathbf{j}^{\lambda n_\lambda} = \frac{\hbar}{2\mu i}\left[\psi_{phys}^{\lambda n_\lambda *}\ \nabla\psi_{phys}^{\lambda n_\lambda} - \psi_{phys}^{\lambda n_\lambda}\left(\nabla\psi_{phys}^{\lambda n_\lambda}\right)^*\right]. \qquad 1$$

The quantity **j** has characteristics analogous to those of the vector field describing the flow of a two-dimensional fluid on a surface.

Madelung's derivation of quantum hydrodynamics leads to an expression of the wavefunction in the form

$$\psi = (\psi^* \psi)^{1/2} e^{(i\varphi/\hbar)} \qquad 2$$

where the probability density is everywhere real and continuous and the phase φ is defined up to an integer multiple of 2π, except at nodal points. Two real hydrodynamical equations can then be obtained from the separation of the Schrödinger equation into its real and imaginary parts

$$\frac{1}{2\mu}\nabla\varphi \bullet \nabla\varphi + V + V_{quant} = E = \left[-\frac{\partial\varphi}{\partial t}\right], \qquad 3$$

$$\nabla \bullet \left[(\psi^*\psi)^{1/2}\nabla\varphi/\mu\right] = 0 = \left[-\frac{\partial(\psi^*\psi)^{1/2}}{\partial t}\right]. \qquad 4$$

Excluding the last term of the first equation, these two expressions are the laws of motion for a fluid of noninteracting classical particles. The classical Hamilton-Jacobi equation is modified by the expression V_{quant} and the expression for the conservation of probability density uses the local mean velocity

$$\mathbf{v} = \nabla\varphi/\mu = \mathbf{j}/(\psi^*\psi)^{1/2} \qquad 5$$

where **j** is the expression for the current density for a quantum mechanical system as written above in equation 1. The extra potential term is created by quantum mechanics and it provides an explanation as to why the quantum fluid can flow into the regions of coordinate space where classical particles are forbidden,

subsequently resulting in tunneling. This term is a function of the probability density,

$$V_{quant} = -(\hbar^2/2\mu)(\psi^*\psi)^{-1/2}\nabla\bullet\nabla(\psi^*\psi)^{1/2}$$
$$= -\left(\frac{\hbar^2}{2\mu}\right)\left[2(\psi^*\psi)^{1/2}\right]^{-1}\nabla\bullet\nabla(\psi^*\psi)^{1/2} \qquad 6$$
$$+\left(\frac{\hbar^2}{2\mu}\right)\left[2(\psi^*\psi)^{1/2}\right]^{-2}\left(\nabla(\psi^*\psi)^{1/2}\right)\bullet\left(\nabla(\psi^*\psi)^{1/2}\right).$$

A streamline of **j** is a curve everywhere tangent to the **j** vector at every point *P* in configuration space. The corresponding equation of motion for the fluid particle is

$$\frac{dR_\lambda}{\mathbf{j}_{\hat{R}_\lambda}^{\lambda n_\lambda}} = \frac{dr_\lambda}{\mathbf{j}_{\hat{r}_\lambda}^{\lambda n_\lambda}}, \qquad 7$$

where $\mathbf{j}_{\hat{R}_\lambda}^{\lambda n_\lambda}$ and $\mathbf{j}_{\hat{r}_\lambda}^{\lambda n_\lambda}$ are the components of the current density vector for each axis. The streamlines are a particular solution to this differential equation. This equation can be solved either by defining the stream function Φ or by integrating starting at any point in configuration space. The stream function is actually a consequence of the continuity of the system and for two dimensional motion in the mathematical space the stream function is defined by

$$\mathbf{j}_{\hat{R}_\lambda}^{\lambda n_\lambda} = \frac{\partial\Phi}{\partial r_\lambda} \qquad 8$$

$$\mathbf{j}_{\hat{r}_\lambda}^{\lambda n_\lambda} = -\frac{\partial\Phi}{\partial R_\lambda}. \qquad 9$$

In contrast to the equations defining the velocity potential, the scalar field whose gradient is the velocity, one of the components of the current density is the negative derivative of the field function. As expected the stream function always satisfies the principle of continuity,

$$\frac{\partial}{\partial R_\lambda}\frac{\partial \Phi}{\partial r_\lambda} - \frac{\partial}{\partial r_\lambda}\frac{\partial \Phi}{\partial R_\lambda} = 0. \qquad 10$$

Lines of constant Φ are found to be streamlines. The equation for the streamlines in terms of the stream function is

$$\frac{\partial \Phi}{\partial R_\lambda} dR_\lambda - \frac{\partial \Phi}{\partial r_\lambda} dr_\lambda = 0. \qquad 11$$

where $\mathbf{j}^{\lambda n_\lambda}_{\hat{R}_\lambda}$ and $\mathbf{j}^{\lambda n_\lambda}_{\hat{r}_\lambda}$ have been used. This equation is the total differential $d\Phi$, with respect to distance, of the function Φ. Hence any streamline can be expressed as a function of Φ and is described by the relation $d\Phi = 0$. Another way of looking at it is to recognize that the streamlines are simply the contour lines of the stream function. In addition, each streamline carries with it an element of flux. The streamlines never cross since everywhere the wavefunction is single-valued and continuous. The concept of streamlines comes from the motion associated with a fluid, whereas the idea of a classical trajectory is associated with the motion of a single particle. The differences become apparent when one considers that through any point in the potential a number of classical trajectories may pass and the direction of the flux through the point is a weighted average of the directions of the trajectories.

It has already been stated that the quantum mechanical streamlines do not cross due to the single-valuedness of the wavefunction. This resulted directly from the continuity equation from which other consequences also arise. Applying the divergence theorem to the vector field shows that for any closed contour C which encircles the reaction zone, the integral

$$\int_A \nabla \bullet \mathbf{j}^{\lambda n_\lambda} dA = \oint_C \mathbf{j}^{\lambda n_\lambda} dl \qquad 12$$

vanishes. The area inclosed by the contour C is denoted by A and the boundary line element is *dl*. The normal flux of $\mathbf{j}$ through a line segment connecting any two

streamlines is independent of the placement or shape of the line. This flux is a constant between the two streamlines and is a consequence of the conservation of particle flux in the chemical reaction. The total flux is related to the incident flux by

$$\mathbf{J}^{\lambda n_\lambda} = \int_L \mathbf{j}^{\lambda n_\lambda} \bullet dl = P^{\lambda n_\lambda} Q_{inc}^{\lambda n_\lambda}. \qquad 13$$

The total current can be devided into three separate kinds which do not mix due to the noncrossing nature of streamlines. If the two streamlines which become tangent to the energy contour of the potential at the total energy E are considered, then the current between these two limiting streamlines is the classical current. This current is confined exclusively to the classically allowed regions of configuration space. Combined, the other two types of currents contribute to tunneling. They can either sample the regions of configuration space where the atoms become very close or where the atoms are spread farther apart than the bonds typically go. These currents are the inner and outer currents respectively. Each type of current is constant across any cut through the potential beginning and ending where the wavefunction is zero. The coefficient arising from taking the ratio of the tunneling flux to the incident flux is multiplied by the total reaction probability to give the tunneling probability for the reaction. If the asymptotic form of the wavefunction consists of only the ground vibrational state, then $\mathbf{j}_{\hat{r}_\lambda} = 0$ and $\mathbf{j}_{\hat{R}_\lambda} = \frac{\hbar k_0}{2\mu}(1-P)$ in the reactant channel. Similarly, in the product channel the magnitude of the component of $\mathbf{j}$ transverse to the channel is zero and the magnitude of the component parallel to the channel is equal to $\mathbf{j}_{\hat{R}_\lambda}$. This means that the streamlines enter the saddle point region parallel to the reactant channel and exit parallel to the product channel. The general form of $\mathbf{j}$ for both asymptotic regions indicates that if more than one vibrational state is energetically available the transverse component of $\mathbf{j}$ no longer vanishes. This results in an expected oscillatory behavior for the streamlines in the asymptotic regions.

Cl + H(D,T)Cl → ClH(D,T) + Cl

REACTIONS

REACTION PROBABILITIES

STREAMLINES

TUNNELING FRACTIONS

RESONANCES

THE Cl + HCl REACTION

Hydrogen atom transfer from one halogen atom to another is a process that constitutes a majority of the reactions whose difficulties in the calculations of reactive cross-sections are a direct consequence of their small skew angles. The exchange of a hydrogen atom between two chlorine atoms is just such a reaction and until the advent of hyperspherical coordinate approaches reliable reactive transition probabilities for this process were unobtainable except through experimental means. Dynamical information about the chemistry of this exchange reaction becomes available with the implementation of a spherical polar representation and the analysis provided by streamline and tunneling fraction calculations.

The Cl + HCl → ClH + Cl reaction[6] and its hydrogen isotope counterparts are important reactions for the experimental and theoretical considerations of the effects of vibrational excitation on reaction probabilities and rate constants. The question addressing the vibrational relaxation of excited reagents is also of concern because the effective vibrational deactivation by potentially reactive atoms, such as Cl, represents a large loss of potential power in some chemical laser systems. They are also fascinating model systems for the study of the many competing energy transfer processes and chemical reactions occurring under nonequilibrium conditions. Vibrational deactivation is considered an important elementary step in the quantitative description of nonequilibrium situations found in flames, electrical discharges, and laser induced chemical reactions.

This reaction has continued to be an evasive one. Although the tight curvature of the reaction path can now be addressed appropriately in the hyperspherical framework, the nature of the potential energy surface still draws investigation both experimentally and theoretically. Saddle point regions of the potential having a wide variety of barrier heights match different sets of experimental data and span a large enough range that quantum calculations produce significantly different results for collinear reaction probabilities. Classical trajectory calculations have also been performed on this reaction.[48,57]

THE ClHCl POTENTIAL ENERGY SURFACE

The nature of the Cl + HCl potential energy surface has been the subject of a great deal of conflict in both the experimental and theoretical literature of the past. One of the original controversial issues stemmed from contradictions to the experimental work of Klein[27] that proposed the ClHCl potential surface contained a well rather than a barrier in the strong interaction region as he proposed. Evidence for this conclusion came about from the assignment of infrared spectra observed in matrix isolation studies by Noble and Pimentel.[ref.6] More recent research has shown that the spectroscopically bound species, leading to the conclusion that the surface contained a well, was ClHCl- rather than ClHCl itself.[43] Even though this issue has been settled, the issue encompassing the height of the reactive barrier has not.

Electronically nonadiabatic processes such as

$$Cl(^2P_{3/2}) + HCl(v=1) \rightarrow Cl(^2P_{1/2}) + HCl(v'=0)$$

are energetically possible, however direct experimental measurements of the rate coefficient for this reaction have shown that the vibration-electronic energy transfer contributions to the deactivation of vibrationally excited HCl constitute less than one percent of the overall process.[28] Thus an electronically adiabatic potential energy surface is typically assumed for describing ground electronic collision dynamics for the collinear dominated reaction.

Klein's experiments of 1964 yielded an Arrhenius activation energy around 0.259 eV. The experimental calculations done by Noble and Pimentel were supported by the results of BOBE calculation in an analysis of symmetric X-H-X species. Both provided a well depth of -0.067 eV. However, it seemed unlikely that the symmetric Cl-H-Cl complex would remain stable with respect to dissociation into ClH and Cl, and two groups have since determined the species observed was the isolated ClHCl- anion. Pulsed HCl chemical laser experiments

by Kneba and Wolfrum[28] have lead to a proposed barrier height of 0.373 eV. *Ab initio* calculations by Meyer[9] gave a barrier height of 1.36 eV at the restricted Hartree Fock self-consistent field level. This valued appeared too high and the coupled electron pair approximation suggested a barrier in the range of 0.725 eV. Addition of the remaining correlation errors reduced the barrier to a value somewhere between 0.083 and 0.311 eV. The best agreement with experimental rate constants was observed for a LEPS surface with a 0.0415 eV barrier. However, the best agreement with vibrational relaxation rate coefficients comes from employing surfaces with wells. The assortment of possible descriptions for the transition region of the potential has not converged towards a conclusive answer and thus reactive scattering using a variety of surfaces still provides valuable information on the reaction.

Garrett and Truhlar have performed *ab initio* POL-CI calculations augmented by a dispersion term to evaluate the potential for the ClHCl reaction.[11] They discovered that the saddle point has a nonlinear geometry and thus the minimum energy path is not collinear as was previously assumed. This was especially surprising for the case with the hydrogen atom in the middle. Their calculations provided a barrier height of 0.446 eV at the POL-CI level and 0.273 eV at the POL-CI plus dispersion level. However, it turns out that the collinear geometry is only about 1 kcal/mole higher in energy than the nonlinear saddle point.

Two different LEPS surfaces[51] were used in the current quantum mechanical calculations. The two potential energy surfaces correspond to those used by Smith[55] for classical trajectory calculations an have parameters listed in Table 1. Surface A has a barrier height of 0.285 eV and conforms closely to the experimentally determined activation energy.[27] This is near the upper limit as established by the *ab initio* calculations[9] and resemble the values predicted after correcting for dispersion interactions in Garrett and Truhlar's work.[11] In contrast, the barrier of surface B lies near the lower limit at 0.096 eV and shows much better agreement with the quasiclassical trajectory calculations and experimental deactivation processes for $^{35}Cl + D^{37}Cl$. Since surfaces A and B have barriers

close to the upper and lower limits for this reaction it is reasonable to expect the actual value of the barrier to lie somewhere in-between. Both surfaces are shown in Figures 2-4 and their corresponding minimum energy path profiles are shown in Figures 5-7 for the Cl + HCl, Cl + DCl, and Cl + TCl reactions respectively. The horizontal lines indicate the vibrational energies of the isolated H(D,T)Cl(v=0) and H(D,T)Cl(v=1) diatomics.

FEATURES OF THE REACTIONS

Results for the collinear Cl + HCl reaction, and its hydrogen isotopic equivalents D and T, are presented with an emphasis on the effects of vibrational excitation on state-to-state and total reaction probabilities and rate constants, for which little attention as previously been directed. The crucial element of curiosity is that the barrier height of the potential surface plays the vital role in determining the final reaction rate when the reagents are vibrationally excited, but in a manner completely contrary to expectations. Other phenomena stemming from the unique structure of highly skewed reactive systems are also found in these three reactions.

All three reactions exhibit an overall oscillatory behavior in the reaction probability verses energy profiles. Two major points of difference arise between the reactive systems under consideration. The first is that the frequency of oscillation increases as the mass of the central atom decreases. Secondly, as the energy increases the curves oscillate more slowly. The oscillatory reaction probability, which has been found to be characteristic of heavy-light-heavy chemical systems and has been observed in quantum mechanical systems such as I + HI $\rightarrow$ IH + I, can be described to some degree quantitatively by a simple semiclassical WKB approximation.[1,4]

By examining the state-to-state reaction probabilities it becomes readily apparent that all three of these reactions are dominated by conservation of the vibrational quantum number. Weighted Delves' polar coordinates are exceptionally useful in the analysis of the adiabatic effects of heavy-light-heavy

reactions. As a result, vibrationally adiabatic molecules are supported in the strong interaction region of the potential energy surface. Many calculations have shown that the vibrational adiabatic approximation improves as the mass ratio of the light atom to that of the heavy atom decreases. It has also been found that the nonadiabatic transitions are nearly equal in the reactive and nonreactive realms.

Superimposed on the reaction probability curves is a very distinct and sharp resonance spectrum. For the hydrogen exchange reaction the surface appears to support more resonances as the barrier height decreases. As the mass of the central atom increases the resonances increase in number on both surfaces. The resonances are most noticeable in the adiabatic transition curves but are also present in the nonadiabatic transitions.

Each of the previously mentioned phenomena will be addressed in turn with the major focus on the differences between isotopic systems and the changes in each feature with varying barrier height. The most crucial question centers around the low reactive probability for vibrationally excited reagents and how the dramatic change with barrier height arises. Quantum mechanical streamlines aid in determining weather or not this odd phenomenon is inherently quantum or classical in nature by mapping out the accessed regions of the different potential energy surfaces by the reactions.

REACTION PROBABILITY PROFILES

Collinear reactive transition probabilities of a Cl atom with a ClH(D,T) diatomic molecule are determined using renormalized Numerov integration in the coupled-channel method and are shown in Figures 8-10. The energy scale is that of the total energy of the system measured from the bottom of the reactant diatomic well, which is also the bottom of the product channel since the reactions are symmetric. For all three isotopic equivalents of this reaction, the change of basis between the sets of surface functions was performed using the inverse of the overlap matrix rather than the transpose. Therefore, all reported symmetry and

unitarity of the logarithmic derivative and scattering matrices is an absolute measurement of the accuracy of the calculation.

For the Cl + HCl → ClH + Cl reaction 20 basis functions were used for all energies. The propagation began at $\rho = 6.0$ bohr and ended at $\rho = 25.34$ bohr with the projection of the logarithmic derivative at $\rho = 25.18$ bohr. Surface functions were calculated numerically every 0.10 bohr and there were 6 integration steps for each $\bar{\rho}$ including $\bar{\rho}$ itself. In all of these calculations $\bar{\rho}$ was taken as the first step in the integration sector. The skew angle of this reaction is very small at 13.54° and therefore the hyperspherical coordinate approach is ideal. Surface A was calculated with a base energy grid of 0.005 eV, however the resonances superimposed upon the reaction probability profile have denser energy grids ranging from 0.0001 to 0.0025 eV depending on the nature of the resonance. The surface B plot was calculated with a base energy grid of 0.0025 eV and the resonances with energy grids ranging from 0.00005 eV to 0.0002 eV. All results shown for energies up to 1.0 eV are converged to better than 0.5% on both surfaces and the highest energy calculations are converged to better than 0.8%.

The Cl + DCl → ClD + Cl reaction probabilities were calculated with 28 surface functions in order to get quality convergence at the highest energies plotted which have 8 to 10 available transitions. Again the surface functions are spaced apart by 0.10 bohr in the ρ coordinate and the calculation goes from $\rho = 6.0$ bohr to $\rho = 25.36$ bohr. The energy grid for surface A is 0.005 eV and the grid for surface B is 0.001 eV. The skew angle is larger than that of the H exchange reaction opening up to an angle of 18.92°. The convergence for this reaction was better than 1.0% for energies below 0.70 eV and better than 2.0% for the higher energies recorded.

Due to the complicated structure in the Cl + TCl → ClT + Cl reaction care was taken to generate accurate results for the transition probabilities without cluttering up the figures, thus the resonances are shown but not in their full form. The energy grids are constant but still fine enough to show the locations of the resonance structure, especially for surface B. Their are 36 surface functions and the integration goes from $\rho = 5.0$ bohr to $\rho = 24.35$ bohr with surface functions

taken every 0.10 bohr. This reaction has a slightly larger skew angle than that for deuterium at 22.92°. Convergence at the lower energies is better than 1.0% and at the higher energies better than 2.5% on both surfaces. State-to-all transition probabilities for the three reactions are compared in Figures 11 and 12 for the ground and first excited vibrational states on surfaces A and B respectively.

Surface A has a barrier of 0.285 eV and all three reactions exhibit similar patterns for the ground state reaction by only displaying significant amplitude approximately 0.1 eV above the opening of the vibrational level and a smooth oscillatory pattern thereafter. A noteworthy point of interest follows if one considers that although the barrier height of this surface is 0.285 eV, there is a non-negligible fraction of both the deuterium and tritium reactions occurring for energies just below this energy. In contrast, the hydrogen exchange reaction probability is on the order of 10^{-7}. This is an odd circumstance since all reactions below the barrier must occur via tunneling and lighter atoms are expected to tunnel more readily than their heavier isotopes, in this case the H more so than either the D or T atoms. Further comparison of the plots reveals that the most outstanding difference is the strong resonance appearing at E = 0.30 eV in the Cl + HCl reaction but which is absent from the heavier isotope exchanges. However, the deuterium and tritium reactions do show sharp resonance peaks at energies just above the opening of higher vibrational states.

The vibrationally excited state reactions on surface A show a very distinct and sharp resonance pattern at the opening of the v=2 state for each isotope. Note that as the mass of the central hydrogen atom increases the resonances become wider. Furthermore, as the reaction changes from using H to T there are fewer resonances appearing in the excited state reaction in contrast to the increase in the number of resonances when considering the ground state case. There is a slight difference in the reaction probability plot for the tritium case compared to the other two. Initially the reactions for the two lighter isotopes are negligible until they suddenly jump to unity at a specific translational energy which occurs well before the opening of the second vibrational state and the resonances, but the reaction involving tritium exchange rises less dramatically, although it is also

negligible until some threshold translational energy is reached. It does not approach unity until well after the opening of the third vibrational state and well past the resonance structure. Compared to the ground state reactions, the excited state reaction probabilities become less regularly sinusoidal in their structure due to the increasing contributions of non-adiabatic transitions.

Surface B reaction probability plots for all three reactions have a great deal more structure than those of surface A and have even more striking differences between isotopes. The barrier height of surface B is 0.096 eV, much lower than that of surface A and no tunneling through the barrier can be observed since the lowest open state for each reaction is higher than this energy. The ground state reactions all have the same general shape but the difference is in the low energy range of the deuterium reaction. Note how steeply the reaction probability rises in this case whereas for the hydrogen and tritium reactions, which are almost identical in shape, it is more gradual, reaching the maximum no less than 0.2 eV after the opening of the state. The second dramatic feature is that of the sets of resonance spectra occurring at the opening of each vibrational state. The ground state transitions for Cl + HCl has first a set of 5 resonances around the energy where v=1 opens followed by a set of 7 resonances just before v=2 opens. The second set of resonances are very small but they do correspond exactly with the 7 resonances in the excited state curve. Notice that each set of resonances occurs just before the opening of a vibrational state. The excited state reaction probability also shows a threshold resonance at an energy barely above v=1. In the Cl + DCl transition the ground vibrational state plot has a set of 4 resonances where v=1 opens and a small residue of the sets of 4 and 6 resonances appearing in the v=1 plot at energies corresponding to the opening of v=2 and v=3. The tritium reaction is even more complicated supporting resonances in sets of 3, 5 and 6 seen in both the ground and first excited state reactions. These resonances are visible in both the adiabatic and nonadiabatic transitions of all three reactions.

Comparing the three excited state plots reveals a startling phenomena. Apparently the reaction is drastically inhibited by vibrational excitation of the reagent diatomic molecule for the light atom reactions but is concurrently

accelerated for the tritium exchange as can be seen in the sudden jump to unity just after the state opens. This is very odd since all the v=1 states are well above the barrier and the reactions went quickly when the barrier was much higher. As previously mentioned, the H exchange reaction on this low barrier surface produces a threshold resonance, however, afterwards the reaction probability is near zero. The deuterium reaction begins initially but is quickly snuffed out until the second vibrational state energy is reached at which point it gradually rises, although whether or not the reaction probability eventually becomes unity or not is inconclusive from the data shown. Contrary to the delay of reaction seen for the lighter two isotopes, the tritium reaction appears to take off violently when the reagents are vibrationally excited. All three have multiple resonances appearing in sets but the hydrogen reaction only displays a single set of resonances, those just before v=2 opens, rather than a set before every opening vibrational state energy as seen with D and T.

Looking at the reactive transition probabilities as they compare across the two surfaces brings out some very important questions. The first question is why does the reaction for ClH and ClD occur so readily for the high barrier surface and so reluctantly for the low barrier surface when the reagents are vibrationally excited? Intuition would suggest the opposite to happen as it does in the tritium case. Secondly, why does the tritium reaction differ from the other two so greatly? If we argue that the mass of the tritium is the difference then why are the other two reactions so similar? After all, the mass ratio of D to H is 2 but the mass ratio of T to D is 1.5. This would seem to indicate that the reaction with T should be more similar to the reaction with D than the D reaction is with the H reaction. Finally, how come the resonances on surface A tend to occur after the vibrational states open but on surface B they occur before the opening of the vibrational states.

ADIABATIC APPROXIMATION

State-to-state transition probabilities for Cl + H(D,T)Cl $\rightarrow$ ClH(D,T) + Cl on both surfaces A and B are shown in Figures 13-18. All three reactions have

oscillating nonadiabatic and adiabatic reaction probabilities, but are dominated by the vibrationally adiabatic transition. Although they are primarily localized on the adiabatic transition plots, the resonance features also appear in the nonadiabatic curves.

It is immediately obvious that over 95% of the reactive probability for hydrogen transfer preserves the vibrational quantum number for the ground state reaction on the high barrier surface at all energies considered, but that the other surface is only dominated by the adiabatic transition at energies below 0.80 eV. When the hydrogen atom is replaced with its deuterium isotope the preservation of the vibrational quantum number continues only not nearly as dramatically as when hydrogen is used. Only 85% of the total reaction probability is due to adiabatic transitions compared to the 95% in the hydrogen case. This is because of the doubling of the mass ratio between the light and heavy atoms of the reaction and the resultant opening of the skew angle. When tritium is used the nonadiabatic transitions contribute 30% to the total reaction probability.

The differences between the isotopic systems are readily explained when one considers how the shape of the potential surface changes with increasing mass ratio. The potential energy surface for this class of reactions is characterized by the presence of two long almost parallel channels connected to a very wide transition state region. Consequently, the classical action variable for the motion parallel to the channel width remains largely unchanged during the slow approach of the reactants due to the modest change of the vibrational well over the vibrational period of a classical trajectory. The ClH vibration is then viewed as being transformed briefly, for half of a vibrational period or so, into the asymmetric stretching vibration of the ClHCl complex. Once the reduced mass has passed into the products channel its trajectory remains in the same vibrational state as the initial reactants. When the mass of the central atom is increased the skew angle also increases and the parallel nature of the potential channels is diminished. This leads to a greater change in the structure of the ClDCl or ClTCl complex as the asymmetric stretch mode along the minimum energy path becomes more complicated. The transfer of the central atom is not the same motion as it was in

the lighter atom case where the classical trajectory would bounce between two parallel repulsive walls. In these cases the classical trajectory can come free of a repulsive wall at an angle causing a different vibrational frequency as the particle of reduced mass continues into the products channel. Therefore, the vibrational quantum number of the products has a much greater chance for variation away from its initial value as the skew angle widens.

When a reaction results in the transfer of a very light atom from one heavy atom to another, as in the case of the Cl + HCl → ClH + Cl, the translational motion of the heavy Cl atoms is hardly influenced. In other words, the translational motion of each Cl atom and of the entire system is almost completely conserved, $E_{react,\ tr} = E_{prod,\ tr}$. Consequently, quasiconstants of the motion, such as the generalized vibrational quantum number, can also be approximately conserved throughout a collision.[4] Separation of the Hamiltonian in an appropriate set of coordinates allows quasiconstants of the motion to be extracted if one of the descriptive coordinates is associated with the desired generalized vibration. As the mass ratio of the light atom to that of the heavy atoms decreases this separation prevails even more and the conservation of vibrational quantum number becomes more absolute. For this classification of reactions the large differences in masses points to an effective Born-Oppenheimer type adiabatic separation between the light atom motion relative to any of the heavy particles and the motion of the heavy particles themselves. In Delves' coordinates the hyperradial coordinate ρ depicts the slow relative motion of the approaching and separating Chlorine particles while the angular coordinate α corresponds to the vibrational movement of the light hydrogen atom. In these coordinates the potential surface is characterized by the nearly parallel nature of the two asymptotic channels arising from the large curvature in the transition state region.

OSCILLATING REACTION PROBABILITY

For a symmetric reaction the potential energy function $V(\rho,\alpha)$ is symmetric about the angle $\theta/2$. Consequently, two independent sets of eigenfunctions, a symmetric set and an antisymmetric set, are supported in the angular coordinate at each hyperradial cut. Because all the coupling elements between the two sets of eigenfunctions vanish, the system of ordinary coupled differential equations in the coupled-channel expansion can be decoupled into two systems for the coefficients of the symmetric and antisymmetric surface functions. In the asymptotic region the potential has separated into two distinct channels and the symmetric and antisymmetric eigenvalues become degenerate. The asymptotic surface functions are written as a linear combination of the diatomic symmetric and antisymmetric states

$$\phi_v^{\alpha,\gamma}\left(r_{\alpha,\gamma}\right) \sim \frac{1}{\sqrt{2}}\left[\phi_v^g \pm \phi_v^u\right].$$

Upon separation of the Hamiltonian an infinite set of ordinary coupled differential equations for the coefficient functions b are obtained. The desired coefficients must then be written as a linear combination of the corresponding symmetric and antisymmetric coefficients in the manner

$$b_v^{\alpha,\gamma}\left(\rho;\bar{\rho}\right) = \frac{1}{\sqrt{2}}\left[b_v^g\left(\rho;\bar{\rho}\right) \pm b_v^u\left(\rho;\bar{\rho}\right)\right].$$

In order to see where the oscillating nature of the reaction probability curves arises it is useful to look at the vibrationally adiabatic transitions which dominate these heavy-light-heavy reactions since the separability of ρ and α causes the coupling elements between the vibrational states of the system to be small. Writing the asymptotic solutions to the Schrödinger equation in terms of the scattering matrix for the adiabatic case gives

$$\psi = \left[e^{(-ikR)} + S^N_{v,v} e^{(ikR)}\right]\phi^{\alpha}_{v}(r) + S^R_{v,v} e^{(ikR)}\phi^{\gamma}_{v}(r).$$

where $S^N_{v,v}$ and $S^R_{v,v}$ are the amplitudes of the nonreactive and reactive outgoing waves respectively. Recall that the scattering matrix elements are complex quantities and therefore have an associated phase. Therefore, the scattering matrix elements can be written in terms of the elastic phase shifts ξ^g_v and ξ^u_v ,

$$S^N_{v,v} = \frac{1}{2}\left[e^{2i\xi^g_v} + e^{2i\xi^u_v}\right] = e^{\left[i\left(\xi^g_v + \xi^u_v\right)\right]}\cos\left(\xi^g_v + \xi^u_v\right)$$

$$S^R_{v,v} = \frac{1}{2}\left[e^{2i\xi^g_v} - e^{2i\xi^u_v}\right] = e^{\left[i\left(\xi^g_v + \xi^u_v\right)\right]}\sin\left(\xi^g_v - \xi^u_v\right).$$

The reactive probability is proportional to the square of the magnitude of $S^R_{v,v}$ thus eliminating the complex phase in the exponential and leaving a real quantity related to the oscillatory nature of trigonometric functions. Hence the zero order approximation to the reactive transition probability in a symmetric hydrogen transfer reaction becomes

$$P^R_{v,v} = \left|S^R_{v,v}\right|^2 = \sin^2\left(\xi^g_v - \xi^u_v\right).$$

This oscillating reaction probability can be understood as a two state interference pattern for scattering on the gerade and ungerade vibrationally adiabatic effective potentials. This phenomena originated from the vibrational adiabaticity of heavy-light-heavy reactions.

It is obvious from the figures that the oscillating reactive probability deviates from the proposed pattern across the energy range sampled. The explanation for this comes from Figures 62-64 which show the eigenvalue curves as a function of the hyperradius ρ. These curves have gerade and ungerade states for each pair of eigenvalues that begin separately but become degenerate in the asymptotic region. At small values of ρ the curves are nearly parallel due to the single well form of the interaction potential near the three atom coincidence. It is this strongly repulsive region of the potential that effects the high energy range of

the reaction probabilities. The result is a phase shift of both the gerade and ungerade states although because the curves are not exactly parallel these shifts change with increasing energy. A semiclassical analysis shows that the change is monotonically increasing as $E^{1/2}$, and is in accord with the infinitely steep wall collision model. At low energies the reaction probability is influenced by the behavior of these curves at larger ρ. In this region the phase ξ_u increases more rapidly with energy than does ξ_g due to the well in ε_g. Therefore the difference in elastic phase shifts decreases slightly for low E. An analytic form incorporating these observances is

$$P_{v,v} \approx \sin^2\left(a + bE_{trans}^{-1/2}\right) .$$

The constant b is related to the mass difference and turning points and the constant a is associated with the low energy realm. In this expression the phase shift difference increases monotonically with E_{trans}.

Oscillations in the reaction probability are clearly seen in Figures 8-10 for the reaction Cl + H(D,T)Cl on surfaces A and B. For the ground state reactions the oscillatory behavior is very regular and smoothly decreases in frequency as both the mass of the central atom becomes larger and the energy increases. The differences between the two surfaces for all three cases include the presence of a very sharp peak in surface A at the lowest energies which is absent from surface B. In the hydrogen exchange reaction this first peak is a very strong resonance, however, it is not for the case of the heavier isotopes. There is no indication of a similar type of quickly oscillating structure in the low energy region on surface B. In fact surface B begins with very slow oscillations in the ground state, oscillating with a frequency more similar to that of the higher energy pattern seen on surface A.

For Cl + HCl the state-to-state reactive probabilities for the energetically accessible transitions all show the sinusoidal tendencies peaking at approximately the same total energy. This pattern is seen on both the high barrier and low barrier surface. When the hydrogen atom is replaced with a deuterium atom and

subsequently a tritium atom the trend almost continues, where the peaks of the profiles occur near the same energy in all three transitions for the reactions on both surfaces in the ground state. The exception appears when tritium is exchanged on surface A. Both the off diagonal transitions tend to zero at the energy in which the adiabatic transition is a maximum.

Looking at the vibrationally excited state transitions a semblance to the sinusoidal pattern exists but is distorted. Surface A has a sudden jump to unity for both of the smaller central atoms followed by a rather steep decrease. For hydrogen the reaction probability comes off of the steep decent into a widening curve at the bottom of the oscillation, appearing to decrease in frequency more rapidly than predicted. In the energy range between 0.8 eV and 1.4 eV the total reaction probability is dominated by the nonadiabatic transitions from the v=1 vibrational state to the v=0 and v=2 states. The breakdown of vibrational adiabaticity becomes apparent in this case and can be attributed to the strongly repulsive nature of the ρ eigenvalue curves and the opening of the second vibrationally excited state.

For the deuterium reaction the decent from unity is slightly thwarted near the v=3 opening energy causing the reaction probability curve to take on a more linear shape and drastically changing the sinusoidal nature of the plot. Comparing the contributions of the reactive transitions show that the shape of the tail of the Cl + DCl reaction for the excited state is heavily influenced by a contribution from vibrational relaxation. The deuterium reaction state-to-state reaction probabilities on both surfaces tend to not have peaks and valleys in the same energy region. The difference from the pattern found in the hydrogen reaction is that the ground and first vibrational state do match each other for surface B but not for surface A. Simultaneously, the second excited state matches well with the ground state oscillations on surface A but with nothing on surface B.

Contrary to both the afore mentioned reactions, the exchange of tritium does exhibit a nicely oscillating structure for the v=1 total reaction probability, even though the requirements for adiabaticity are not as well satisfied for the heavier isotope. However, the state-to-state transitions in this case show that

excitation to the second vibrational level has the same qualitative shape as the adiabatic transition on both surfaces and that neither match the relaxation process. Overall is appears that many of the oscillations are synchronized but that the few which are not tend to be more random with increasing isotope mass and lead to the deviations from pure oscillatory behavior of the total reaction probability curves.

A small skew angle and therefore a favoritism towards adiabatic transitions promotes the oscillating behavior of reaction probability *verses* energy curves of the collinear light atom exchange reaction between chlorine atoms. However, this same structure is seen in the off diagonal transitions and in some cases provides the overwhelming structure of the total reaction probability, especially at higher energies.

REACTION RATE CONSTANTS:

One of the clearest means of viewing the effects of the different barrier heights on the rate of reaction between the two surfaces is with state-to-all reaction rate constant plots. The microcanonical rate constant is a function of energy and absolute temperature and can be calculated from the reaction probability by the relation

$$k(T,n)=\left(\frac{1}{2\pi k_B T}\right)^{1/2}\int_0^{\infty} P(E_n)e^{-\frac{E_n}{k_B T}}dE_n.$$

In this expression it is important to note that the energy here is the relative translational energy and not the total energy of the system. An exponential term multiplies the probability of reaction and the area under the product curve is integrated. The constant in front of the integral is a normalization factor with the crucial point that the reduced mass used is that for atom A with the center of mass of molecule BC and not the total Delves' scaled reduced mass of the reaction. Rate constants in this form have units cm molecule^{-1} sec^{-1} because this is a collinear reaction and is in one dimension.

The rate constants for the reactions are shown in Figures 19-21. Each picture shows both the ground state reaction and the excited state reaction on the same surface. Both the hydrogen and deuterium exchange reactions feature a slower rate constant on the lower barrier LEPS surface than on the higher barrier surface for vibrationally excited reagents. Clearly the ground state reaction rate on surface A is slower than the excited state reaction rate. It is also slower than the ground state reaction rate on surface B. Both of these observations make sense since the reaction should proceed more quickly if there is either less hindrance for completion, as seen with the lower barrier of surface B, or more energy available, as in the case of the excited diatomic molecules. Looking at the reaction rate curve for the excited state reagents on the low barrier surface however, does not make sense. This reaction rate is not only slower than the excited state reaction rate for surface A, but also the ground state reaction rate of surface B. At temperatures above 500° even the ground state rate constant for surface A is higher than that of the excited state rate constant on surface B. The reaction coordinate profiles show that there is more than sufficient energy to overcome the barrier, and with the reaction rate so much higher than that of the ground state on the A surface, there is no indication that vibrational excitation subverts reaction.

The tritium reaction does not appear to be inhibited in the same manner when vibrational energy is added to the system. As one would expect, the rate is always faster for the excited state than for the ground state reaction. Secondly, the rate of reaction is substantially higher for the low barrier surface than for the high barrier surface for each comparative quantum level, especially in the low temperature range. For temperatures approaching 1500° the differences in rates on the two surfaces are relatively small.

Somehow the reactions on the two surfaces are drastically dependent on the saddle point region of the potential giving completely different reaction mechanisms for different vibrational states. The phenomenon occurs for the light atoms H and D so one immediate argument is that tunneling contributions through the barrier are dominating the reactions on the high barrier surface. This suggestion has some merit, but the details of the tunneling paths are equally as

informative about the role of tunneling in favoring one reaction path over another. Whether or not the high barrier promotes reaction or the low barrier inhibits reaction will be determined most clearly with the aid of streamline plots of the current density and tunneling fractions of the reaction probability.

STREAMLINE ANALYSIS

Answering questions about the reactive mechanism behind the transfer of H, D or T from one chlorine atom to another is best accomplished through the calculation of quantum mechanical streamlines and flux density contours. Information analogous to that contained in the vector fields describing fluid flows can be extracted for the flow of a reaction through a potential surface with the probability current density **j**. This quantity not only traces out the path for reactive scattering through the potential surface but also provides a particle density map along that path. Knowing how tight or loose the particle flow is in particular regions provides the best insight of how and to what degree the surface features effect the reaction.

The streamlines for the hydrogen, deuterium and tritium exchange reactions on surfaces A and B are plotted for a range of energies at the top of Figures 22-49. Each set of streamlines has been superimposed on the potential energy contours of the appropriate surface to explicitly show how the various regions effect the particle flow at each energy and how the flux changes as the energy increases. The dashed contour line labeled E is the potential contour at the specified energy for the streamlines. This contour represents the classical limits of the surface and any streamline which crosses E is inherently associated with tunneling flux.

Another important aspect is that concerning the quantum vortices that exist in the streamline plots but which are not shown on the streamline figures themselves. These are circular flows, as can be seen in the schematic of Figure 49.a, which contain no particle flux and in some cases may be associated with resonances. Streamlines starting at points in the region of a vortex form closed curves forming a boundary which no flux originating outside of may penetrate. The vortex is analogous to placing a solid object into a flowing stream and thus has the ability to force the flow of the particle flux in one direction or another.

Typically five streamlines are superimposed on the potential contours. Each streamline is defined as the line tangent to the current density vector at every

point. In the figures, the streamlines are drawn with a select group of the current density vectors in tact, denoted by the arrows. The current density vectors have a magnitude calculated at the center of the portrayed arrow and are drawn so that they conform to the curvature of the streamline as a whole. The center streamline is that for the largest current density calculated at the energy and the two streamlines on each side are spaced from the center line and from each other at a distance inversely proportional to the length of the current density vector at the point. The outer most sets of current density vectors carry very little of the reactive flux, a combined total of less than 5%, and are shown mearly as visible aids to the completeness of the figure. This is easily conferred through the current density profiles which will be discussed next.

The plots accompanying the streamlines are the probability current density profiles. These diagrams show the cross-section of flux normal to each of the five cut lines placed perpendicular to the minimum energy path. Because of the continuity equation and its results the total flux though each of the five cuts is identical and is represented by the area of each curve. Therefore, the area under each curve is normalized and the amount of reactive flux passing through a general area of the potential can be estimated or calculated by looking at the fraction of the area of the curve that is in intersected by the current of interest. As the reaction proceeds through the surface the curves change shape either spreading out into a flatter shape, which means the flow is less constricted and more evenly distributed, or pulling up into a high peak indicative of a more condensed flow though a small cross-section of the potential. In some cases these curves have negative components which arise from the presence of vortices who's centers are at the nodes in the current density profiles. Two streamlines are superimposed on the potential surface along with the current density profiles. These two streamlines are the limiting streamlines of the reaction and are tangent to the energy contour E at one point.. Any streamlines lying between these two limiting streamlines carry exclusively classical flux, reactive flux that samples only the classical regions of configuration space. All other streamlines carry tunneling flux.

The five visible streamlines in each of the Figures 22-24 and Figures 25-27 clearly show that the ground state reactions on surfaces A and B are quite different for the Cl + HCl $\rightarrow$ ClH + Cl reaction. When the reagents are in the ground vibrational state, the majority of the reactive flux passes through the strong interaction region of the potential on the corner cutting side of the saddle point for the high barrier surface. In other words, the reaction is more likely to occur if the configuration of the triatom complex has two stretched bonds. The bonds are longer and more strained than the minimum energy configuration which would be synchronous with the location of the saddle point. As the energy increases, the streamlines gradually shift towards the deep corner of the potential and the preferred mechanism of reaction comes close to resembling that predicted by the minimum energy path passing through the saddle point. This can easily be seen in the sequence of Figures 22-24, where the energy changes from 0.40 eV to 0.80 eV and the current density passing through the saddle point increases from nearly nothing to about 40% of the total flux. At the lowest energy, where only one vibrational state in the product channel is open, the streamlines tend to follow a straight path in the asymptotic regions of configuration space. However, as the total energy increases, surpassing the opening of additional vibrational states, the streamlines become more oscillatory. This is a result of the nonzero value in the transverse component of the current density vector introduced by the additional open states. In the current density profile diagram of Figure 24 the cut along the saddle point has a node, which can be attributed to a single vortex as shown in the top picture of Figure 49.a. This vortex is exclusively in the classically forbidden part of the potential.

The reaction on surface B is different from that of surface A in that the preferred reaction path traverses to the left of the saddle point rather than to the right. This means that the reaction mechanism has a transition state complex in which the three atoms are more compressed, having typical bond lengths near or slightly shorter than those of the minimum energy configuration. Although the streamline plots show the largest set of current density vectors passing to the left of the saddle point in Figures 25-27, it is important to note that at each energy the

streamline to the right of center has arrows at least two to three times longer than those in the streamline left of center. From the current density profiles this is clearly emphasized and the resulting conclusion is that even though the largest current density vector tends to pass left of the saddle point, the largest fraction of reacting systems do follow the mechanism through the saddle point having the lowest energy configurations. This is especially true for the reaction with lower total energy. The reason for the favoritism towards this choice of reaction path becomes more clear when the saddle point cut of the normal flux density is considered. At the lowest energy a node, and therefore a vortex, is present at a point well within the energetically accessible region of the potential to the right of the saddle point. No such feature was seen for the low energy A surface case. The reactive flux is forced to go around the vortex and can therefore not cut the corner as it did in surface A. As the energy increases the vortex moves more towards the saddle point as in Figure 26. When the reaction becomes high enough a second vortex appears next to the first with the appearance of a second node in the normal flux curve. The lower schematic in Figure 49.a shows this feature, though obviously the streamlines near the vortices carry an extremely small amount of flux.

Figures 28-31 show the streamline and current density plots for the Cl + HCl vibrationally excited reaction. The reaction on surface A has two vortices, one right on the saddle point and a second slightly to the right of it, which move very little as the energy increases from 0.60 eV to 0.80 eV. Apparently these vortices are far enough into the corner of the potential that the reaction shortcuts its path by cutting the corner or passing to the right of the vortices. Surface B, on the other hand, has its two vortices blocking the region of the potential to the right of the saddle point. The reaction again has to proceed almost exclusively by means of a compressed transition state leading to a bobsleading type mechenism through the potential surface. This causes a problem for the vibrationally excited state reaction which results in the small reaction probability observed in Figure 8. there is also a vortex present earlier in the reagents channel.

From the streamline plots it is clear that the Cl + HCl → ClH + Cl reaction proceeds *via* a stretched transition state on surface A and a compressed transition state on surface B. For a diatomic reagent ClH in the ground vibrational state the reaction has no trouble reacting in either configuration since the ground state diatomic wavefunction has the largest amplitude near the equilibrium, or minimum energy, bondlength and due to its near symmetric distribution about this point can easily access both the compressed and extended configurations. Therefore, either mechanism is easily accessed and the reaction readily occurs for both surfaces A and B. For the vibrationally excited ClH molecule surface A still requires a stretched intermediate and surface B a compressed one. The vibrational wavefunction of the diatomic ClH is nearly antisymmetric although because the potential is a real function and not a harmonic oscillator, the vibration covers a larger extended bond range than it does a compressed bond range. This means that the hydrogen atom, which accounts for most of the vibrational motion as it bounces against the massive chlorine atom, spends more of its time further away from the Cl than it does when in the ground state. For surface A this is ideal since now the ClH bond is on average longer and the reaction can take place readily through the mechanism of a stretched three atom state. Consequently the reaction probability is very high as can be seen in Figure 8. However, this same situation applies to the B surface, but since the vortices of the B surface block critical regions if the potential and force the reactive mechanism to take on a compact configuration the reaction is hindered. From Figures 30 and 31 the streamlines clearly show that the reaction only occurs for diatomics with small transverse components of the current density vector, even at the higher energy where a second vibrational state is open. With the reaction in such a high vibrational state the hydrogen atom can potentially hinder the approaching Cl atom and keep it from getting close enough to have an effect on the diatomic Cl to initiate the reaction.

The Cl + DCl → ClD + Cl reaction streamlines are shown in Figures 32-41. The streamlines indicate that for surface A the reaction mechanism is the same as when hydrogen was used for both the ground and excited vibrational reagents.

The difference is the lack of appearance of the vortex at 0.80 eV for the ground state reaction. The deuterium reaction does take a path slightly closer to the saddle point than did the hydrogen reaction which is consitant with the deuterium atom having a larger mass and therefore a lower frequency vibration and a smaller deviation about the equilibrium bond length. The reaction on surface B is also similar to that of the hydrogen reaction except that again there is no vortex in the lowest energy diagram for the ground state and the two vortices for the excited state have moved outward from the saddle point region with increasing energy.

The reaction involving tritium exchange also exhibits the same dynamic features in the streamline plots as the other two reactions for the high and low barriers. However, from Figure 10 we see that the reaction probability is strongly enhanced by the vibrational excitation on surface B although the mechanism still involves a compressed intermediate. This can be accounted for by the mass difference of the tritium atom which again causes the frequency of the vibration to decrease and the vibrational motion to remain much more confined to the region about the equilibrium bond length. The tritium atom spends more time closer to the Cl than did the H or D atoms upon an absolute time scale. This means that the tritium is not as easily accessed for long bond interaction and the A surface reaction probability is lower than for the other two isotopes. The B surface reaction is more favored with tritium for two reasons. First, the tritium is moving more slowly with respect to the Cl and the incoming Cl atom doesn't encounter the tritium as often as it would a H of D in the same vibrational mode. This allows the Cl to get closer for reaction with out having the central reaction jump across prematurely. Secondly, the ClT diatomic has a center of mass more towards the T than in either the H or D case. The mass of T makes it less insignificant to the translational motion of the diatomic and as it vibrates the Cl is effected. It is then possible that upon compression of the vibrating diatomic the Cl is brought closer to the approaching Cl atom by its extra motion in the vibrational mode and the reaction configuration is more readily achieved.

In summery, the reaction on Cl with HCl or DCl favors an elongated three atom configuration and with the presence of two vortices when v=1 on the high

barrier potential surface this transition state is forced giving a high reaction rate. In contrast, the two vortices on surface B are further from the saddle point location and actually block the potential region sampled by the reaction in surface A. Consequently, the reaction on surface B is forced to occur from a condensed three atom configuration which is less favored when the diatomic reagent is vibrationally excited. The result is a hindered reaction rate on surface B compared to that on surface A.

TUNNELING COEFFICIENTS

The streamline representation provides a method for performing an exact tunneling calculation for the reaction on the two surfaces. The tunneling current is defined as the current that originates in the reactant channel and arrives in the product channel by traversing a path which at some point cuts through the classically inaccessible region of configuration space marked by the contour E. The current density profiles give the best view of the amount of tunneling occurring in the reaction, and from them the tunneling fraction can be decomposed into its two types which either sample the repulsive portions of the potential walls or the dissociative plateau.

The current density profile curves have plotted with them the limiting streamlines for the energy if the reaction of choice. As mentioned earlier the limiting streamlines are streamlines which are tangent to the energy contour E at a single point. There are thus two limiting streamlines for all the plots in this discussion since all the energies considered are higher than the barrier heights on the two surfaces. If the energy is lower than the barrier then all the reactive current is attributable to tunneling, since the reaction must tunnel through the barrier even at the saddle point. The two limiting streamlines separate the reactive current into three parts. Current flowing between the streamlines is classical current since it only samples the classically allowed regions of the potential. The other two parts of the reactive current are the inner and outer tunneling currents. Inner tunneling current crosses into the regions of configuration space where the potential is highly repulsive because either the diatomic molecule is compressed too far and the nuclear repulsion causes the energy to be very high, or the three atom complex is compressed to the point where nuclear repulsion or electronic cloud overlap again make the configuration energetically undesirable. The outer tunneling current is associated with stretched bonds that in an extreme case would result in dissociation.

To calculate the tunneling contribution the area under the current density profiles are normalized and then separated in to three regions marked by the

intersection of the limiting streamlines' normal component with the cut transverse to the minimum energy path. The area of the curve is then separated in the three areas that correspond to the three types of current. The fraction of the total area is equivelent to the tunneling coefficients for the two types of tunneling.

Figures 50-61 show the inner, outer and total tunneling percent of each reaction as a function of energy, as well as the inner, outer and total reaction probabilities due to tunneling. Surface A show 100% tunneling for all three reactions at the energies below 0.285 eV, which is the barrier height. In general the tunneling is very high for surface A at low energies but drops off drastically around 0.60 eV for all three reactions. Well over 95% of the tunneling is due to outer tunneling which corresponds to cutting the corner on the right side of the strong interaction region. This clearly fits with the streamline analysis of the reactive mechanism on surface A. At higher energies the inner and outer tunneling fractions are nearly equal though they both contribute less than 5% to the entire reaction probability. The excited state reactions do not have as much tunneling but again most of what is there comes from tunneling in the outer regions.

Surface B also shows significant amounts of tunneling but for the excited state reaction the tunneling is dominated by the inner fraction. This is also consistent with the streamline analysis on the B surface which followed the reaction around the left side of the vortices. For the ground state reactions on this surface the outer tunneling is still higher than the inner tunneling but the inner tunneling is substantially larger than recorded for surface A. The outer tunneling is largely because of the nonzero contribution to the transverse component of the current density at the energies above the opening of the first vibrational state.

Overall the tunneling fractions and reaction probabilities follow from the streamline analysis and correspond to the reaction paths for the two surfaces accurately. Tunneling in the tritium reaction for v=1 on surface B definitely contributes to the high reaction probability although most of the tunneling is from the bobsledding mechanism. The tritium atom definitely spends a greater amount of time in close quarters with its partner Cl for the B surface and therefore promotes the reaction which prefers this configuration.

QUANTUM MECHANICAL RESONANCES

Resonances in molecular collisions justifiably draw a great deal of attention because of their profound effects on partial, differential and total scattering cross sections. They stem from the particular characteristics of the corresponding potential energy surface and are critically sensitive to the detailed topology of the surface. Resonances are a quantum mechanical phenomena that produce a sharp variation of the reaction probability at some resonant energy associated with the existence of a metastable state. Quantum mechanically, a metastable state is produced as a quasibound state trapped either in a well behind a barrier or between barriers. Therefore, in the case of reactive scattering over a barrier, resonances are invariably associated with the nearly bound states found in the well of effective potentials. Such metastable states associated with reaction barriers correspond to poles in the scattering matrix just as definitely as trapped states in classical mechanics correspond to standing waves in wells.

The spectrum of resonances appearing in the collinear Cl + HCl $\rightarrow$ ClH + Cl reaction is clearly an outstanding feature in the reactive probability profiles. To understand the origin of these resonances it is most useful to return to the vibrationally adiabatic approximation that originally separated out and accounted for much of the structure of the curves.

The Schrödinger equation for the collinear reaction in mass scaled Delves' polar coordinated is a function of a radial and angular variable as mentioned earlier. The wavefunction is expanded in terms of the vibrational functions which are solutions of the Schrödinger equation at fixed values of ρ. As before, this leads to a set of second order coupled differential equations for the expansion coefficients g_v. The vibrationally adiabatic approximation consists of retaining only the terms with v'=v in the integrations over the angular variable giving

$$\left[-\frac{\hbar^2}{2\mu}\frac{d}{d\rho^2}+U_v(\rho)-E\right]g_v(\rho;\bar{\rho})=0, \qquad 1$$

where the effective potential is defined in terms of the eigenvalues of the diatomics,

$$U_v(\bar{\rho}) = \varepsilon_v(\bar{\rho}) - \frac{\hbar^2}{8\mu\bar{\rho}^{-2}} - \frac{\hbar^2}{2\mu}\int \phi_v \frac{\partial^2}{\partial\rho^2}\phi_v \, d\alpha. \qquad 2$$

The diagonal term remains in this expression for U_v leading to the approximation called the diagonally corrected vibrationally adiabatic hyperspherical model, (DIVAH).[6] The spectrum of resonances can be analyzed to some degree using equation 2.

For symmetric exchange reactions the symmetry of the potential gives rise to both symmetric and antisymmetric eigenfunctions for the angular variable. The corresponding eigenvalues are ε_v^g and ε_v^u. The eigenvalue *verses* ρ effective potential curves are shown in Figures 62-64 for the ClHCl, ClDCl and ClTCl reactions respectively. The eigenvalues are obtained numerically during the evaluation of the surface functions. At large values of ρ the gerade and ungerade curve become degenerate and correspond to the diatomic reactant and product vibrations. In the interaction region these curves are separate with the gerade curve always lying below the ungerade curve. The various shapes of the curves gives rise to the possibility of bound states in the gerade plot and v $\rightarrow$ v shape resonances when the one dimensional Schrödinger equation is solved. It also implies the possibility of Feshbach resonances in other diagonal and off-diagonal reaction probabilities. The adiabatic potentials ε_v^g and ε_v^u are similar but not identical to the U_{vg} and U_{vu} potentials, producing bound states to within fair agreement of each other. If the diagonal corrections are neglected, some spurious resonances are predicted arising from the vibrationally adiabatic polar coordinate description of the scattering.

Comparison of the adiabatic effective potentials for the two different surfaces suggests that for all three isotopes surface B can support more bound states than surface A. The ground state eigenvalue curves for surface A are

strictly repulsive for all three reactions whereas they contain effective wells for surface B. In this case it is not surprising that resonance structure is found in the ground state reaction probability plots of surface B and not in those for surface A. From these pictures it is also hypothesized that the four sharp resonances found on the vibrationally excited reaction probability plot of Figure 8 for surface A, correspond to four quasibound states caught in the effective potential well of the v=2 gerade curve. Similarly, the two sets of four and seven resonances in Figure 8 should correspond to bound states on the v=1 and v=2 gerade curves respectively, for surface B. Comparing the shapes of the pairs of v=1 and v=2 gerade curves for the two surfaces in Figure 62 shows that the B curve wells are deeper than those for the A surface, therefore it is not surprising to find more resonances for this system. The well depth of these plots is directly associated with the barrier height of the surface. Since the B surface has a much lower barrier and therefore a deeper well, more states can be supported.

The same features appear to follow through the analysis of Figures 9 and 10 for the ClDCl and ClTCl systems. These two systems have strong resonance structure occurring in sets, which suggests that several of the adiabatic effective potential curves support many bound states. From the figures it is also clear as to why the resonances for the hydrogen system occur just before the opening of the next vibrational state and for the deuterium and tritium systems they occur, or seem to occur, just after the vibrational state opens. In reality the resonances are still showing up at energies just below the new vibrational state and the bound states are found in the effective potential wells as they are in the hydrogen case. The difference is that the effective potentials are much closer in energy and the minima of some of the higher gerade plots tend to drop below the asymptotic value of the nearest eigenstate. Therefore the bound state energies appear at or just above a vibrational eigenvalue. Note that as the energy increases, the resonances seem to overlap more and the sets of spectra become less distinguishable.

To determine the exact energies of the quasibound state the phase shifts $\eta_v^g(E)$ can be calculated, from which the resonant energies are found from the local maxima of the time delay function

$$\tau_v(E) = 2\hbar \frac{d\eta_v(E)}{dE}. \qquad 3$$

The resonances for the ClHCl reaction are shown in Figures 65-81 for the two surfaces. With them are plotted the corresponding Argand diagrams, which are simply the diagonal scattering matrix elements shown in the complex plane. The real and imaginary components are parametrized by the total energy of the reaction. In the absence of resonances Argand diagrams are almost circular in shape about the origin of the system of axes and traverse clockwise with respect to increasing energy. In this manner the magnitude of the diagonal scattering matrix element varies slowly and its phase decreases. This is characteristic of a direct reaction mechanism. The resonances, on the other hand, cause the phase of the scattering matrix element to rapidly increase, therefore abruptly changing the direction of the Argand plot from clockwise to counterclockwise. This is readily observed in Figures 65-81 where the resonances are so strong that they abruptly reverse the direction of the phase in a manner very unlike the typical smooth motion seen for other systems including H + H_2, F + D_2, F + H_2, and F + HD. The sets of resonances all have a Breit-Wigner shape and the lack of symmetry is due to the interference with the background or direct contribution to the probability which, as discussed previously, is weakly energy dependent.

Figures 65 and 74 show the two resonances that occur at the opening of the ground vibrational state of surface A and the excited state of surface B. Obviously these two resonances are quite different than the others both in their shape and in their Argand plots. The resonance in Figure 65 is much broader than the others and the resonance in Figure 74 is much smaller. These are threshold resonances and are associated with the opening of the state. Friedman and Truhlar[10] show that chemical reaction thresholds are resonances, of the same type as those responsible for the sharp peaks seen in state-to-state reaction

probabilities though broader. Thus resonances are ubiquitous in chemical reactions.

As mentioned earlier, a simple but intuitive physical interpretation is that often resonances, specifically shape resonances, can be associated with the trapping of the reactive system in a well. However, in these reactions, since there is no potential well the trapping is of a more sophisticated dynamic nature involving Feshbach processes.[32] For this to occur, the reacting system must have at least two degrees of freedom. The essence of the mechanism is then that the energy becomes trapped in internal coordinates and the system is only able to separate into products if enough energy flows back into the reactive degree of freedom. This differs from the case of shape resonances in which the energy can be trapped in the same degree of freedom leading to reaction.

For the Cl + HCl reaction the two degrees of freedom are ρ and α. The eigenvalue curves exhibit minima as functions of ρ and can support bound state eigenfunctions and eigenvalues E or long-lived virtual states. The dynamic resonances can be associated with these bound or virtual eigenvalues E which may be less than the vibrational quantum energy of the original state. When this happens, the energy of the system flows from the external degree of freedom, ρ, into eigenstates of the internal degree of freedom, α, which can be asymptotically closed but are locally open. This is called a closed-channel resonance. It is also possible for the system to have open channel resonances. The system becomes trapped in a state of the internal degrees of freedom leaving the external motion subject to the afore mentioned effective potential. The hyperspherical coordinates separate in a manner similar to the separation of the electronic and nuclear motion in the Born-Oppenheimer approximation for molecules. The angular coordinate plays a role similar to that of the electronic coordinate and the hyperradius to that of the nuclear coordinate. This was discussed earlier when the motion of the light atom, H, was very rapid compared to the motion of the heavy Cl atoms and had essentially no effect on their translational motion.

The resonances are attributed to trapped states in the effective potentials of the external motion coordinate. The two chlorine atoms separated by a hydrogen atom form a quasibound complex with energy highly concentrated in the motion of the central atom. The Chlorine atoms are hardly moving with respect to each and the motion of the hydrogen atom corresponds to that of a normal vibrational mode of the complex. A more detailed analysis of the lifetime scale for such a complex is possible and the exact assignment of the quantum states corresponding to each resonance can be obtained though an analysis of the wavefunction.

CONCLUSION

The Cl + H(D,T)Cl → ClH(D,T) + Cl reactions have been studied on two analytical potential energy surfaces which correspond with the different results obtained in various experiments. The barrier height of the reaction is not known and therefore collinear reactive scattering results giving different conclusions about the reaction mechanism provide valuable insight to the determination of a more accurate surface and act as a precursor to three-dimensional studies of this reaction. The streamline and current density discussions of the vibrationally excited reaction aid in explaining the curious effect of an enhanced reaction rate for a high barrier and an arrested rate on a low barrier. Quantum vortices play a leading role in promoting this phenomena by prohibiting access to particularly critical regions of the potential in the strong interaction part of the two surfaces. They essentially promote the reaction on the high barrier surface by forcing the reaction to proceed via an elongated three atom configuration. The reaction on the low barrier is inhibited by the presence of two vortices which keep it from occurring either in an elongated transition or even at the low energy saddle point equilibrium configuration. The reaction is forced to occur through an unfavorable compressed three atom configuration that is even less favored when the vibrational state of the diatom is excited. The contributions to this effect from tunneling are actually higher for the reactions on the low barrier surface, which has almost no reactive flux, than they are for the high barrier surface. Therefore, tunneling does not play a major role in the obscure differences in the dynamics of the reaction on the two surfaces but seems to be rather a consequence of the concurring mechanism. The restriction to collinearity is an obvious limitation in assessing the importance of the effect in three-dimensions. However, approximate three-dimensional quantum mechanical calculations on this system have been reported for ground state reagents and indicate that at least the oscillatory behavior in the reaction probabilities with energy persist.[5] Therefore it is not impossible that the

inhibition to the reaction rate for vibrationally excited systems on low barrier surfaces might also persist in three-dimensions since it is a quantum behavior due to vortices.

REFERENCES

1. N. Abusalbi, D. J. Kouri, V. Lopez, V. K. Babamov, and R. A. Marcus, *Chem. Phys. Lett.* **103** (1984) 458.
2. N. Albulsalbi, S. H. Kim, D. J. Kouri, and M. Baer, *Chem. Phys. Lett.* **112** (1984) 502.
3. V. Aquilanti, G. Grossi and A. Lagana, *J. Chem. Phys.* **76** (1982) 1587; G. Grossi, *J. Chem. Phys.* **81** (1984) 3355.
4. V. K. Babamov and R. A. Marcus, *J. Chem. Phys.* **74** (1981) 1790.
5. M. Baer and I. Last, *Chem. Phys. Lett.* **119** (1985) 393.
6. D. K. Bondi and J. N. L. Connor, *Mol. Phys.* **50** (1983) 467.
7. D. K. Bondi and J. N. L. Connor, J. Manz and J. Römelt, *Mol. Phys.* **50** (1983) 488.
8. D. K. Bondi and J. N. L. Connor, B. C. Garrett, and D. G. Truhlar, *J. Chem. Phys.* **78** (1983) 5981.
9. P. Botschwina and W. Meyer, *Chem. Phys. Lett.* **44** (1976) 449.
10. R. S. Friedman and D. G. Truhlar, University of Minnesota Supercomputer Institute Research Report, (1991).
11. B. C. Garrett, D. G. Truhlar, A. F. Wagner, and T. H. Dunning Jr., *J. Chem. Phys.* **78** (1983) 4400.
12. P. L. Gertitschke, J. Manz, J. Römelt and H. R. R. Schor, *J. Chem. Phys.* **83** (1985) 205.
13. P. L. Gertitischke, J. Manz, J. Römelt, and H. H. R. Schor, *J. Chem. Phys.* **83** (1985) 208.
14. R. Gordon, *J. Chem. Phys.* **51** (1969) 14.
15. G. Hauke, J. Manz, and J. Römelt, *J. Chem phys.* **73** (1980) 5040.

16. C. Hiller, J. Manz, W. H. Miller, and J. Römelt, *J. Chem. Phys.* **78** (1983) 3850.

17. J. O. Hirshfelder, A. C. Christoph, and W. E. Palke, *J. Chem. Phys.* **61** (1974) 5435.

18. J. O. Hirshfelder, C. J. Goebel, and L. W. Bruch, *J. Chem. Phys.* **61** (1974) 5456.

19. J. O. Hirschfelder and K. T. Tang, *J. Chem. Phys.* **64** (1976) 760.

20. J. O. Hirschfelder and K. T. Tang, *J. Chem. Phys.* **65** (1976) 470.

21. B. R. Johnson, *J. Chem. Phys.* **67** (1977) 4086.

22. B. R. Johnson, *J. Chem. Phys.* **69** (1978) 4678.

23. B. R. Johnson, *J. Chem. Phys.* **73** (1980) 5051; **79** (1989) 1906, 1916.

24. J. A. Kaye and A. Kuppermann, *Chem. Phys. Lett.* **77** (1981) 573.

25. J. A. Kaye and A. Kuppermann, *Chem. Phys. Lett.* **92** (1982) 574.

26. J. A. Kaye, Ph.D. Thesis, California Institute of Technology, Pasadena, CA (1982).

27. F. S. Klein, A. Persky and R. E. Weston, *J. Chem. Phys.* **41** (1964) 1799; **59** (1973) 2775.

28. M. Kneba and J. Wolfrum, *J. Phys. Chem.* **83** (1979) 69.

29. A. Kupperman, Theoretical Chemistry; Advances and Perspectives **6A.** (1981) 79.

30. A. Kuppermann, *Chem. Phys. Lett.* **32** (1975) 374.

31. A. Kuppermann, *Theoretical Aspects of the Mechanism of Simple Chemical Reactions*, in the Proceedings of the Summer School on Chemical Photophysics, Les Houches, Frances, 18-30 June 1979, P. Glorieux, D. Lecler, and R. Vetter, Eds. (Centre de la Recherche Scientifique, Paris, 1979), p. 293.

32. A. Kuppermann, Potential Energy Surfaces and Dynamics Calculations, ed. D. G. Truhlar (Plenum Publishing Corporation, 1981).

33. A. Kuppermann, J. A. Kaye, and J. P. Dwyer, *Chem. Phys. Lett.* **74** (1980) 257.

34. A. Kuppermann, J. T. Adams and D. G. Truhlar, 8th International Conference on the Physics of Electronic and Atomic Collisions, 1973, Belgrade, Yugoslavia, p. 149 of Abstracts.

35. I. Last and M. Baer, *J. Chem. Phys.* **80** (1984) 3246.

36. S. L. Lathan, J. F. McNutt, R. E. Wyatt, *J. Chem. Phys.* **54** (1971) 3578.

37. J. M. Launay and M. Le Dourneuf, *J. Chem. Phys.* **B 15** (1982) L455.

38. J. Manz and J. Römelt, *Chem. Phys. Lett.* **76** (1980) 337.

39. J. Manz and J. Römelt, *Chem. Phys. Lett.* **77** (1981) 573.

40. J. Manz W. H. Miller and J. Römelt, *J. Chem. Phys.* **78 II** (1983) 3850.

41. J. Manz and H. H. R. Schor, *Chem Phys. Lett.* **107** (1984) 594.

42. J. Manz, *Comments At. Mol. Phys.* **17** (1985) 91.

43. R. B. Metz, T. Kitsopoulos, A. Weaver, and D. M. Newmark, *J. Chem. Phys.* **88** (1988) 1463.

44. E. A. McCullough and R. E. Wyatt, *J. Chem. Phys.* **54** (1971) 3578.

45. J. F. McNutt and R. E. Wyatt, in: Potential Energy Surfaces and Dynamics Calculations, ed. D. G. Truhlar (Plenum Press, New York 1981), p. 495.

46. E. Pollak, *Comments At. Mol. Phys.* **15**, **23** and references therein (1984).

47. E. Pollak in; NATO ASI Series, Vol. C 170. The Theory of Chemical Reaction Dynamics, ed. D. C. Clary (Reidel, Dordrecht, 1986) p. 135.

48. R. N. Porter and L. M. Raff in: Dynamics of molecular Collisions, Part B, ed. W. H. Miller (Plenum Press, New York, 1976), p. 1.

49. M. E. Riley and A. Kuppermann, *Chem. Phys. Lett.* **1** (1968) 537.

50. J. Römelt in; NATO ASI Series, Vol. C 170. The Theory of Chemical Reaction Dynamics, ed. D. C. Clary (reidel, Dordrecht, 1986) p. 77.

51. S. Sato, *J. Chem. Phys.* **23** (1955) 592, 2465.

52. G. Schatz, *Ann. Rev. Phys. Chem.* **39** (1988) 317.

53. C. L. Shoemaker, N. Abusalbi, D. J. Kouri, *J. Phys. Chem.* **87** (1983) 5389.

54. F. T. Smith, *J. Math. Phys.* **3** (1962) 735.

55. I. W. M. Smith, *J. Chem. Soc. Farad. Trans.* **II 71** (1975) 1970.

56. B. W. Shore, *J. Chem. Phys.* **59** (1973) 6450.

57. D. G. Truhlar and J. T. Muckerman in Atom-Molecule Collision Theory, ed. R. B. Berstein (Plenum Press, New York, 1979), p. 505.

58. R. E. Weston Jr., *J. Phys. Chem.* **83** (1979) 61.

59. R. C. Whitten and F. T. Smith, *J. Math. Phys.* **9** (1968) 1103.

60. Y. M. Wu, Ph.D. Thesis, California Institute of Technology, Pasadena, Ca (1992).

Table 1: Parameters and properties of LEPS potential energy surfaces A and B[a].

	HCl	Cl_2
β (bohr^{-1})	0.9892	1.0626
R_e (bohr)	2.4060	3.7791
D_e (eV)	4.6258	2.5169
$\Delta \quad A$	0.138	0.138
$\Delta \quad B$	0.185	0.185
Saddle Point Location (bohr)		
A	(2.757,2.757)	
B	(2.727,2.727)	
Barrier Height (kcal/mole)		
A	6.21	
B	1.28	

a. Masses used: $m_{Cl} = 34.6974\ m_H$.

Table 1

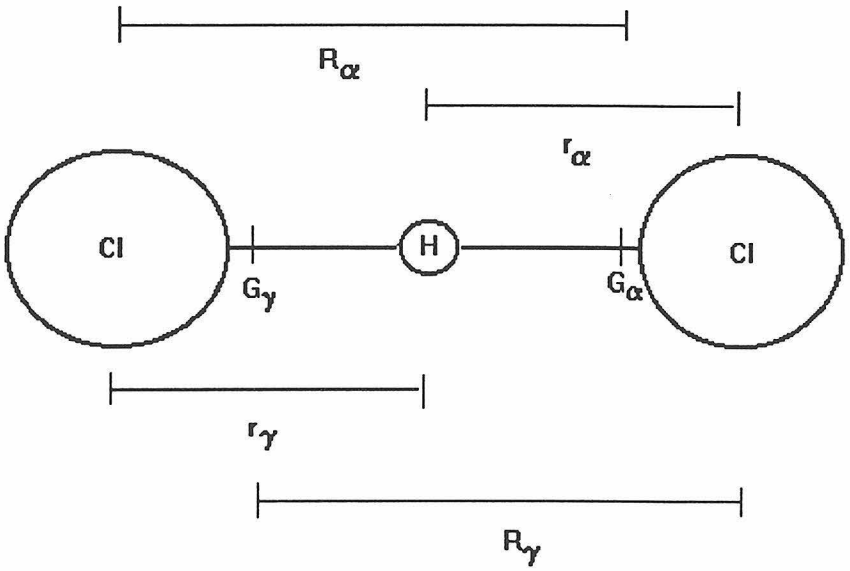

Figure 1

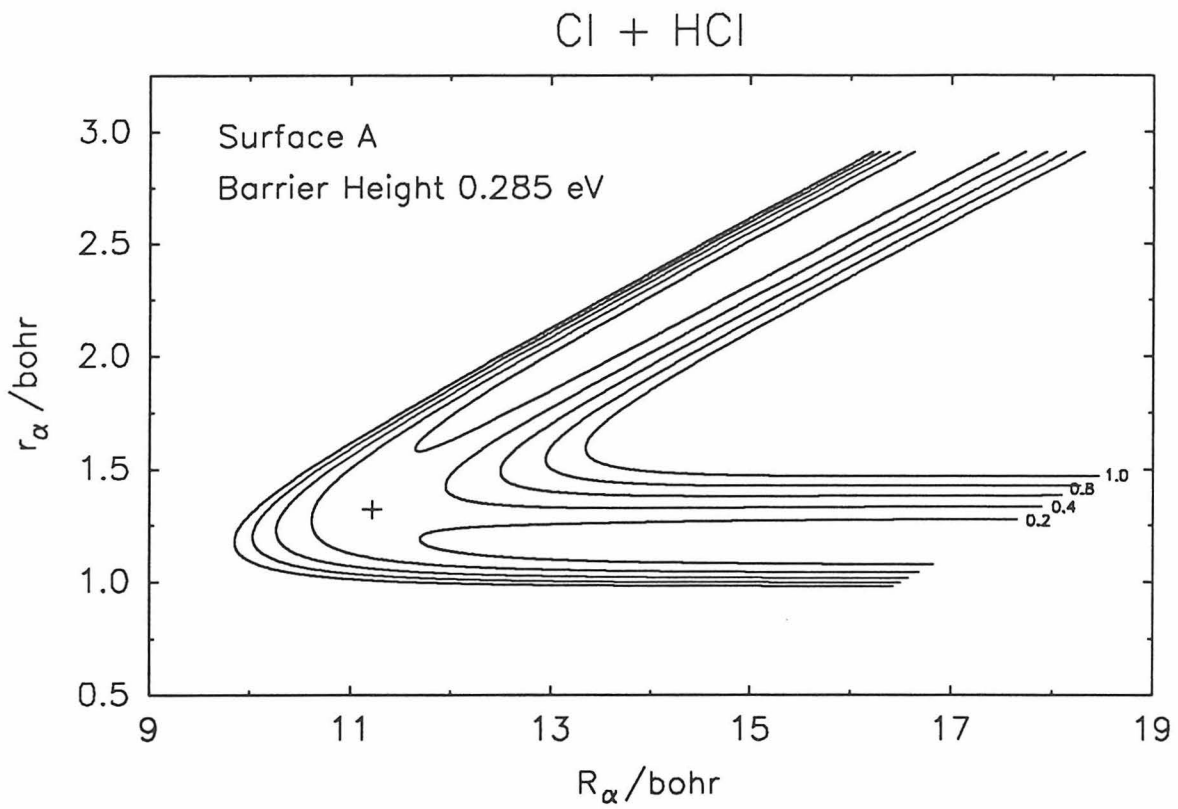
Cl + HCl
Surface A
Barrier Height 0.285 eV
3.0
2.5
2.0
1.5
1.0
0.5
r_α /bohr
9
11
13
15
17
19
R_α /bohr
1.0
0.8
0.4
0.2

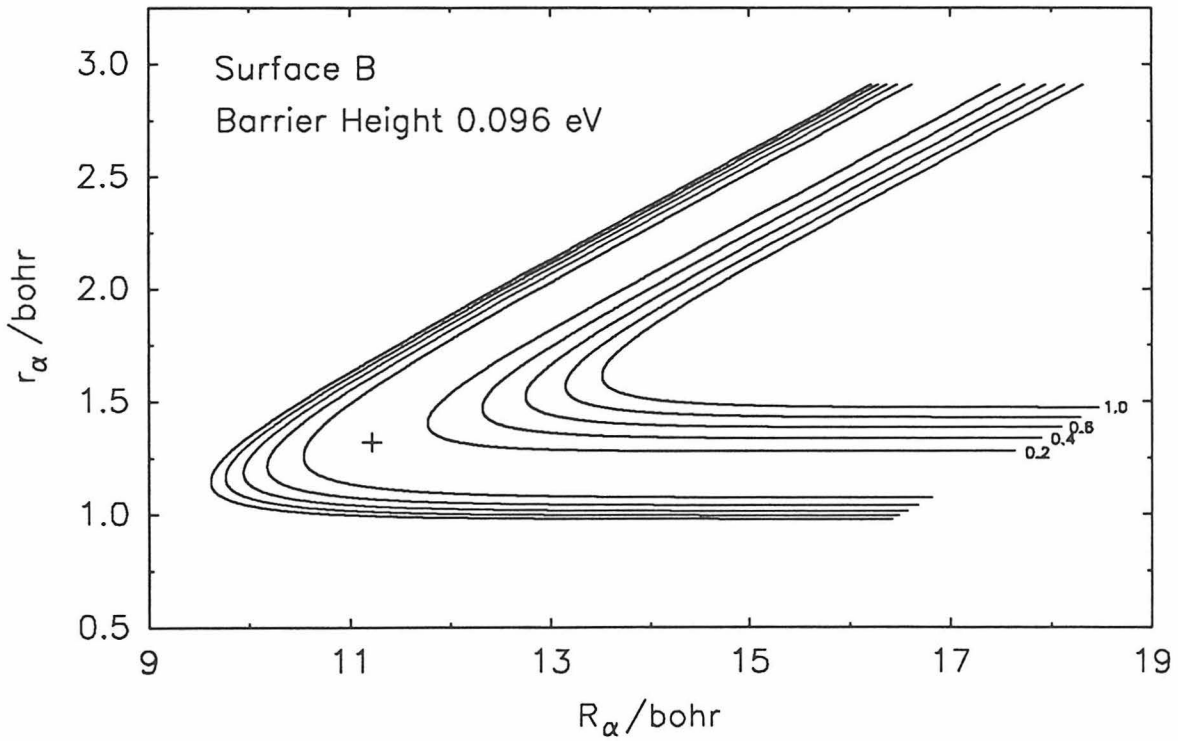
Surface B
Barrier Height 0.096 eV
3.0
2.5
2.0
1.5
1.0
0.5
r_α /bohr
9
11
13
15
17
19
R_α /bohr
1.0
0.8
0.4
0.2

Figure 2

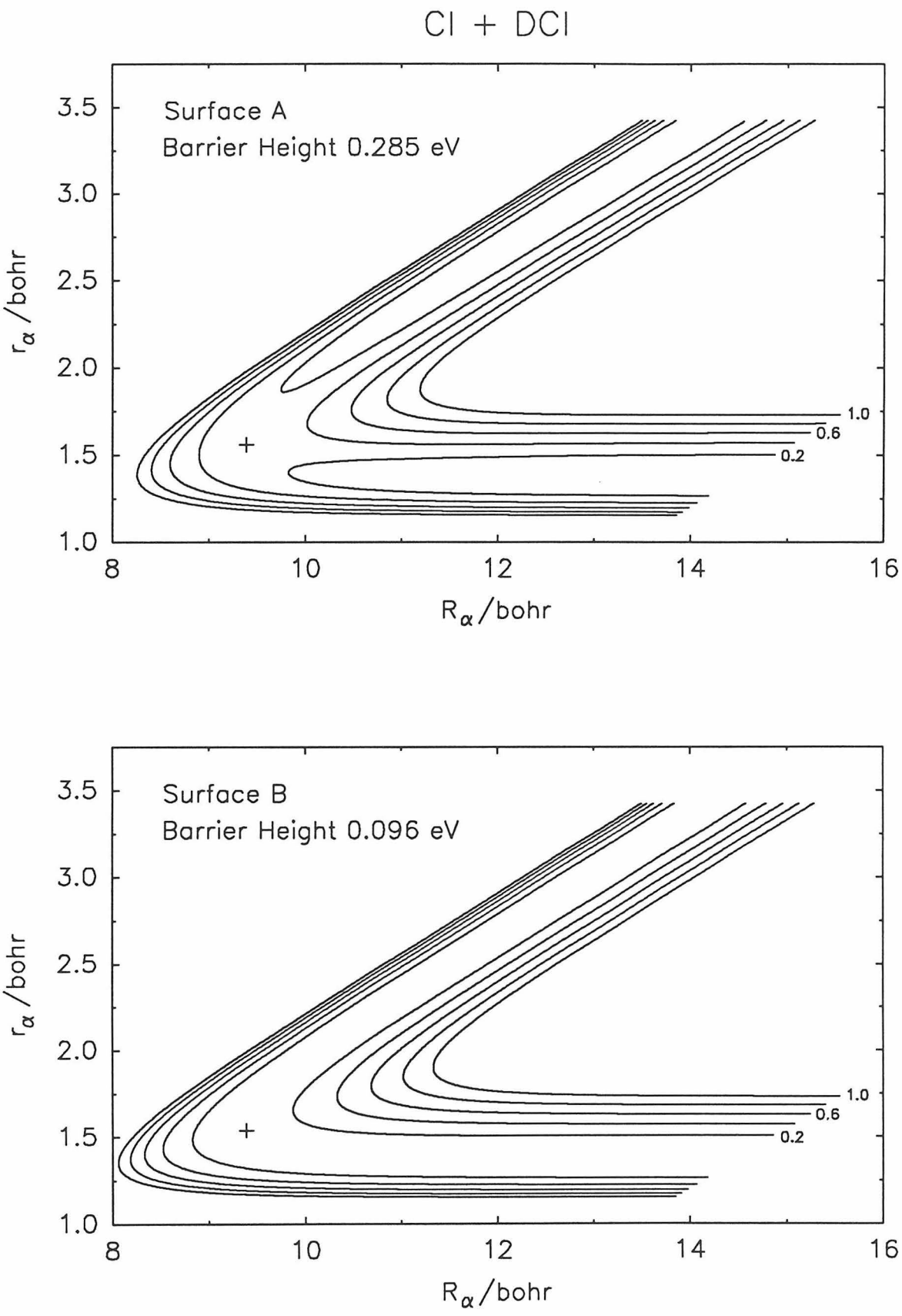
Cl + DCl
Surface A
Barrier Height 0.285 eV
Surface B
Barrier Height 0.096 eV
1.0
0.6
0.2
3.5
3.0
2.5
2.0
1.5
1.0
8
10
12
14
16
r_α /bohr
R_α /bohr

Figure 3

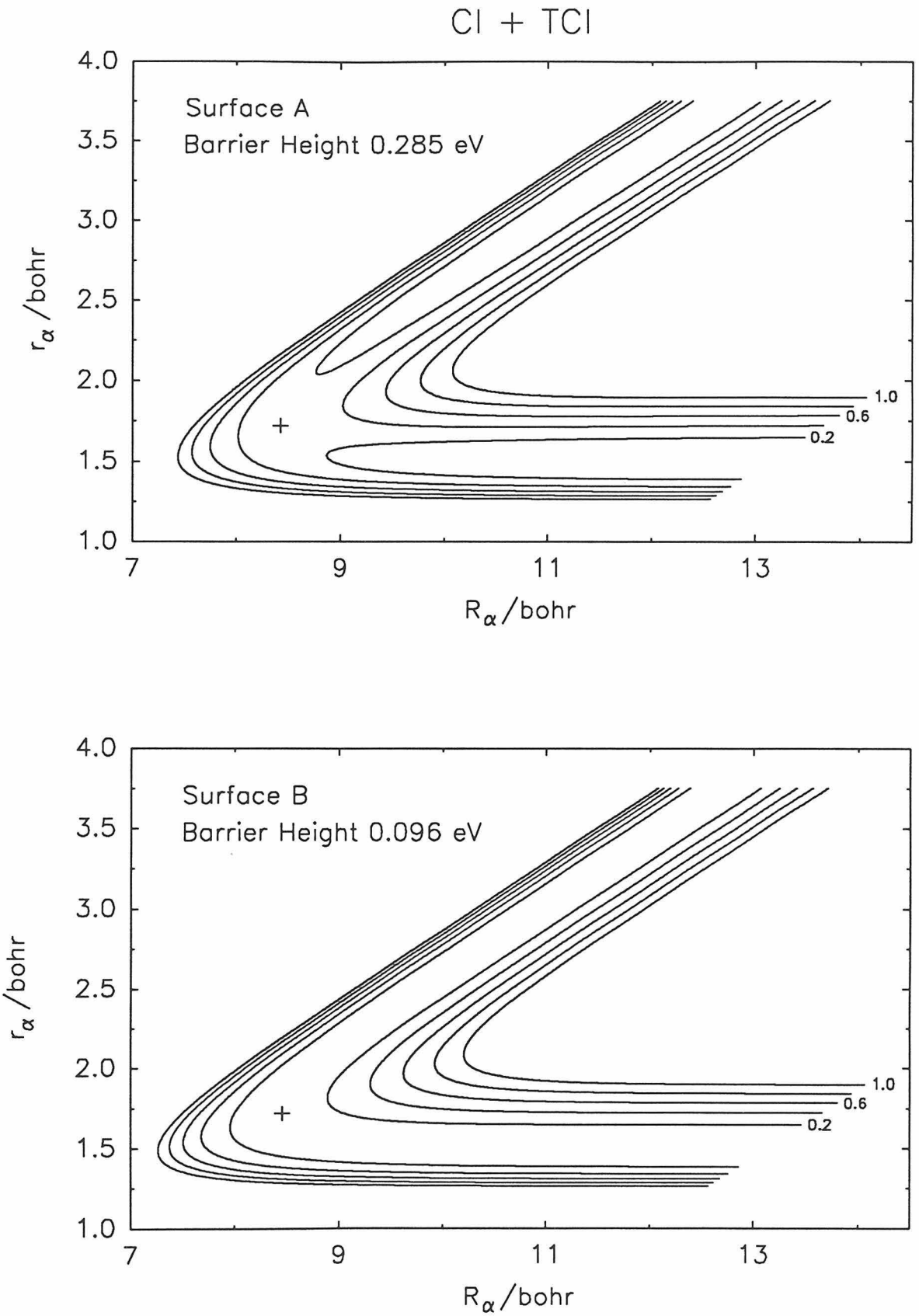
Cl + TCl
Surface A
Barrier Height 0.285 eV
Surface B
Barrier Height 0.096 eV
1.0
0.6
0.2
4.0
3.5
3.0
2.5
2.0
1.5
1.0
7
9
11
13
r_α /bohr
R_α /bohr

Figure 4

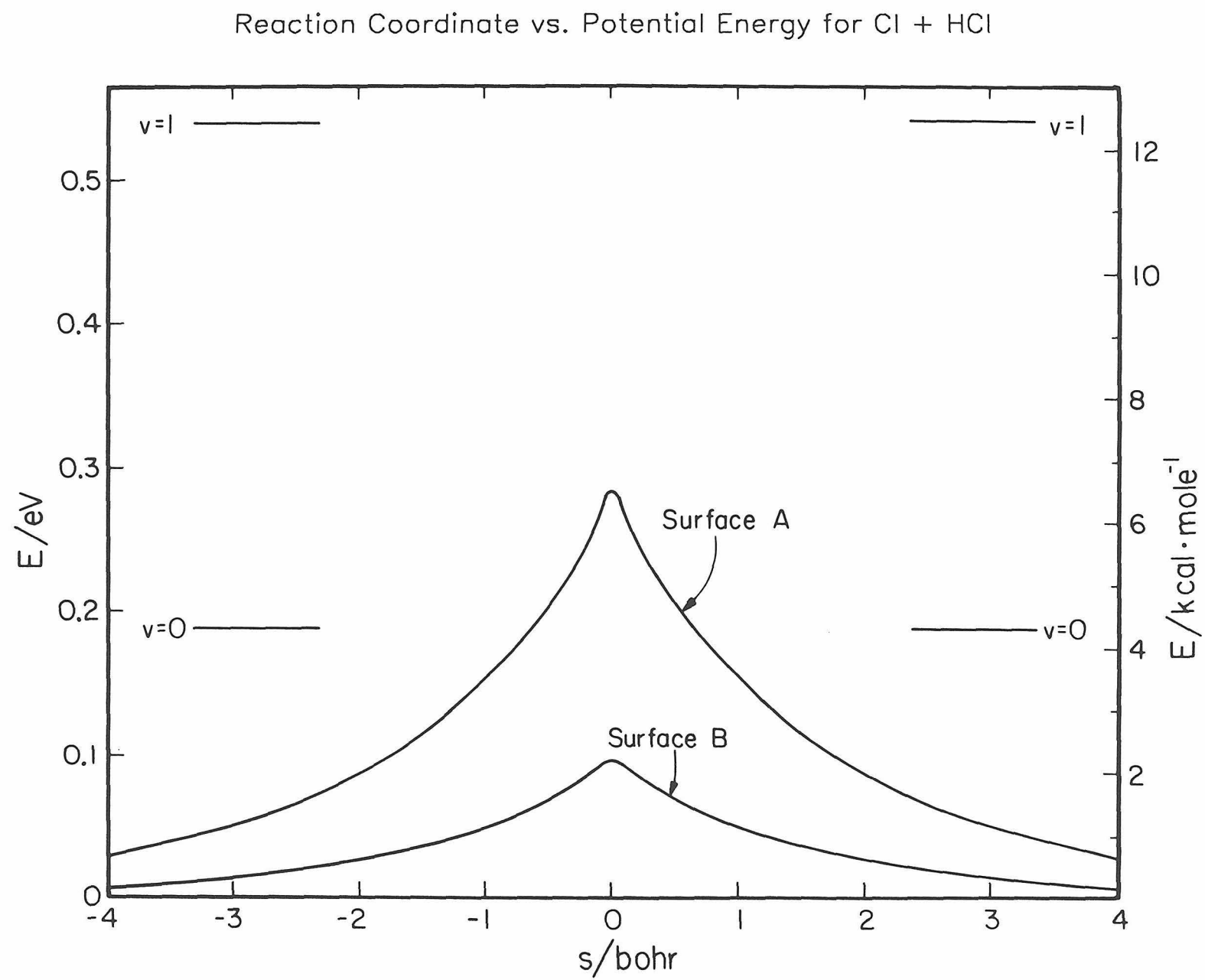
Reaction Coordinate vs. Potential Energy for Cl + HCl
v=1
v=1
v=0
v=0
Surface A
Surface B
E/eV
E/kcal·mole⁻¹
s/bohr
0
0.1
0.2
0.3
0.4
0.5
2
4
6
8
10
12
-4
-3
-2
-1
0
1
2
3
4

Figure 5

Figure 6

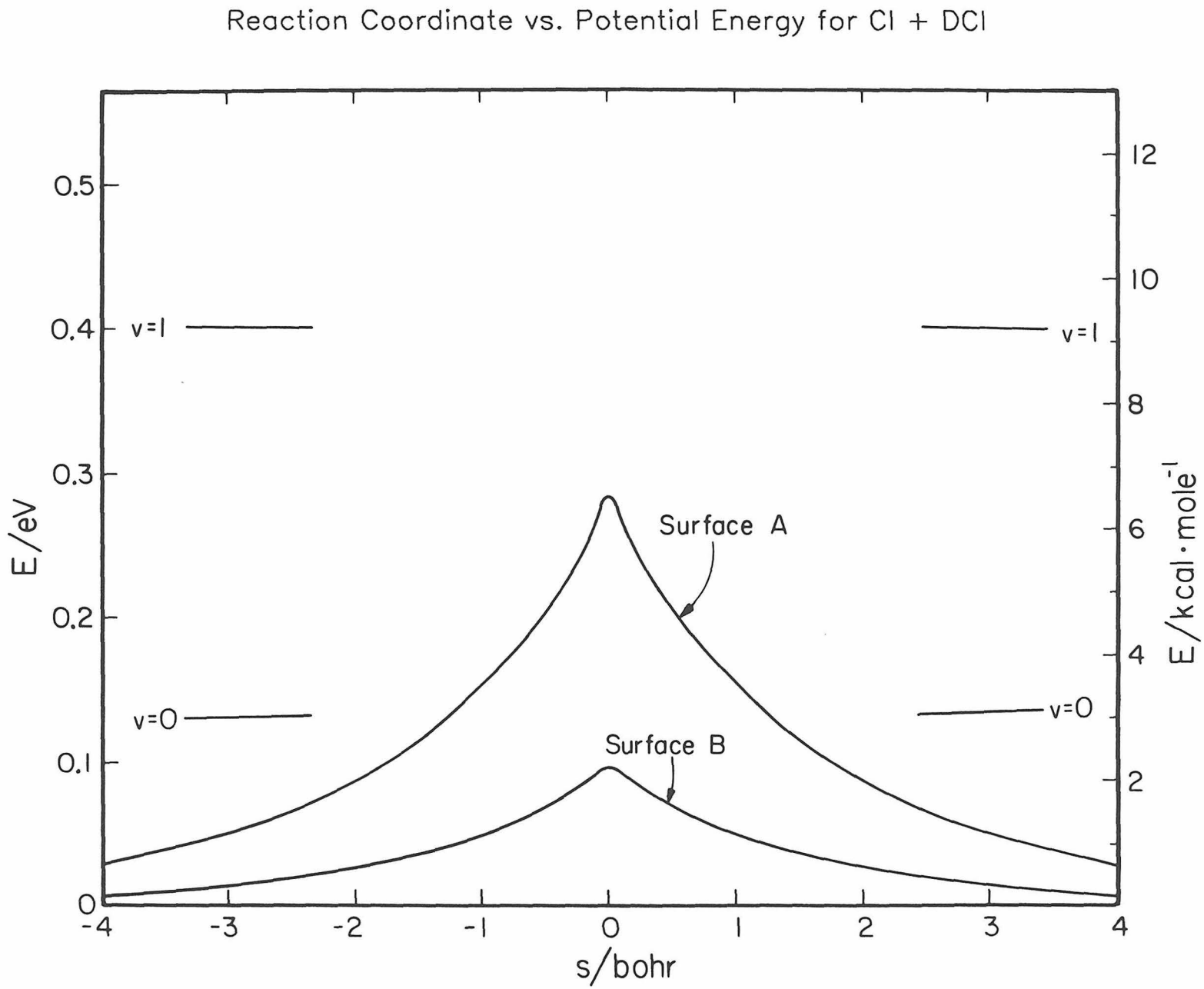
Reaction Coordinate vs. Potential Energy for Cl + DCl
E/eV
E/kcal·mole⁻¹
s/bohr
v=1
v=0
Surface A
Surface B
0
0.1
0.2
0.3
0.4
0.5
2
4
6
8
10
12
-4
-3
-2
-1
0
1
2
3
4

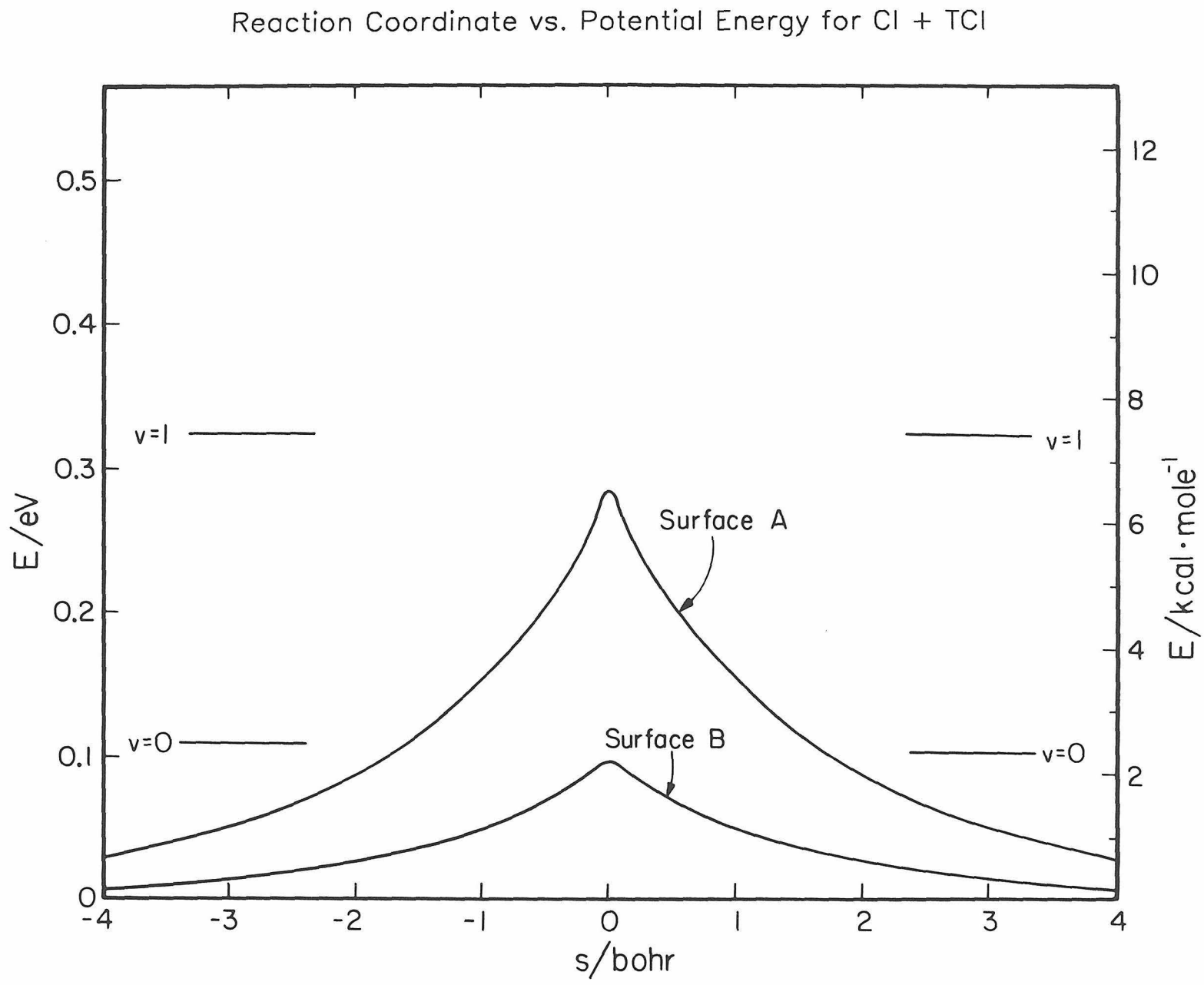
Reaction Coordinate vs. Potential Energy for Cl + TCl
E/eV
E/kcal·mole⁻¹
s/bohr
v=1
v=0
Surface A
Surface B
0.5
0.4
0.3
0.2
0.1
0
12
10
8
6
4
2
-4
-3
-2
-1
0
1
2
3
4

Figure 7

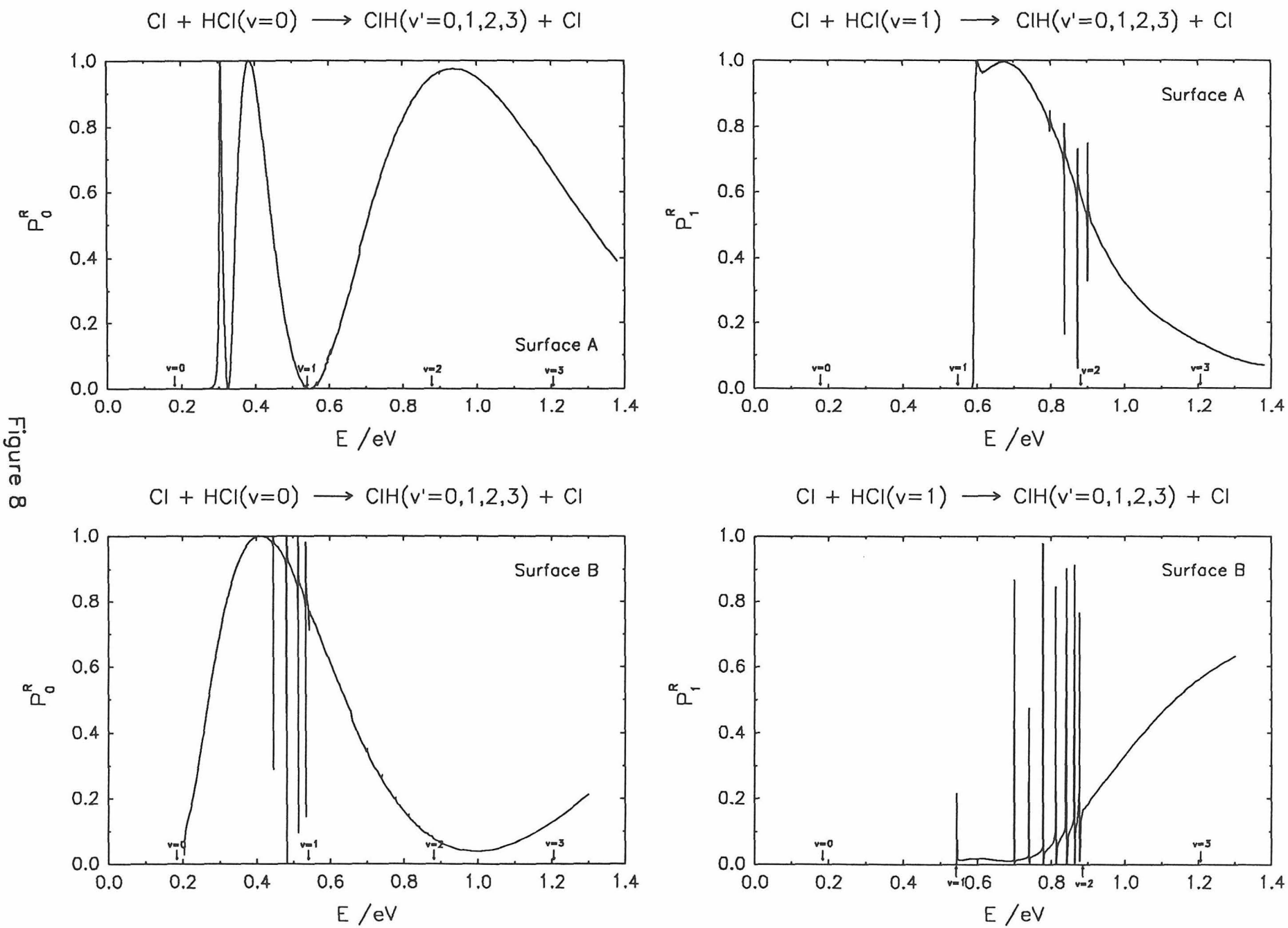
Cl + HCl(v=0) ⟶ ClH(v'=0,1,2,3) + Cl
Cl + HCl(v=1) ⟶ ClH(v'=0,1,2,3) + Cl
Cl + HCl(v=0) ⟶ ClH(v'=0,1,2,3) + Cl
Cl + HCl(v=1) ⟶ ClH(v'=0,1,2,3) + Cl
P_0^R
P_1^R
E /eV
Surface A
Surface B
v=0
v=1
v=2
v=3
0.0
0.2
0.4
0.6
0.8
1.0
1.2
1.4

Figure 8

Figure 9

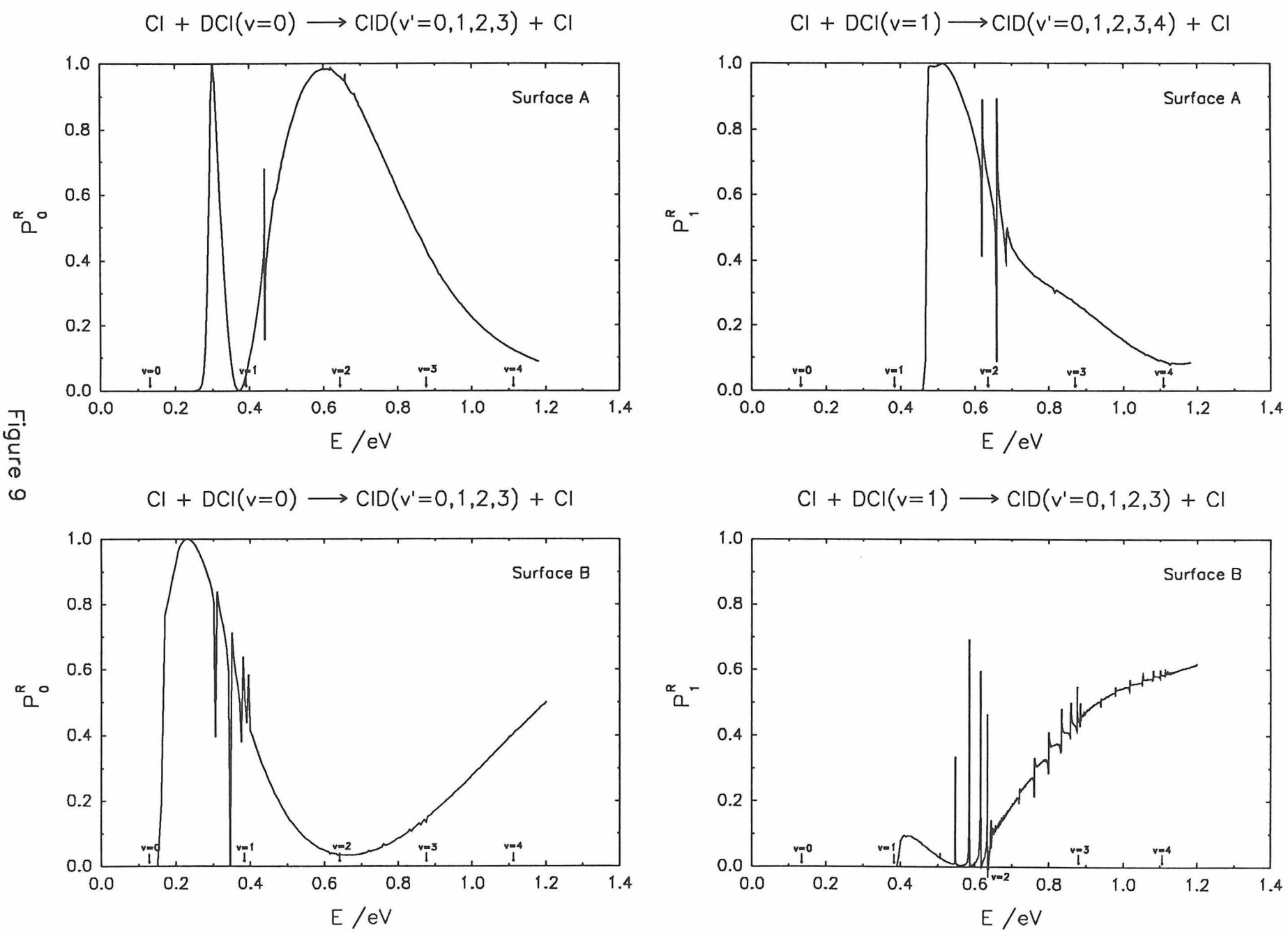
Cl + DCl(v=0) ⟶ ClD(v'=0,1,2,3) + Cl
Surface A
P_0^R
E /eV
v=0
v=1
v=2
v=3
v=4
Cl + DCl(v=1) ⟶ ClD(v'=0,1,2,3,4) + Cl
Surface A
P_1^R
E /eV
Cl + DCl(v=0) ⟶ ClD(v'=0,1,2,3) + Cl
Surface B
P_0^R
E /eV
Cl + DCl(v=1) ⟶ ClD(v'=0,1,2,3) + Cl
Surface B
P_1^R
E /eV

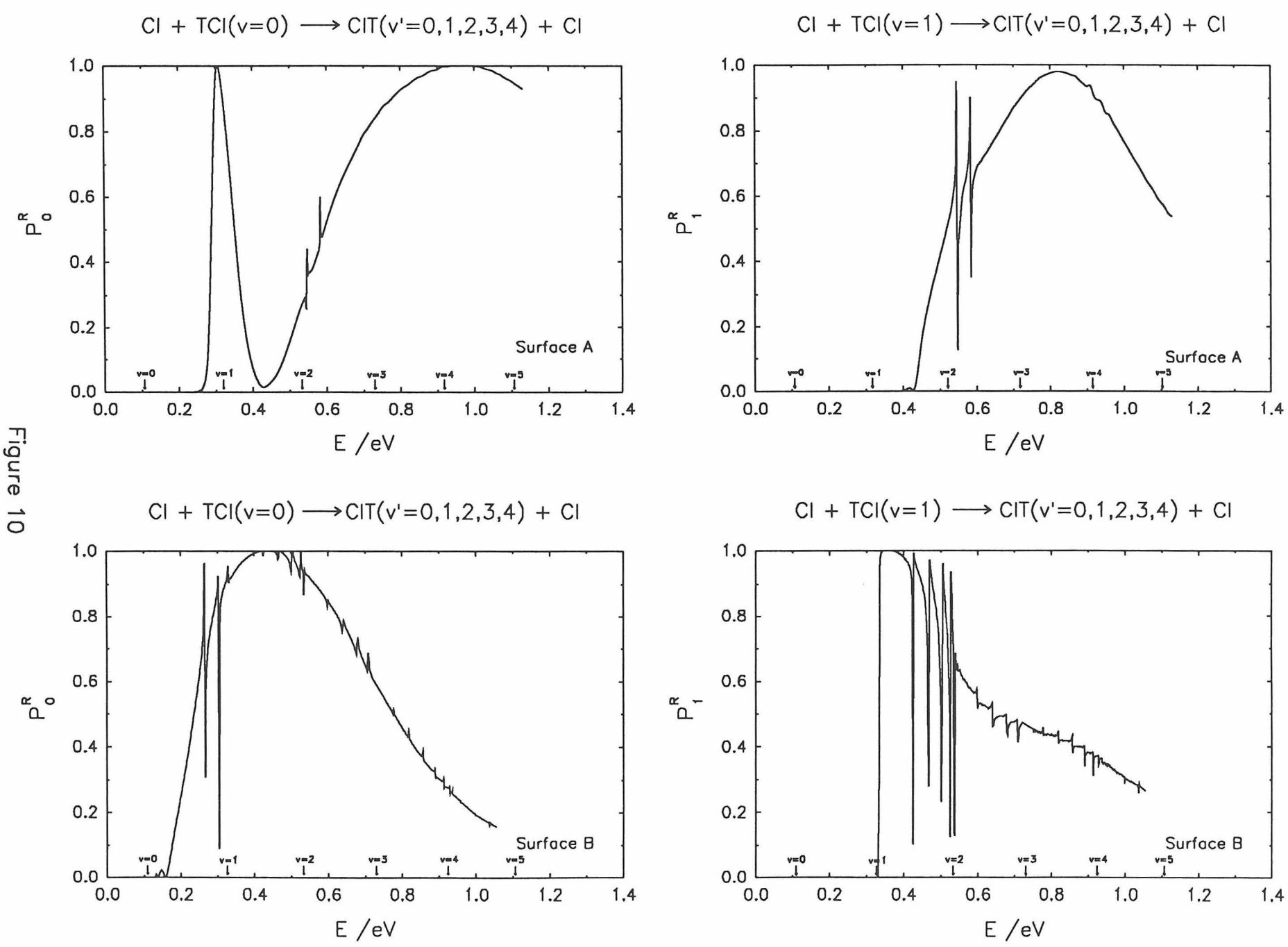
Cl + TCl(v=0) ⟶ ClT(v'=0,1,2,3,4) + Cl
Cl + TCl(v=1) ⟶ ClT(v'=0,1,2,3,4) + Cl
Cl + TCl(v=0) ⟶ ClT(v'=0,1,2,3,4) + Cl
Cl + TCl(v=1) ⟶ ClT(v'=0,1,2,3,4) + Cl
P_0^R
P_1^R
E /eV
Surface A
Surface B
v=0
v=1
v=2
v=3
v=4
v=5
0.0
0.2
0.4
0.6
0.8
1.0
1.2
1.4

Figure 10

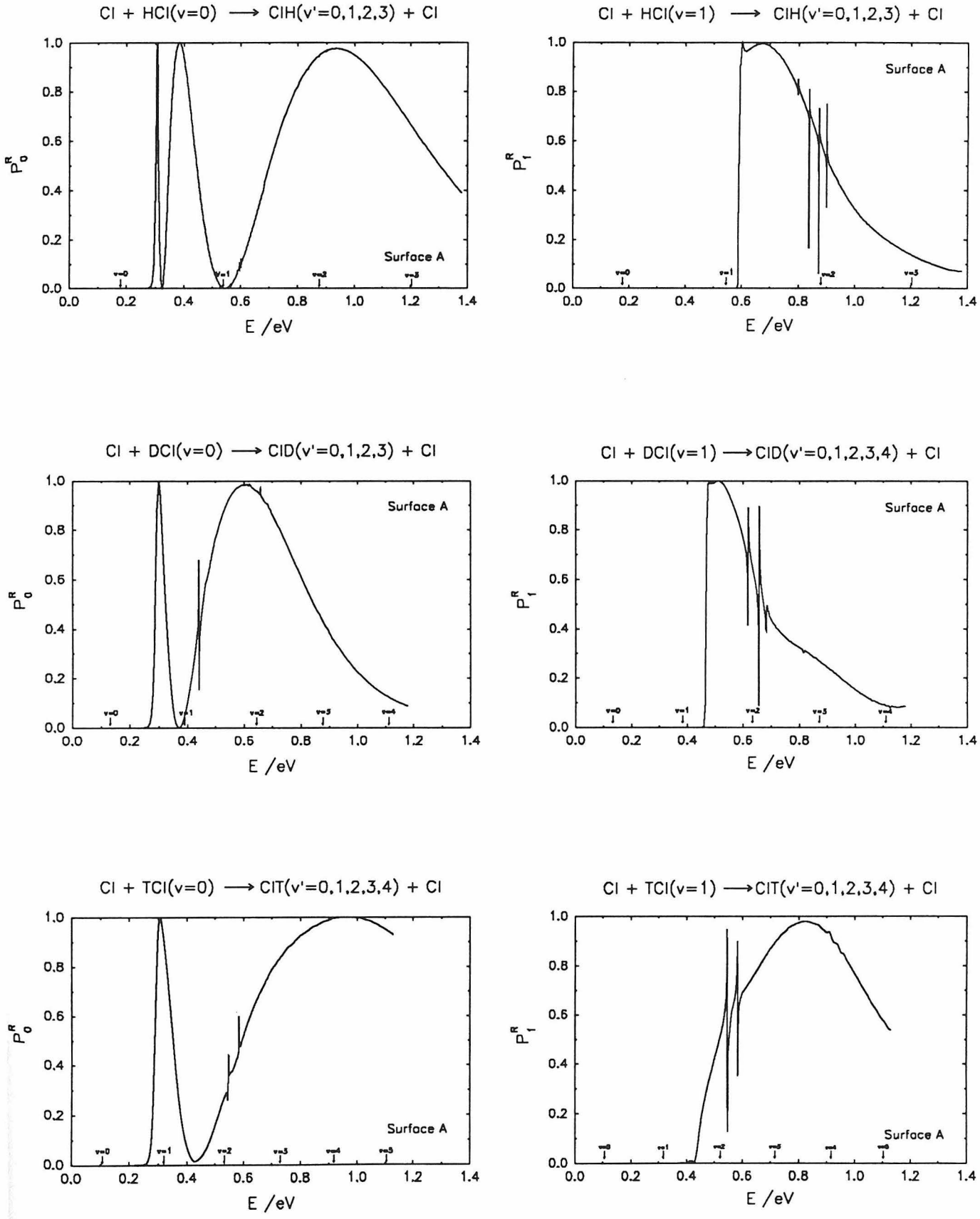
Cl + HCl(v=0) ⟶ ClH(v'=0,1,2,3) + Cl
Cl + HCl(v=1) ⟶ ClH(v'=0,1,2,3) + Cl
Cl + DCl(v=0) ⟶ ClD(v'=0,1,2,3) + Cl
Cl + DCl(v=1) ⟶ ClD(v'=0,1,2,3,4) + Cl
Cl + TCl(v=0) ⟶ ClT(v'=0,1,2,3,4) + Cl
Cl + TCl(v=1) ⟶ ClT(v'=0,1,2,3,4) + Cl
Surface A
P_0^R
P_1^R
E /eV

Figure 11

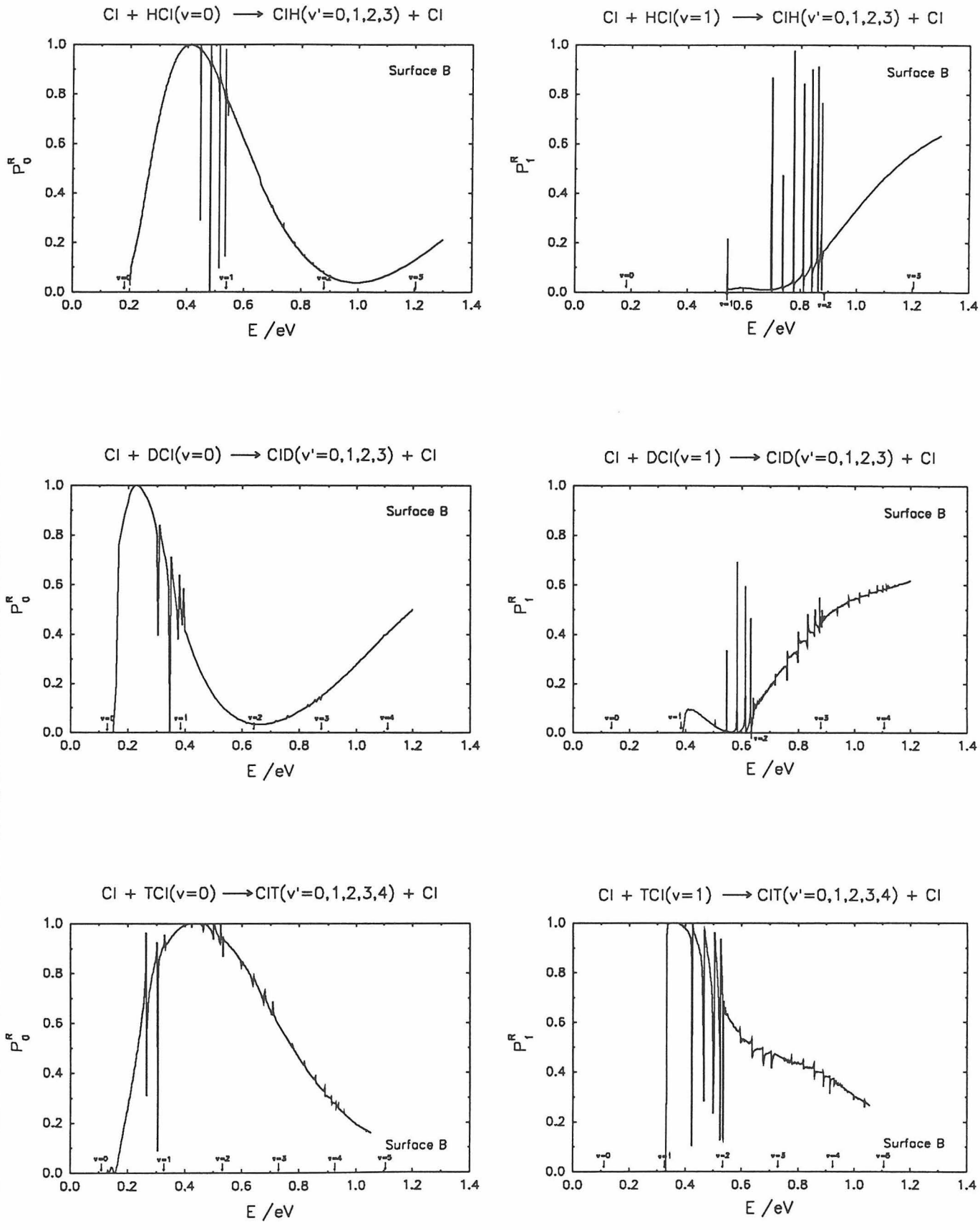
Cl + HCl(v=0) ⟶ ClH(v'=0,1,2,3) + Cl
Cl + HCl(v=1) ⟶ ClH(v'=0,1,2,3) + Cl
Cl + DCl(v=0) ⟶ ClD(v'=0,1,2,3) + Cl
Cl + DCl(v=1) ⟶ ClD(v'=0,1,2,3) + Cl
Cl + TCl(v=0) ⟶ ClT(v'=0,1,2,3,4) + Cl
Cl + TCl(v=1) ⟶ ClT(v'=0,1,2,3,4) + Cl
Surface B
P_0^R
P_1^R
E /eV

Figure 12

State–to–state reaction probabilities

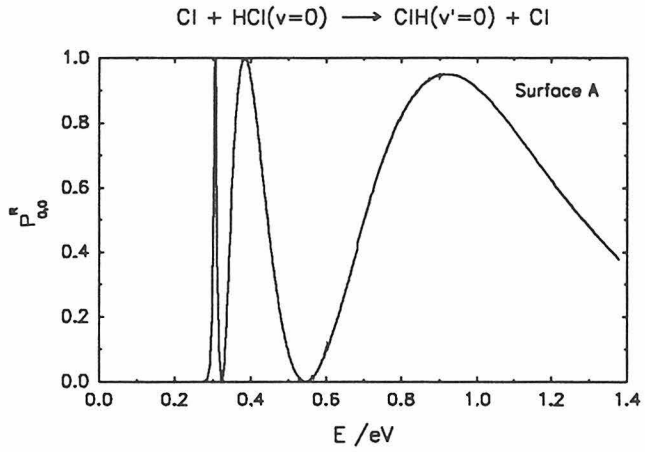

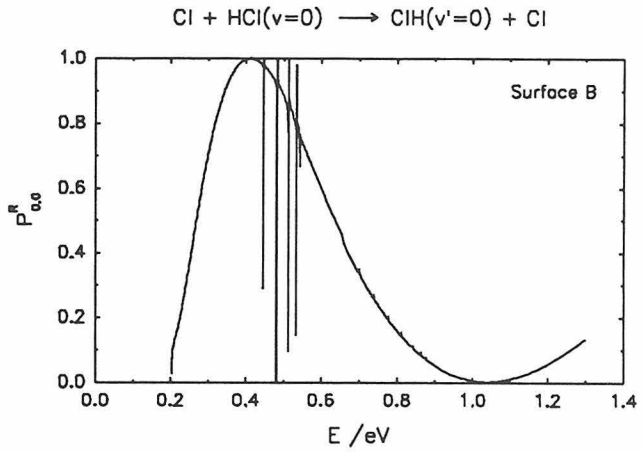

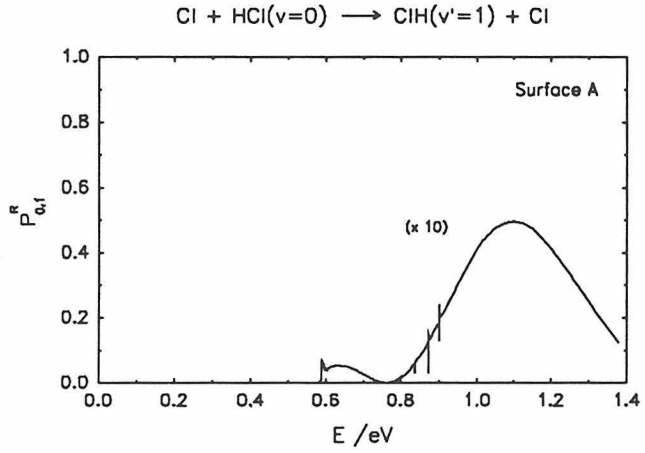

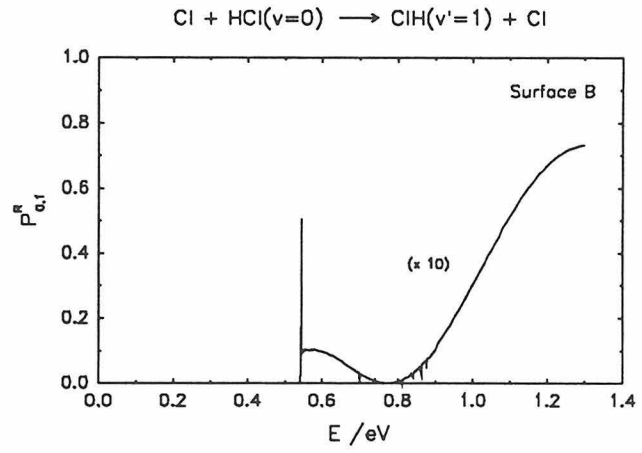

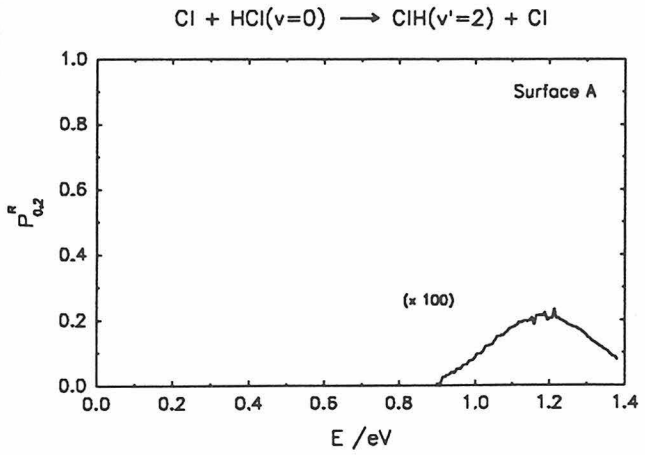

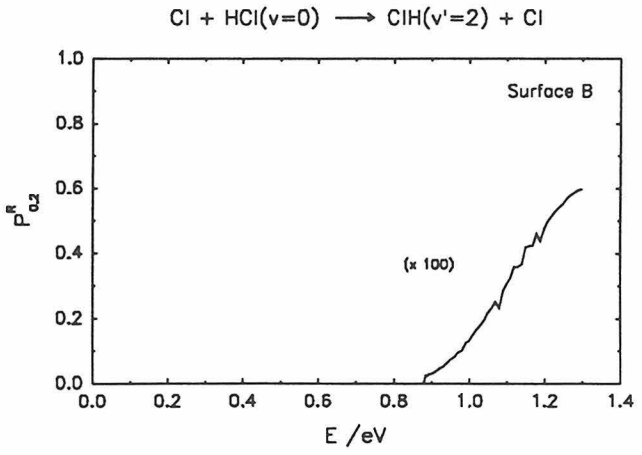

Figure 13

State–to–state reaction probabilities

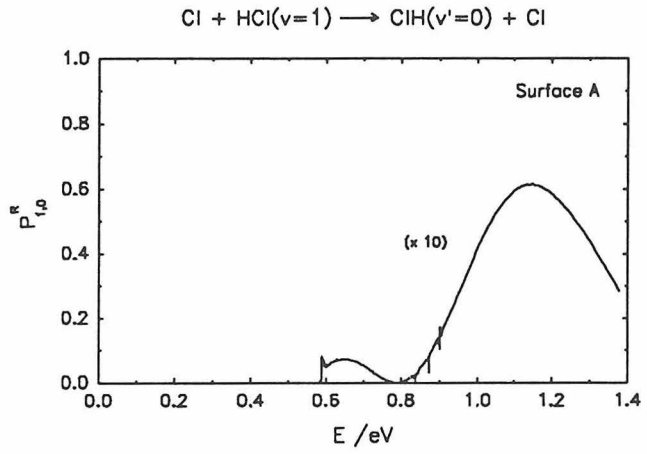

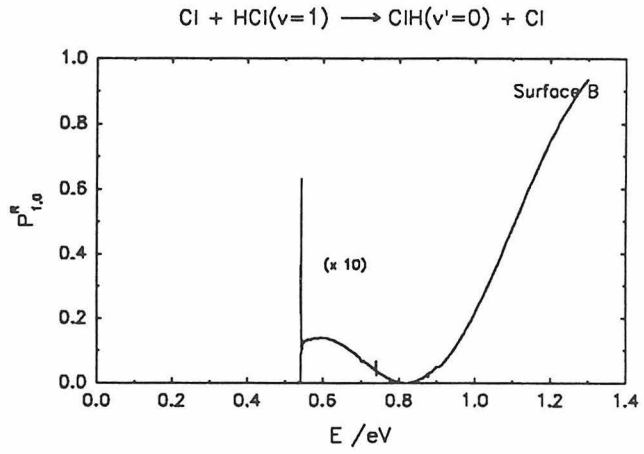

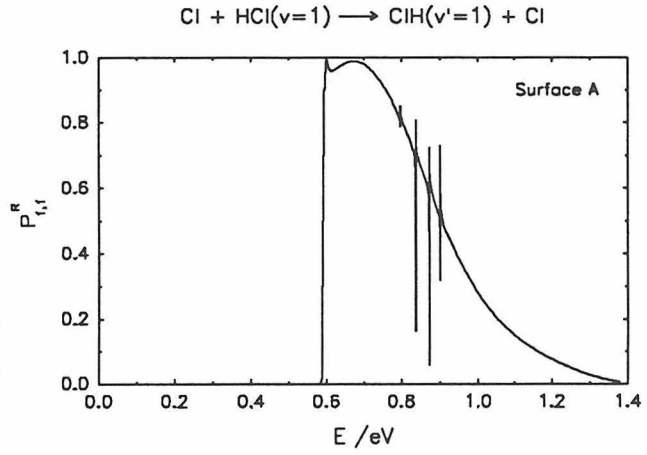

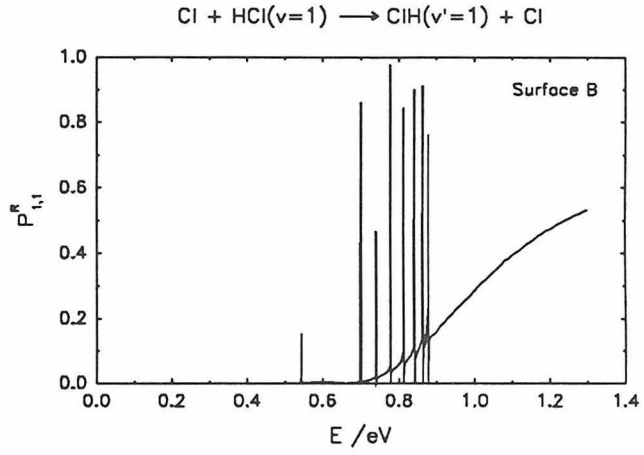

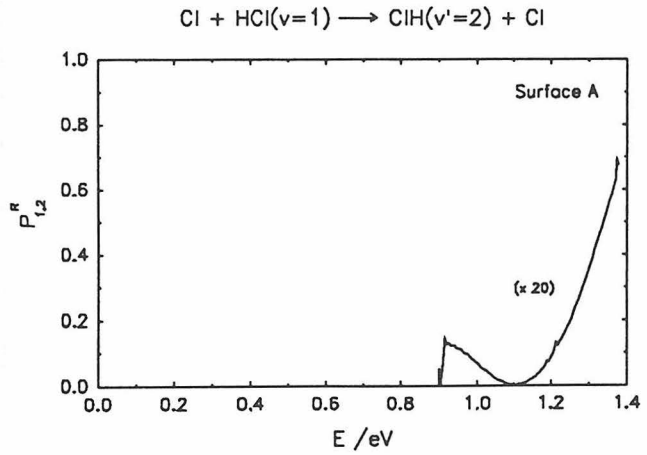

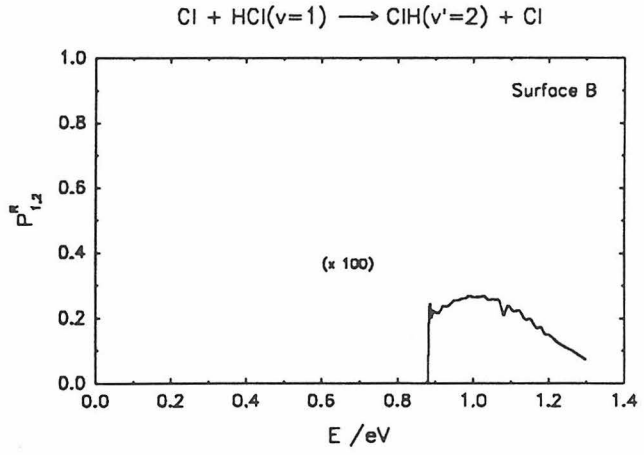

Figure 14

State–to–state reaction probabilities

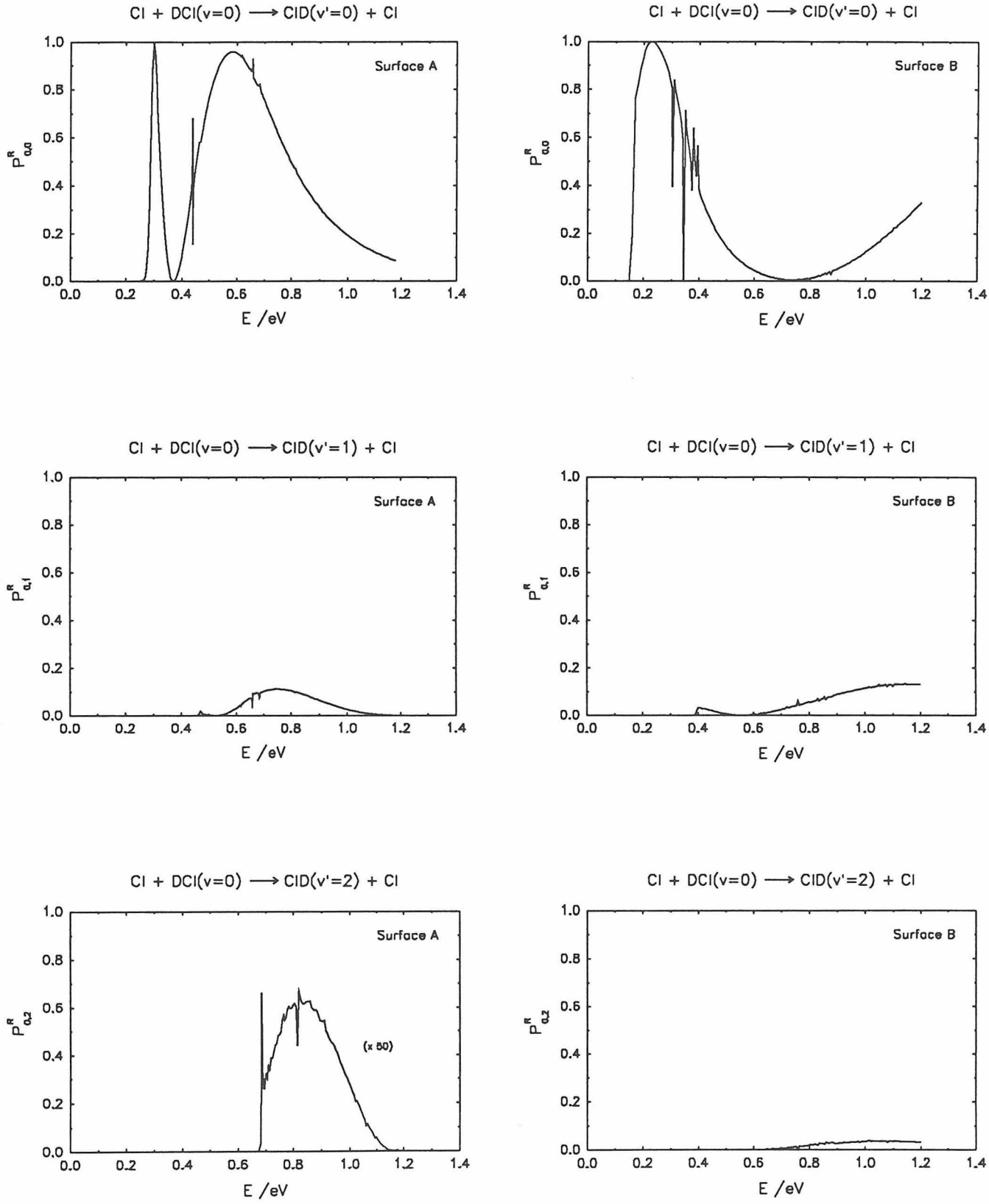

Figure 15

State–to–state reaction probabilities

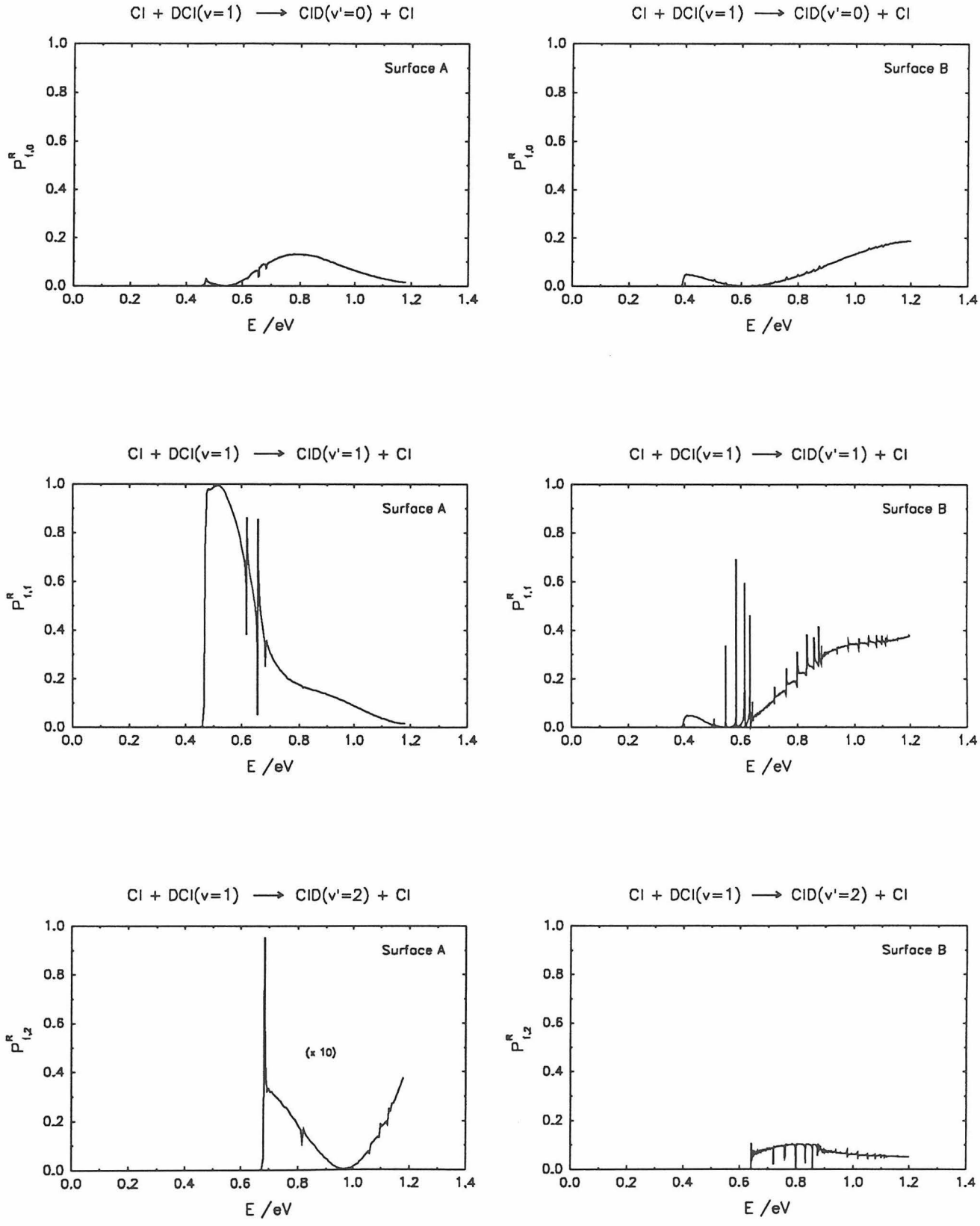

Figure 16

State–to–state reaction probabilities

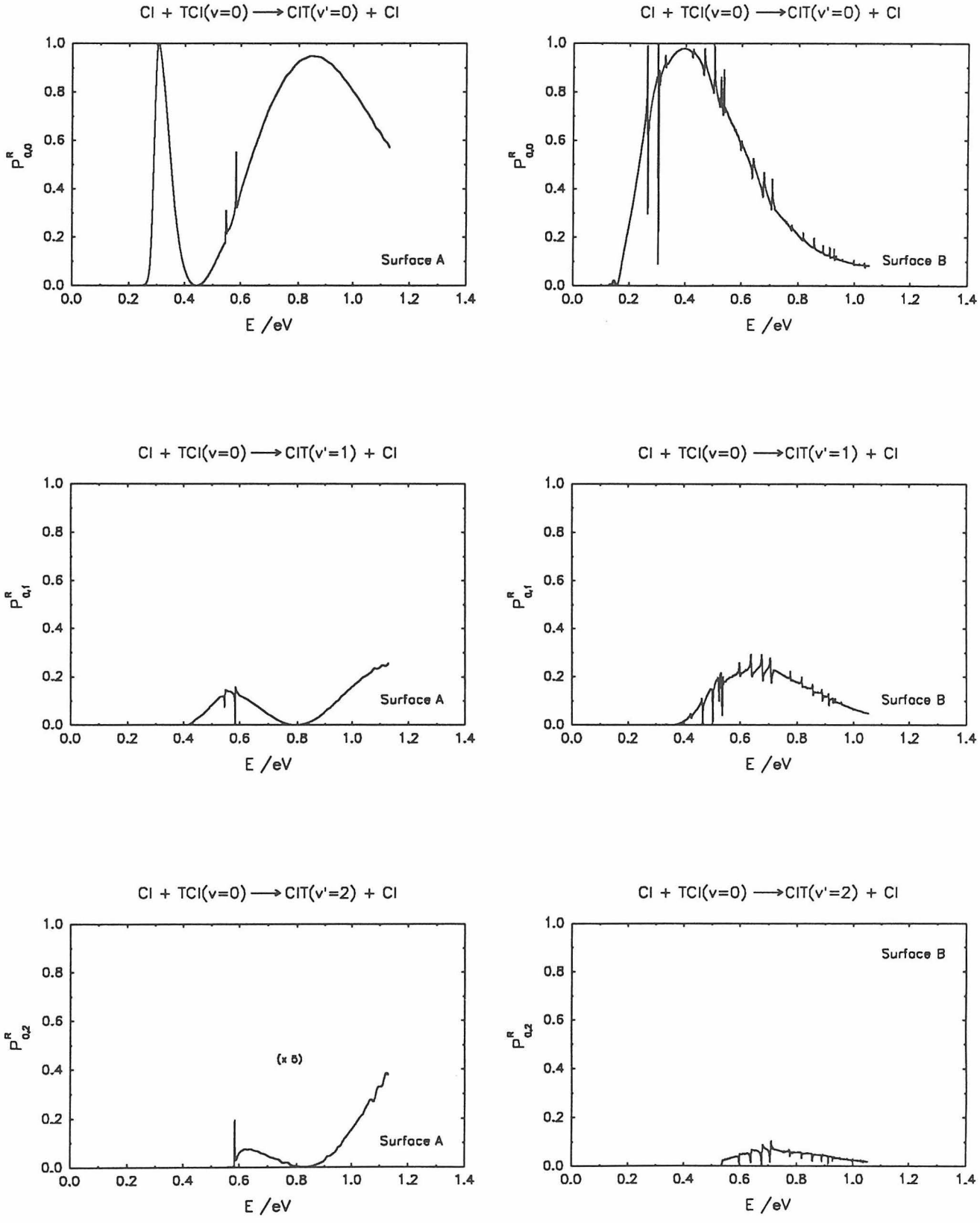

Figure 17

State–to–state reaction probabilities

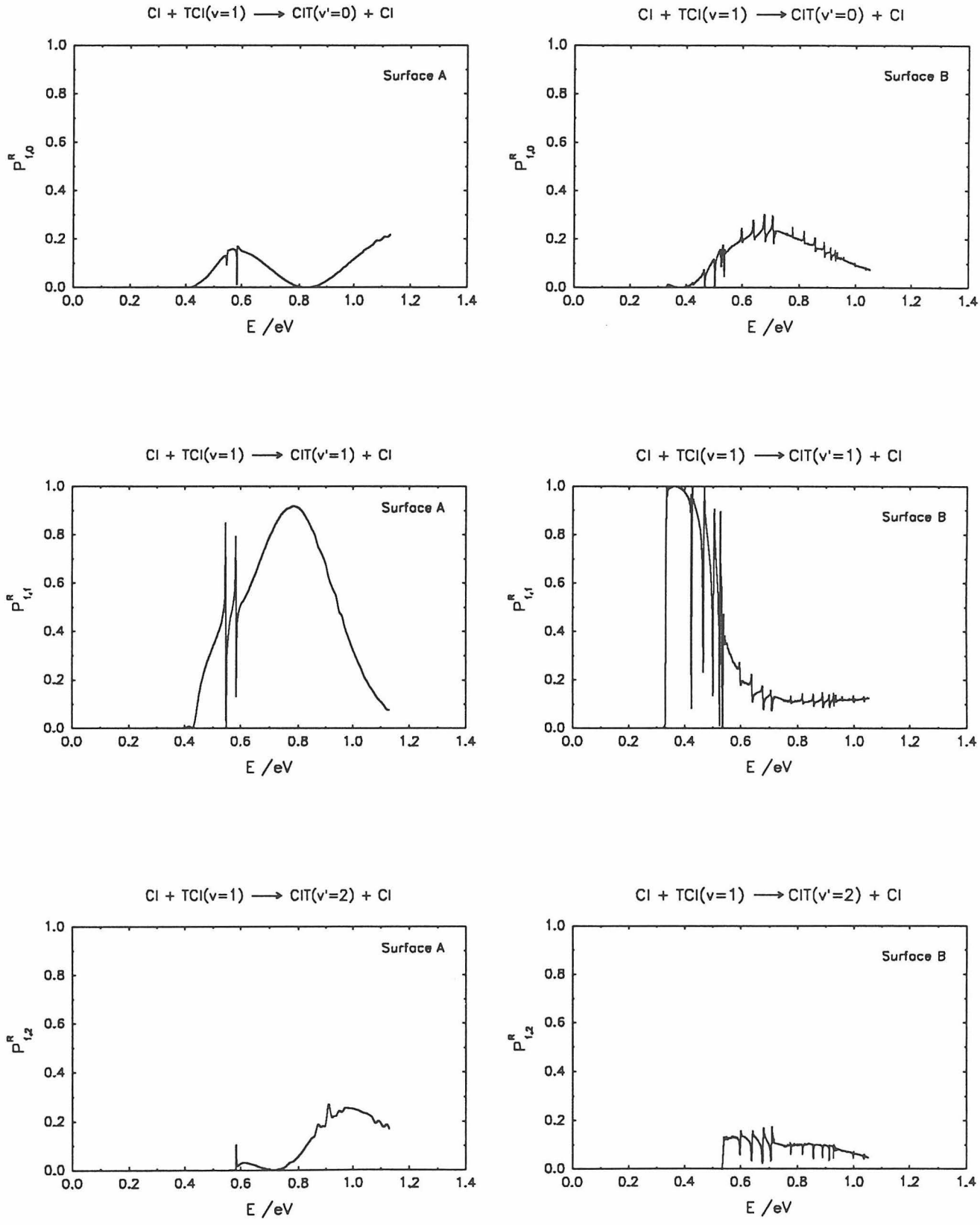

Figure 18

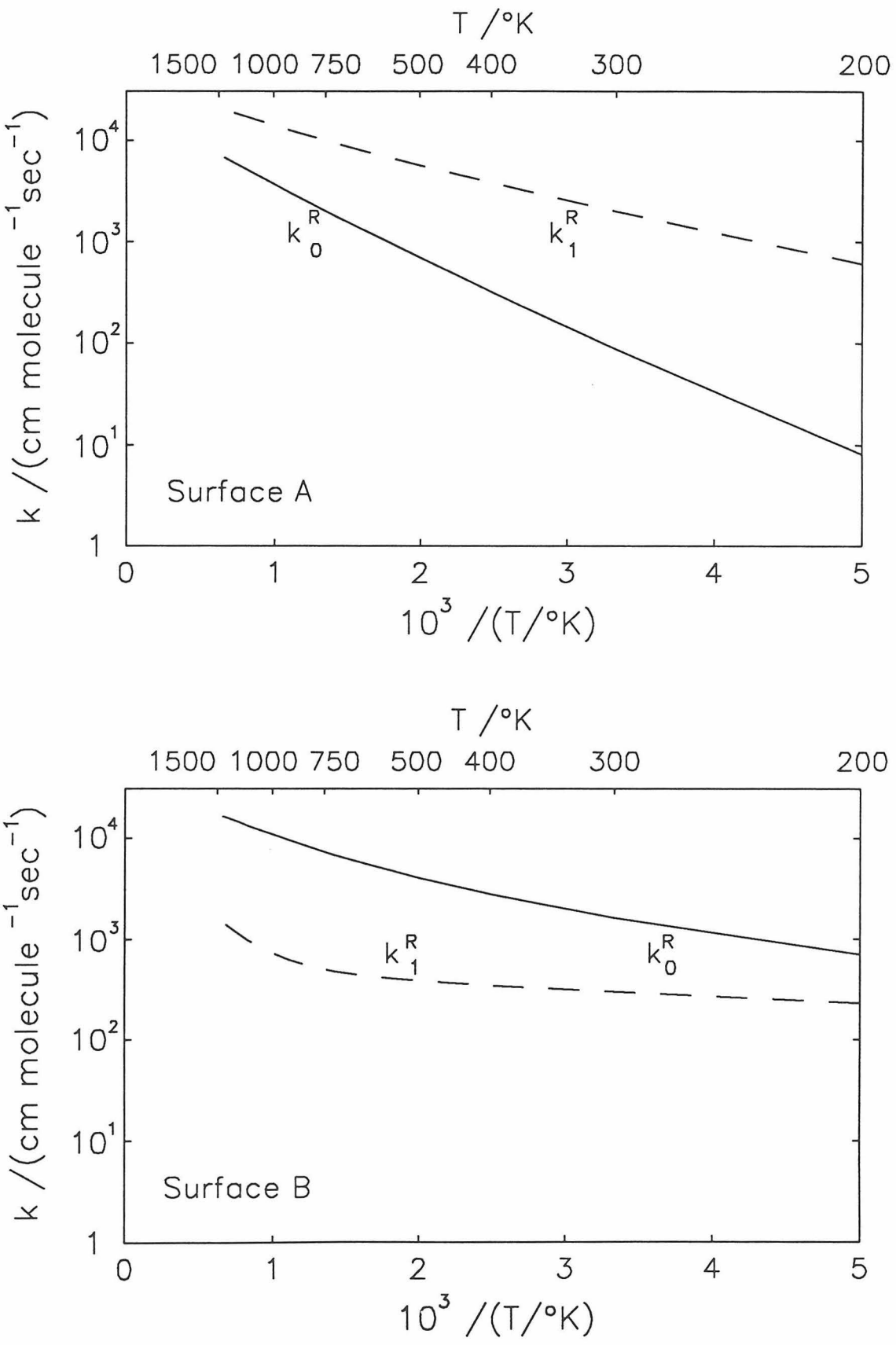
Rateconstants for Cl + HCl
T /°K
1500 1000 750 500 400 300 200
k /(cm molecule $^{-1}$sec^{-1})
10^4
10^3
10^2
10^1
1
k_0^R
k_1^R
Surface A
0 1 2 3 4 5
10^3 /(T/°K)
T /°K
1500 1000 750 500 400 300 200
k /(cm molecule $^{-1}$sec^{-1})
10^4
10^3
10^2
10^1
1
k_1^R
k_0^R
Surface B
0 1 2 3 4 5
10^3 /(T/°K)

Figure 19

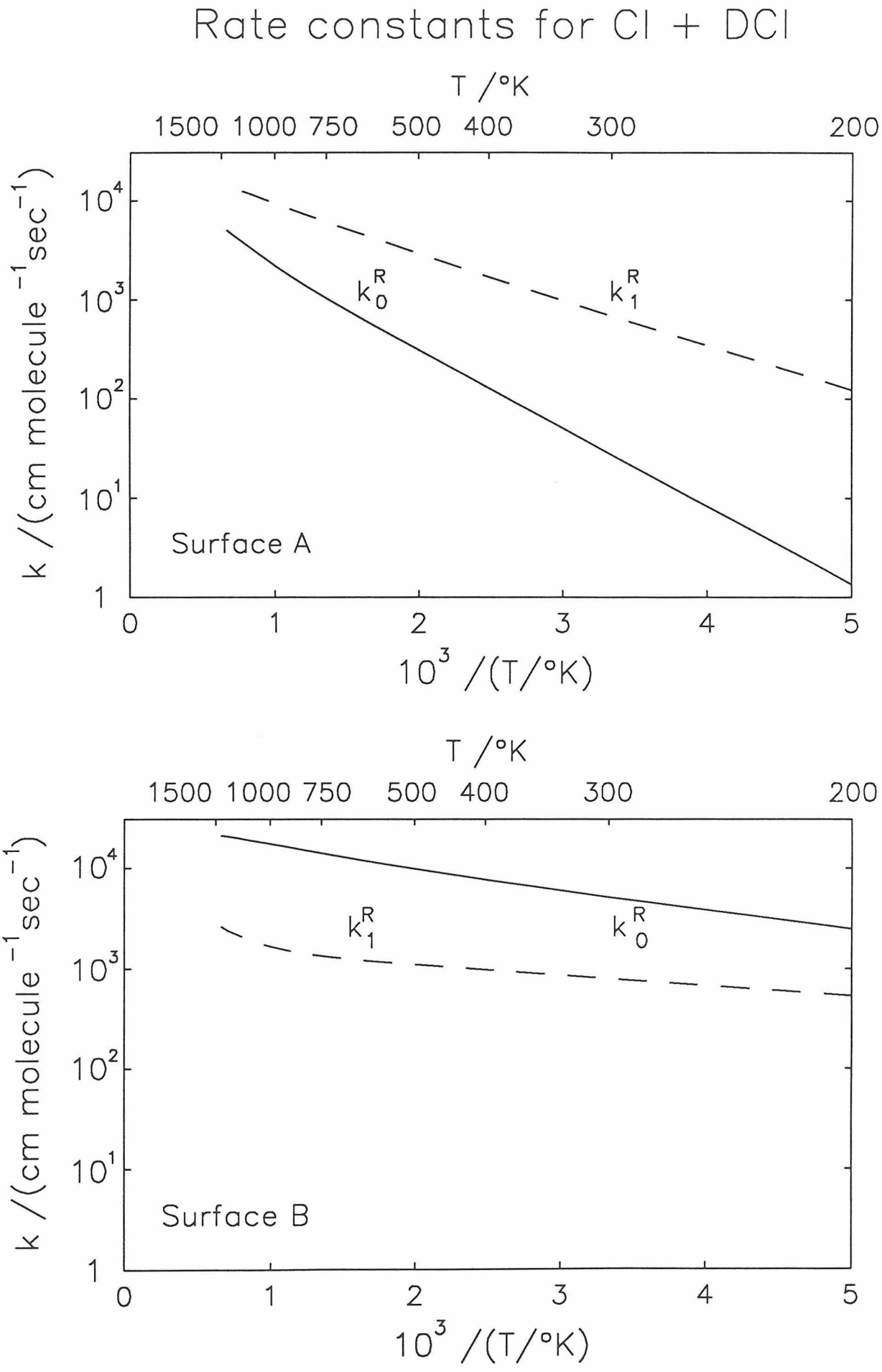
Rate constants for Cl + DCl
T /°K
1500 1000 750 500 400 300 200
k /(cm molecule^{-1}sec^{-1})
10^4
10^3
10^2
10^1
1
k_0^R
k_1^R
Surface A
0 1 2 3 4 5
10^3 /(T/°K)
T /°K
1500 1000 750 500 400 300 200
k /(cm molecule^{-1}sec^{-1})
10^4
10^3
10^2
10^1
1
k_1^R
k_0^R
Surface B
0 1 2 3 4 5
10^3 /(T/°K)

Figure 20

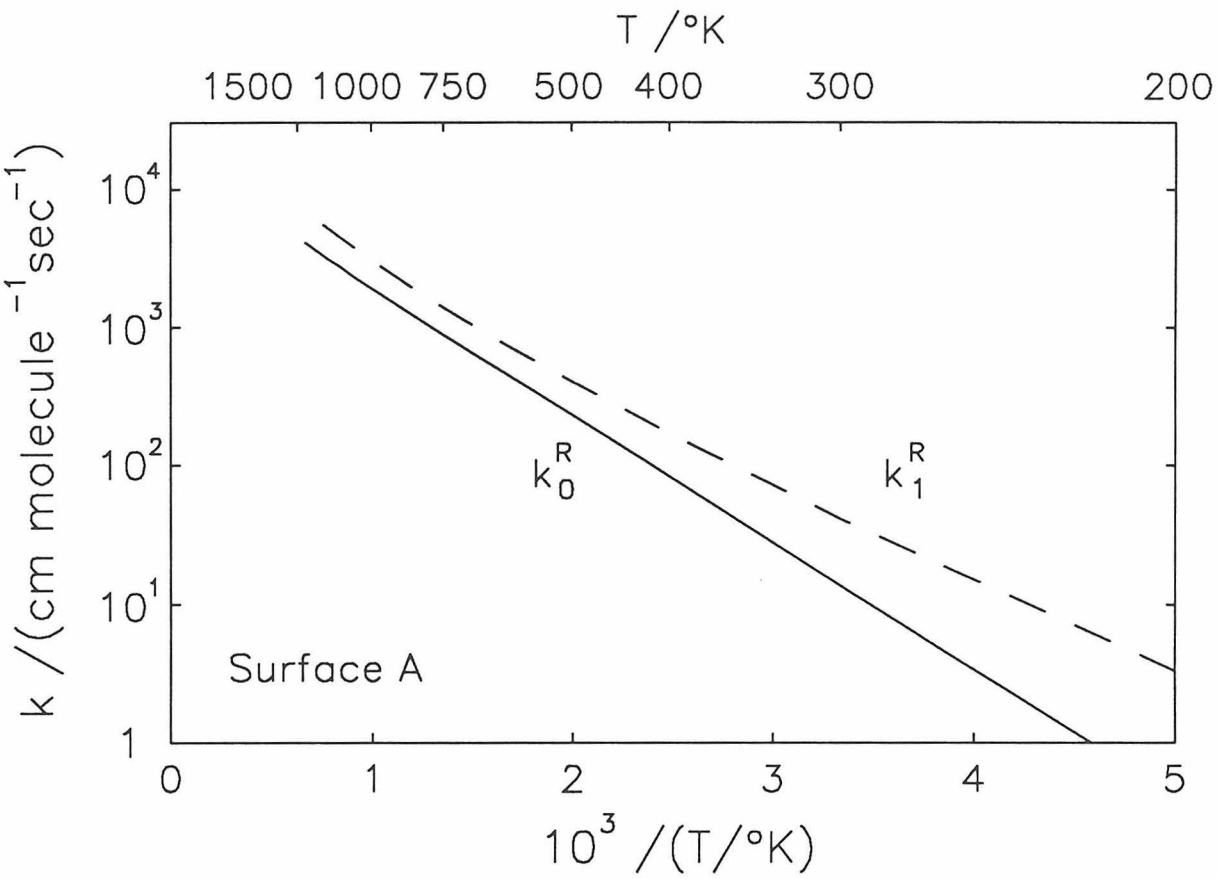
Rate constants for Cl + TCl
T /°K
1500 1000 750 500 400 300 200
k /(cm molecule^{-1}sec^{-1})
10^4
10^3
10^2
10^1
1
k_0^R
k_1^R
Surface A
0 1 2 3 4 5
10^3 /(T/°K)

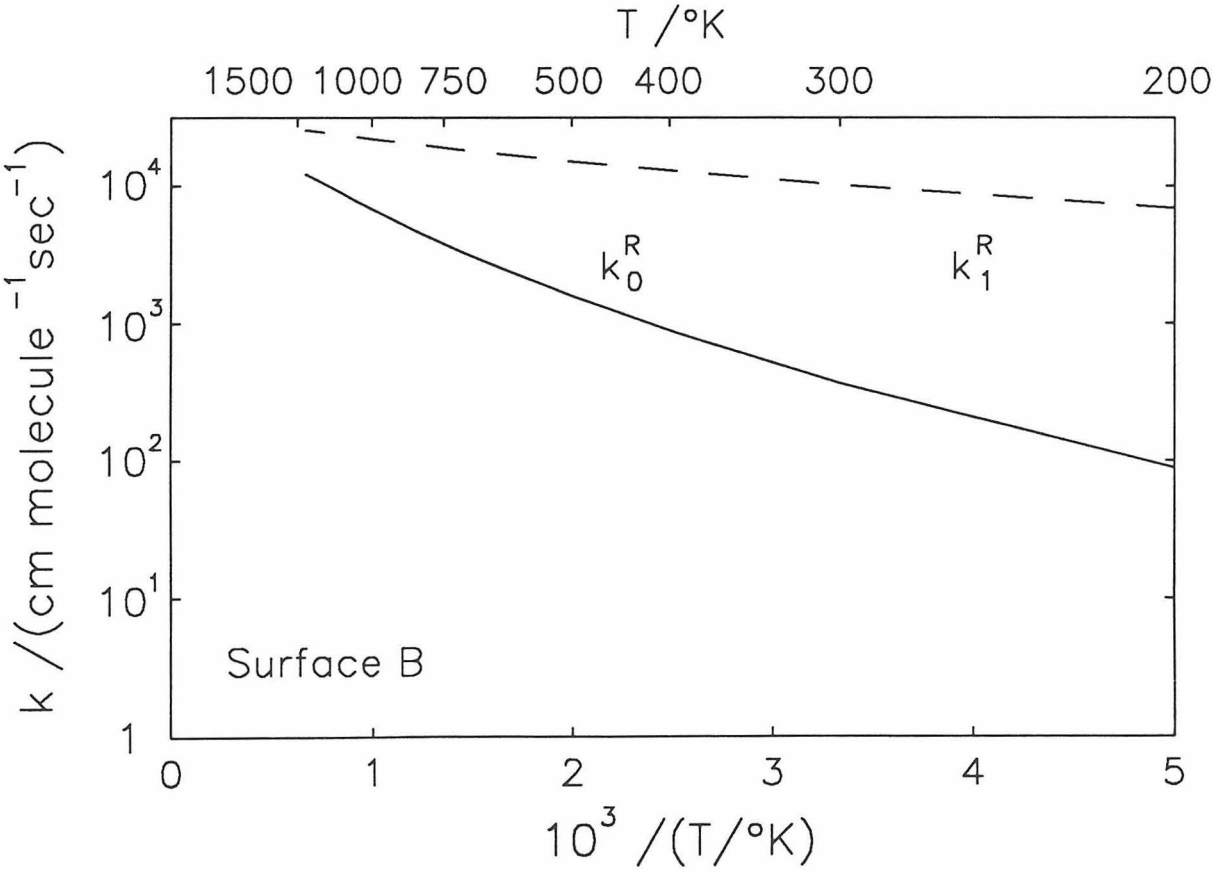
T /°K
1500 1000 750 500 400 300 200
k /(cm molecule^{-1}sec^{-1})
10^4
10^3
10^2
10^1
1
k_0^R
k_1^R
Surface B
0 1 2 3 4 5
10^3 /(T/°K)

Figure 21

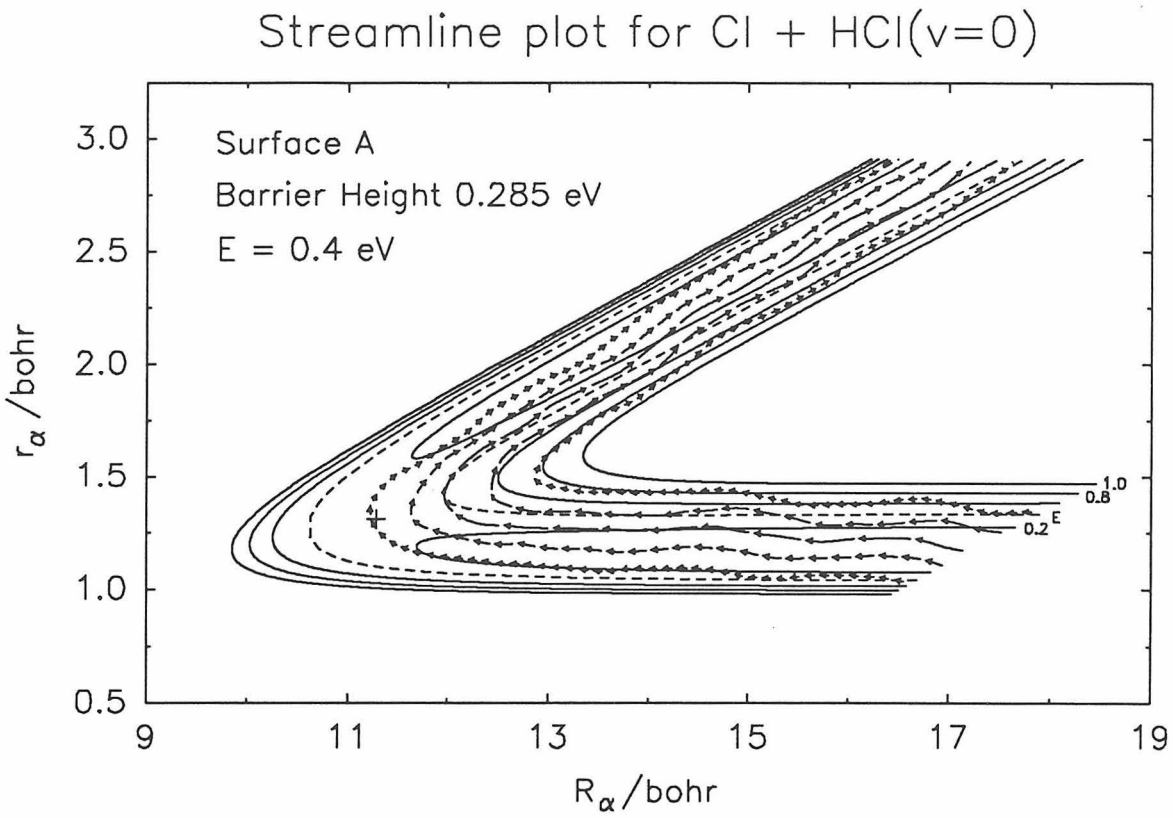
Streamline plot for Cl + HCl(v=0)
Surface A
Barrier Height 0.285 eV
E = 0.4 eV
1.0
0.8
0.2
E
3.0
2.5
2.0
1.5
1.0
0.5
9
11
13
15
17
19
r_α /bohr
R_α /bohr

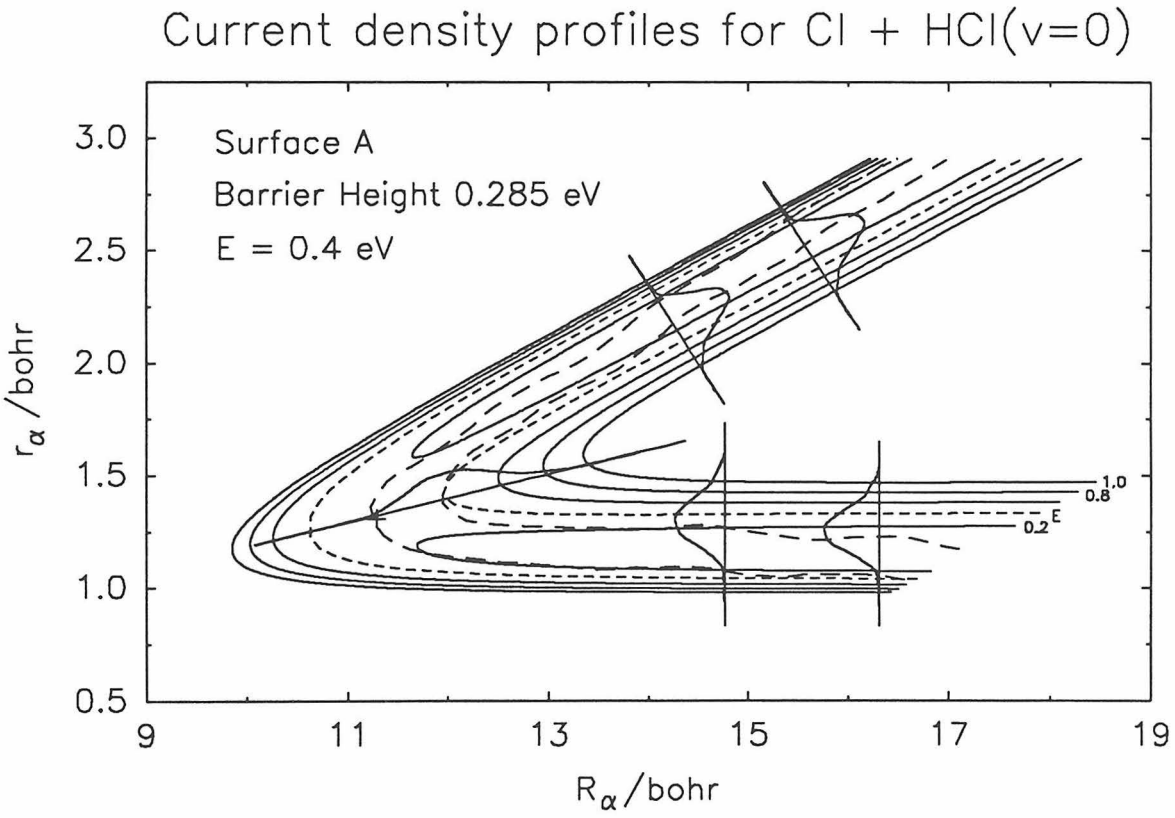
Current density profiles for Cl + HCl(v=0)
Surface A
Barrier Height 0.285 eV
E = 0.4 eV
1.0
0.8
0.2
E
3.0
2.5
2.0
1.5
1.0
0.5
9
11
13
15
17
19
r_α /bohr
R_α /bohr

Figure 22

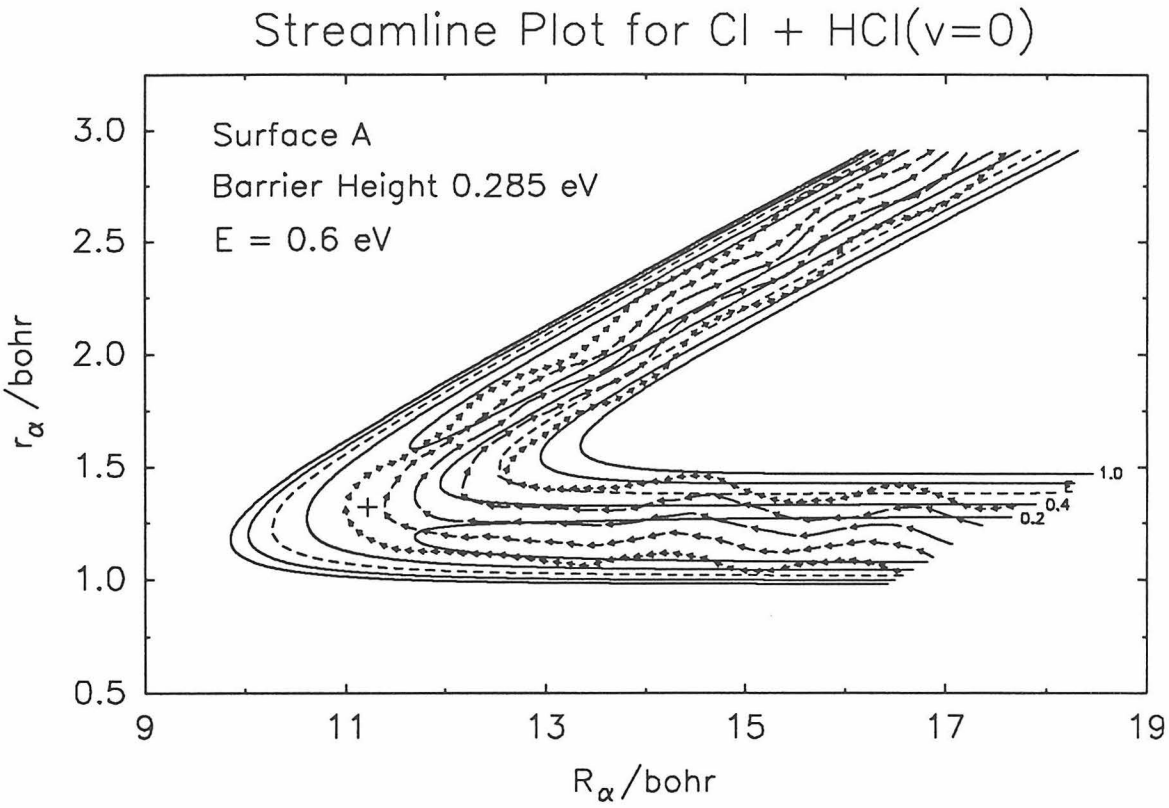
Streamline Plot for Cl + HCl(v=0)
Surface A
Barrier Height 0.285 eV
E = 0.6 eV
3.0
2.5
2.0
1.5
1.0
0.5
9
11
13
15
17
19
r_α /bohr
R_α /bohr
1.0
E
0.4
0.2

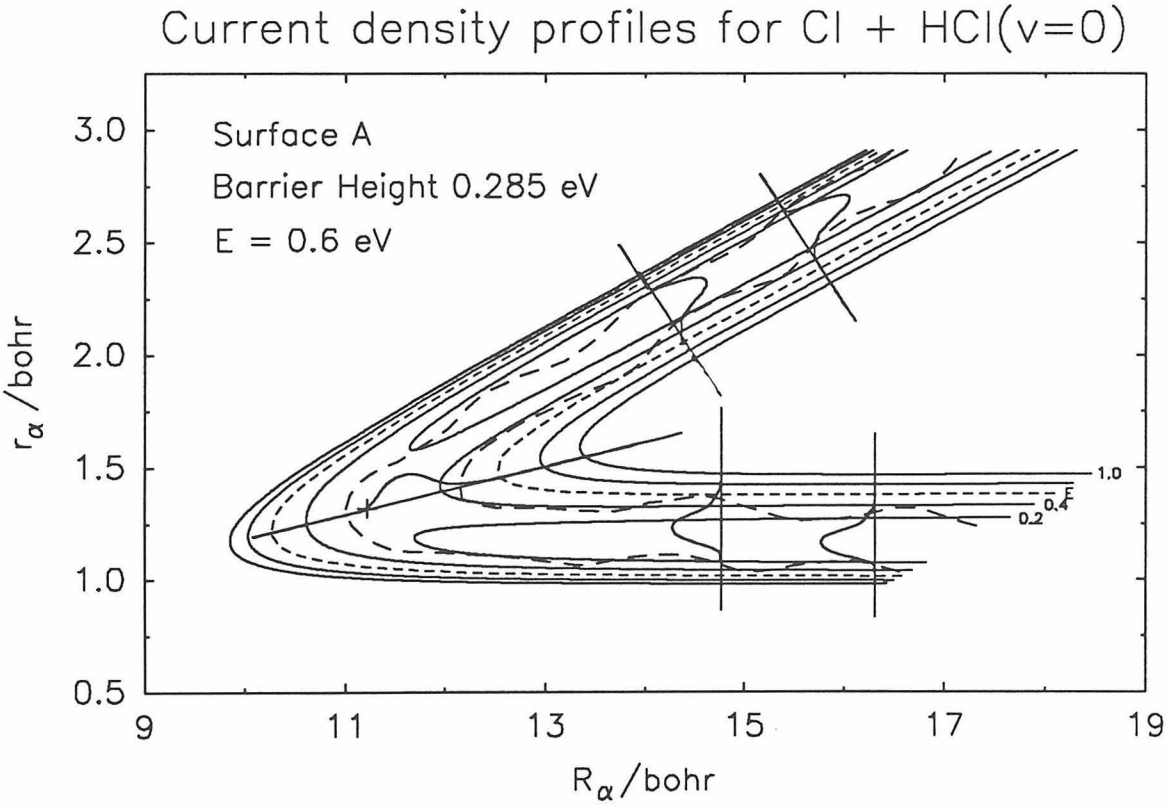
Current density profiles for Cl + HCl(v=0)
Surface A
Barrier Height 0.285 eV
E = 0.6 eV
3.0
2.5
2.0
1.5
1.0
0.5
9
11
13
15
17
19
r_α /bohr
R_α /bohr
1.0
E
0.4
0.2

Figure 23

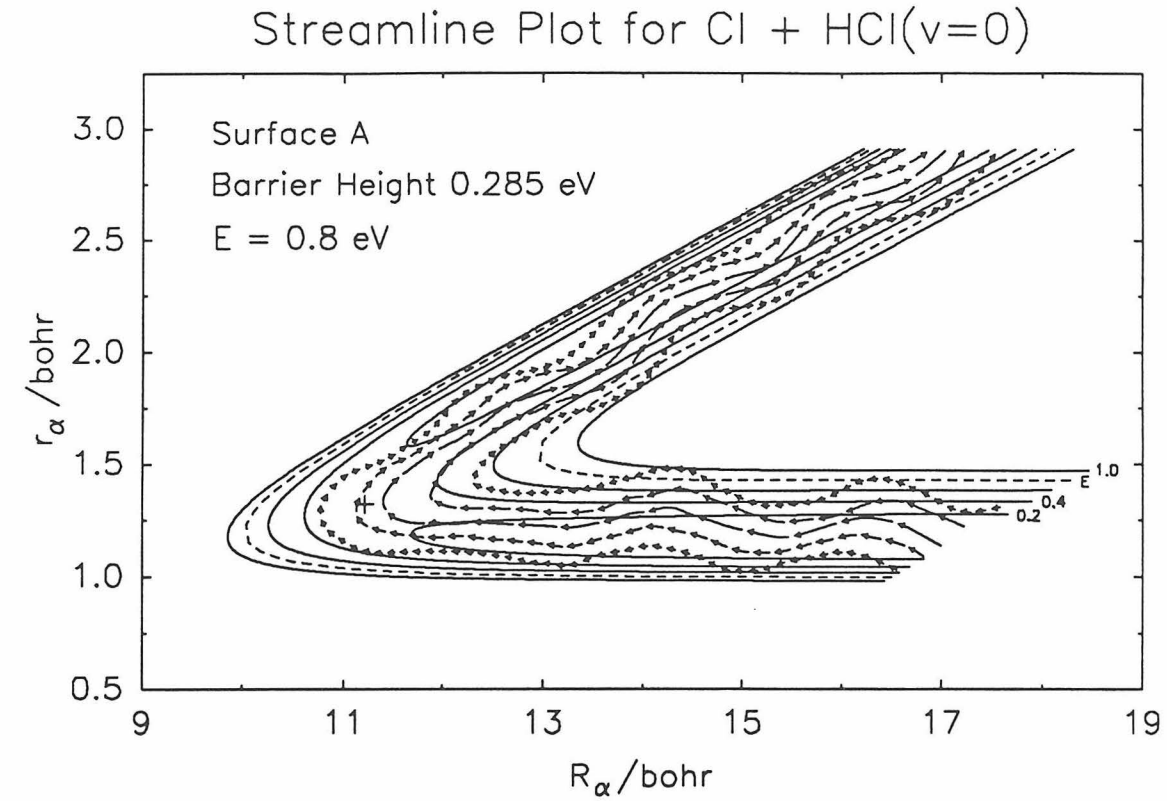
Streamline Plot for Cl + HCl(v=0)
Surface A
Barrier Height 0.285 eV
E = 0.8 eV
3.0
2.5
2.0
1.5
1.0
0.5
r_α /bohr
9
11
13
15
17
19
R_α /bohr
1.0
E
0.4
0.2

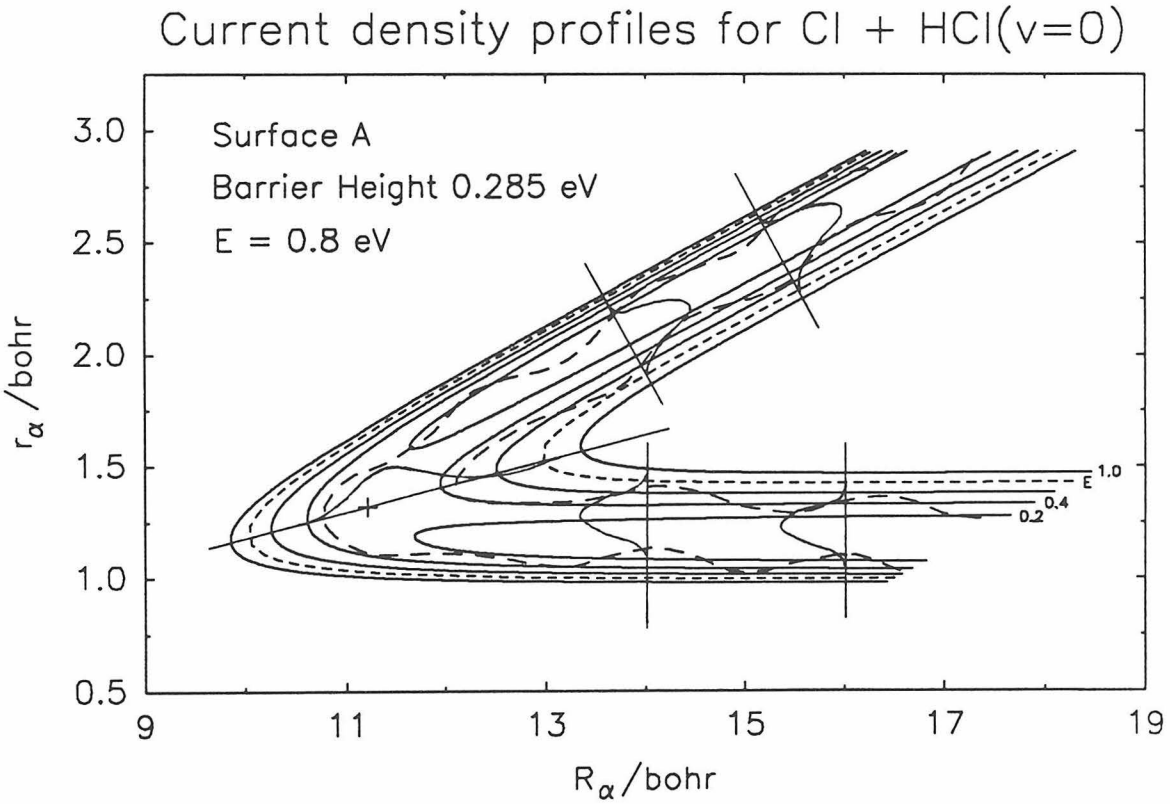
Current density profiles for Cl + HCl(v=0)
Surface A
Barrier Height 0.285 eV
E = 0.8 eV
3.0
2.5
2.0
1.5
1.0
0.5
r_α /bohr
9
11
13
15
17
19
R_α /bohr
1.0
E
0.4
0.2

Figure 24

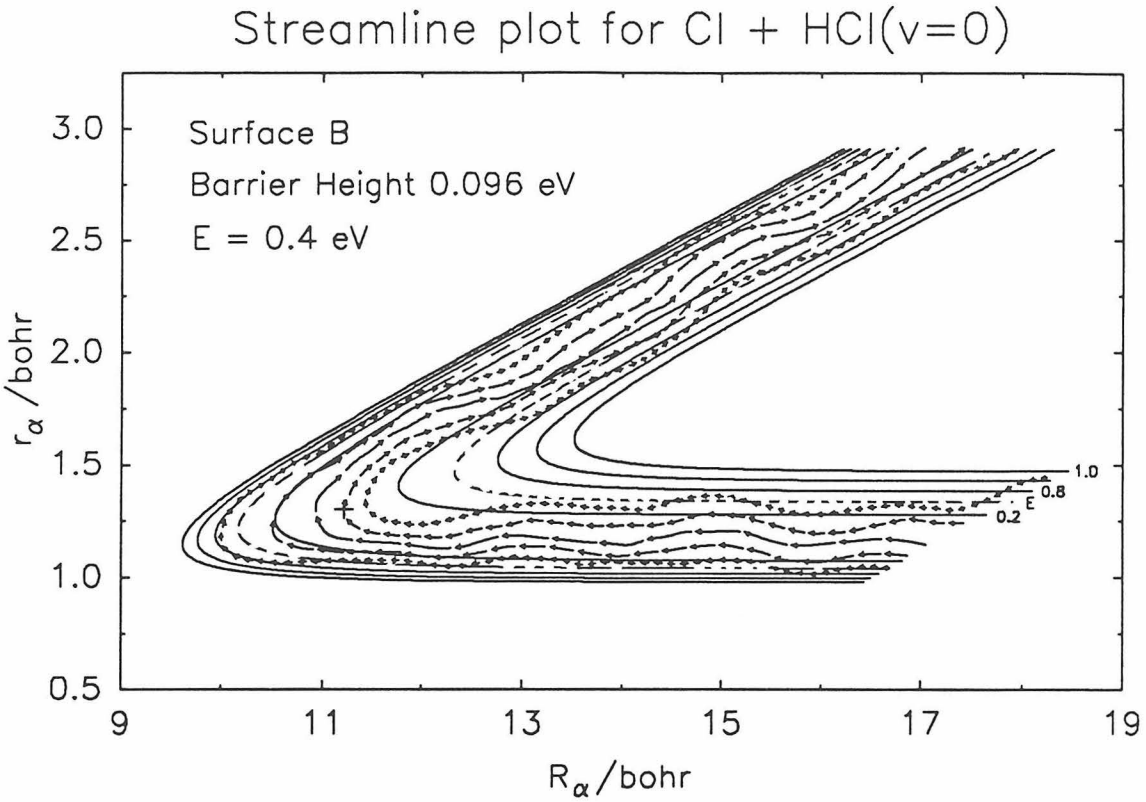
Streamline plot for Cl + HCl(v=0)
Surface B
Barrier Height 0.096 eV
E = 0.4 eV
3.0
2.5
2.0
1.5
1.0
0.5
r_α /bohr
9
11
13
15
17
19
R_α /bohr
1.0
0.8
E
0.2

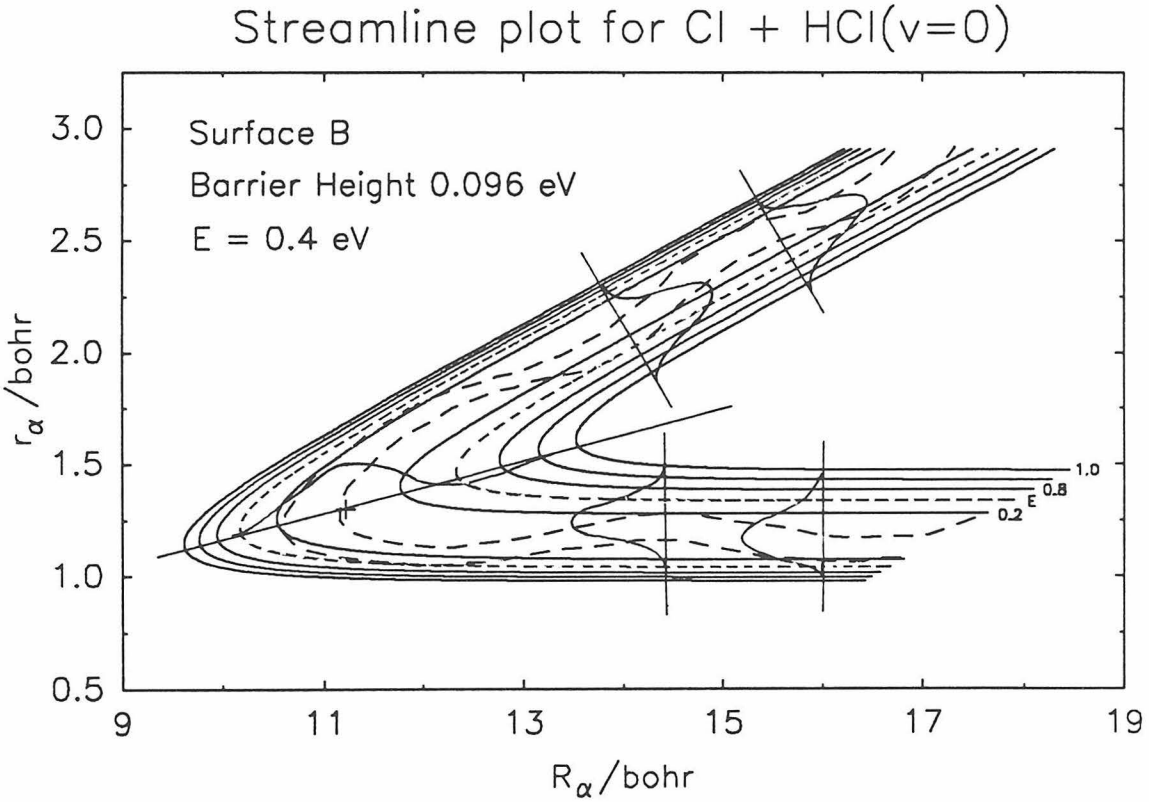
Streamline plot for Cl + HCl(v=0)
Surface B
Barrier Height 0.096 eV
E = 0.4 eV
3.0
2.5
2.0
1.5
1.0
0.5
r_α /bohr
9
11
13
15
17
19
R_α /bohr
1.0
0.8
E
0.2

Figure 25

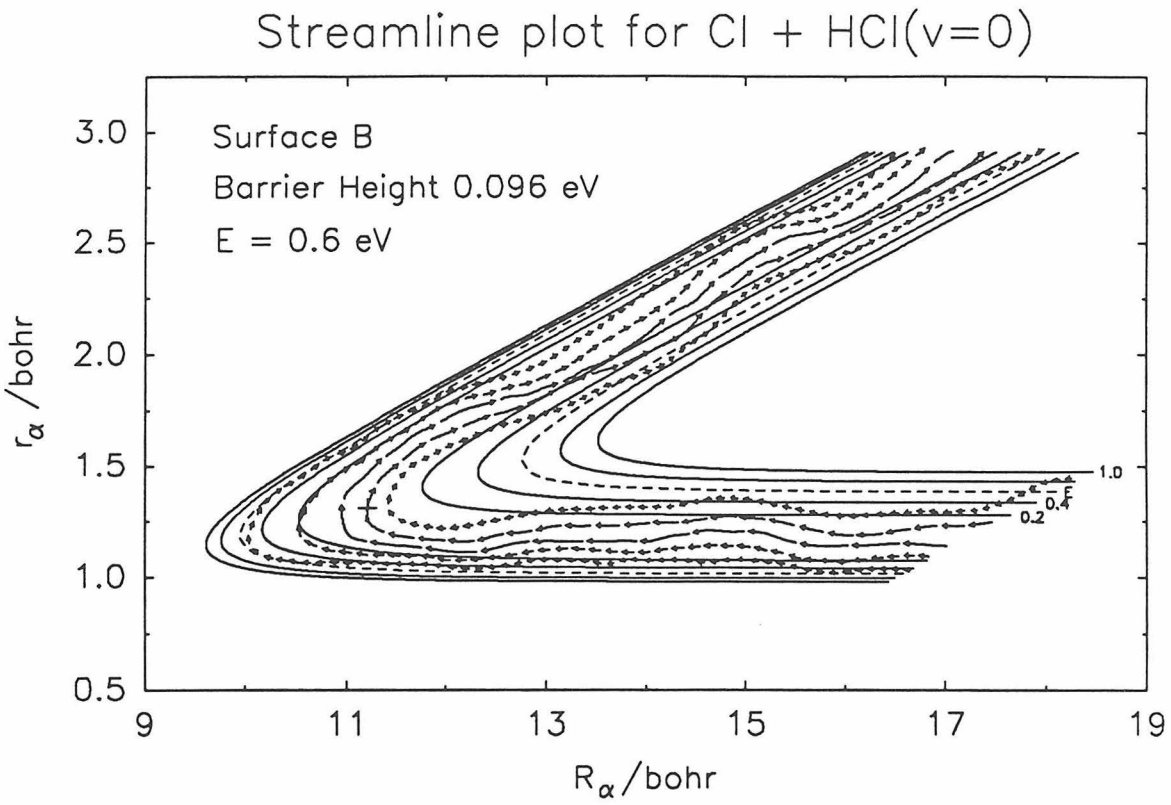
Streamline plot for Cl + HCl(v=0)
Surface B
Barrier Height 0.096 eV
E = 0.6 eV
3.0
2.5
2.0
1.5
1.0
0.5
9
11
13
15
17
19
r_α /bohr
R_α /bohr
1.0
0.4
E
0.2

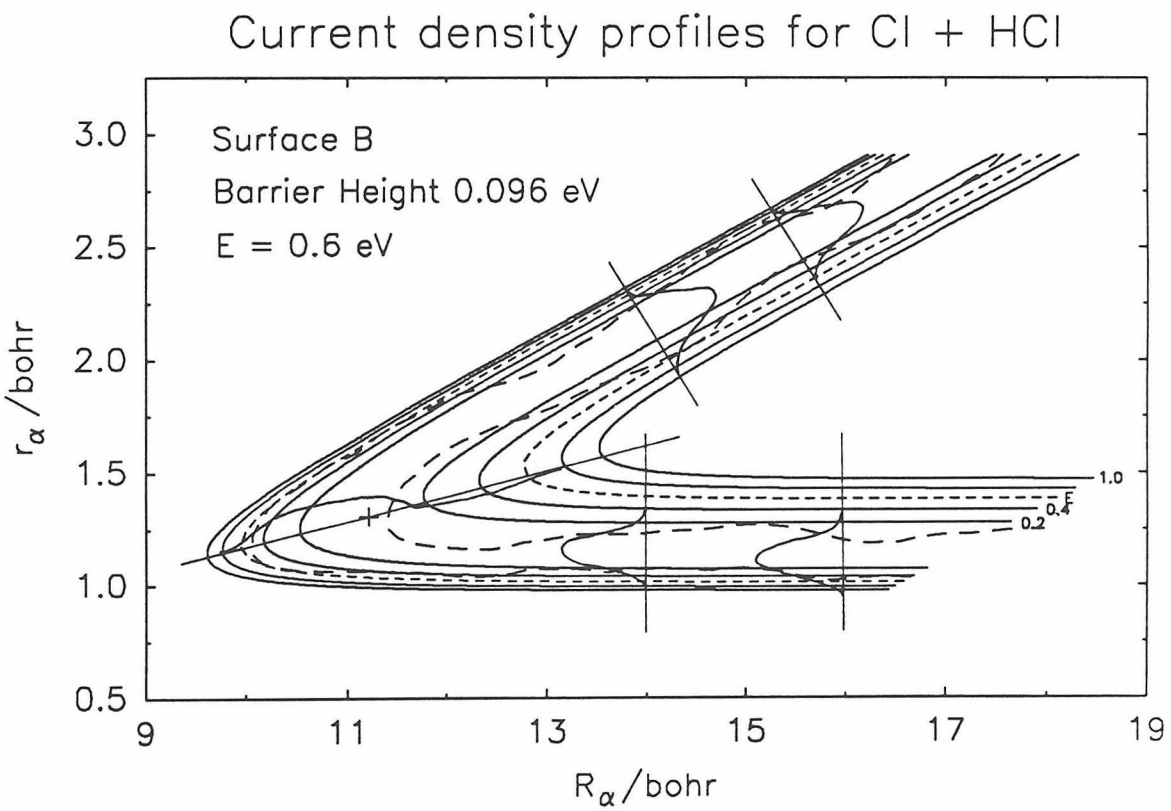
Current density profiles for Cl + HCl
Surface B
Barrier Height 0.096 eV
E = 0.6 eV
3.0
2.5
2.0
1.5
1.0
0.5
9
11
13
15
17
19
r_α /bohr
R_α /bohr
1.0
0.4
E
0.2

Figure 26

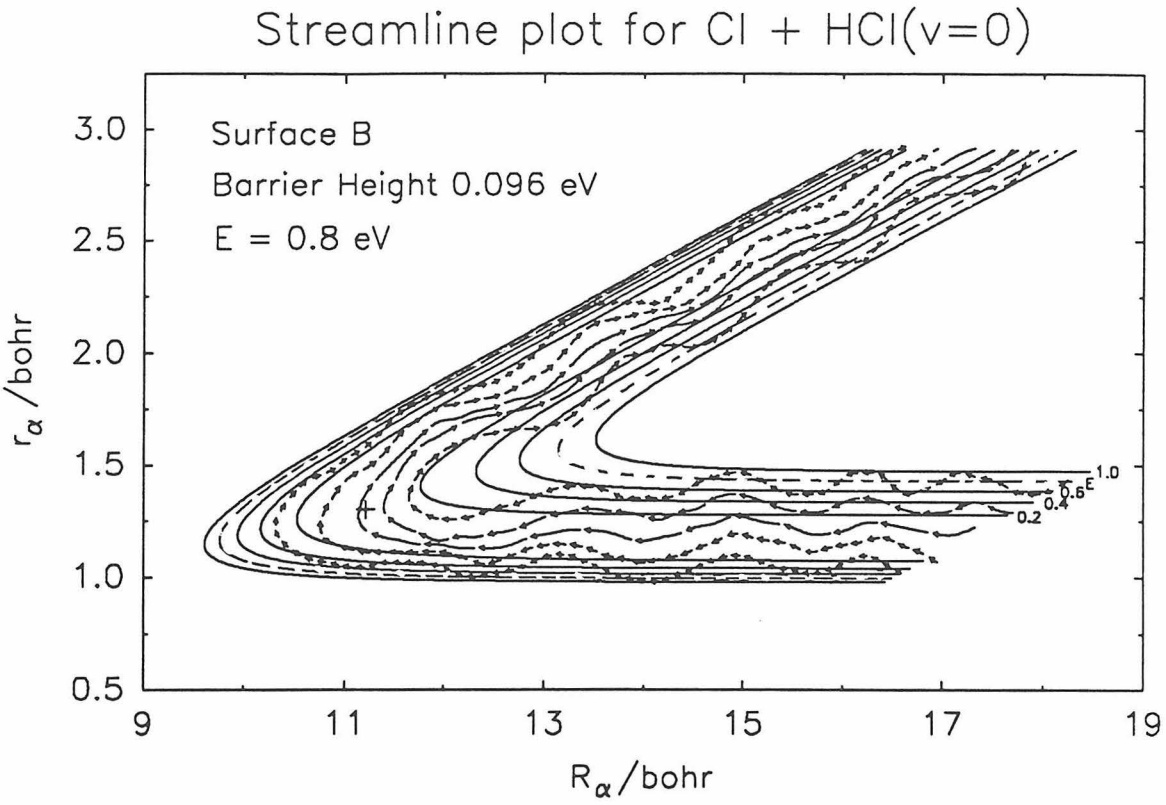
Streamline plot for Cl + HCl(v=0)
Surface B
Barrier Height 0.096 eV
E = 0.8 eV
3.0
2.5
2.0
1.5
1.0
0.5
9
11
13
15
17
19
r_α /bohr
R_α /bohr
0.2
0.4
0.6
E
1.0

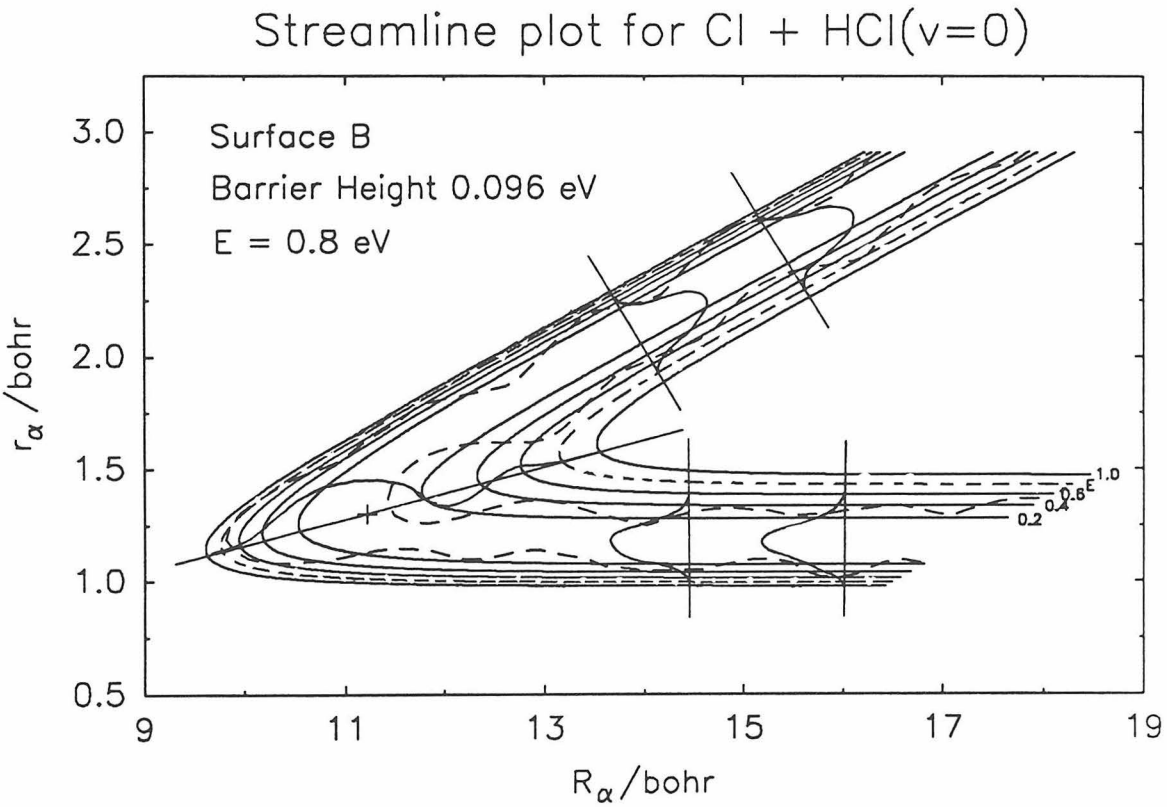
Streamline plot for Cl + HCl(v=0)
Surface B
Barrier Height 0.096 eV
E = 0.8 eV
3.0
2.5
2.0
1.5
1.0
0.5
9
11
13
15
17
19
r_α /bohr
R_α /bohr
0.2
0.4
0.6
E
1.0

Figure 27

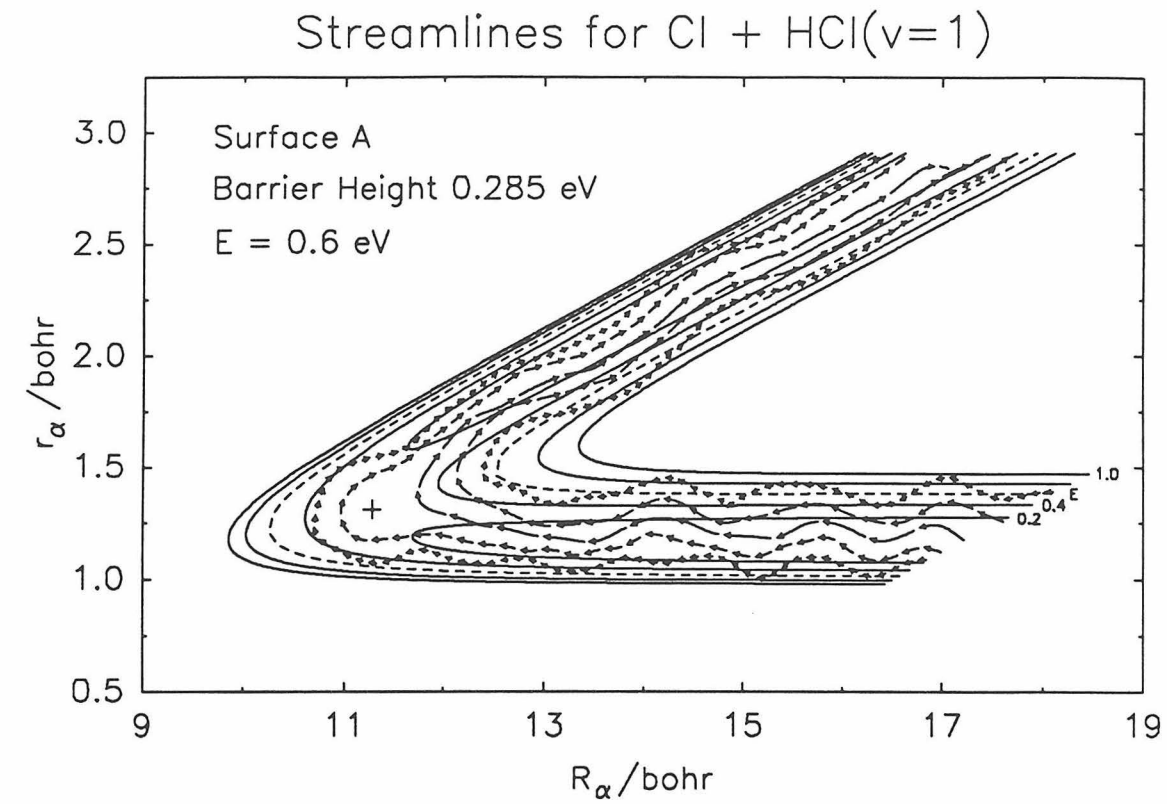
Streamlines for Cl + HCl(v=1)
Surface A
Barrier Height 0.285 eV
E = 0.6 eV
3.0
2.5
2.0
1.5
1.0
0.5
9
11
13
15
17
19
r_α /bohr
R_α /bohr
1.0
0.4
0.2
E

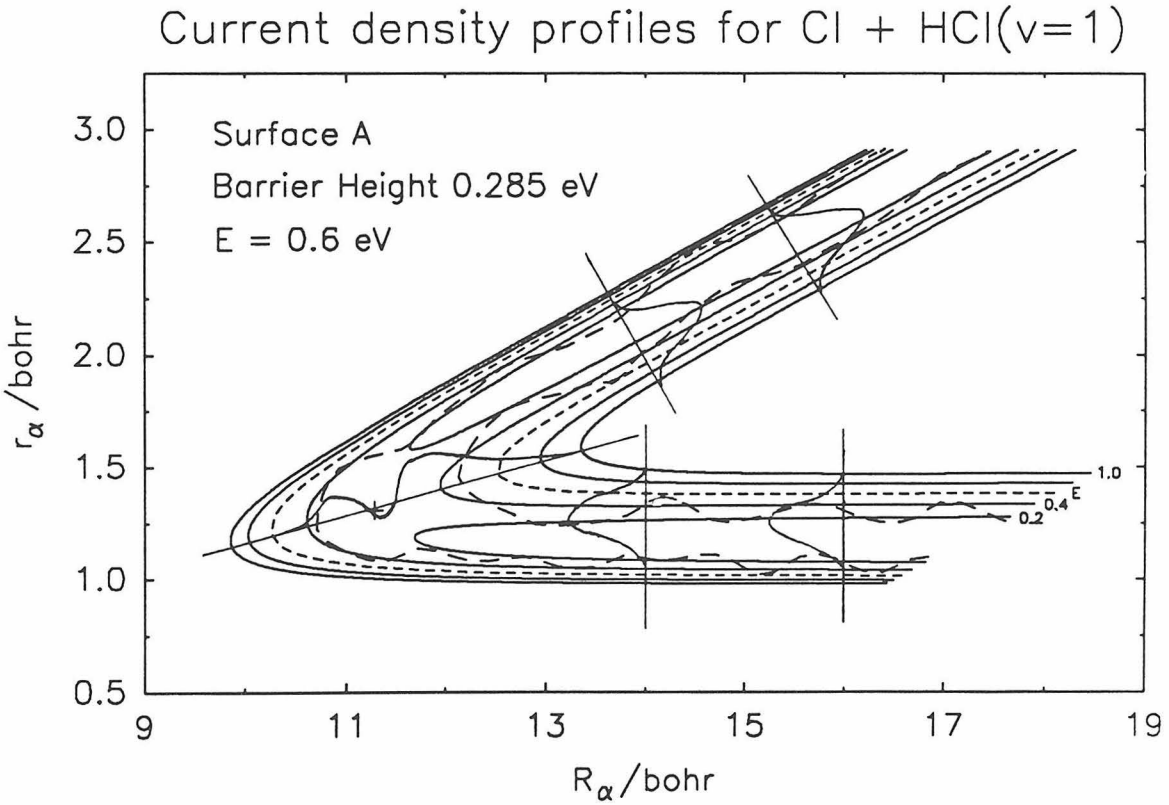
Current density profiles for Cl + HCl(v=1)
Surface A
Barrier Height 0.285 eV
E = 0.6 eV
3.0
2.5
2.0
1.5
1.0
0.5
9
11
13
15
17
19
r_α /bohr
R_α /bohr
1.0
0.4
0.2
E

Figure 28

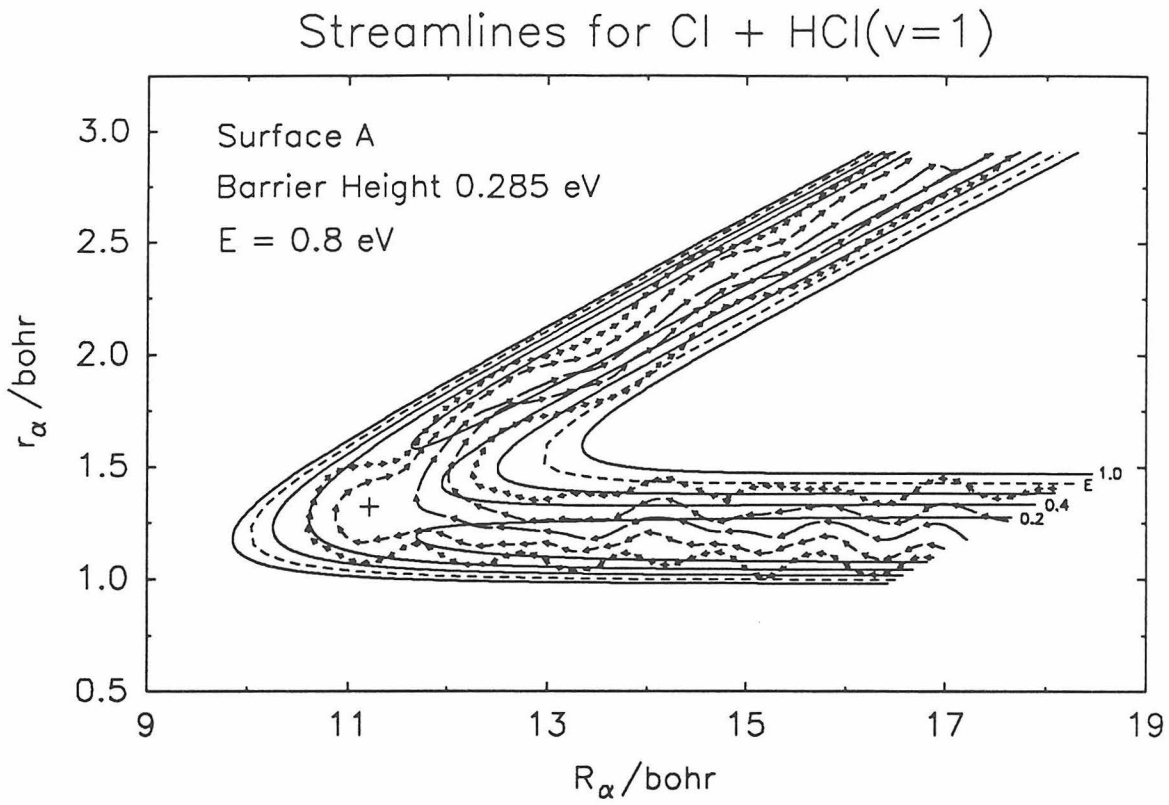
Streamlines for Cl + HCl(v=1)
Surface A
Barrier Height 0.285 eV
E = 0.8 eV
E
1.0
0.4
0.2
3.0
2.5
2.0
1.5
1.0
0.5
9
11
13
15
17
19
r_α /bohr
R_α /bohr

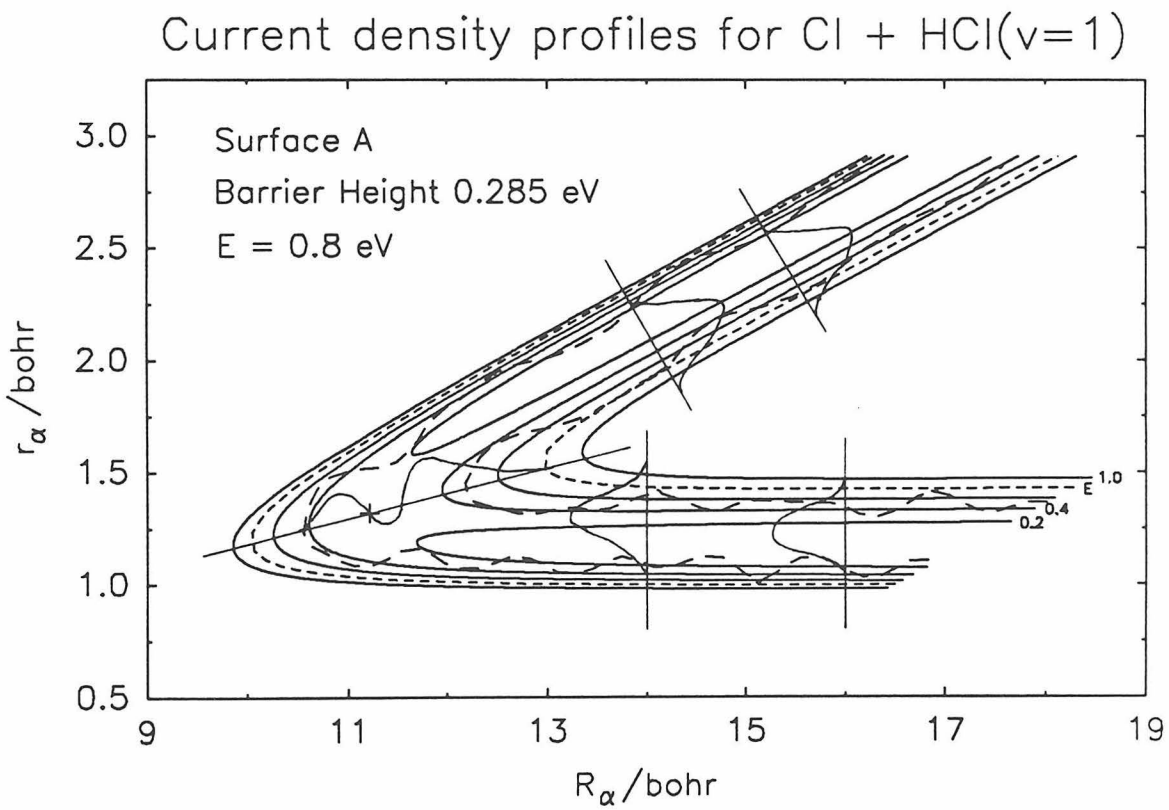
Current density profiles for Cl + HCl(v=1)
Surface A
Barrier Height 0.285 eV
E = 0.8 eV
E
1.0
0.4
0.2
3.0
2.5
2.0
1.5
1.0
0.5
9
11
13
15
17
19
r_α /bohr
R_α /bohr

Figure 29

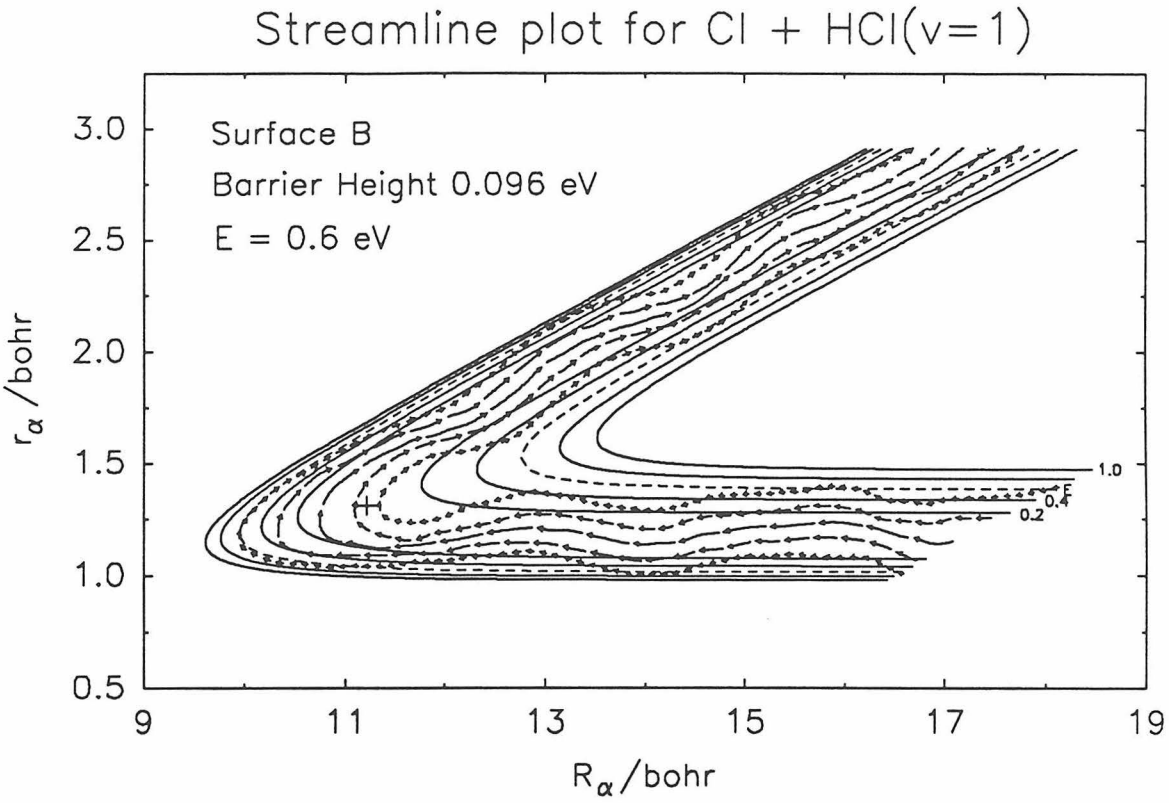
Streamline plot for Cl + HCl(v=1)
Surface B
Barrier Height 0.096 eV
E = 0.6 eV
3.0
2.5
2.0
1.5
1.0
0.5
r_α /bohr
9
11
13
15
17
19
R_α /bohr
1.0
0.4
0.2
F

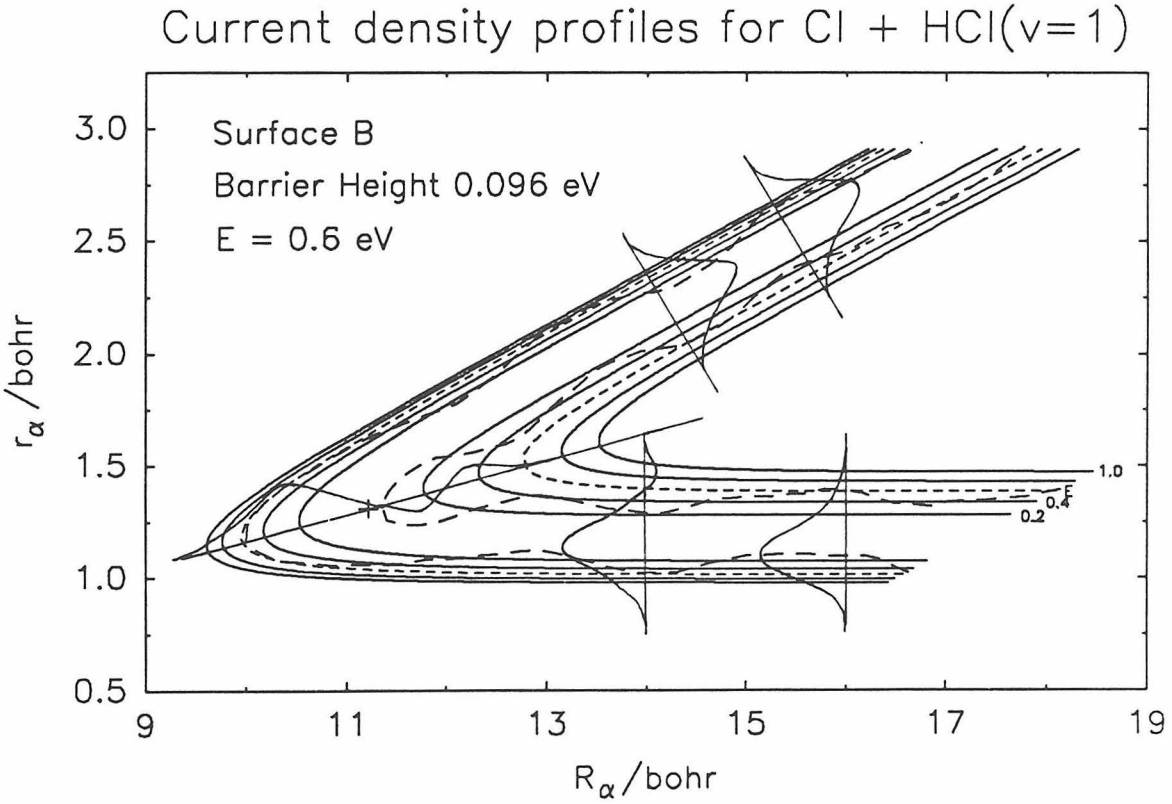
Current density profiles for Cl + HCl(v=1)
Surface B
Barrier Height 0.096 eV
E = 0.6 eV
3.0
2.5
2.0
1.5
1.0
0.5
r_α /bohr
9
11
13
15
17
19
R_α /bohr
1.0
0.4
0.2
F

Figure 30

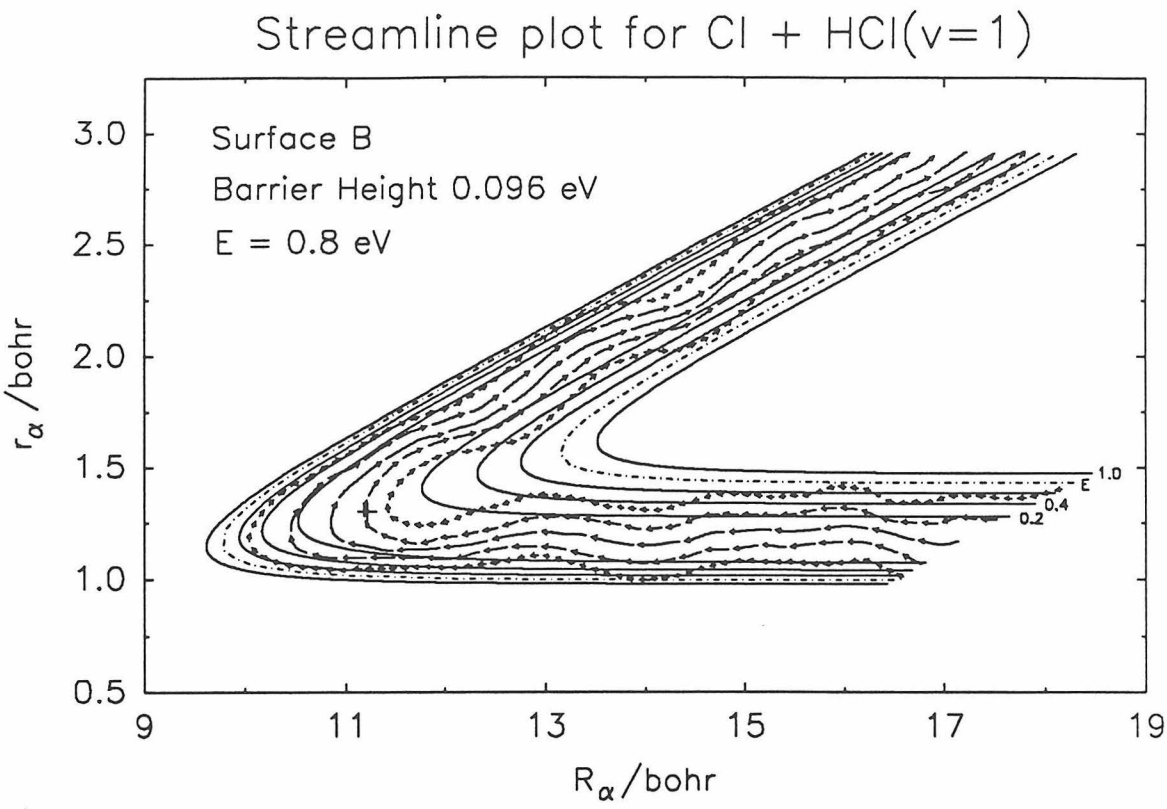
Streamline plot for Cl + HCl(v=1)
Surface B
Barrier Height 0.096 eV
E = 0.8 eV
3.0
2.5
2.0
1.5
1.0
0.5
9
11
13
15
17
19
r_α /bohr
R_α /bohr
1.0
E
0.4
0.2

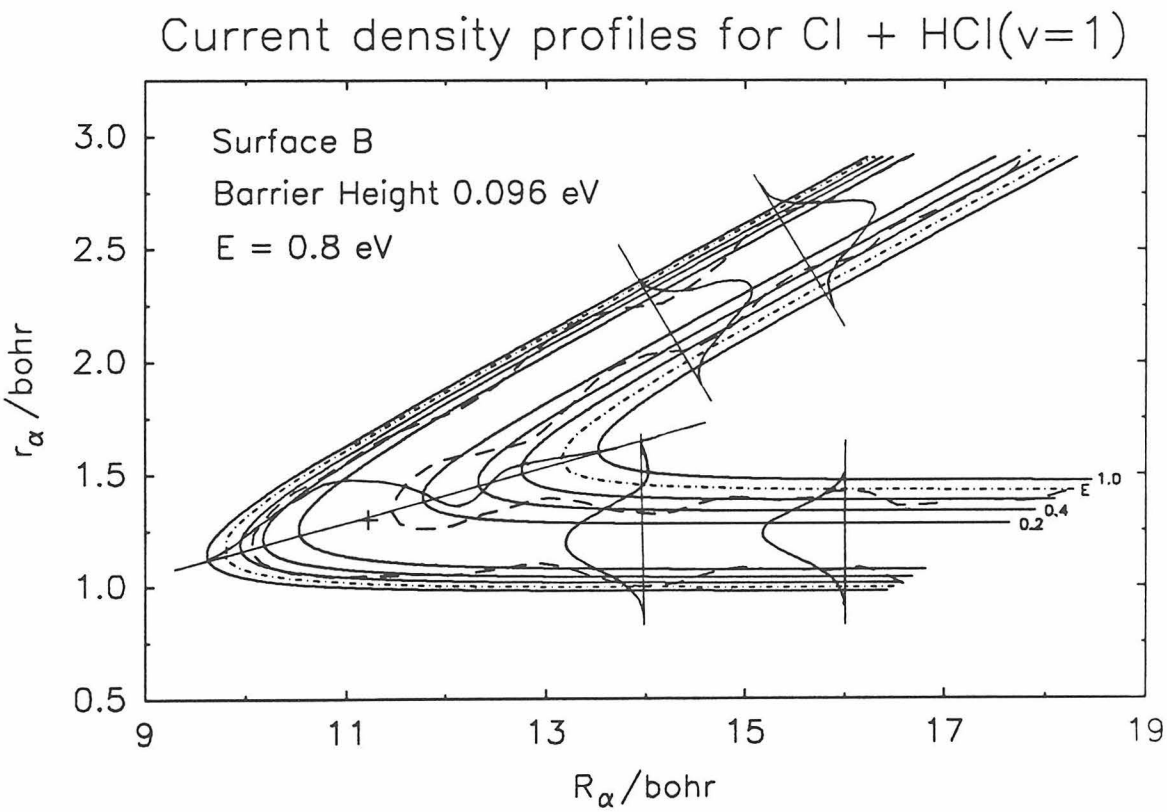
Current density profiles for Cl + HCl(v=1)
Surface B
Barrier Height 0.096 eV
E = 0.8 eV
3.0
2.5
2.0
1.5
1.0
0.5
9
11
13
15
17
19
r_α /bohr
R_α /bohr
1.0
E
0.4
0.2

Figure 31

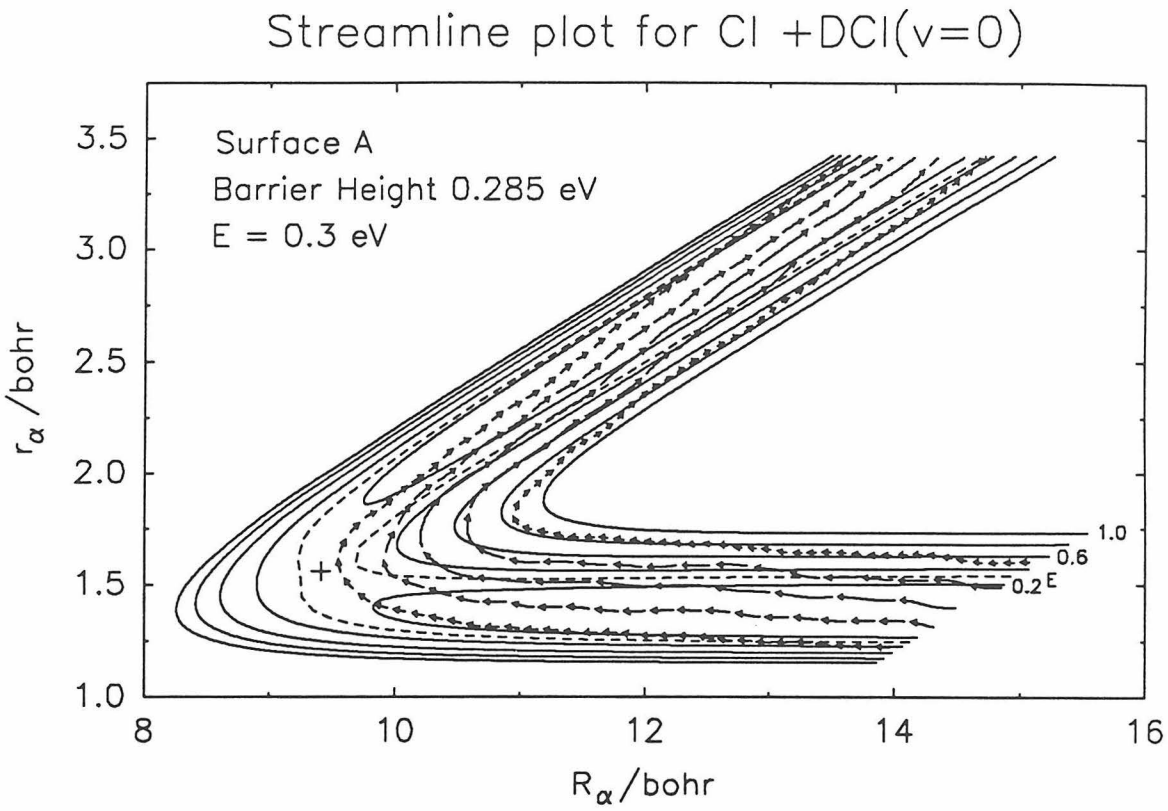
Streamline plot for Cl +DCl(v=0)
Surface A
Barrier Height 0.285 eV
E = 0.3 eV
3.5
3.0
2.5
2.0
1.5
1.0
8
10
12
14
16
r_α /bohr
R_α /bohr
1.0
0.6
0.2 E

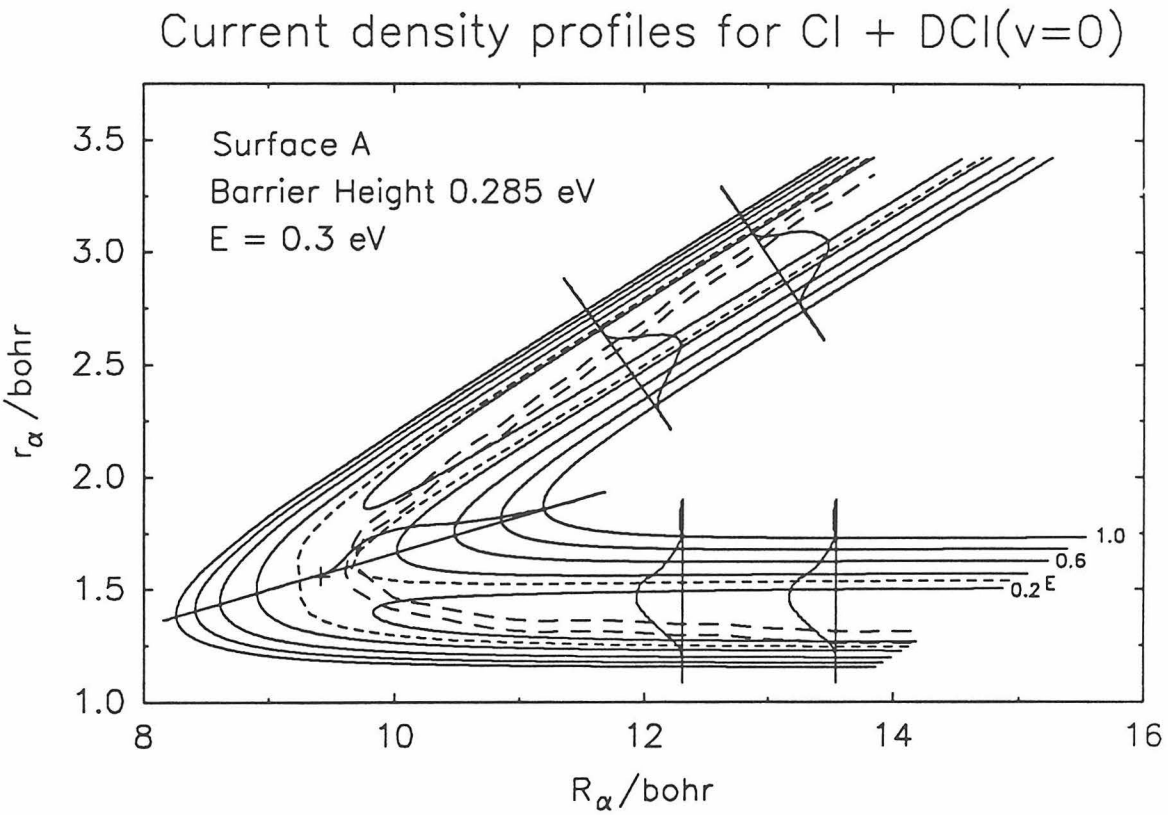
Current density profiles for Cl + DCl(v=0)
Surface A
Barrier Height 0.285 eV
E = 0.3 eV
3.5
3.0
2.5
2.0
1.5
1.0
8
10
12
14
16
r_α /bohr
R_α /bohr
1.0
0.6
0.2 E

Figure 32

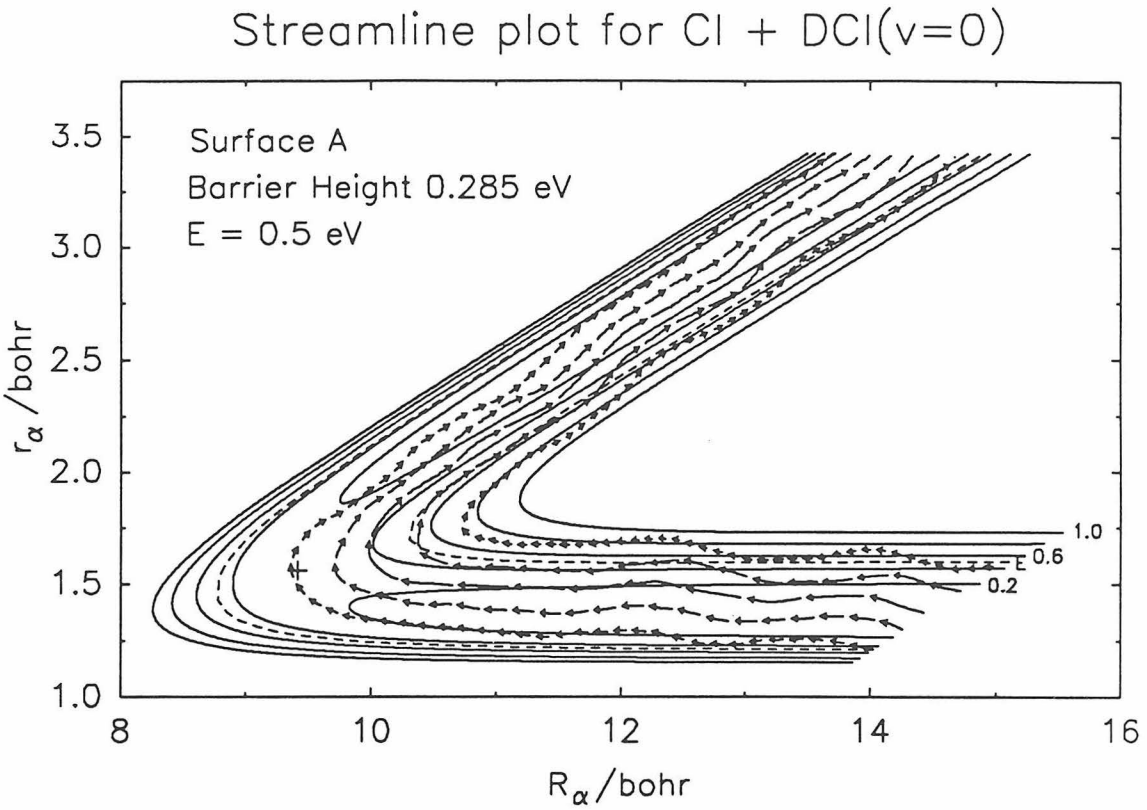
Streamline plot for Cl + DCl(v=0)
Surface A
Barrier Height 0.285 eV
E = 0.5 eV
3.5
3.0
2.5
2.0
1.5
1.0
r_α /bohr
8
10
12
14
16
R_α /bohr
1.0
0.6
E
0.2

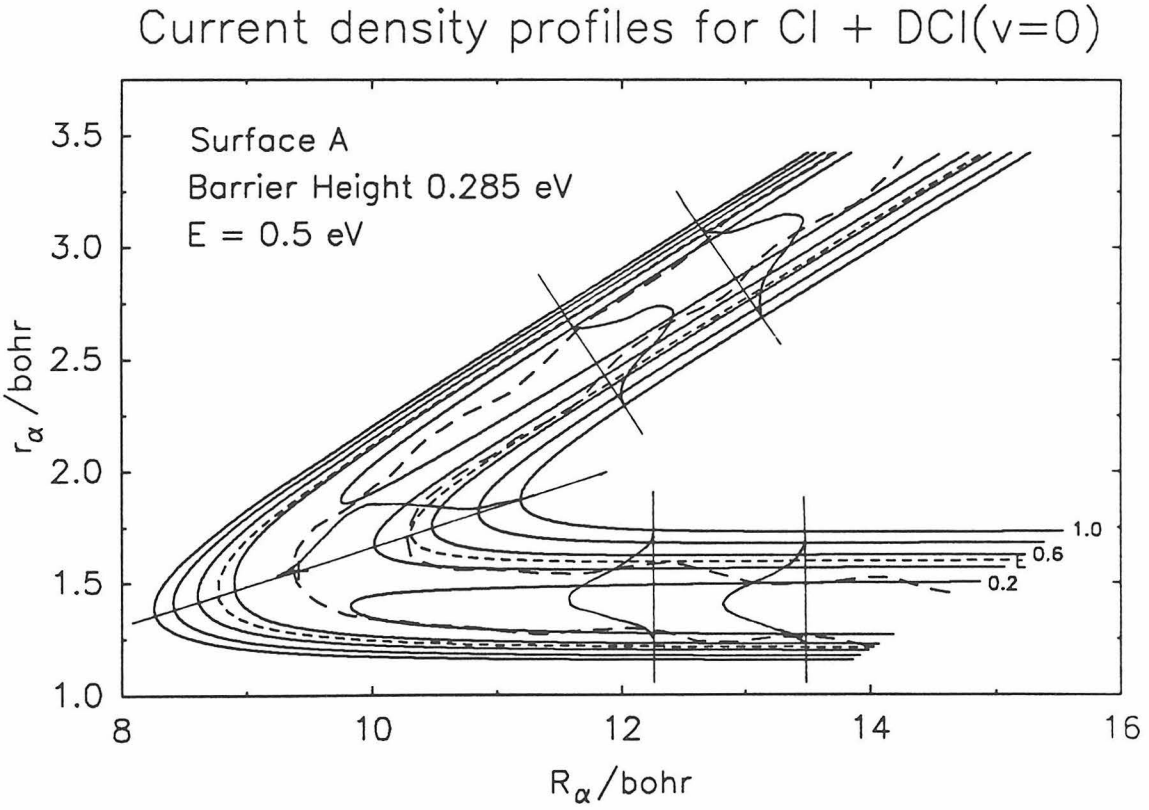
Current density profiles for Cl + DCl(v=0)
Surface A
Barrier Height 0.285 eV
E = 0.5 eV
3.5
3.0
2.5
2.0
1.5
1.0
r_α /bohr
8
10
12
14
16
R_α /bohr
1.0
0.6
E
0.2

Figure 33

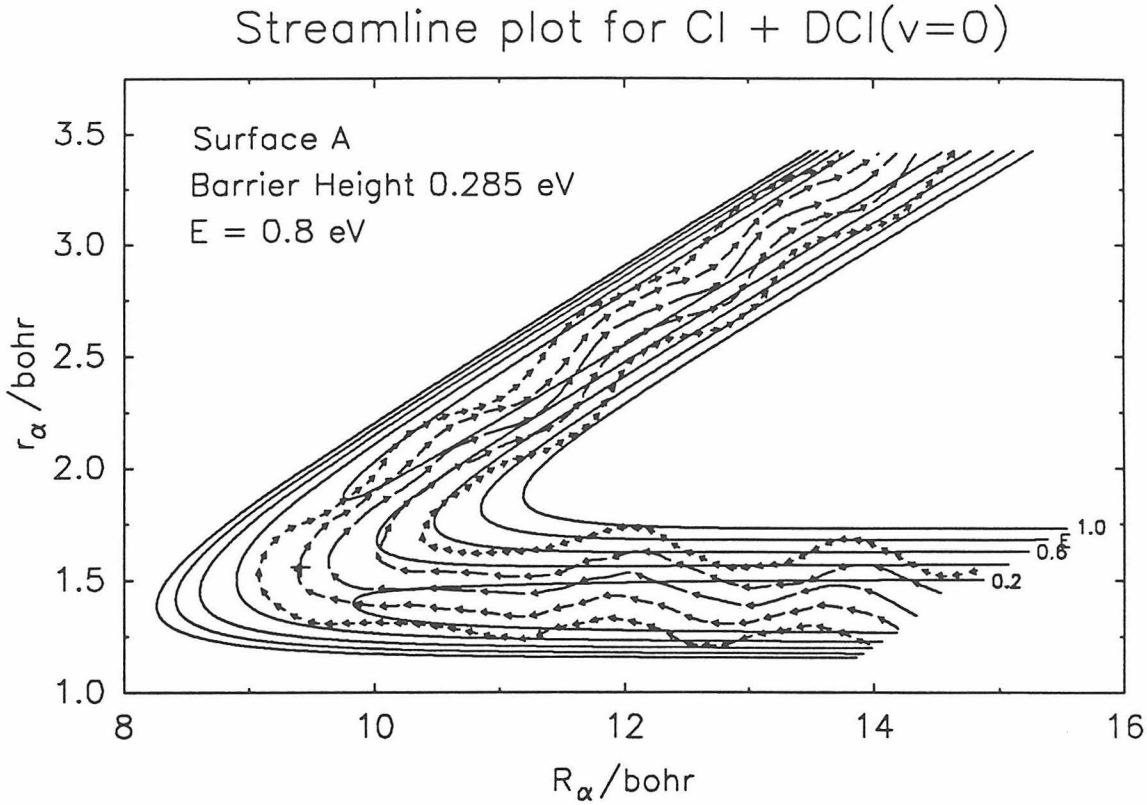
Streamline plot for Cl + DCl(v=0)
Surface A
Barrier Height 0.285 eV
E = 0.8 eV
3.5
3.0
2.5
2.0
1.5
1.0
r_α /bohr
8
10
12
14
16
R_α /bohr
1.0
0.6
0.2
E

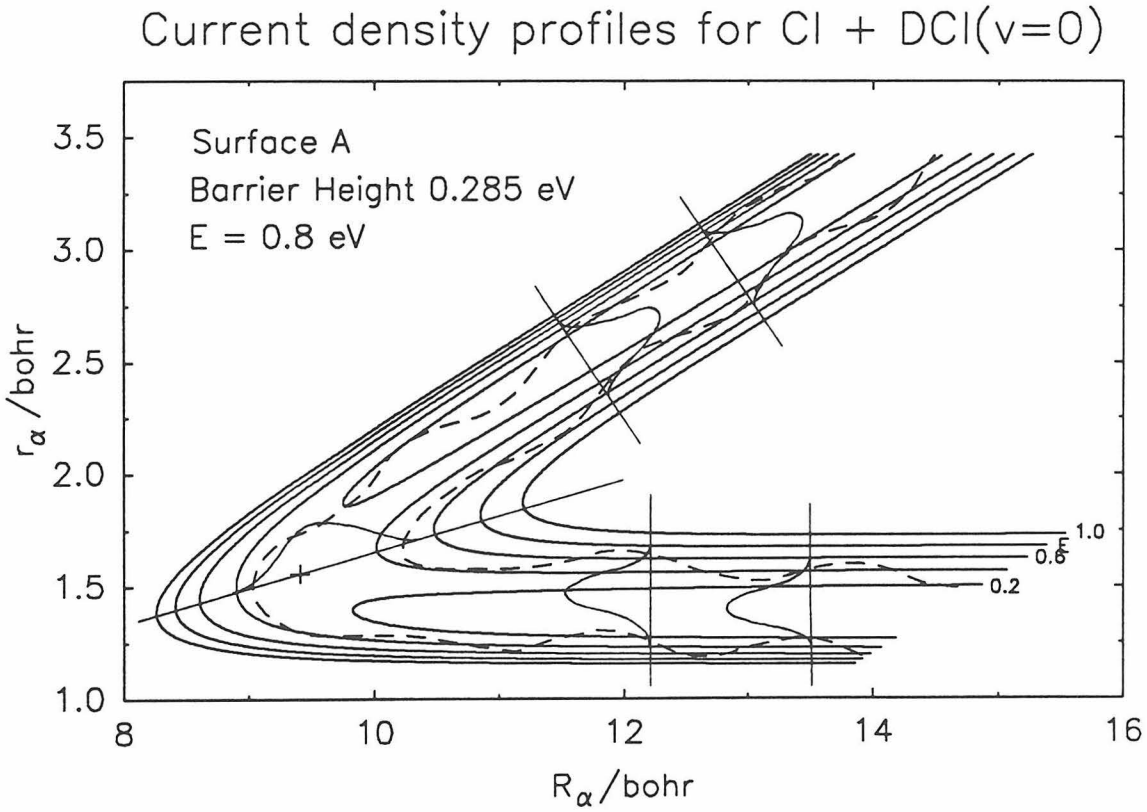
Current density profiles for Cl + DCl(v=0)
Surface A
Barrier Height 0.285 eV
E = 0.8 eV
3.5
3.0
2.5
2.0
1.5
1.0
r_α /bohr
8
10
12
14
16
R_α /bohr
1.0
0.6
0.2
E

Figure 34

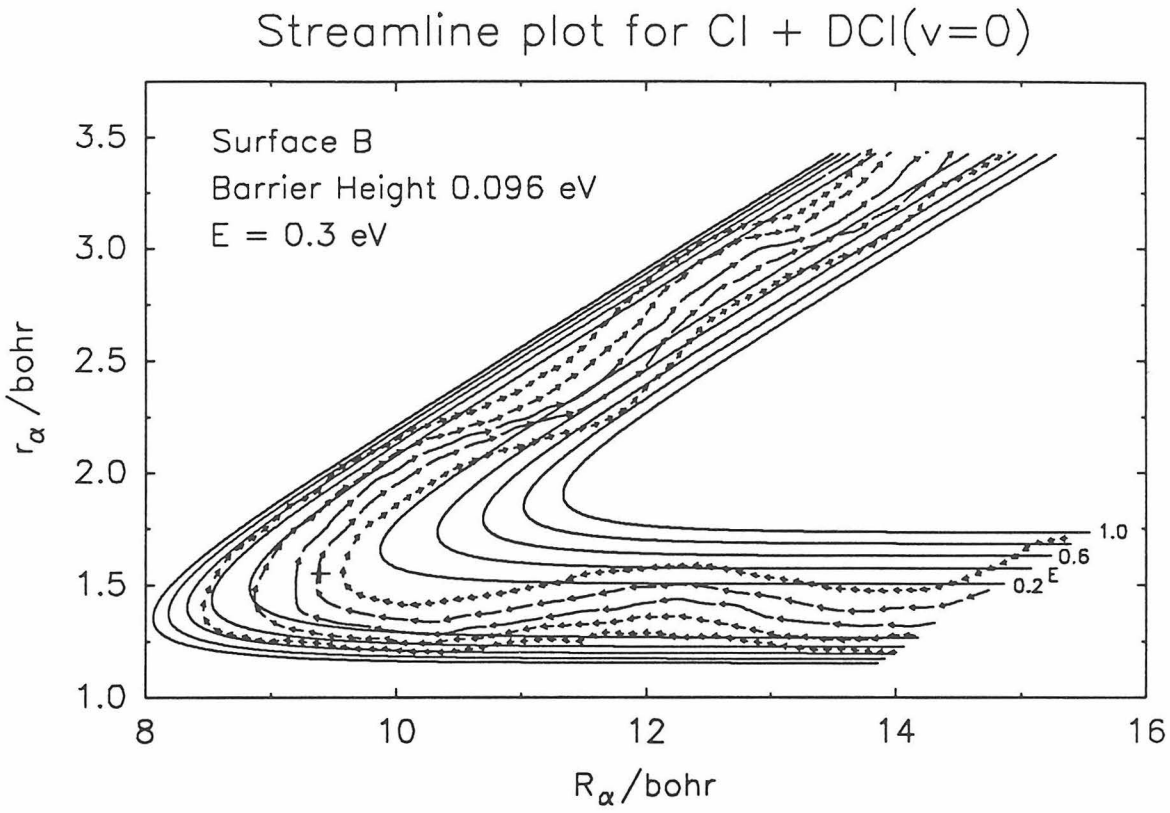
Streamline plot for Cl + DCl(v=0)
Surface B
Barrier Height 0.096 eV
E = 0.3 eV
1.0
0.6
0.2
E
3.5
3.0
2.5
2.0
1.5
1.0
8
10
12
14
16
r_α /bohr
R_α /bohr

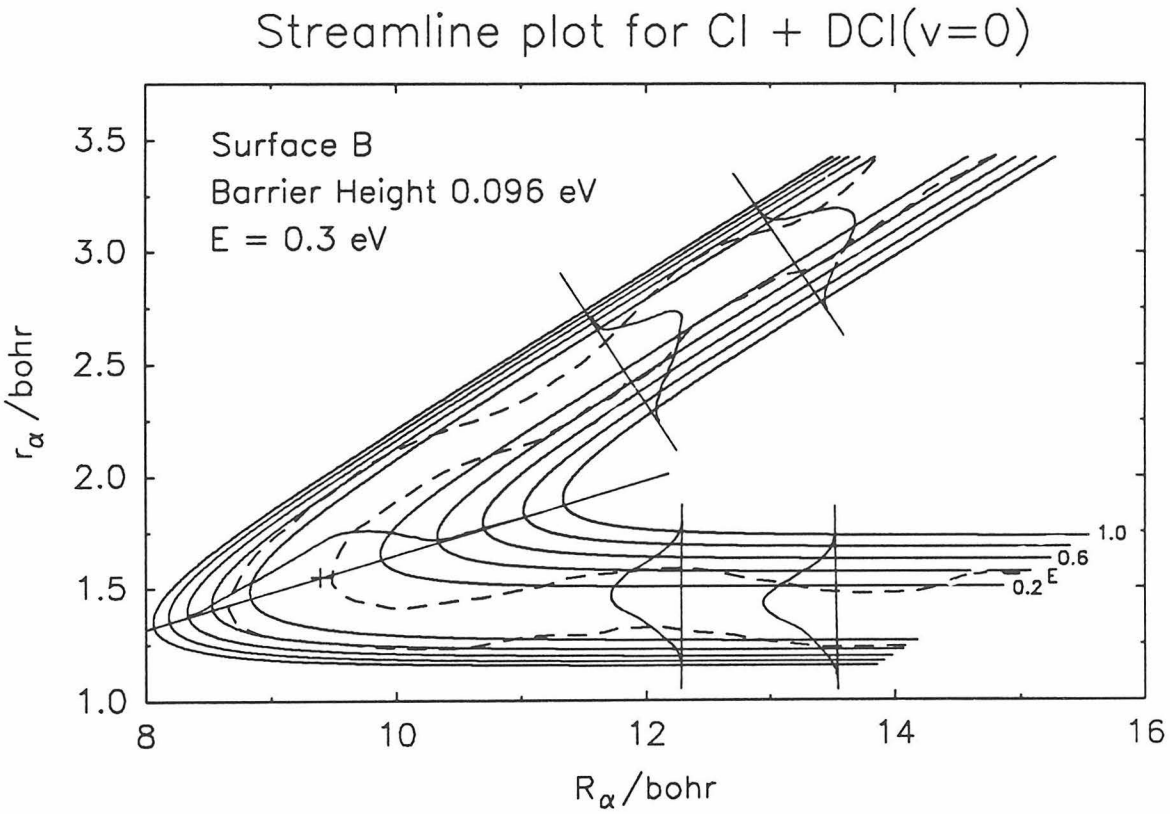
Streamline plot for Cl + DCl(v=0)
Surface B
Barrier Height 0.096 eV
E = 0.3 eV
1.0
0.6
0.2
E
3.5
3.0
2.5
2.0
1.5
1.0
8
10
12
14
16
r_α /bohr
R_α /bohr

Figure 35

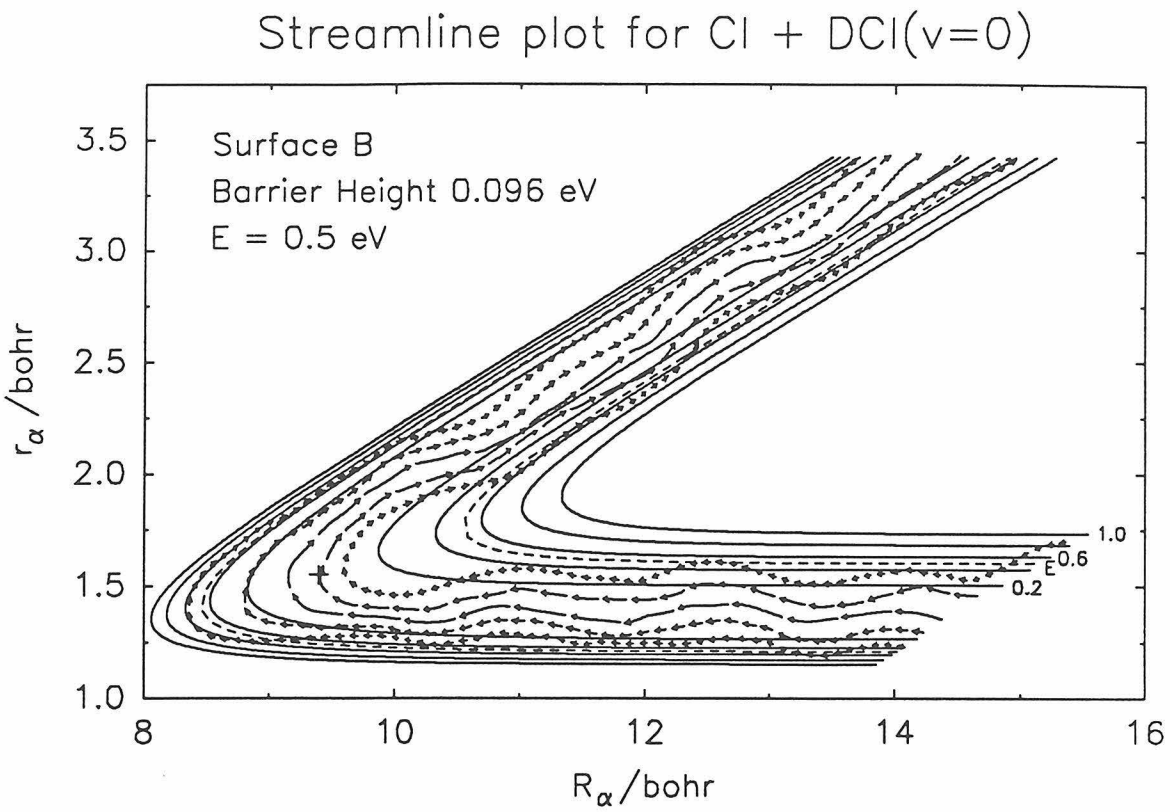
Streamline plot for Cl + DCl(v=0)
Surface B
Barrier Height 0.096 eV
E = 0.5 eV
3.5
3.0
2.5
2.0
1.5
1.0
8
10
12
14
16
r_α /bohr
R_α /bohr
1.0
0.6
E
0.2

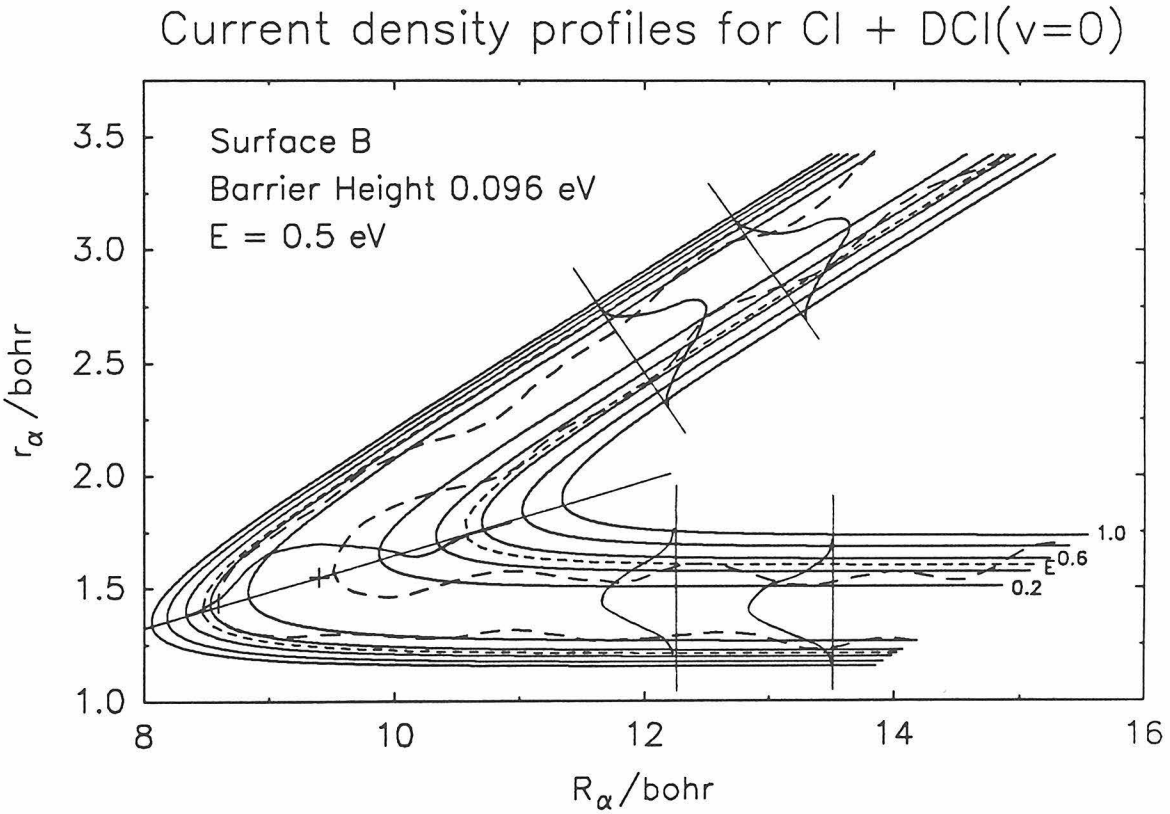
Current density profiles for Cl + DCl(v=0)
Surface B
Barrier Height 0.096 eV
E = 0.5 eV
3.5
3.0
2.5
2.0
1.5
1.0
8
10
12
14
16
r_α /bohr
R_α /bohr
1.0
0.6
E
0.2

Figure 36

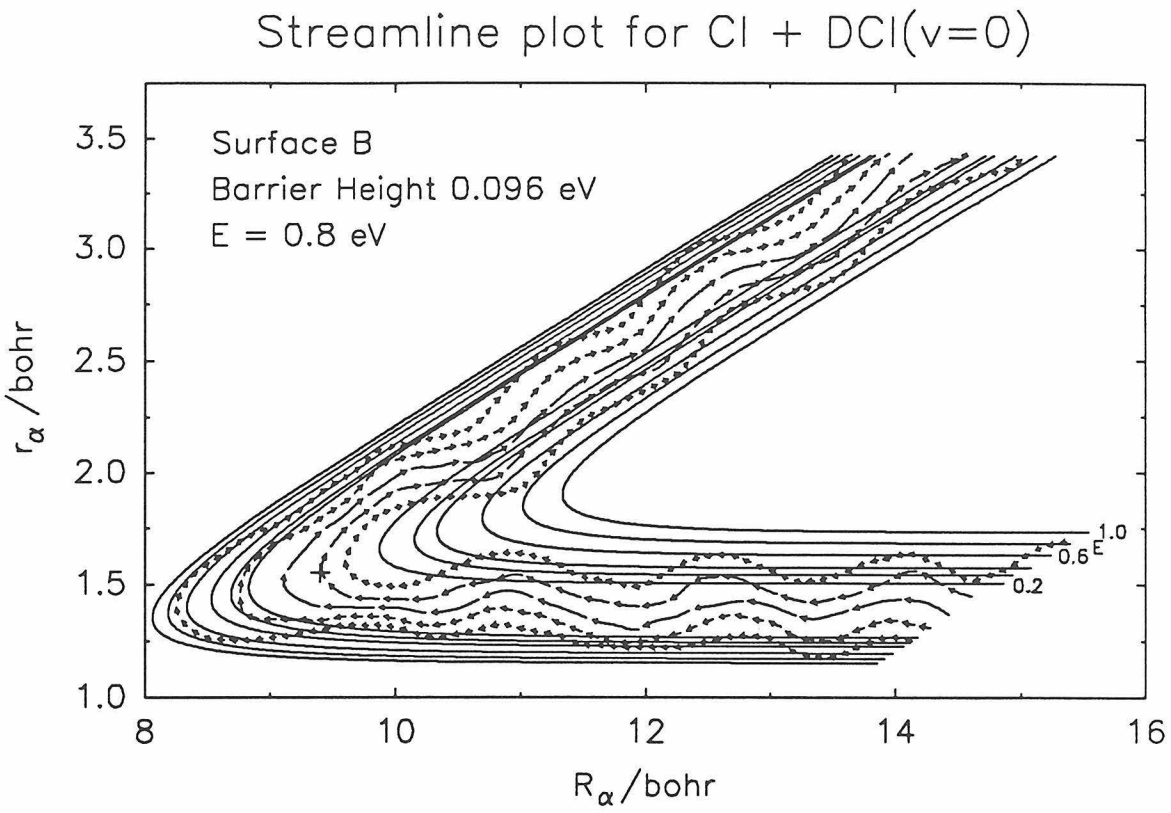
Streamline plot for Cl + DCl(v=0)
Surface B
Barrier Height 0.096 eV
E = 0.8 eV
3.5
3.0
2.5
2.0
1.5
1.0
8
10
12
14
16
r_α /bohr
R_α /bohr
1.0
0.6
0.2
E

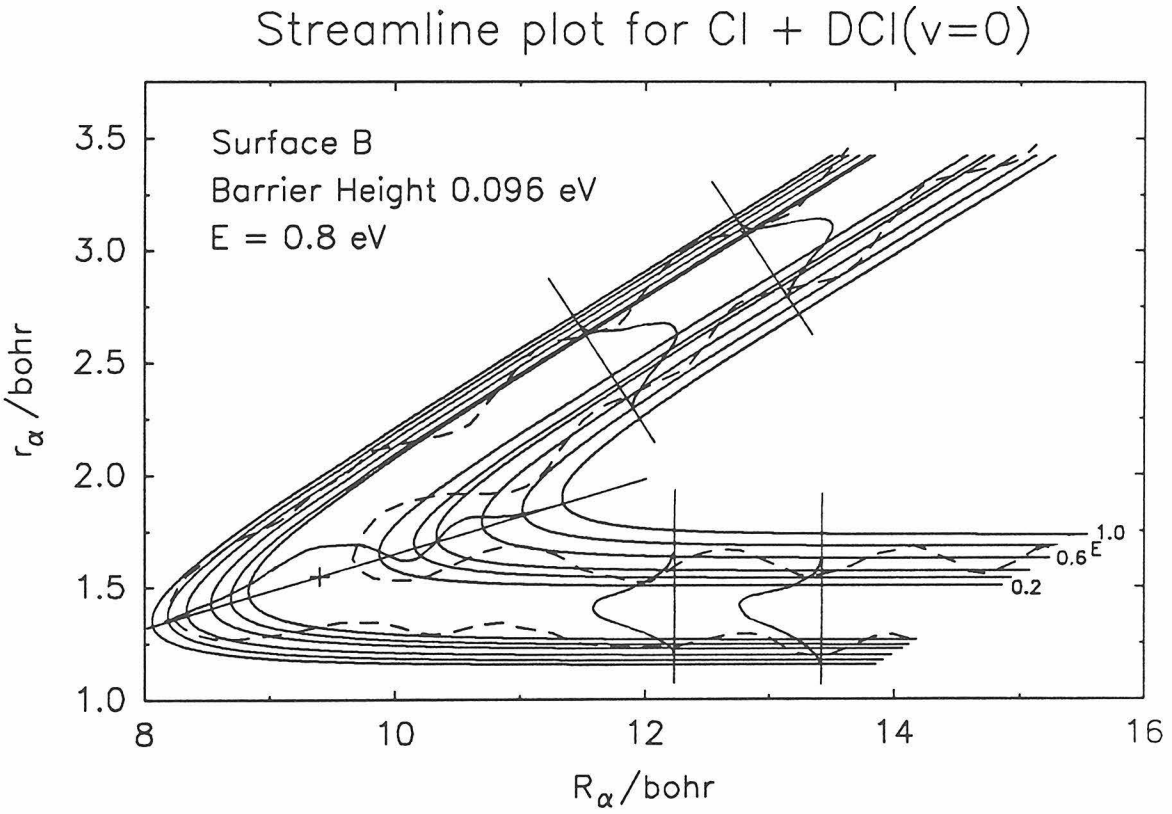
Streamline plot for Cl + DCl(v=0)
Surface B
Barrier Height 0.096 eV
E = 0.8 eV
3.5
3.0
2.5
2.0
1.5
1.0
8
10
12
14
16
r_α /bohr
R_α /bohr
1.0
0.6
0.2
E

Figure 37

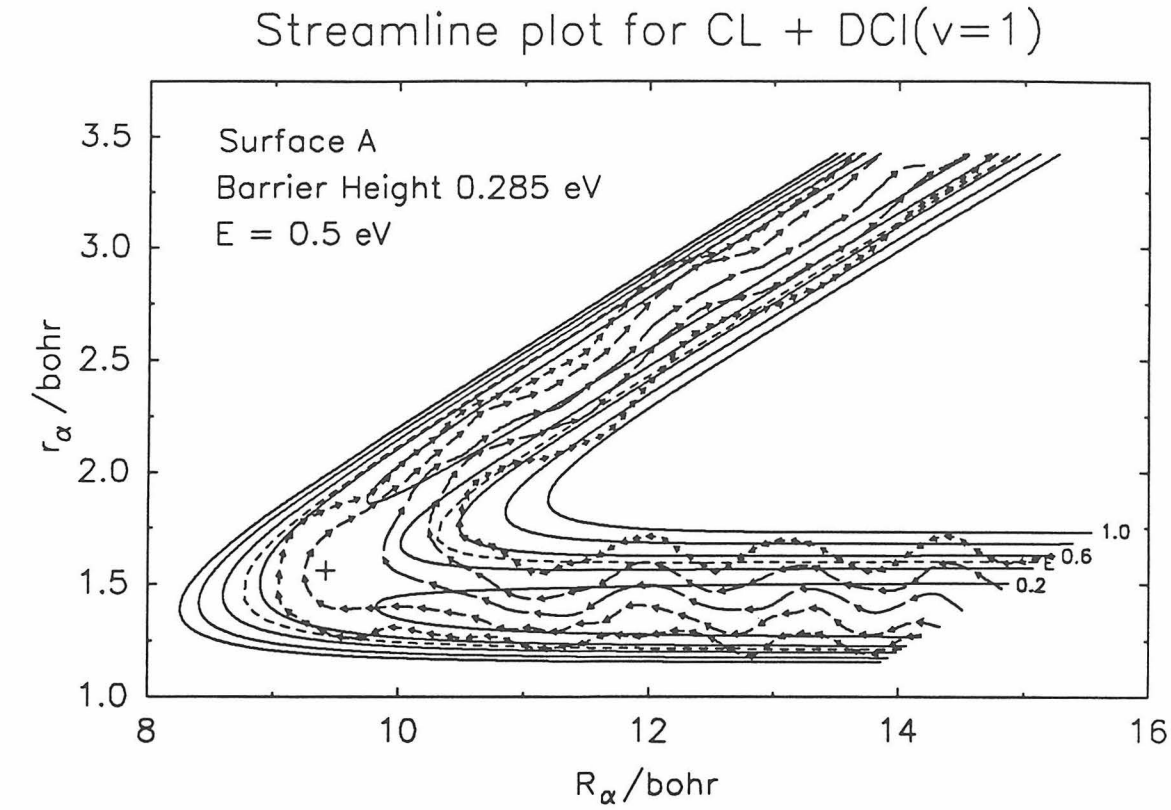
Streamline plot for CL + DCl(v=1)
Surface A
Barrier Height 0.285 eV
E = 0.5 eV
3.5
3.0
2.5
2.0
1.5
1.0
r_α /bohr
8
10
12
14
16
R_α /bohr
1.0
0.6
E
0.2

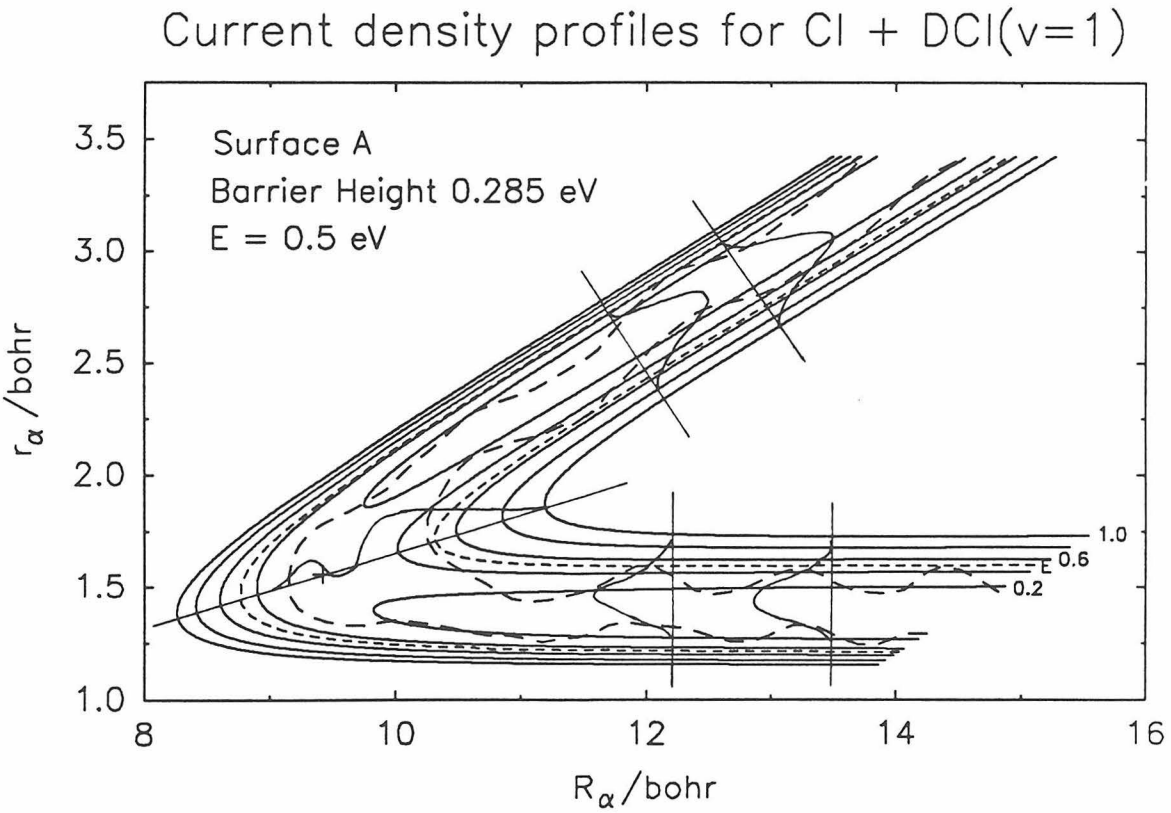
Current density profiles for Cl + DCl(v=1)
Surface A
Barrier Height 0.285 eV
E = 0.5 eV
3.5
3.0
2.5
2.0
1.5
1.0
r_α /bohr
8
10
12
14
16
R_α /bohr
1.0
0.6
E
0.2

Figure 38

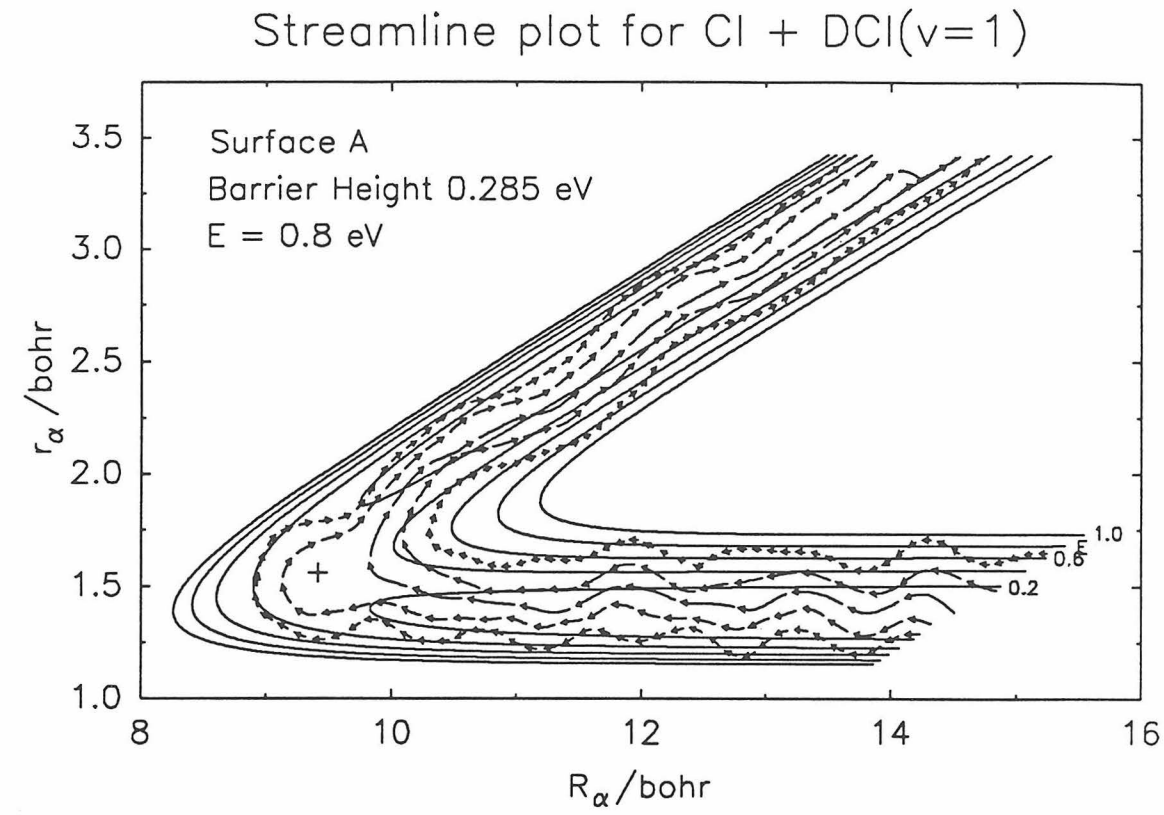
Streamline plot for Cl + DCl(v=1)
Surface A
Barrier Height 0.285 eV
E = 0.8 eV
3.5
3.0
2.5
2.0
1.5
1.0
8
10
12
14
16
r_α /bohr
R_α /bohr
1.0
0.6
E
0.2

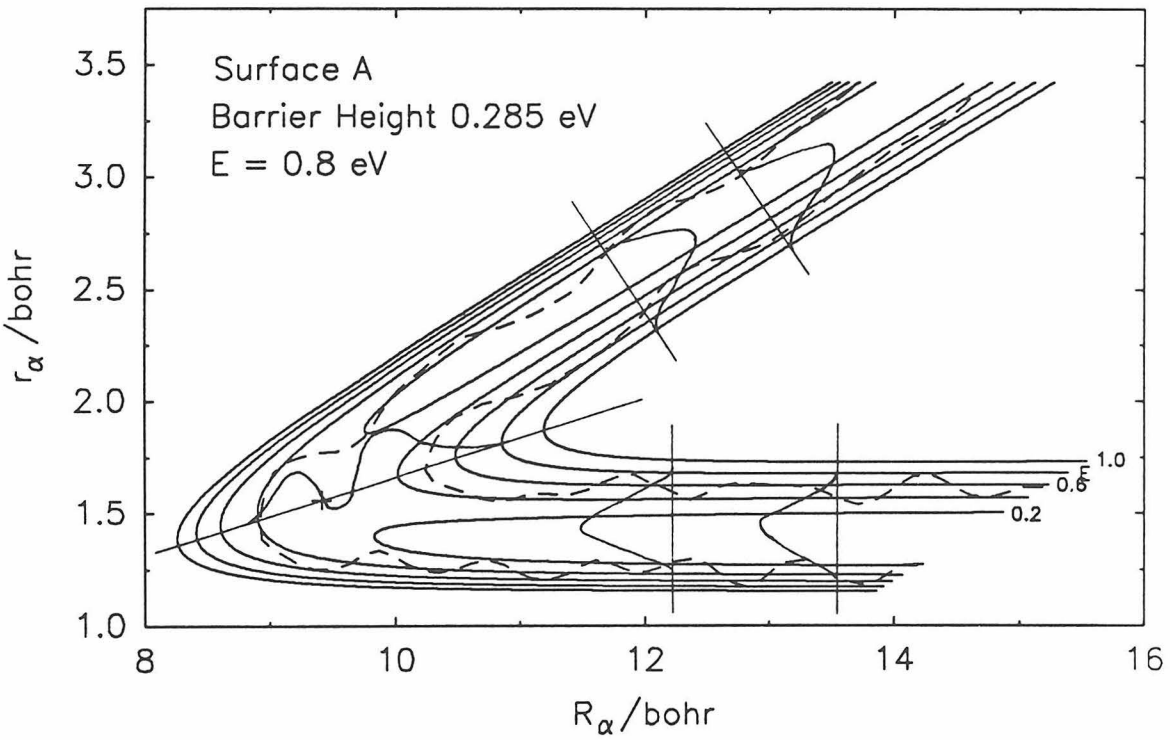
Current density profiles for Cl + DCl(v=1)
Surface A
Barrier Height 0.285 eV
E = 0.8 eV
3.5
3.0
2.5
2.0
1.5
1.0
8
10
12
14
16
r_α /bohr
R_α /bohr
1.0
0.6
E
0.2

Figure 39

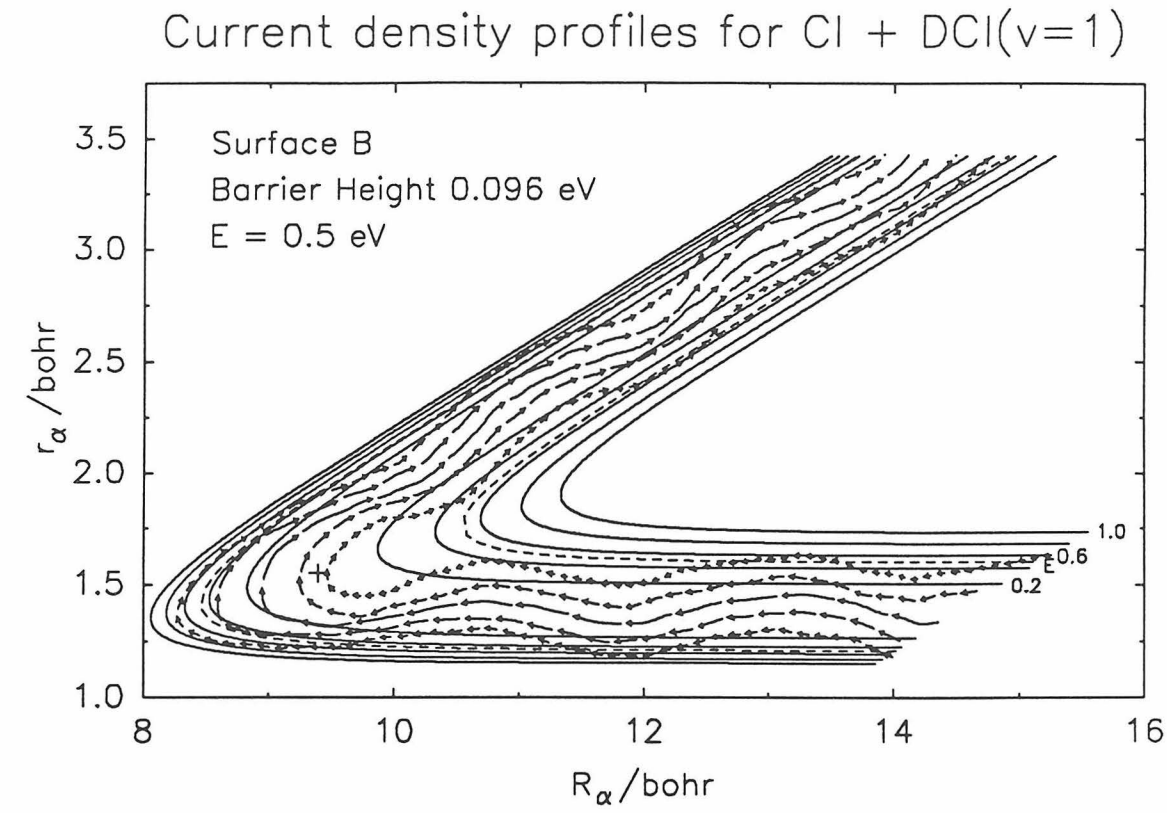
Current density profiles for Cl + DCl(v=1)
Surface B
Barrier Height 0.096 eV
E = 0.5 eV
3.5
3.0
2.5
2.0
1.5
1.0
r_α /bohr
8
10
12
14
16
R_α /bohr
1.0
0.6
E
0.2

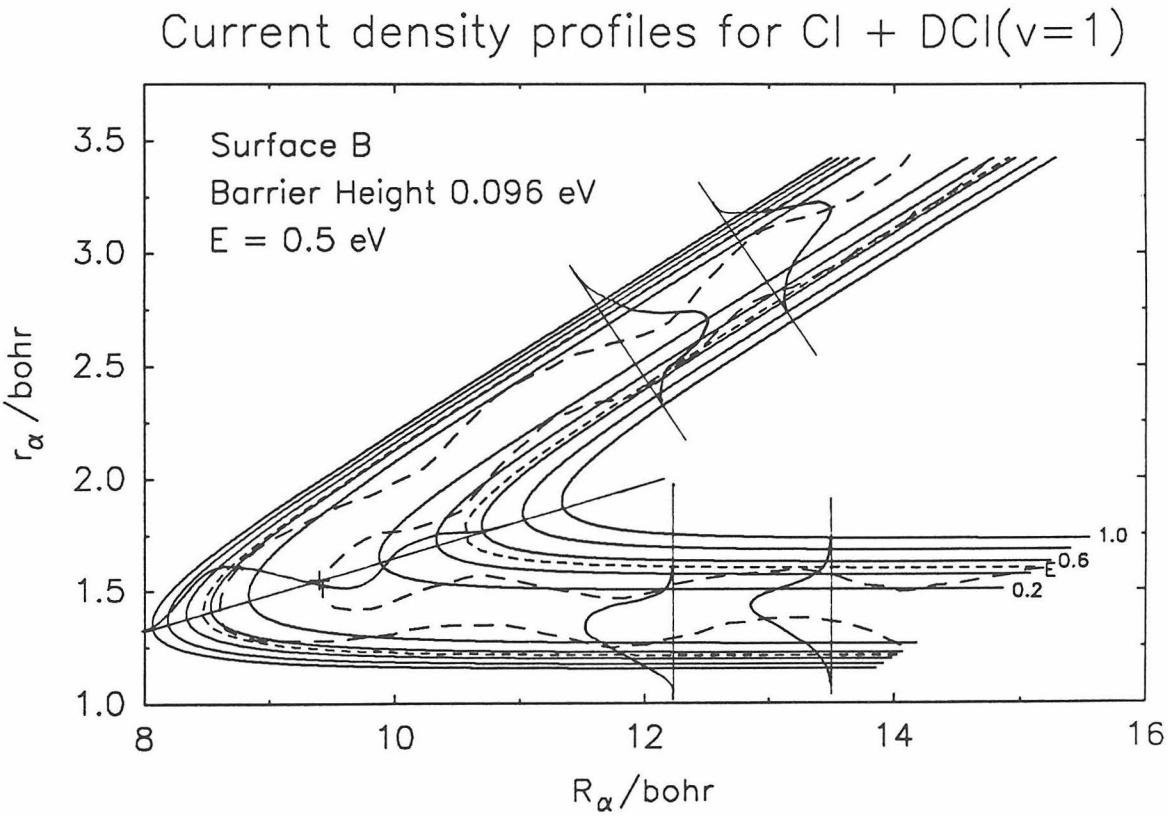
Current density profiles for Cl + DCl(v=1)
Surface B
Barrier Height 0.096 eV
E = 0.5 eV
3.5
3.0
2.5
2.0
1.5
1.0
r_α /bohr
8
10
12
14
16
R_α /bohr
1.0
0.6
E
0.2

Figure 40

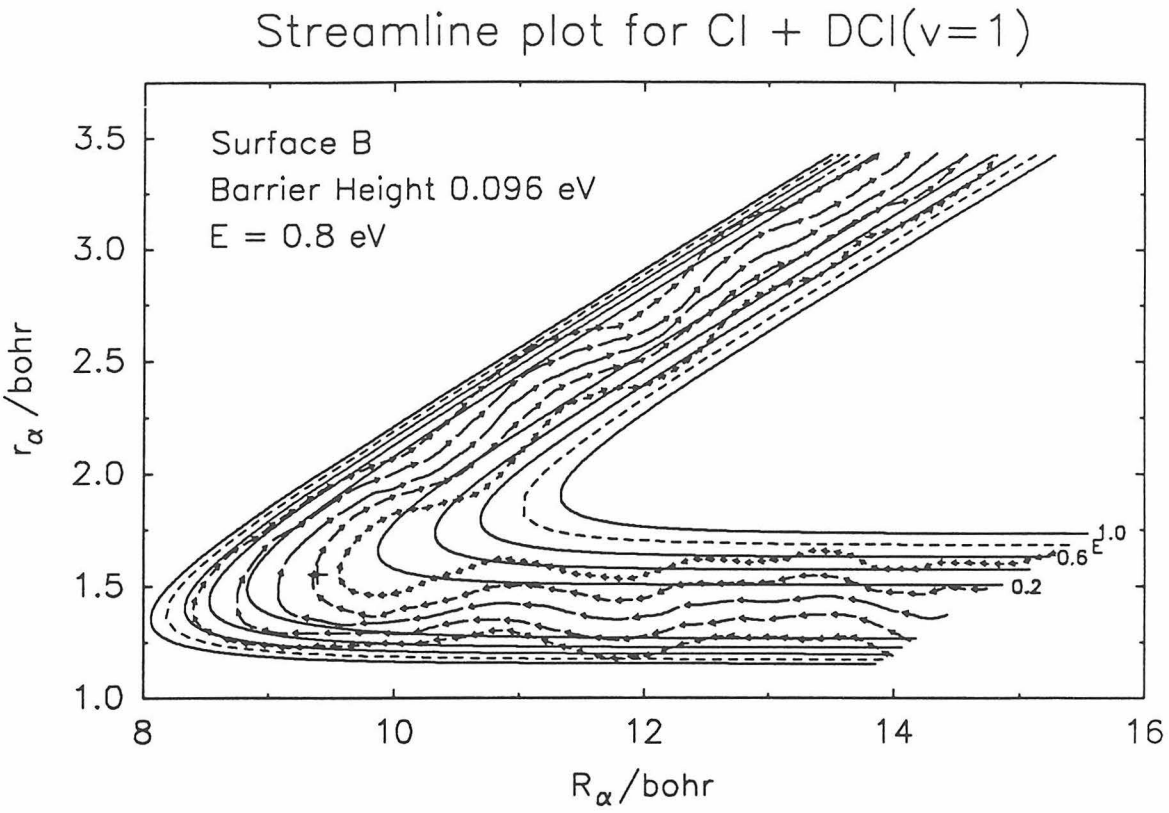
Streamline plot for Cl + DCl(v=1)
Surface B
Barrier Height 0.096 eV
E = 0.8 eV
1.0
0.6
0.2
E
3.5
3.0
2.5
2.0
1.5
1.0
8
10
12
14
16
r_α /bohr
R_α /bohr

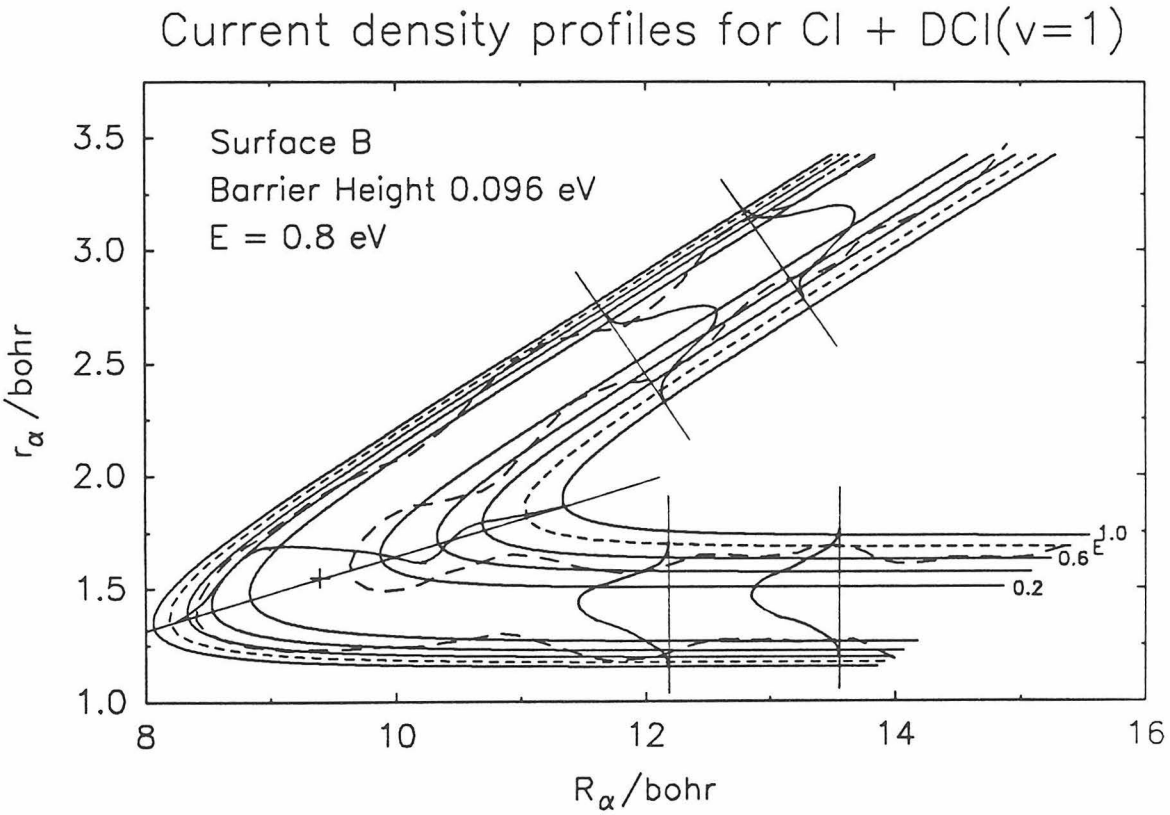
Current density profiles for Cl + DCl(v=1)
Surface B
Barrier Height 0.096 eV
E = 0.8 eV
1.0
0.6
0.2
E
3.5
3.0
2.5
2.0
1.5
1.0
8
10
12
14
16
r_α /bohr
R_α /bohr

Figure 41

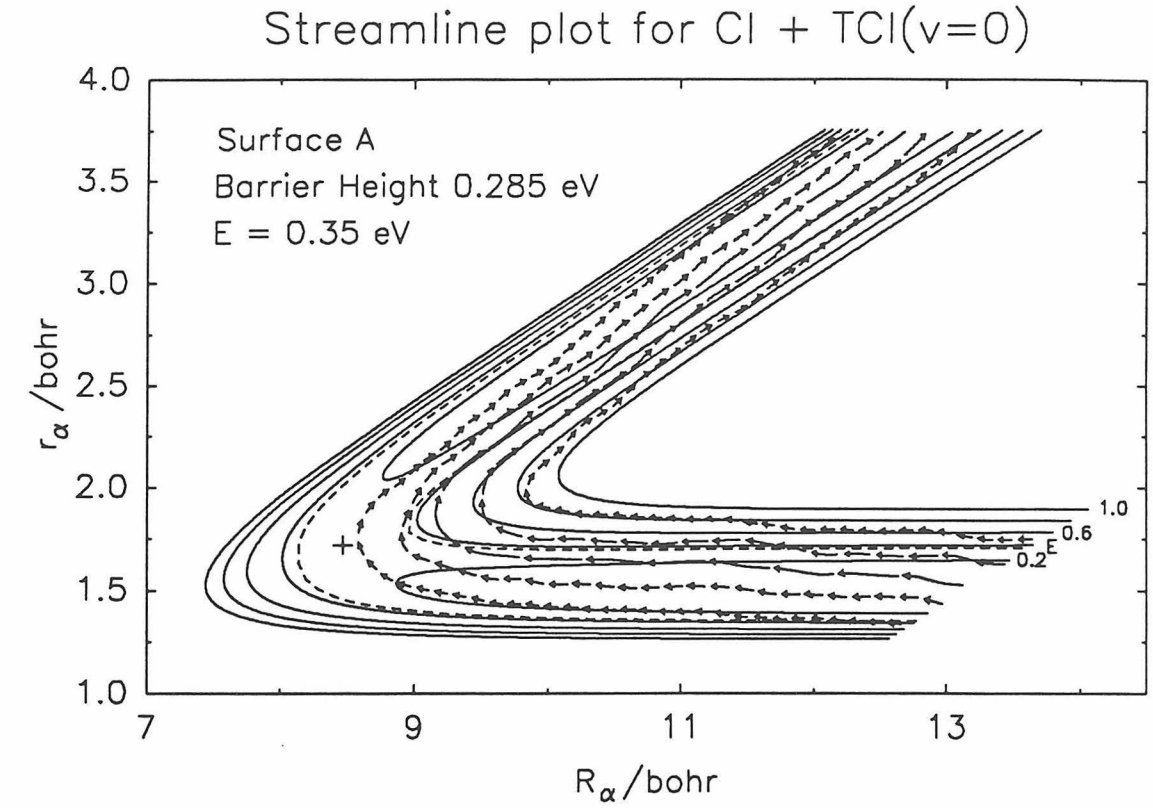
Streamline plot for Cl + TCl(v=0)
Surface A
Barrier Height 0.285 eV
E = 0.35 eV
1.0
0.6
0.2
E
4.0
3.5
3.0
2.5
2.0
1.5
1.0
7
9
11
13
r_α /bohr
R_α /bohr

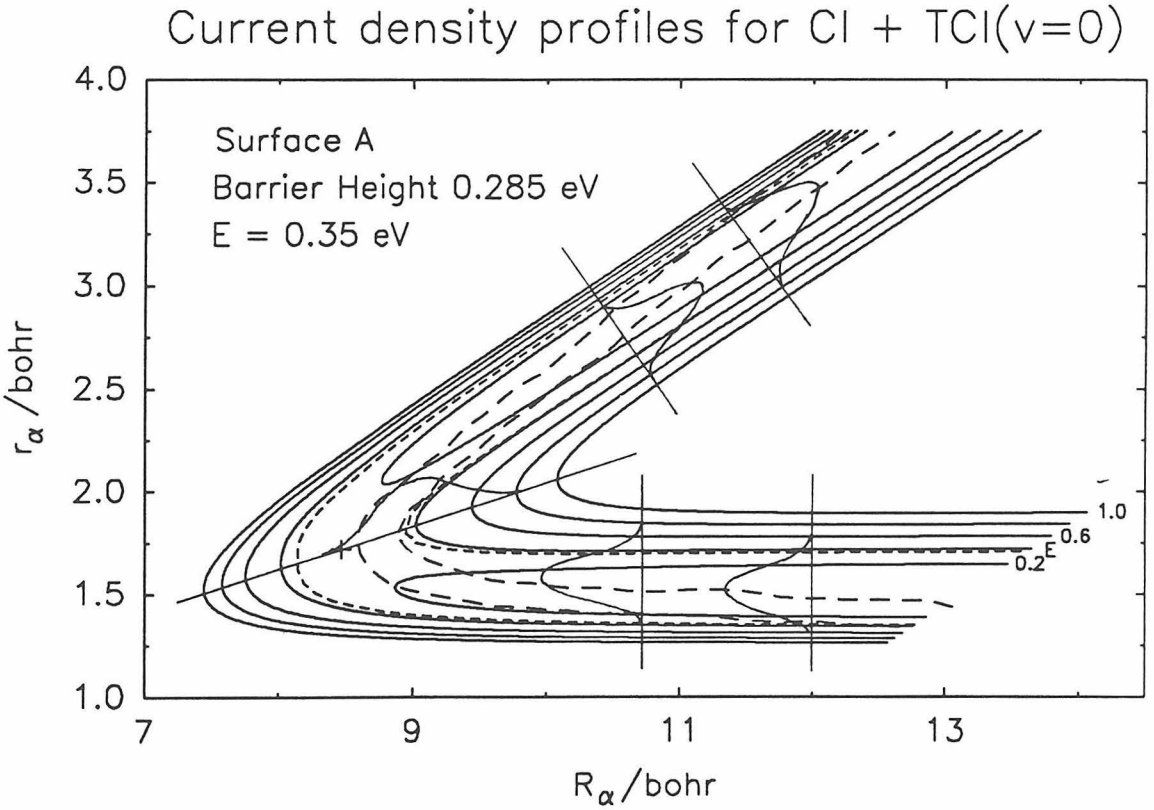
Current density profiles for Cl + TCl(v=0)
Surface A
Barrier Height 0.285 eV
E = 0.35 eV
1.0
0.6
0.2
E
4.0
3.5
3.0
2.5
2.0
1.5
1.0
7
9
11
13
r_α /bohr
R_α /bohr

Figure 42

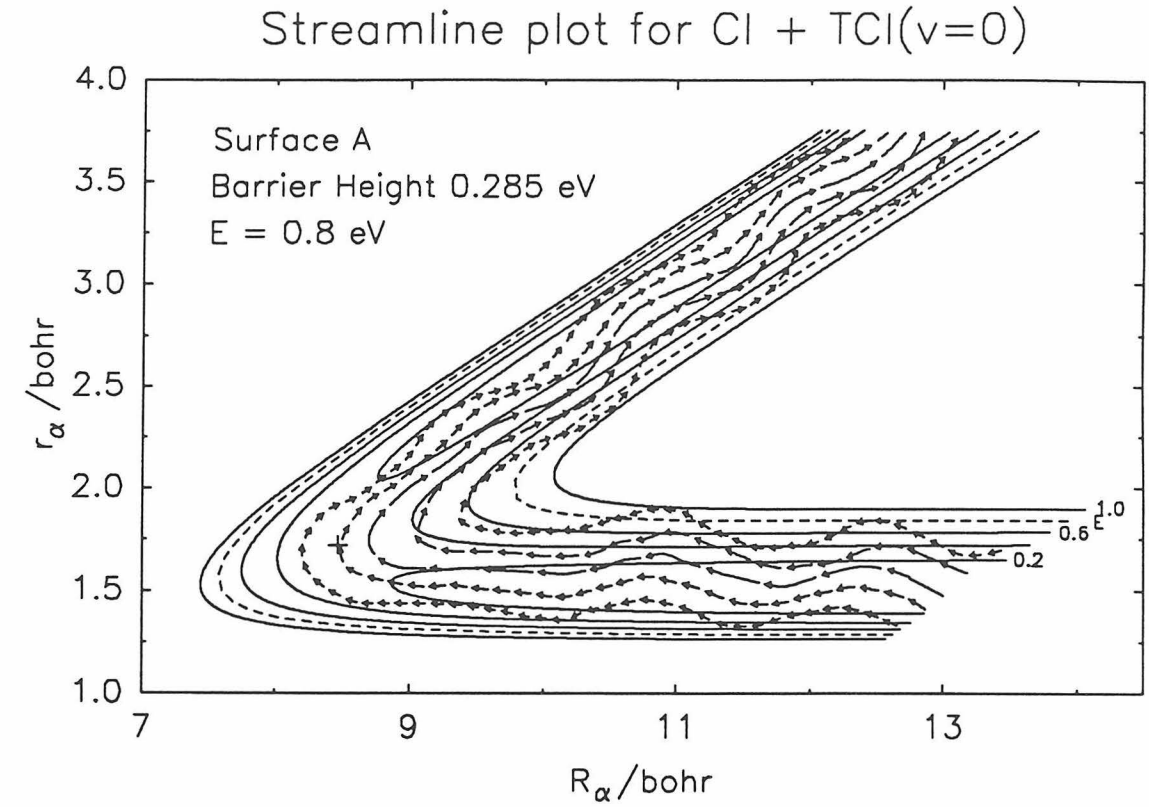
Streamline plot for Cl + TCl(v=0)
Surface A
Barrier Height 0.285 eV
E = 0.8 eV
4.0
3.5
3.0
2.5
2.0
1.5
1.0
7
9
11
13
r_α /bohr
R_α /bohr
1.0
0.6
0.2
E

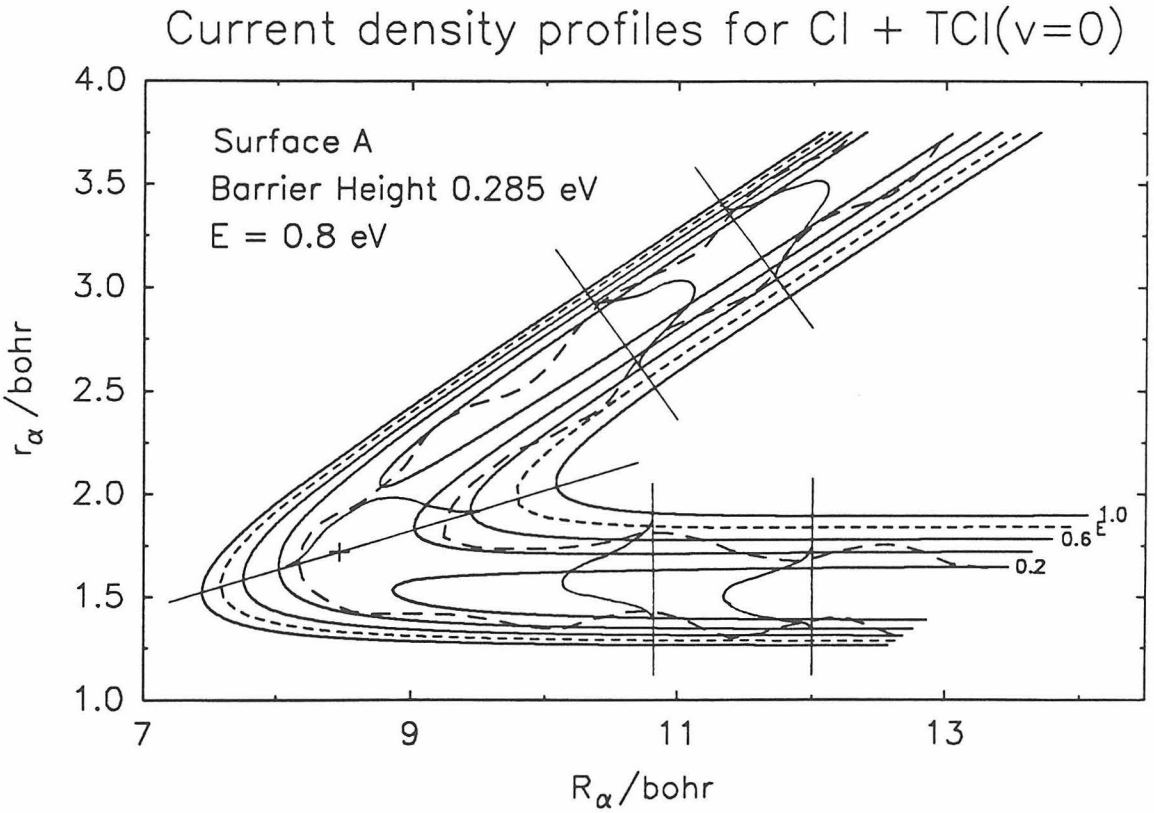
Current density profiles for Cl + TCl(v=0)
Surface A
Barrier Height 0.285 eV
E = 0.8 eV
4.0
3.5
3.0
2.5
2.0
1.5
1.0
7
9
11
13
r_α /bohr
R_α /bohr
1.0
0.6
0.2
E

Figure 43

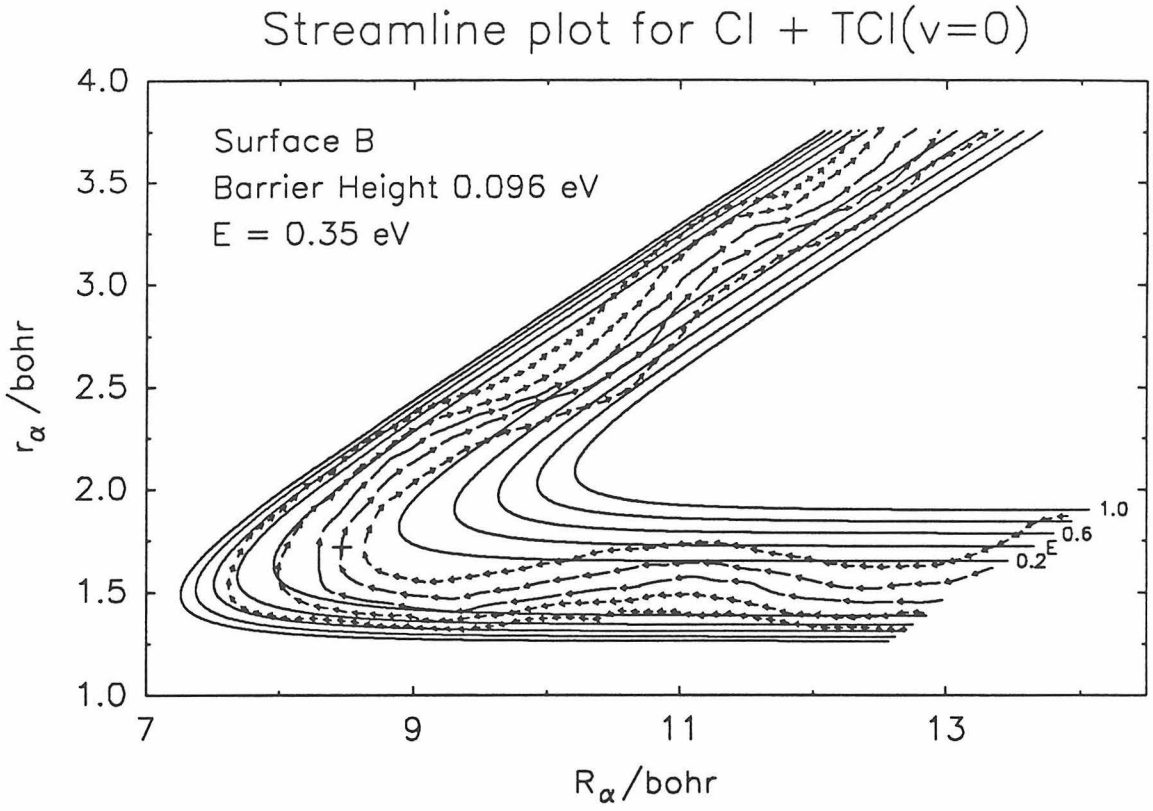
Streamline plot for Cl + TCl(v=0)
Surface B
Barrier Height 0.096 eV
E = 0.35 eV
4.0
3.5
3.0
2.5
2.0
1.5
1.0
7
9
11
13
r_α /bohr
R_α /bohr
1.0
0.6
0.2
E

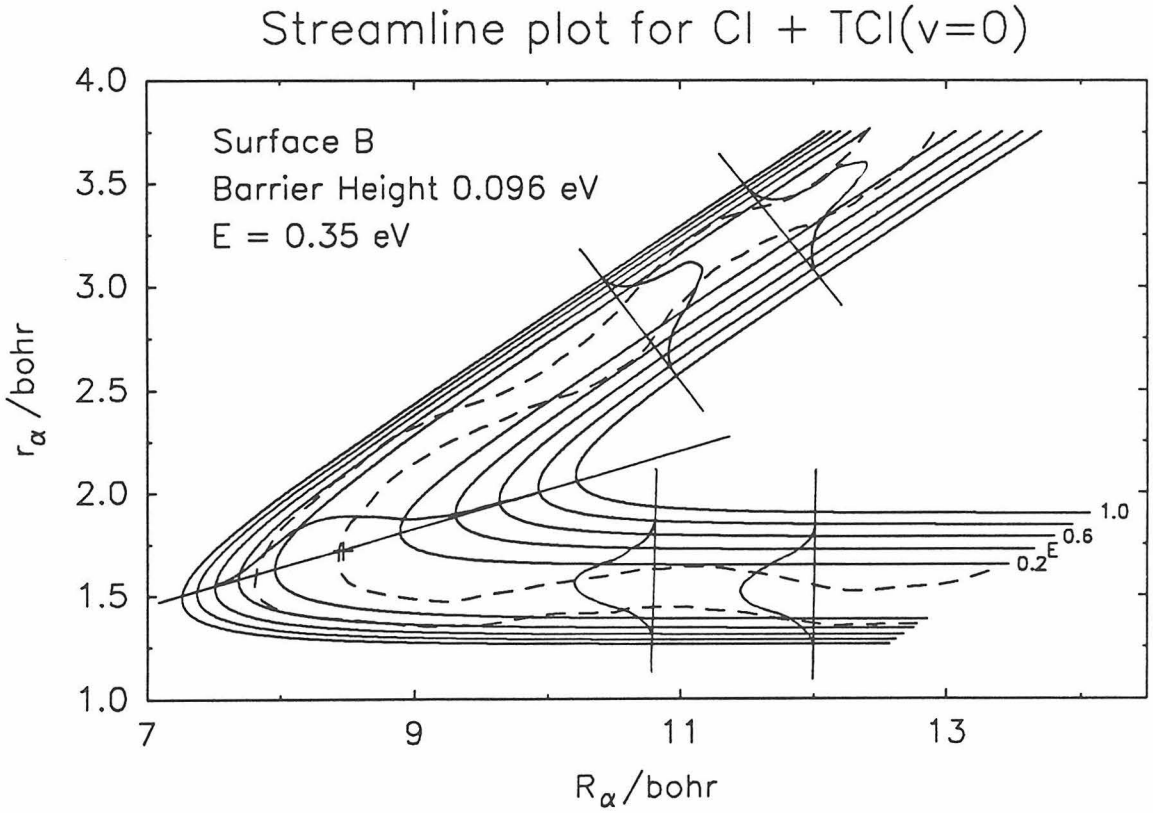
Streamline plot for Cl + TCl(v=0)
Surface B
Barrier Height 0.096 eV
E = 0.35 eV
4.0
3.5
3.0
2.5
2.0
1.5
1.0
7
9
11
13
r_α /bohr
R_α /bohr
1.0
0.6
0.2
E

Figure 44

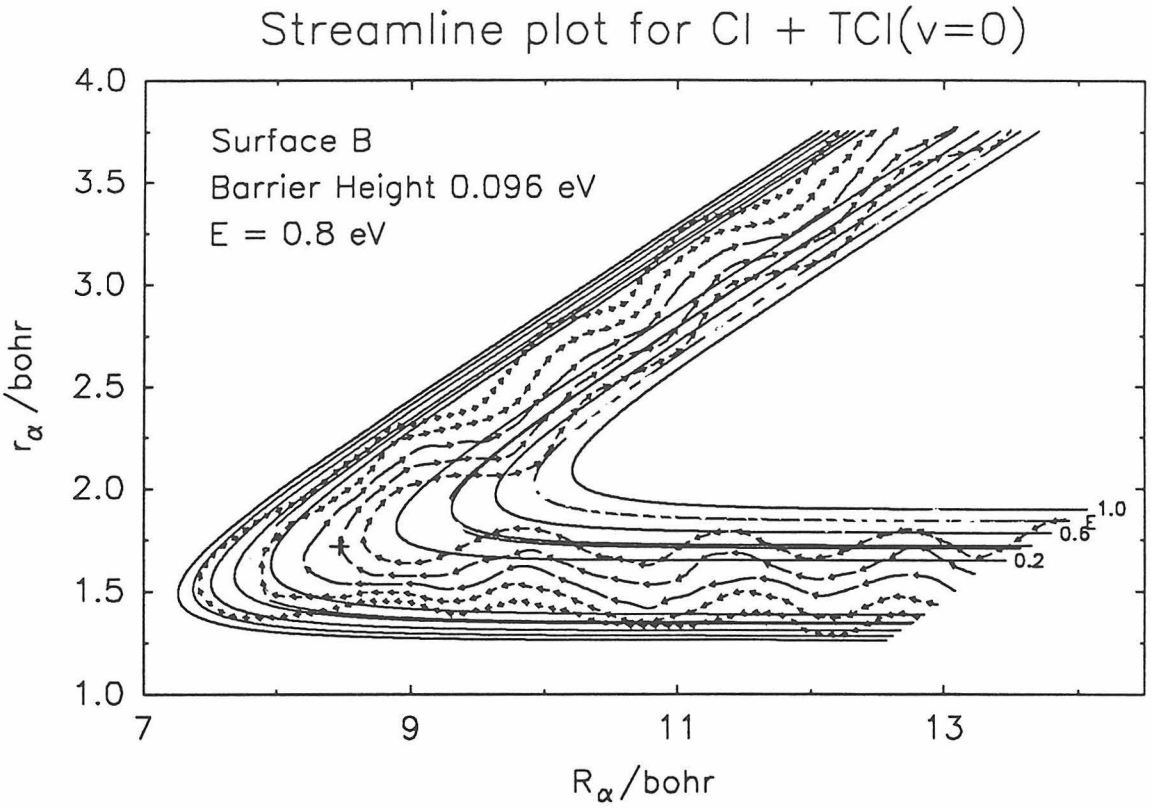
Streamline plot for Cl + TCl(v=0)
Surface B
Barrier Height 0.096 eV
E = 0.8 eV
4.0
3.5
3.0
2.5
2.0
1.5
1.0
7
9
11
13
r_α /bohr
R_α /bohr
E
1.0
0.6
0.2

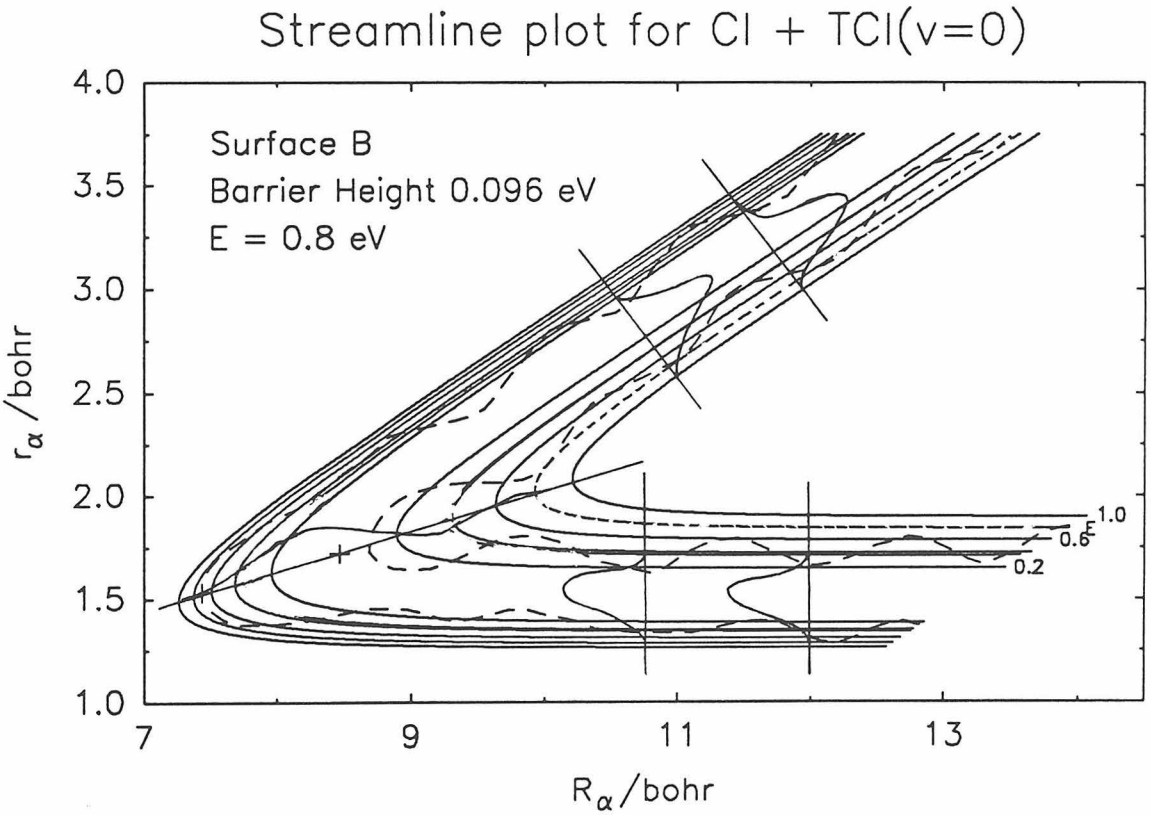
Streamline plot for Cl + TCl(v=0)
Surface B
Barrier Height 0.096 eV
E = 0.8 eV
4.0
3.5
3.0
2.5
2.0
1.5
1.0
7
9
11
13
r_α /bohr
R_α /bohr
E
1.0
0.6
0.2

Figure 45

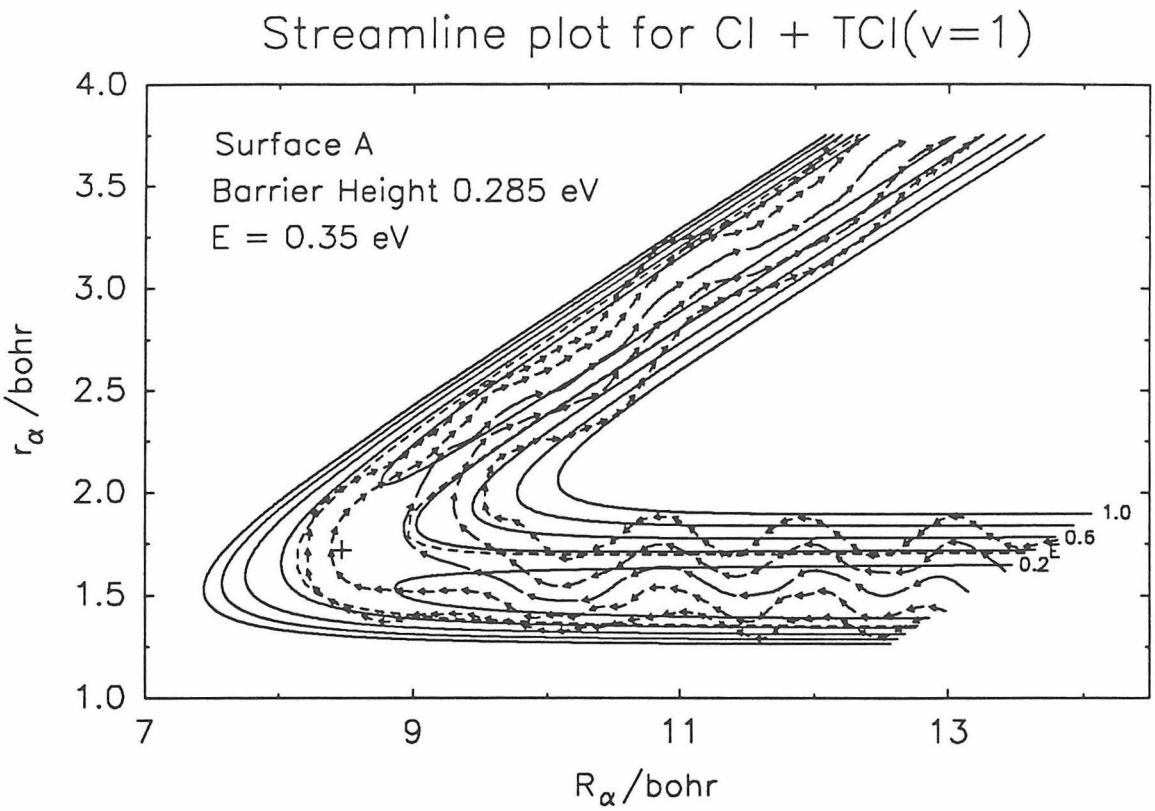
Streamline plot for Cl + TCl(v=1)
Surface A
Barrier Height 0.285 eV
E = 0.35 eV
4.0
3.5
3.0
2.5
2.0
1.5
1.0
7
9
11
13
r_α /bohr
R_α /bohr
1.0
0.6
0.2
E

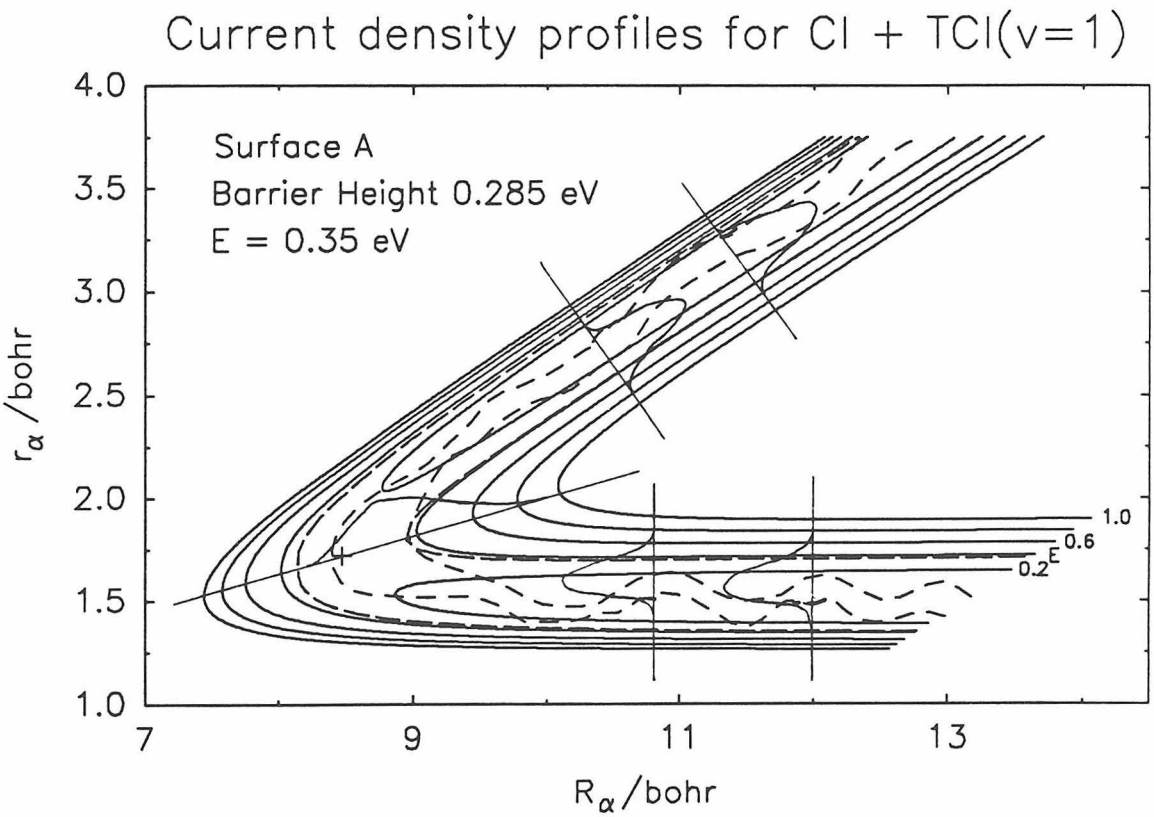
Current density profiles for Cl + TCl(v=1)
Surface A
Barrier Height 0.285 eV
E = 0.35 eV
4.0
3.5
3.0
2.5
2.0
1.5
1.0
7
9
11
13
r_α /bohr
R_α /bohr
1.0
0.6
0.2
E

Figure 46

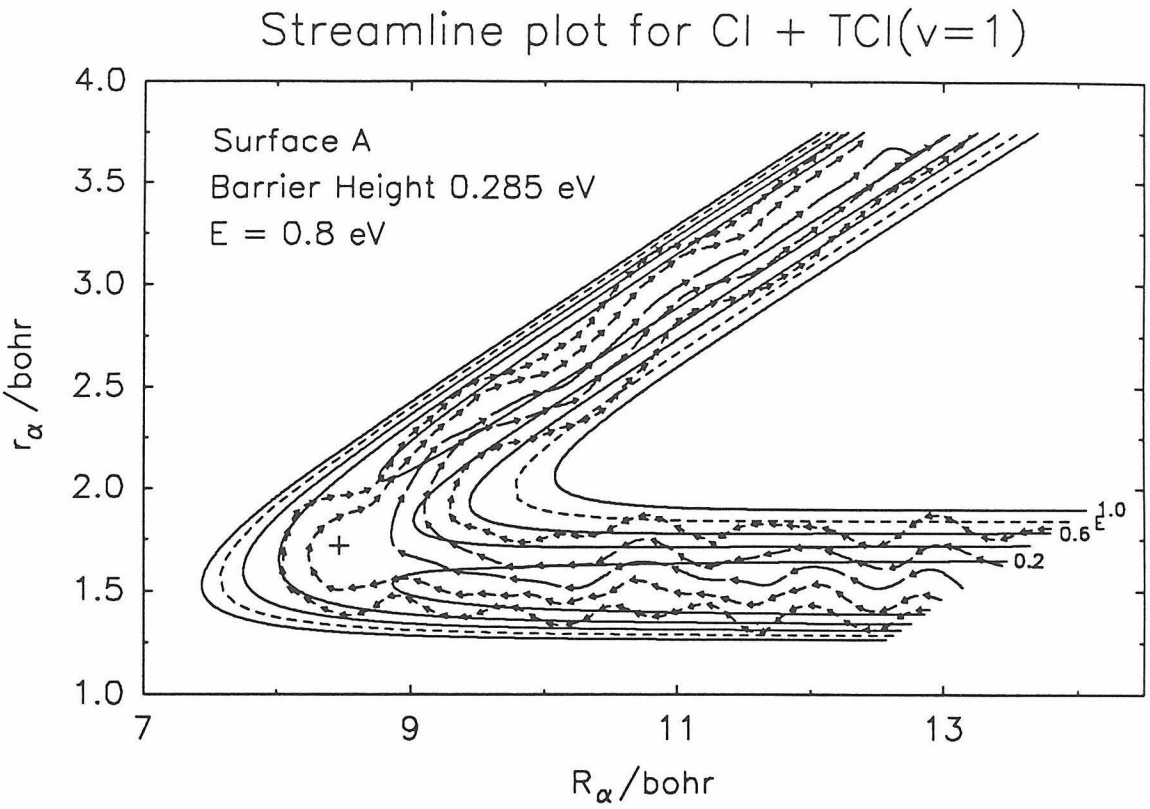
Streamline plot for Cl + TCl(v=1)
Surface A
Barrier Height 0.285 eV
E = 0.8 eV
4.0
3.5
3.0
2.5
2.0
1.5
1.0
7
9
11
13
r_α /bohr
R_α /bohr
E
1.0
0.6
0.2

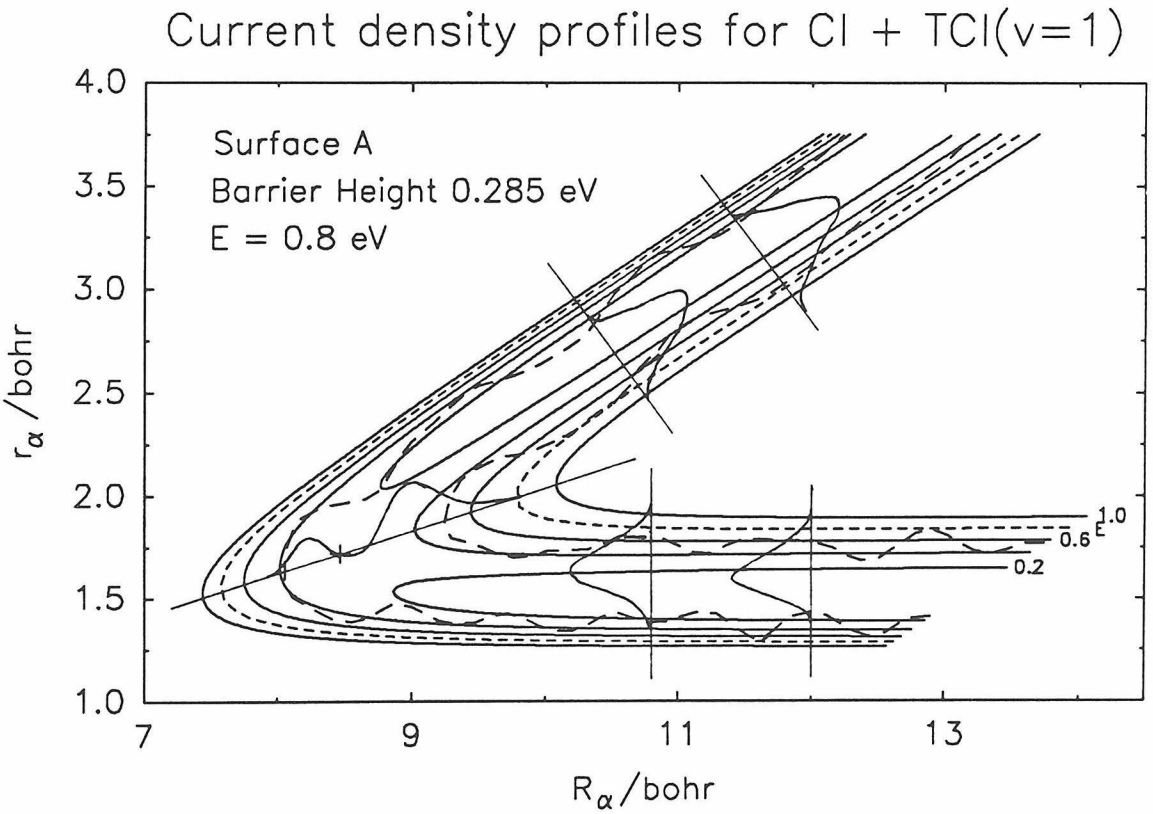
Current density profiles for Cl + TCl(v=1)
Surface A
Barrier Height 0.285 eV
E = 0.8 eV
4.0
3.5
3.0
2.5
2.0
1.5
1.0
7
9
11
13
r_α /bohr
R_α /bohr
E
1.0
0.6
0.2

Figure 47

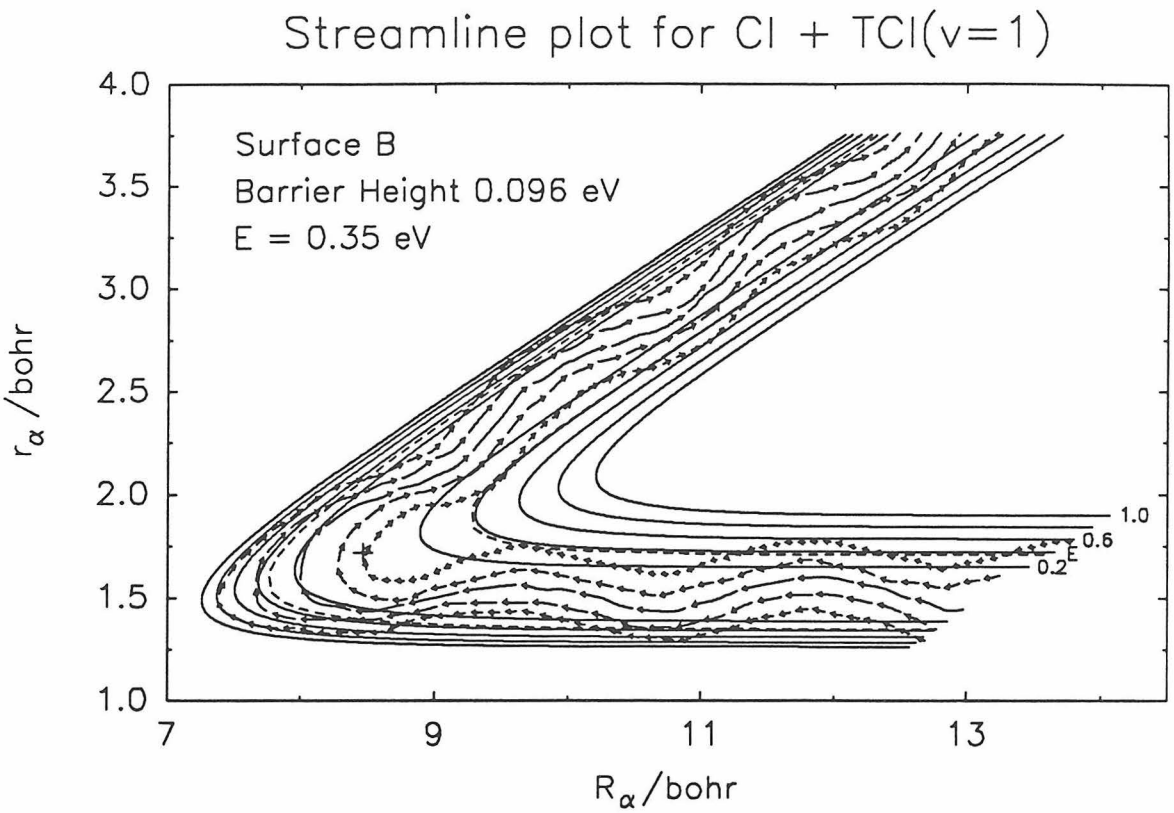
Streamline plot for Cl + TCl(v=1)
Surface B
Barrier Height 0.096 eV
E = 0.35 eV
4.0
3.5
3.0
2.5
2.0
1.5
1.0
7
9
11
13
r_α /bohr
R_α /bohr
1.0
0.6
0.2
E

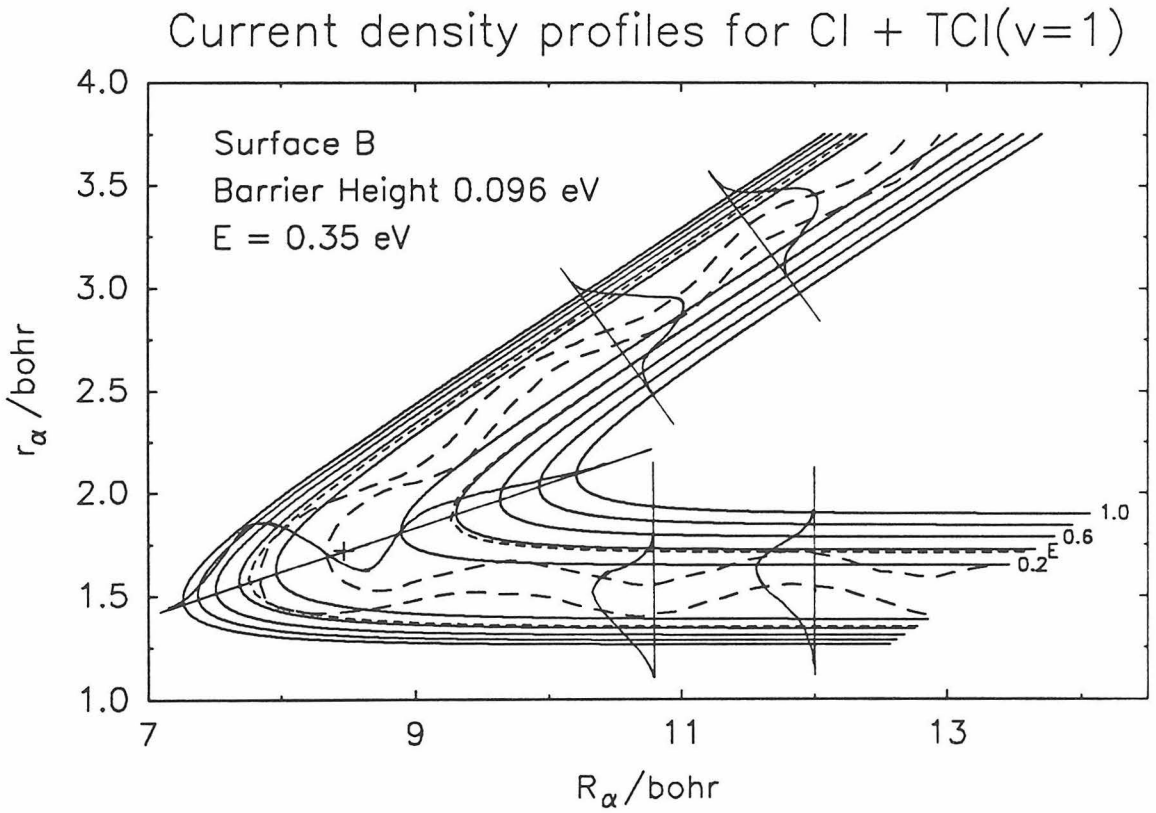
Current density profiles for Cl + TCl(v=1)
Surface B
Barrier Height 0.096 eV
E = 0.35 eV
4.0
3.5
3.0
2.5
2.0
1.5
1.0
7
9
11
13
r_α /bohr
R_α /bohr
1.0
0.6
0.2
E

Figure 48

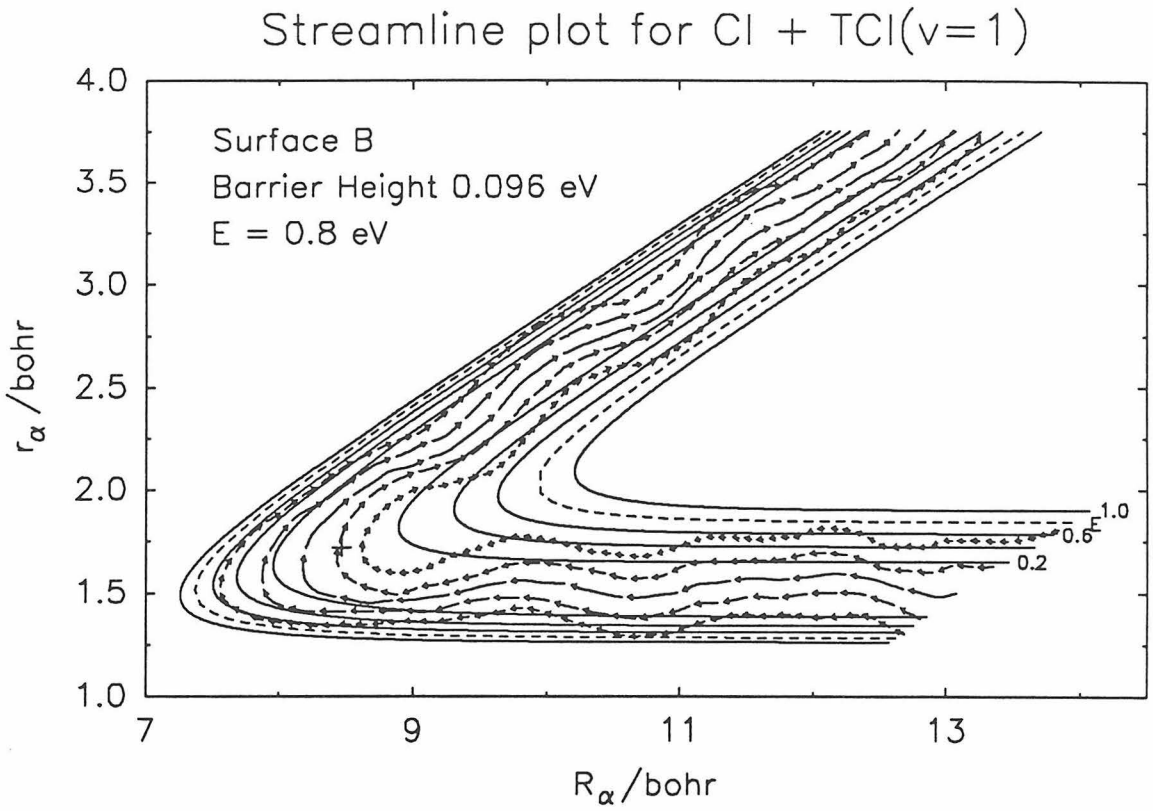
Streamline plot for Cl + TCl(v=1)
Surface B
Barrier Height 0.096 eV
E = 0.8 eV
4.0
3.5
3.0
2.5
2.0
1.5
1.0
7
9
11
13
r_α /bohr
R_α /bohr
E
1.0
0.6
0.2

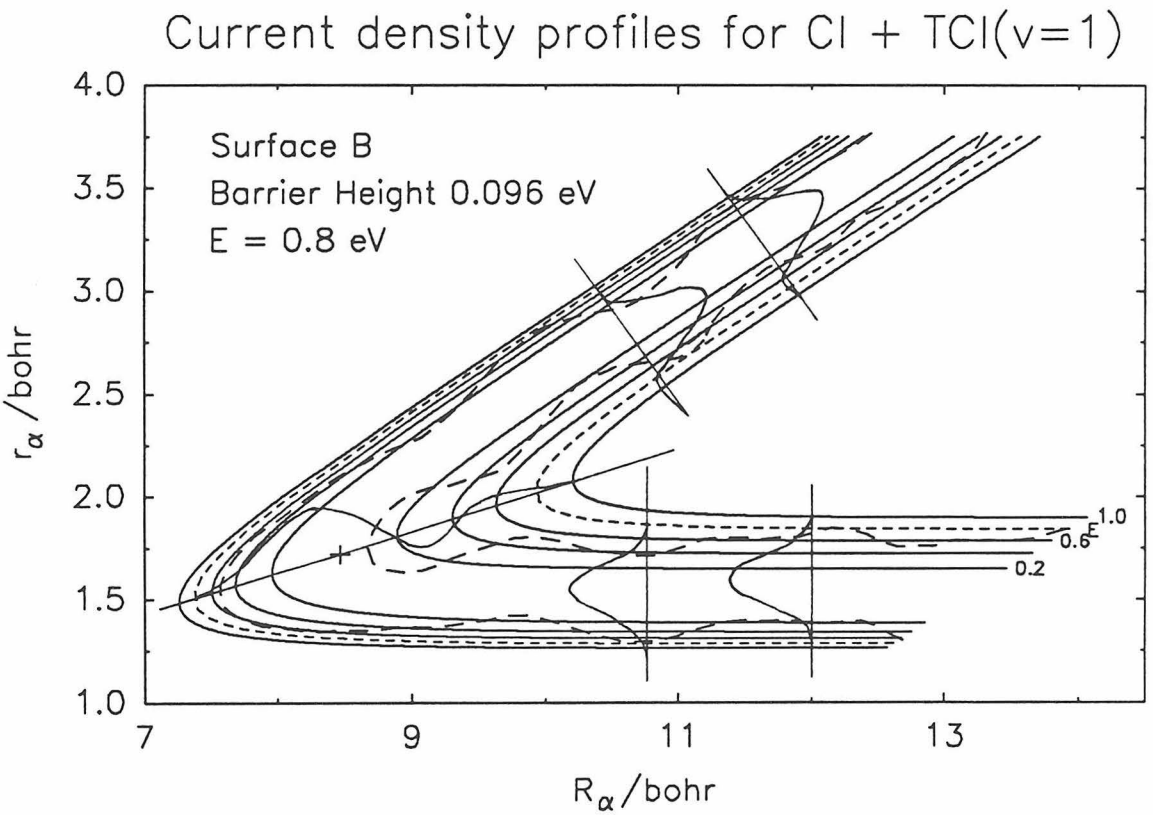
Current density profiles for Cl + TCl(v=1)
Surface B
Barrier Height 0.096 eV
E = 0.8 eV
4.0
3.5
3.0
2.5
2.0
1.5
1.0
7
9
11
13
r_α /bohr
R_α /bohr
E
1.0
0.6
0.2

Figure 49

Single quantum mechanical vortex

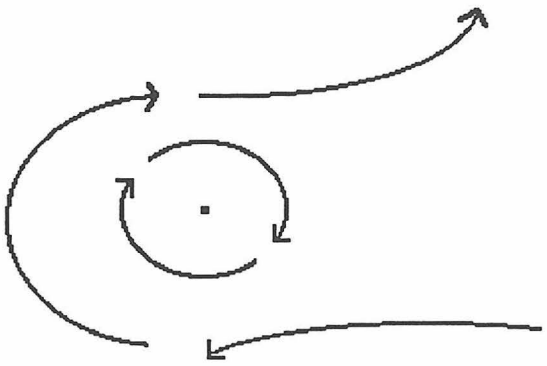

Pair of quantum mechanical vortices

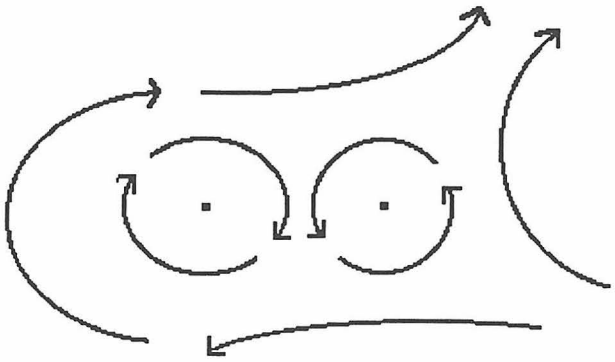

Figure 49.a

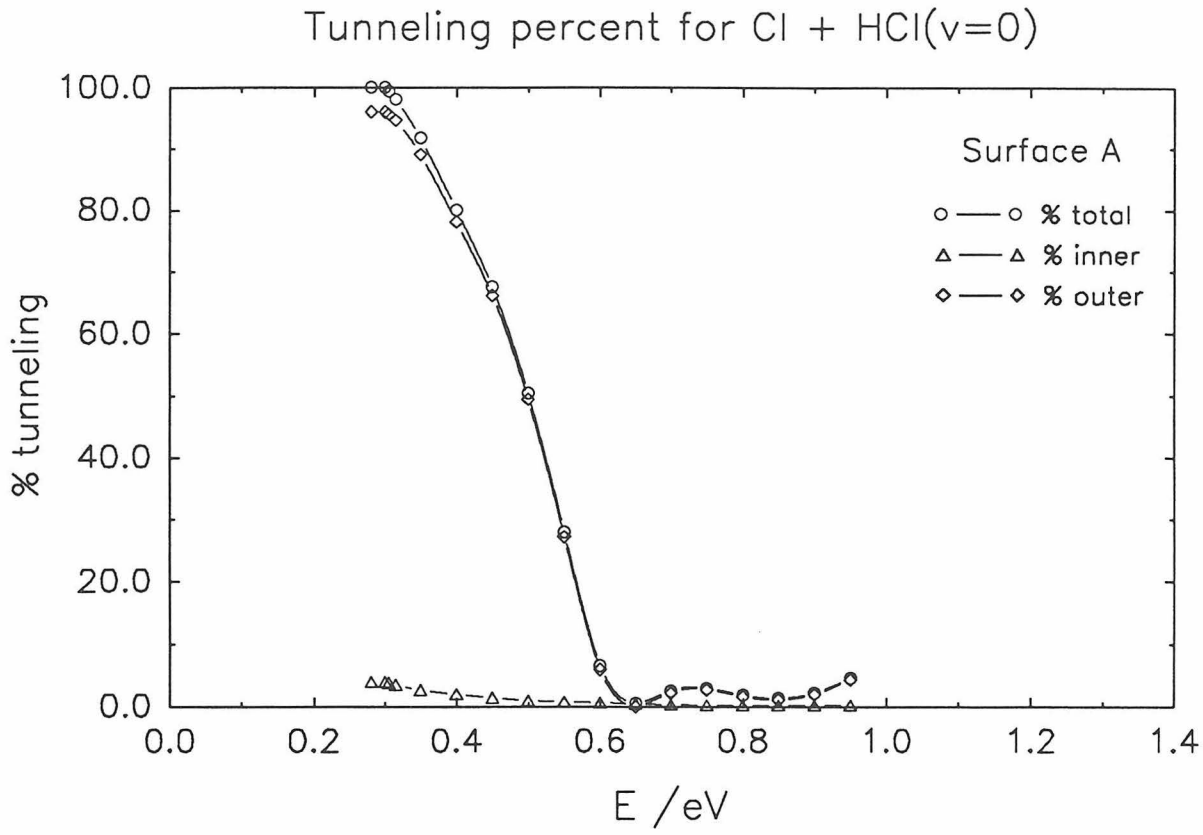
Tunneling percent for Cl + HCl(v=0)
100.0
80.0
60.0
40.0
20.0
0.0
% tunneling
0.0
0.2
0.4
0.6
0.8
1.0
1.2
1.4
E /eV
Surface A
% total
% inner
% outer

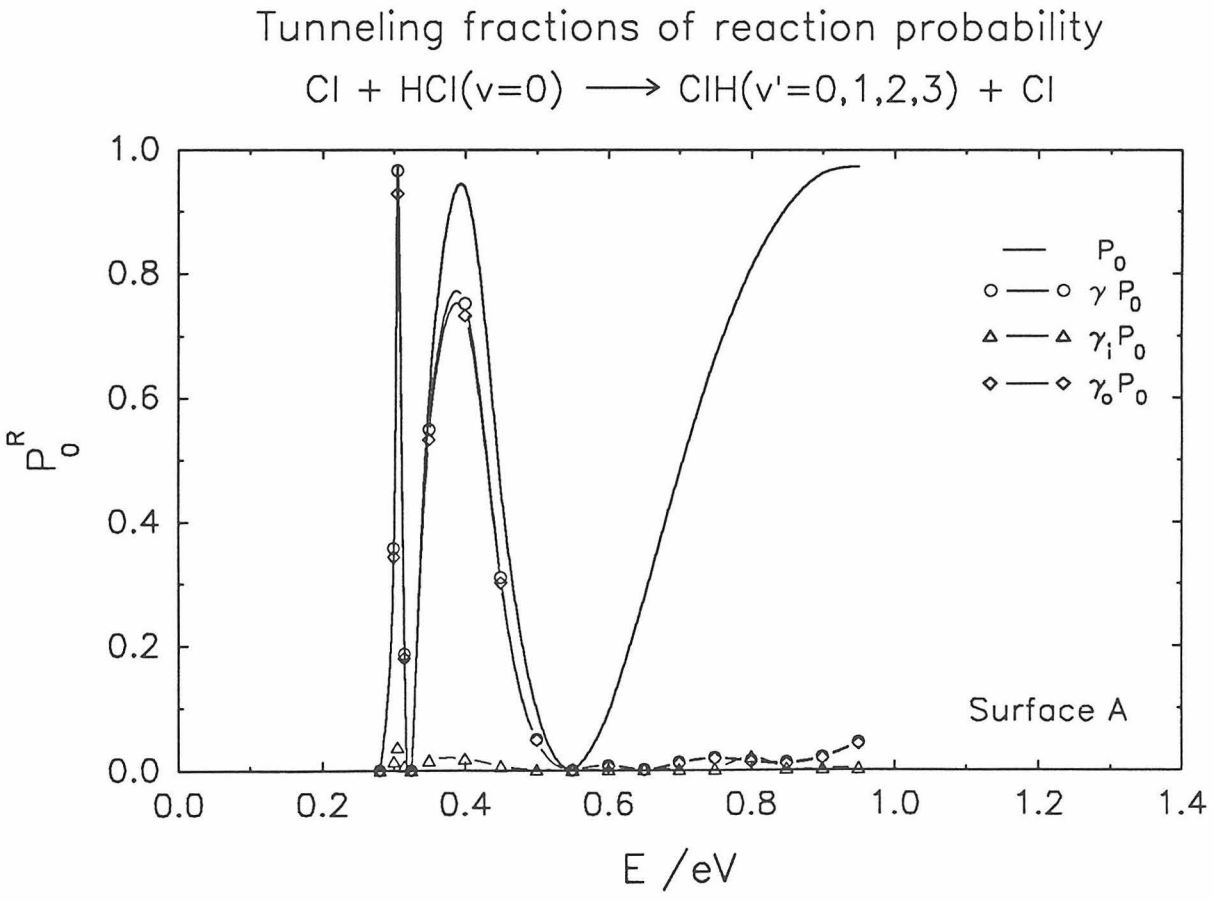
Tunneling fractions of reaction probability
Cl + HCl(v=0) ⟶ ClH(v'=0,1,2,3) + Cl
1.0
0.8
0.6
0.4
0.2
0.0
P_0^R
0.0
0.2
0.4
0.6
0.8
1.0
1.2
1.4
E /eV
P_0
γP_0
$\gamma_i P_0$
$\gamma_o P_0$
Surface A

Figure 50

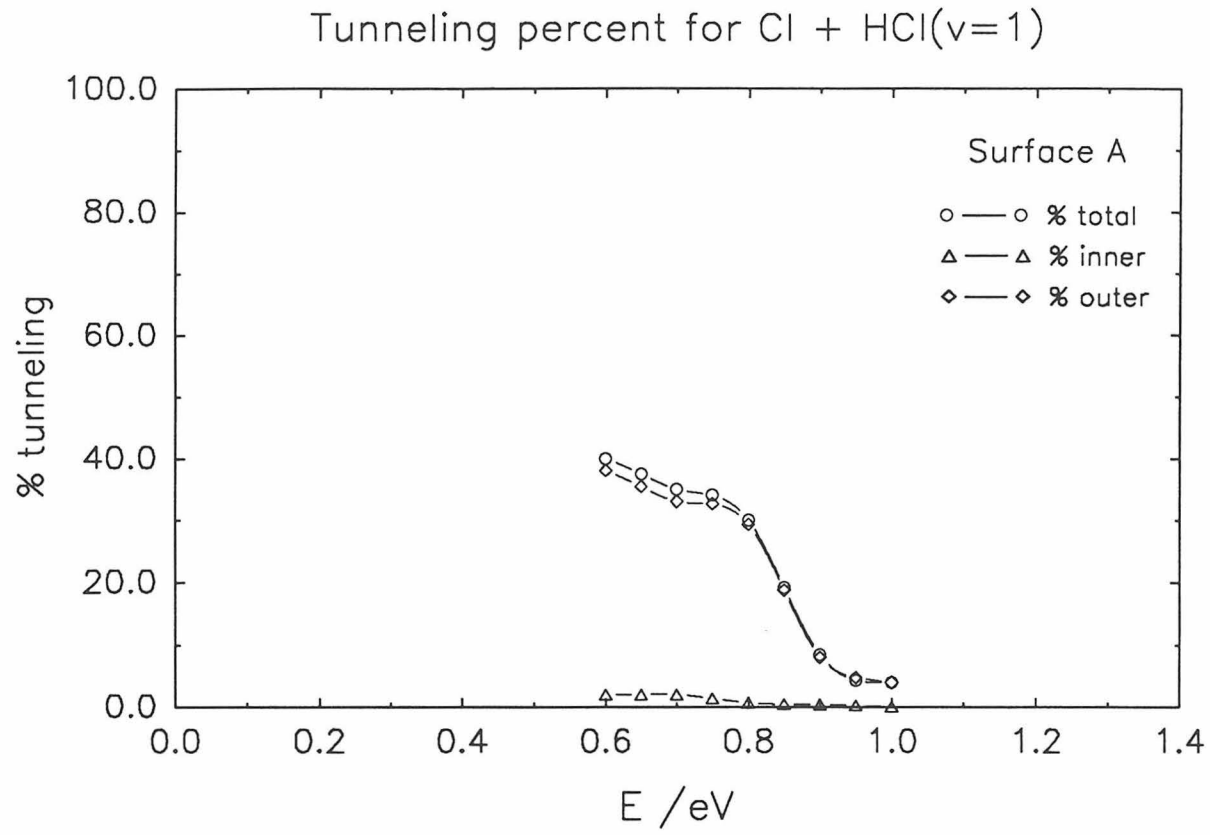
Tunneling percent for Cl + HCl(v=1)
Surface A
% total
% inner
% outer
% tunneling
100.0
80.0
60.0
40.0
20.0
0.0
0.0
0.2
0.4
0.6
0.8
1.0
1.2
1.4
E /eV

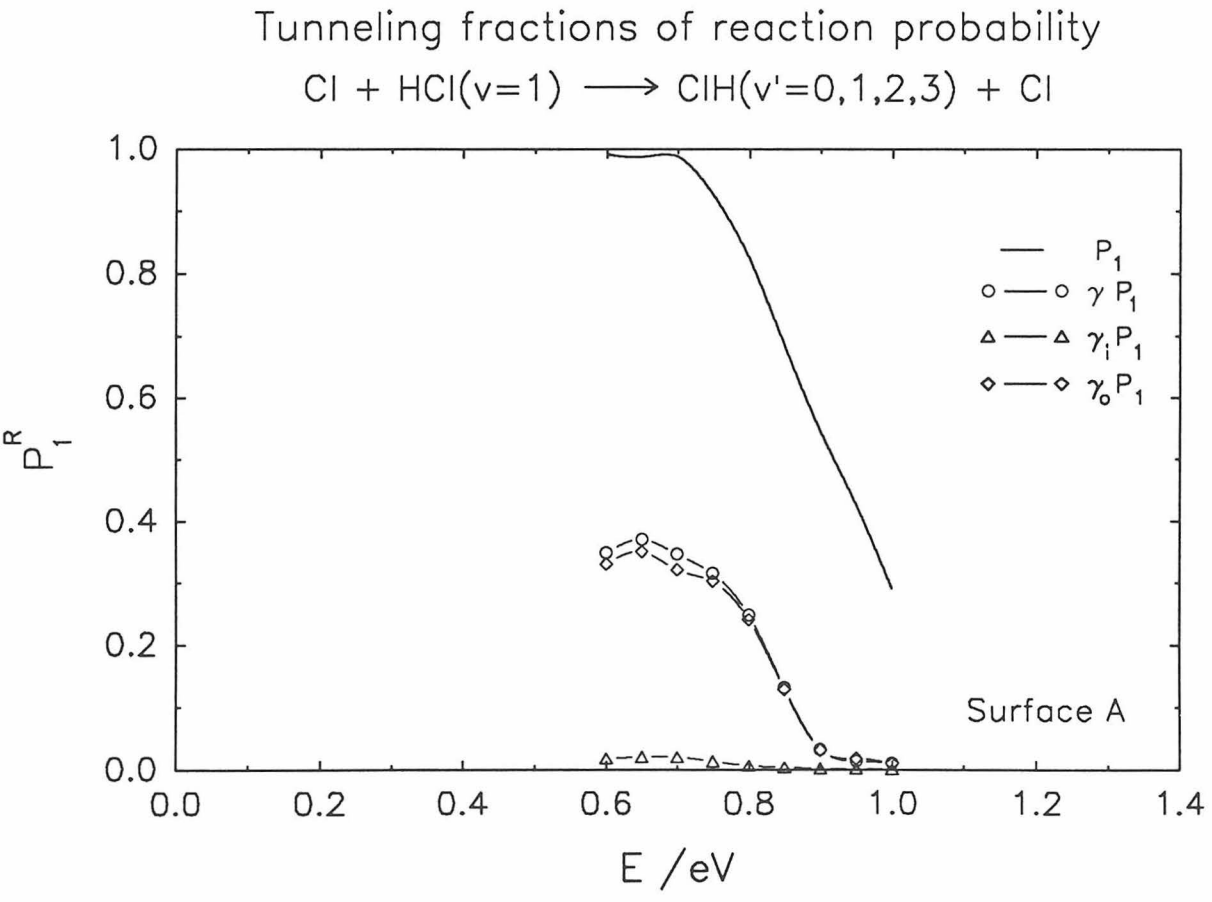
Tunneling fractions of reaction probability
Cl + HCl(v=1) ⟶ ClH(v'=0,1,2,3) + Cl
P_1
γP_1
$\gamma_i P_1$
$\gamma_o P_1$
P_1^R
Surface A
1.0
0.8
0.6
0.4
0.2
0.0
0.0
0.2
0.4
0.6
0.8
1.0
1.2
1.4
E /eV

Figure 51

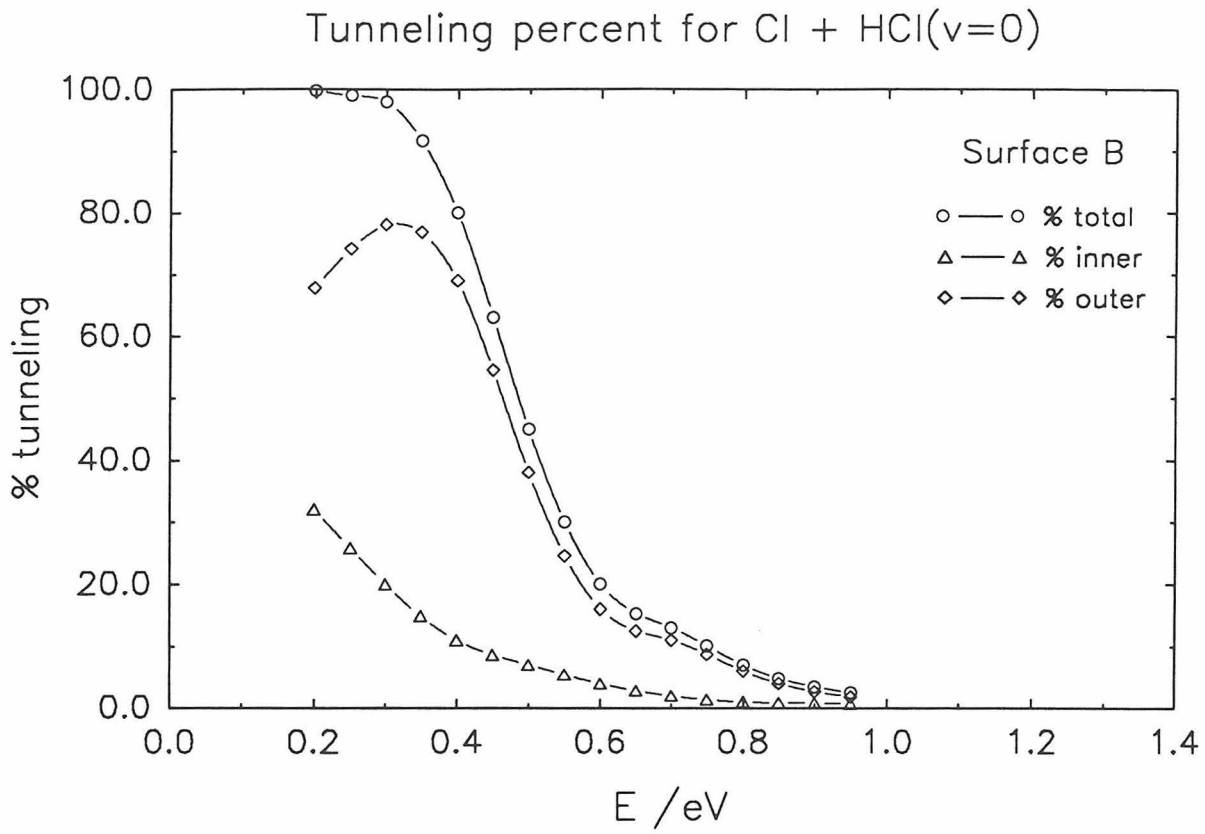
Tunneling percent for Cl + HCl(v=0)
100.0
80.0
60.0
40.0
20.0
0.0
% tunneling
0.0
0.2
0.4
0.6
0.8
1.0
1.2
1.4
E /eV
Surface B
% total
% inner
% outer

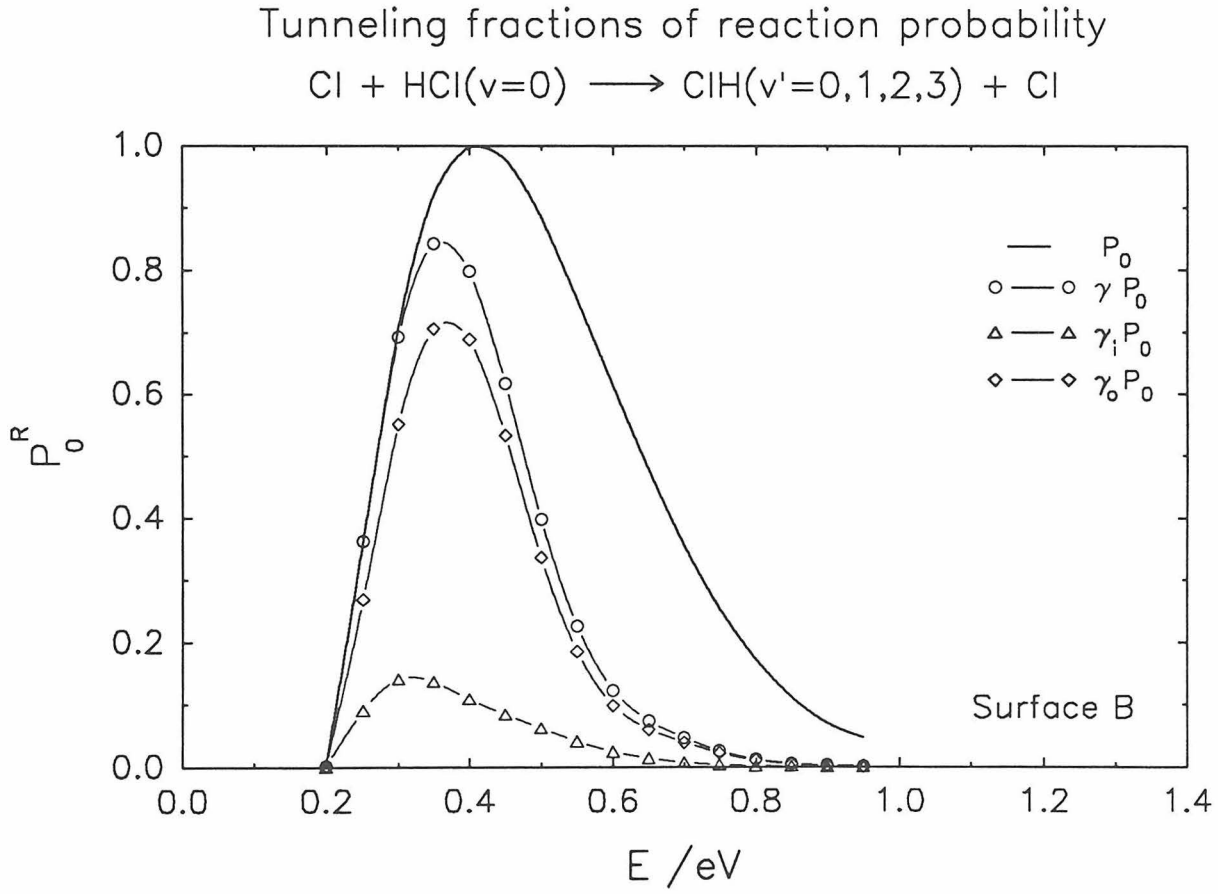
Tunneling fractions of reaction probability
Cl + HCl(v=0) ⟶ ClH(v'=0,1,2,3) + Cl
1.0
0.8
0.6
0.4
0.2
0.0
P_0^R
0.0
0.2
0.4
0.6
0.8
1.0
1.2
1.4
E /eV
P_0
γP_0
$\gamma_i P_0$
$\gamma_o P_0$
Surface B

Figure 52

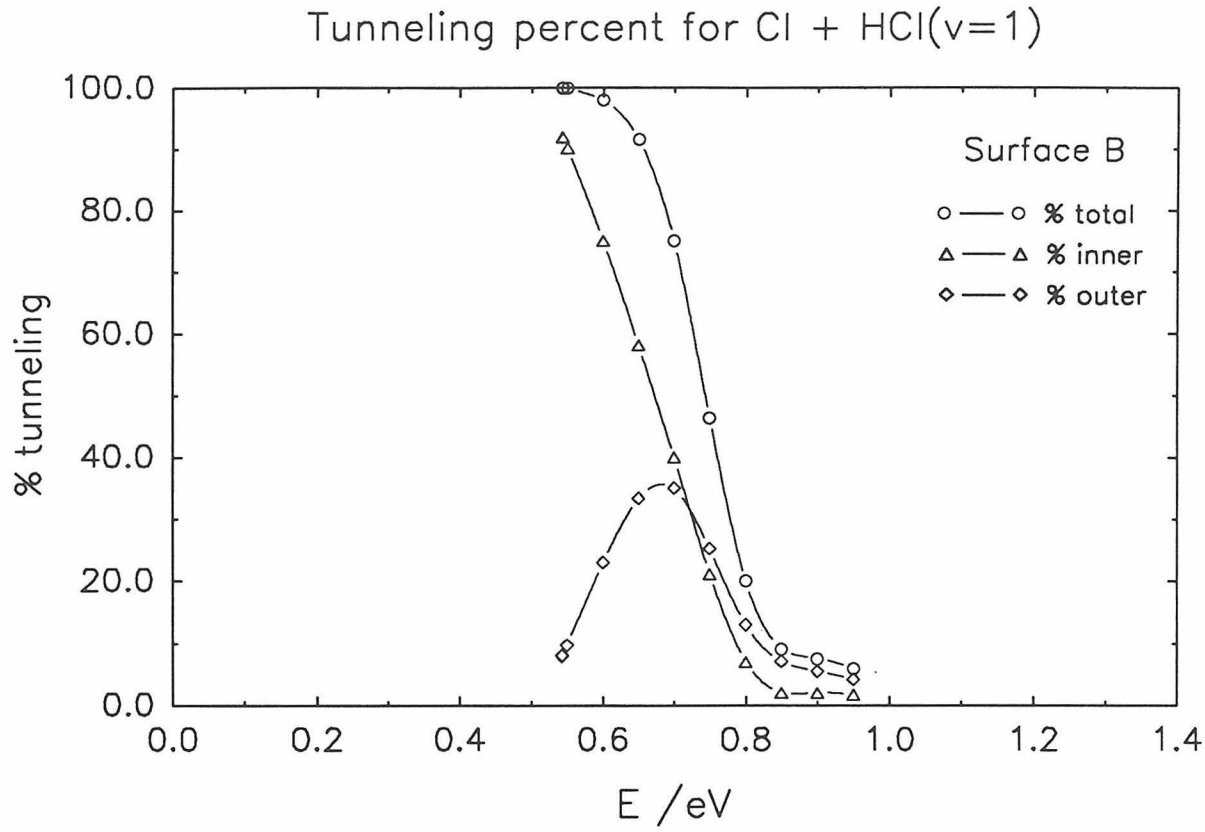
Tunneling percent for Cl + HCl(v=1)
100.0
80.0
60.0
40.0
20.0
0.0
% tunneling
0.0
0.2
0.4
0.6
0.8
1.0
1.2
1.4
E /eV
Surface B
% total
% inner
% outer

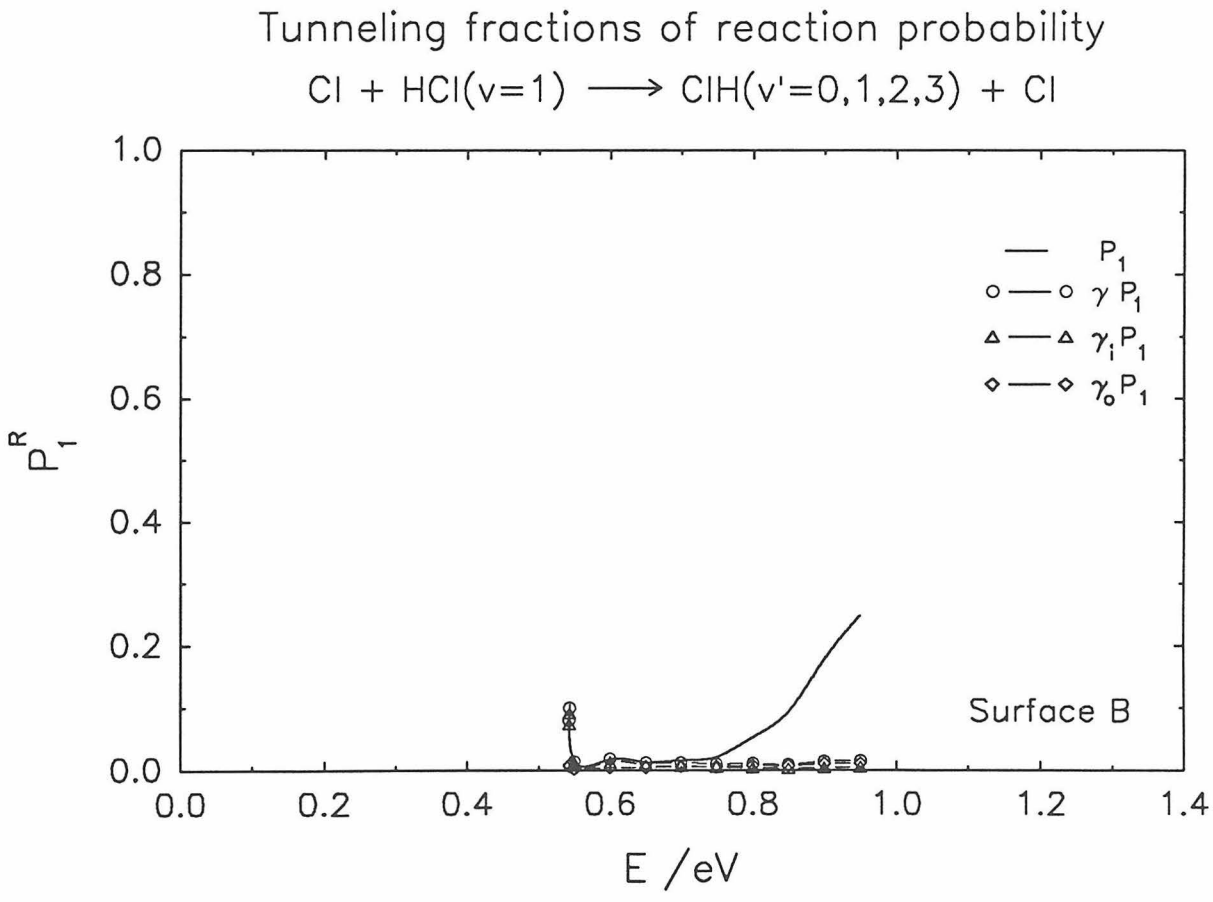
Tunneling fractions of reaction probability
Cl + HCl(v=1) ⟶ ClH(v'=0,1,2,3) + Cl
1.0
0.8
0.6
0.4
0.2
0.0
P_1^R
0.0
0.2
0.4
0.6
0.8
1.0
1.2
1.4
E /eV
P_1
γP_1
$\gamma_i P_1$
$\gamma_o P_1$
Surface B

Figure 53

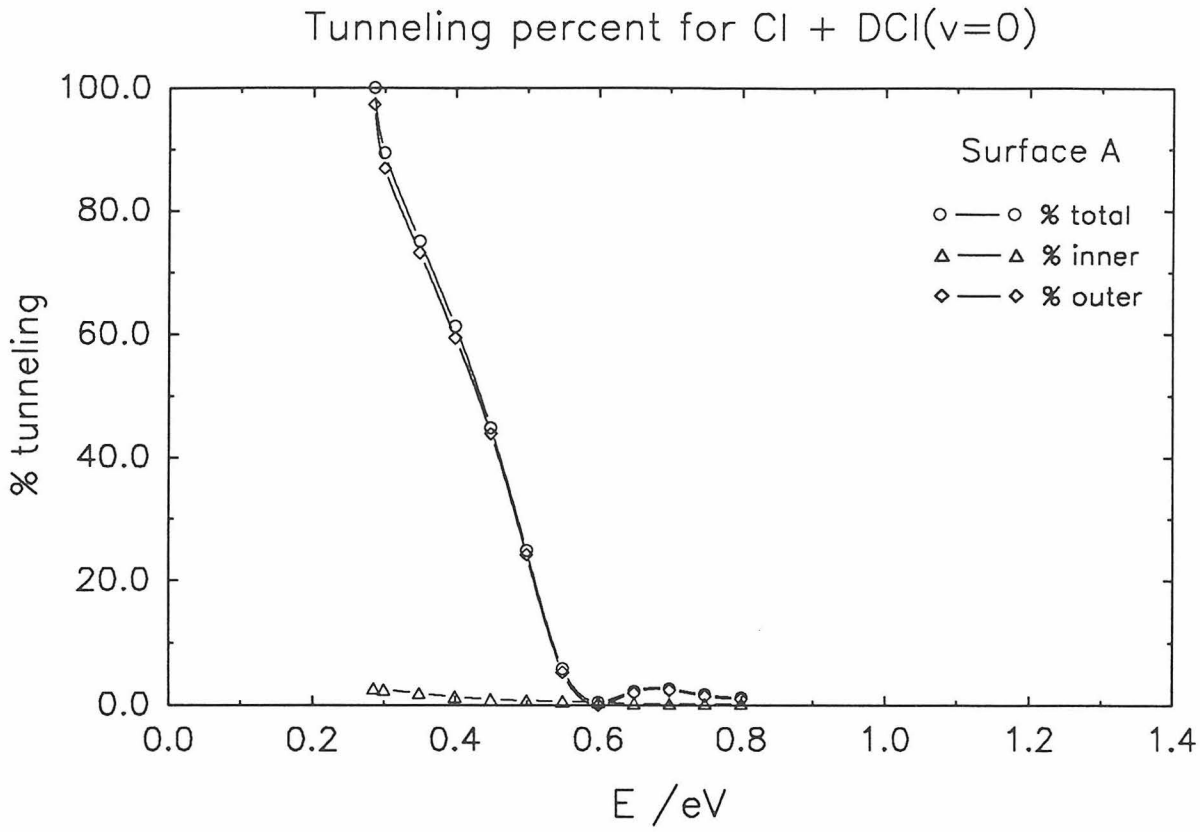
Tunneling percent for Cl + DCl(v=0)
100.0
80.0
60.0
40.0
20.0
0.0
% tunneling
Surface A
% total
% inner
% outer
0.0
0.2
0.4
0.6
0.8
1.0
1.2
1.4
E /eV

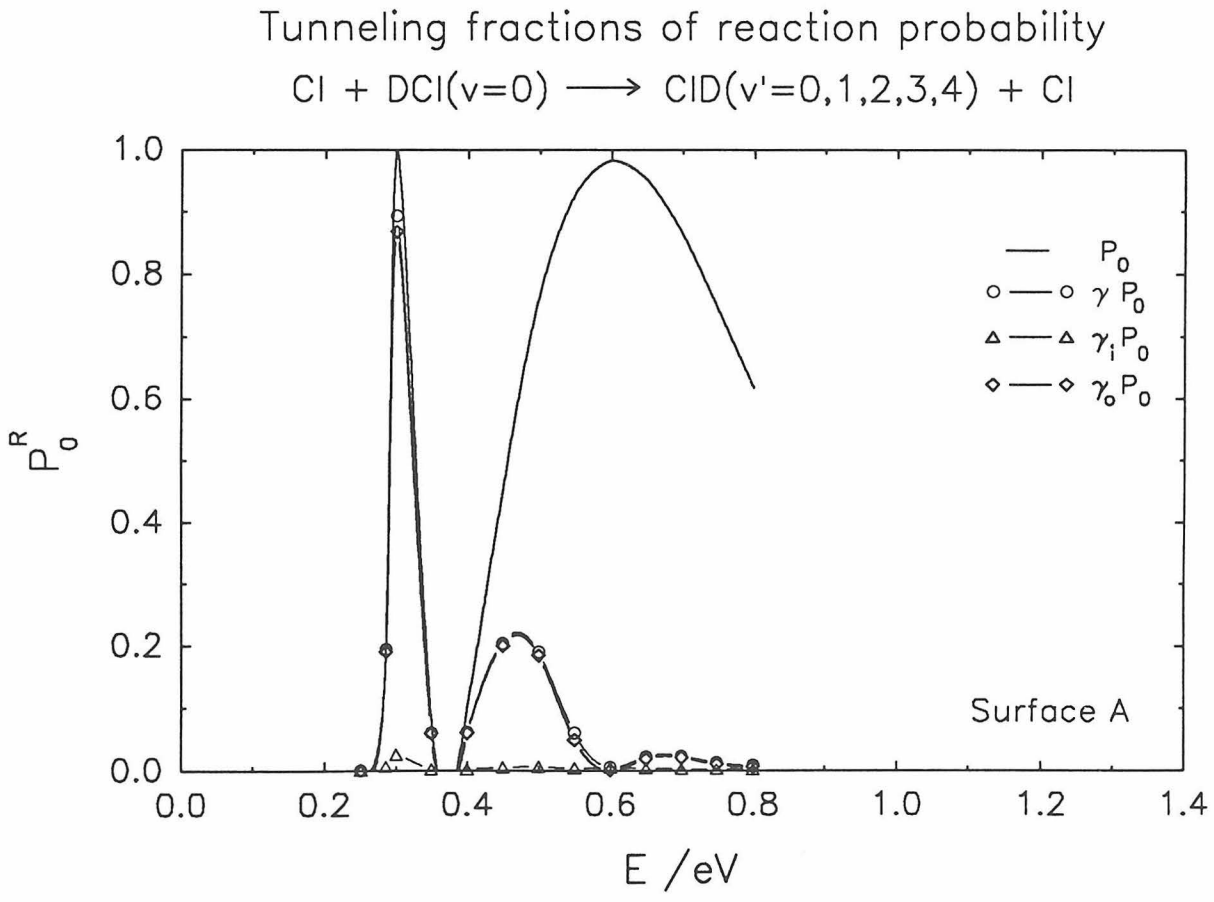
Tunneling fractions of reaction probability
Cl + DCl(v=0) ⟶ ClD(v'=0,1,2,3,4) + Cl
1.0
0.8
0.6
0.4
0.2
0.0
P_0^R
P_0
γP_0
$\gamma_i P_0$
$\gamma_o P_0$
Surface A
0.0
0.2
0.4
0.6
0.8
1.0
1.2
1.4
E /eV

Figure 54

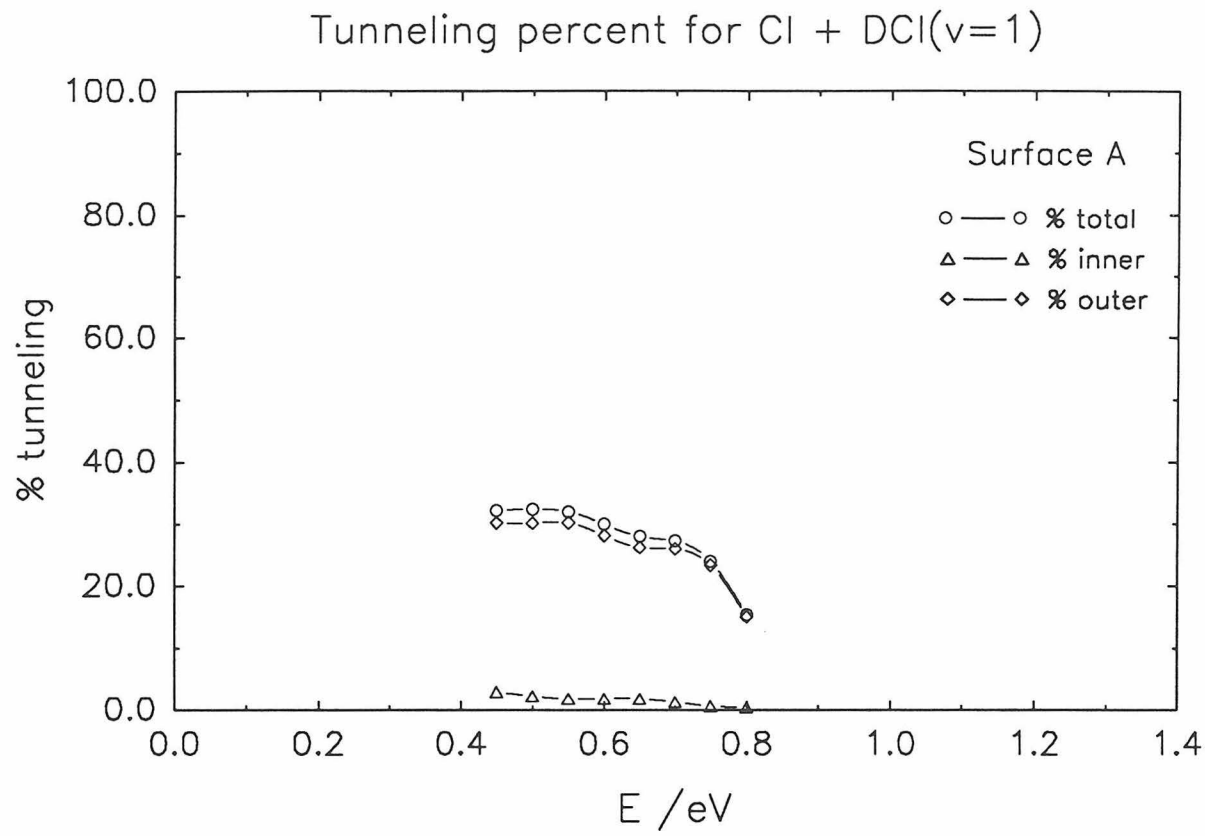
Tunneling percent for Cl + DCl(v=1)
100.0
80.0
60.0
40.0
20.0
0.0
% tunneling
0.0
0.2
0.4
0.6
0.8
1.0
1.2
1.4
E /eV
Surface A
% total
% inner
% outer

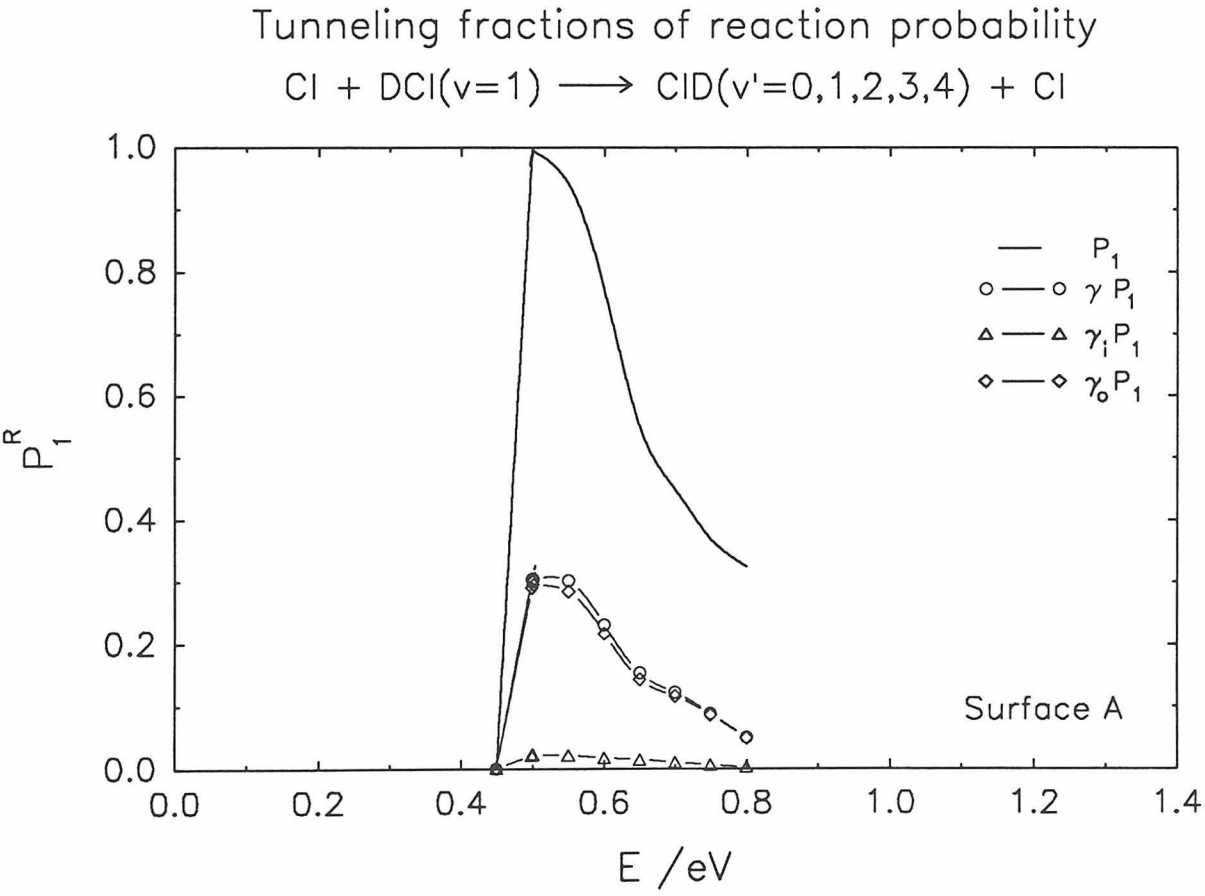
Tunneling fractions of reaction probability
Cl + DCl(v=1) ⟶ ClD(v'=0,1,2,3,4) + Cl
1.0
0.8
0.6
0.4
0.2
0.0
P_1^R
0.0
0.2
0.4
0.6
0.8
1.0
1.2
1.4
E /eV
P_1
γP_1
$\gamma_i P_1$
$\gamma_o P_1$
Surface A

Figure 55

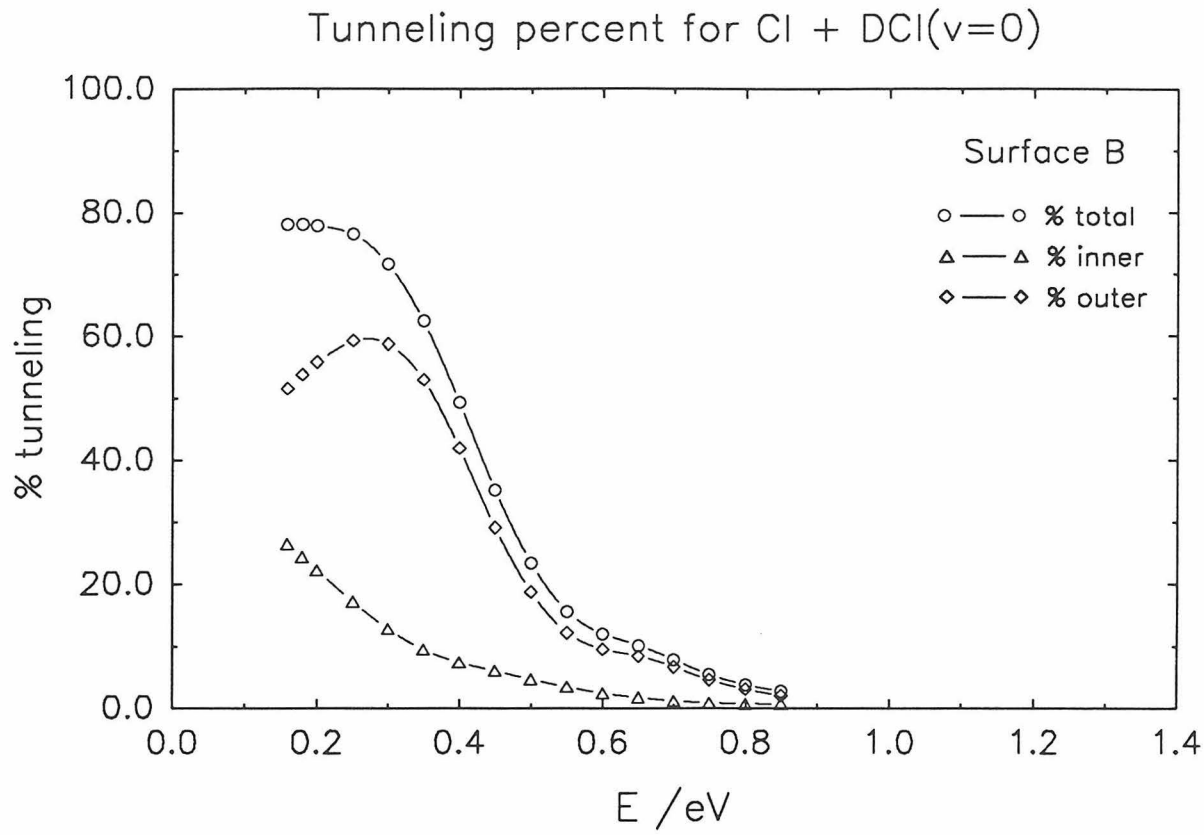
Tunneling percent for Cl + DCl(v=0)
Surface B
% total
% inner
% outer
% tunneling
E /eV
100.0
80.0
60.0
40.0
20.0
0.0
0.0
0.2
0.4
0.6
0.8
1.0
1.2
1.4

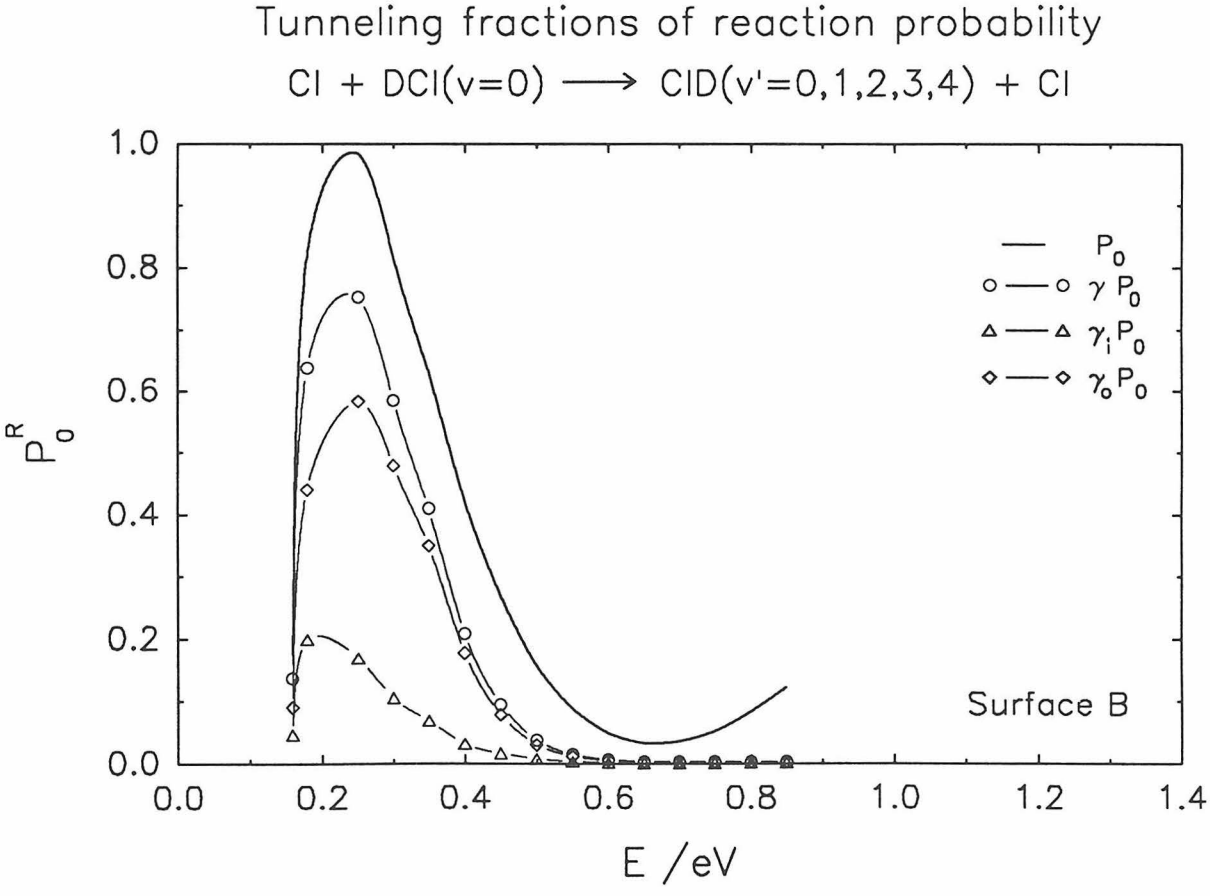
Tunneling fractions of reaction probability
Cl + DCl(v=0) ⟶ ClD(v'=0,1,2,3,4) + Cl
P_0
γP_0
$\gamma_i P_0$
$\gamma_o P_0$
P_0^R
Surface B
E /eV
1.0
0.8
0.6
0.4
0.2
0.0
0.0
0.2
0.4
0.6
0.8
1.0
1.2
1.4

Figure 56

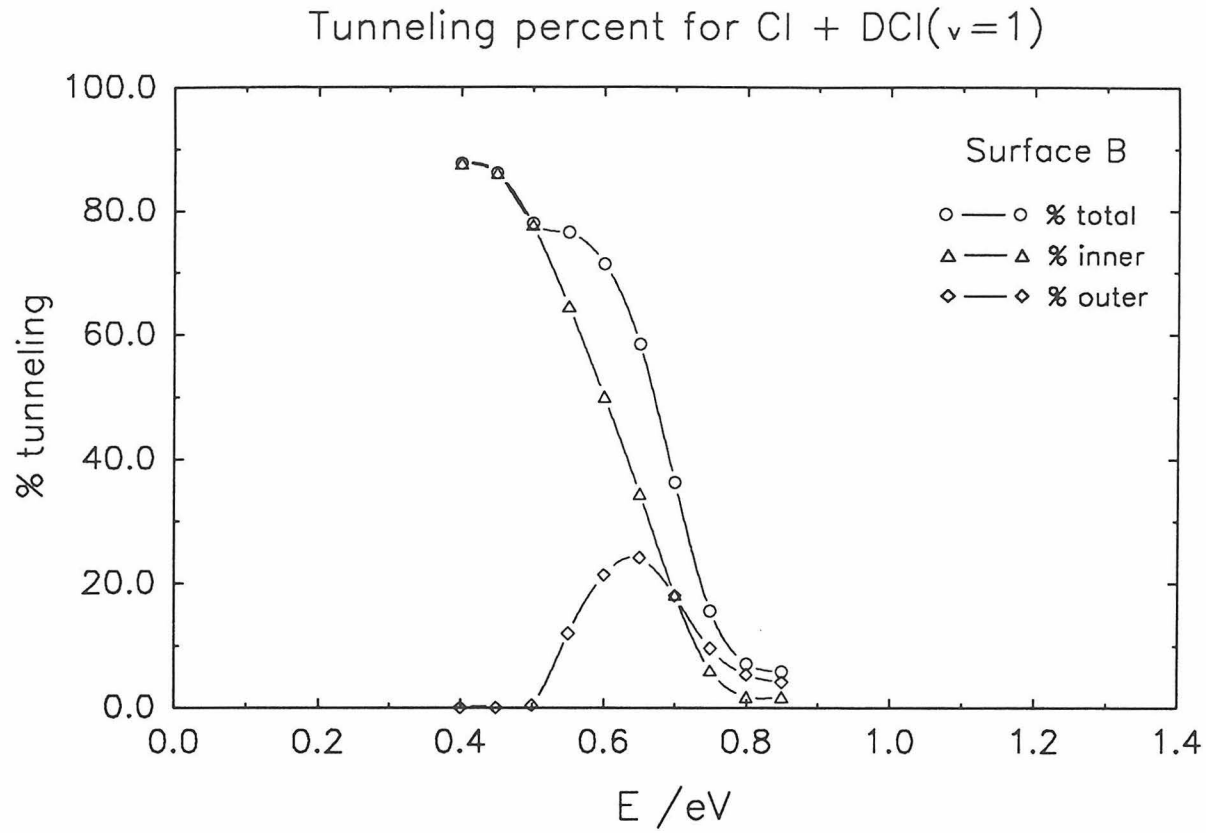
Tunneling percent for Cl + DCl(v=1)
Surface B
% total
% inner
% outer
% tunneling
E /eV
100.0
80.0
60.0
40.0
20.0
0.0
0.0
0.2
0.4
0.6
0.8
1.0
1.2
1.4

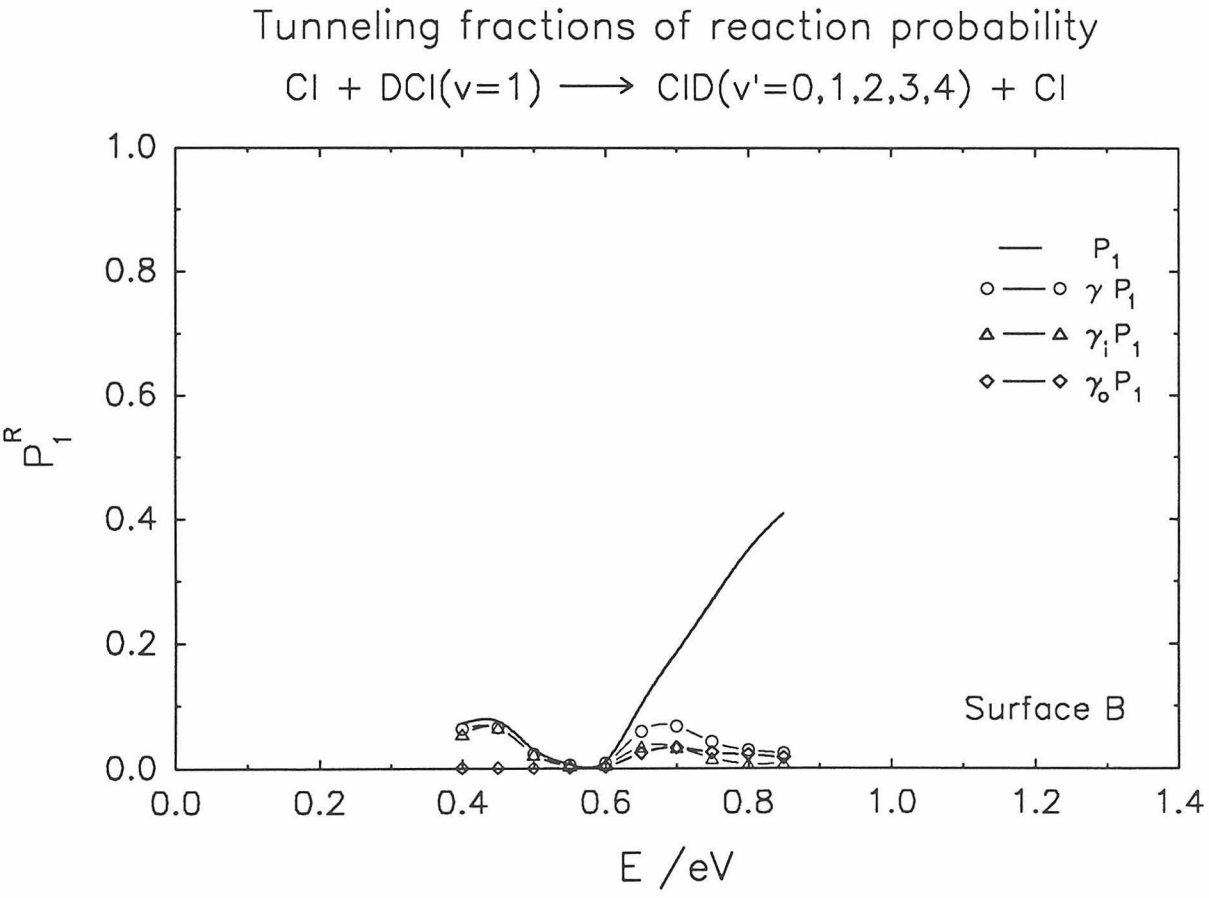
Tunneling fractions of reaction probability
Cl + DCl(v=1) ⟶ ClD(v'=0,1,2,3,4) + Cl
P_1
γP_1
$\gamma_i P_1$
$\gamma_o P_1$
Surface B
P_1^R
E /eV
1.0
0.8
0.6
0.4
0.2
0.0
0.0
0.2
0.4
0.6
0.8
1.0
1.2
1.4

Figure 57

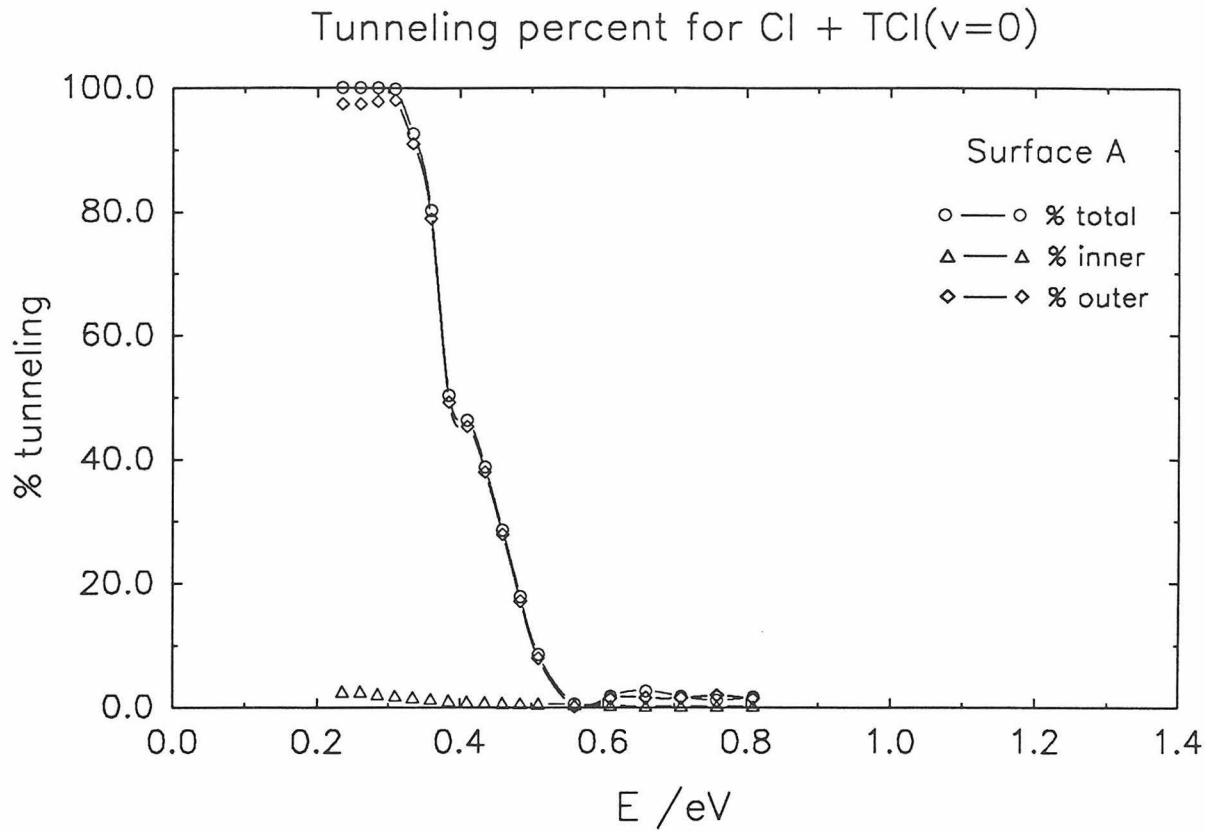
Tunneling percent for Cl + TCl(v=0)
100.0
80.0
60.0
40.0
20.0
0.0
% tunneling
0.0
0.2
0.4
0.6
0.8
1.0
1.2
1.4
E /eV
Surface A
% total
% inner
% outer

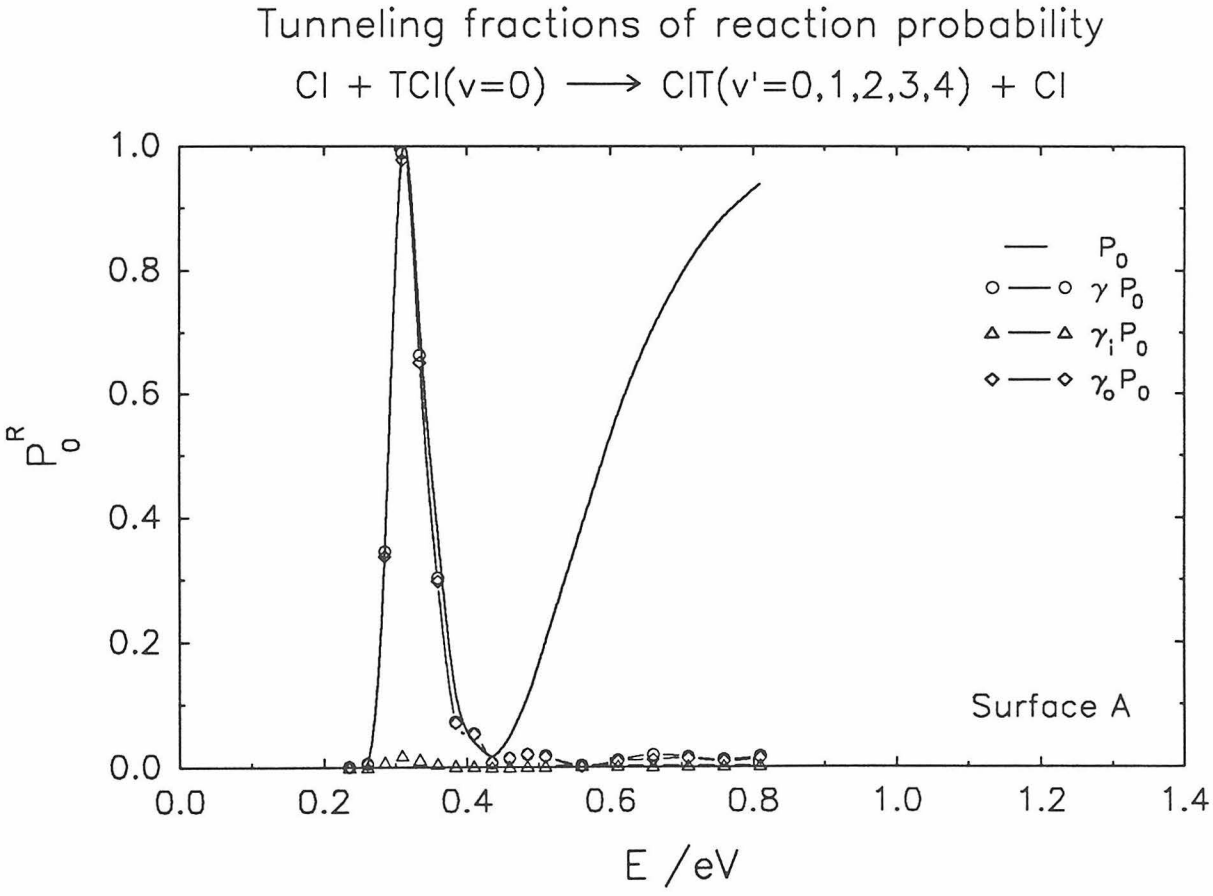
Tunneling fractions of reaction probability
Cl + TCl(v=0) ⟶ ClT(v'=0,1,2,3,4) + Cl
1.0
0.8
0.6
0.4
0.2
0.0
P_0^R
0.0
0.2
0.4
0.6
0.8
1.0
1.2
1.4
E /eV
P_0
γP_0
$\gamma_i P_0$
$\gamma_o P_0$
Surface A

Figure 58

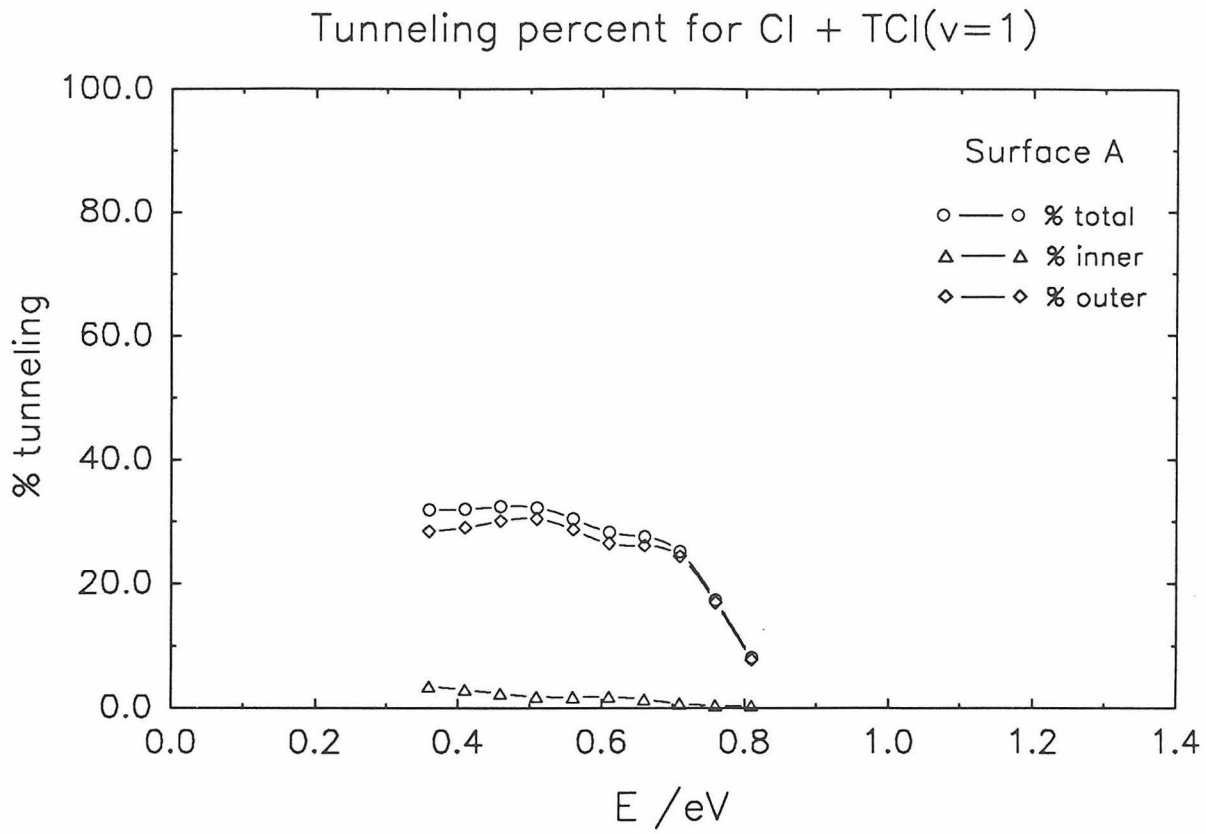
Tunneling percent for Cl + TCl(v=1)
100.0
80.0
60.0
40.0
20.0
0.0
% tunneling
Surface A
% total
% inner
% outer
0.0
0.2
0.4
0.6
0.8
1.0
1.2
1.4
E /eV

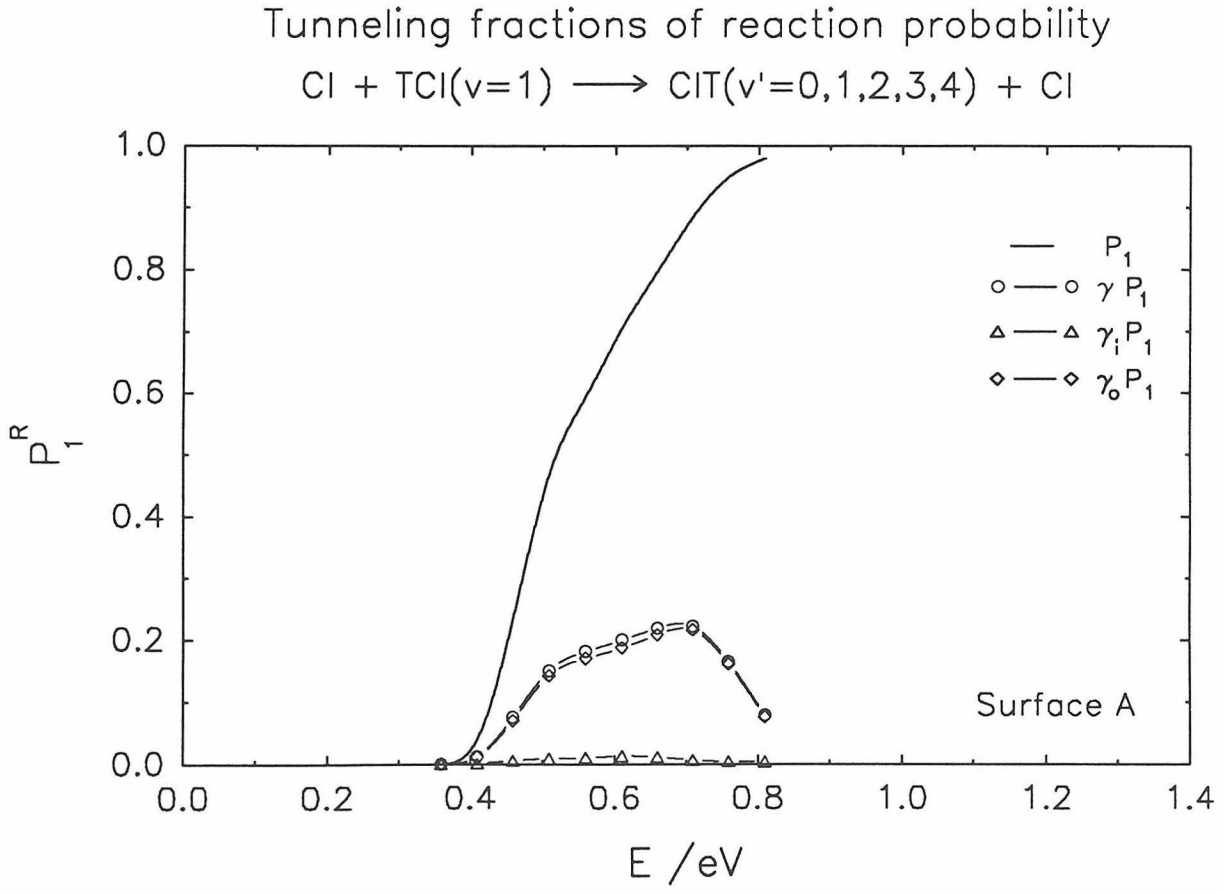
Tunneling fractions of reaction probability
Cl + TCl(v=1) ⟶ ClT(v'=0,1,2,3,4) + Cl
1.0
0.8
0.6
0.4
0.2
0.0
P_1^R
P_1
γP_1
$\gamma_i P_1$
$\gamma_o P_1$
Surface A
0.0
0.2
0.4
0.6
0.8
1.0
1.2
1.4
E /eV

Figure 59

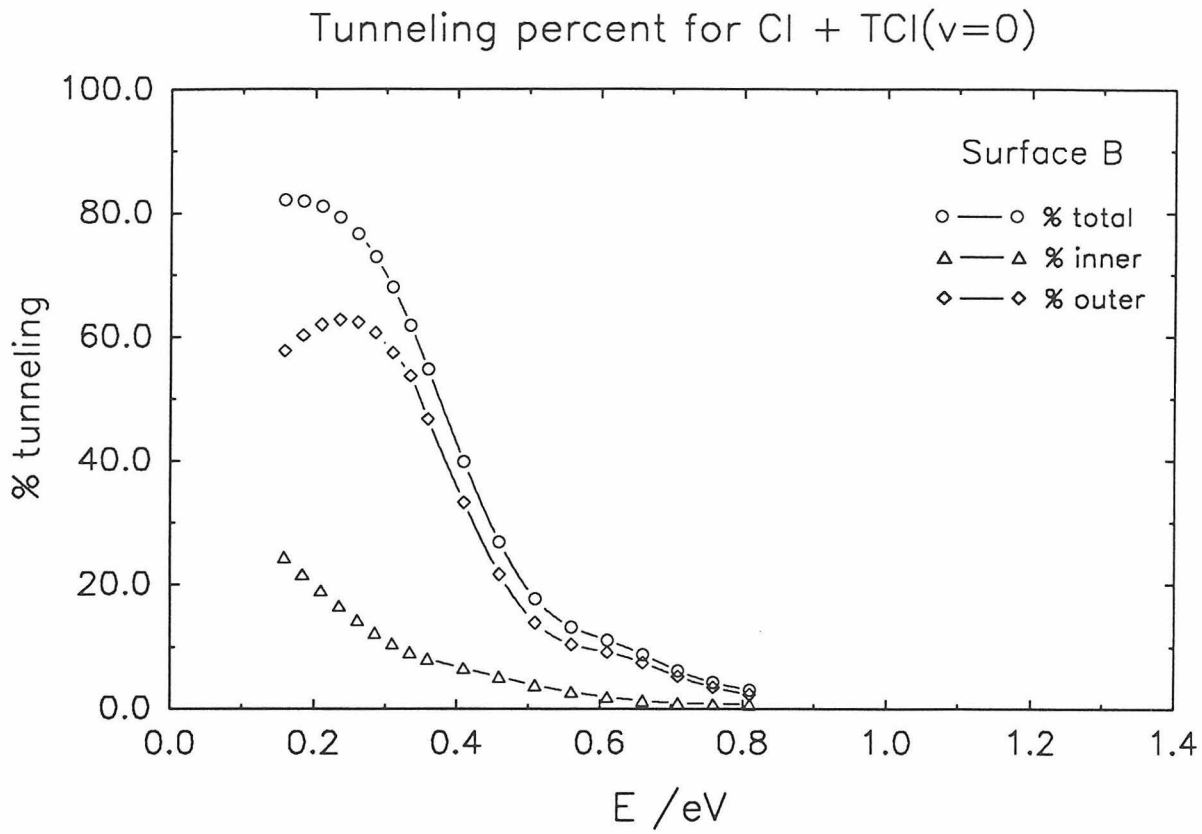
Tunneling percent for Cl + TCl(v=0)
100.0
80.0
60.0
40.0
20.0
0.0
% tunneling
0.0
0.2
0.4
0.6
0.8
1.0
1.2
1.4
E /eV
Surface B
% total
% inner
% outer

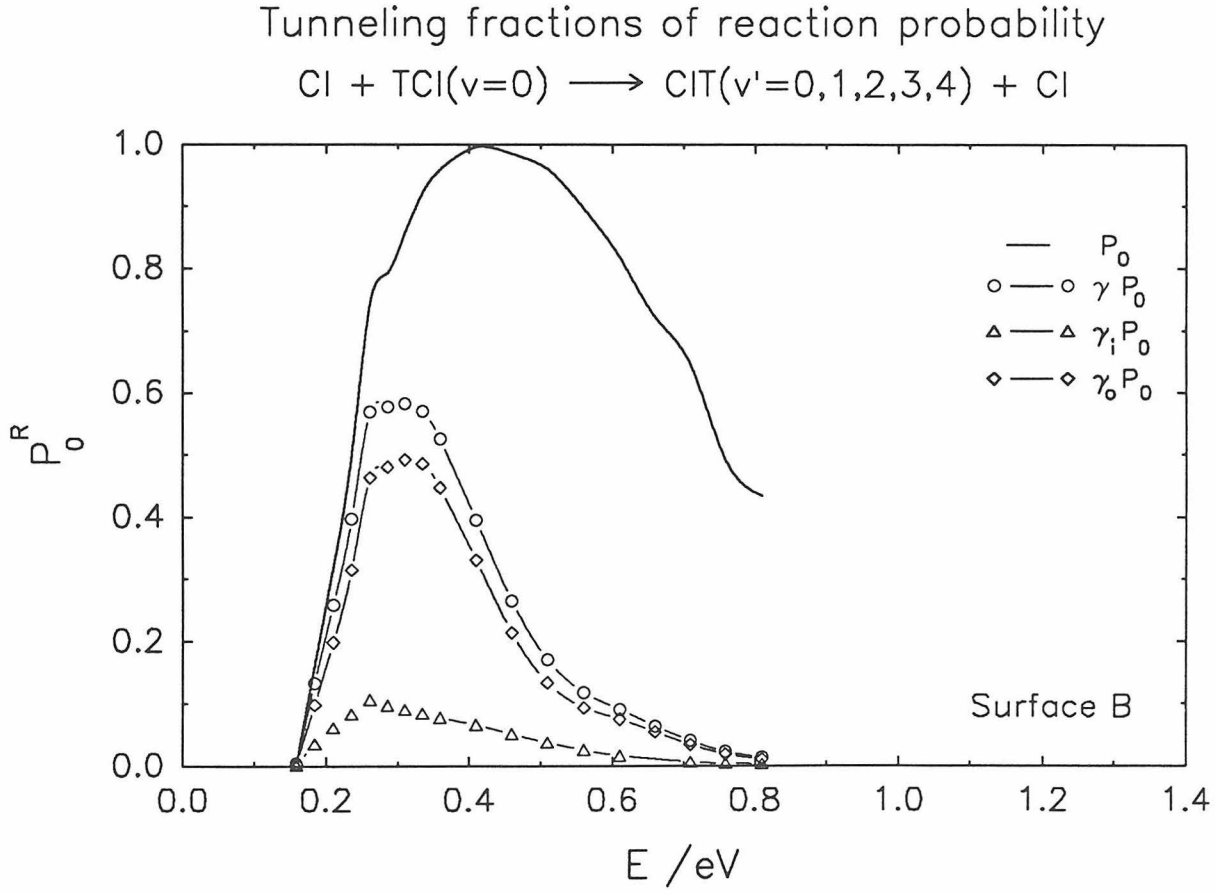
Tunneling fractions of reaction probability
Cl + TCl(v=0) ⟶ ClT(v'=0,1,2,3,4) + Cl
1.0
0.8
0.6
0.4
0.2
0.0
P_0^R
0.0
0.2
0.4
0.6
0.8
1.0
1.2
1.4
E /eV
P_0
γP_0
$\gamma_i P_0$
$\gamma_o P_0$
Surface B

Figure 60

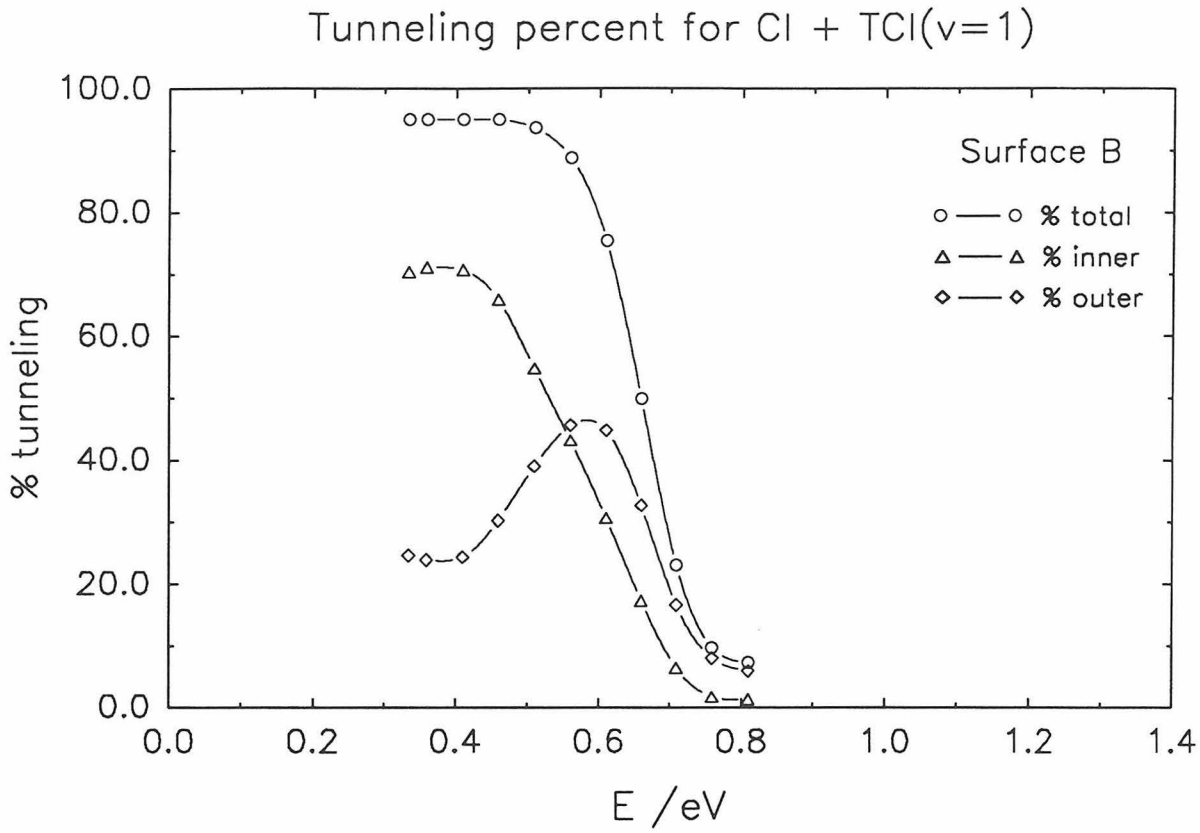
Tunneling percent for Cl + TCl(v=1)
Surface B
% total
% inner
% outer
% tunneling
E /eV
100.0
80.0
60.0
40.0
20.0
0.0
0.0
0.2
0.4
0.6
0.8
1.0
1.2
1.4

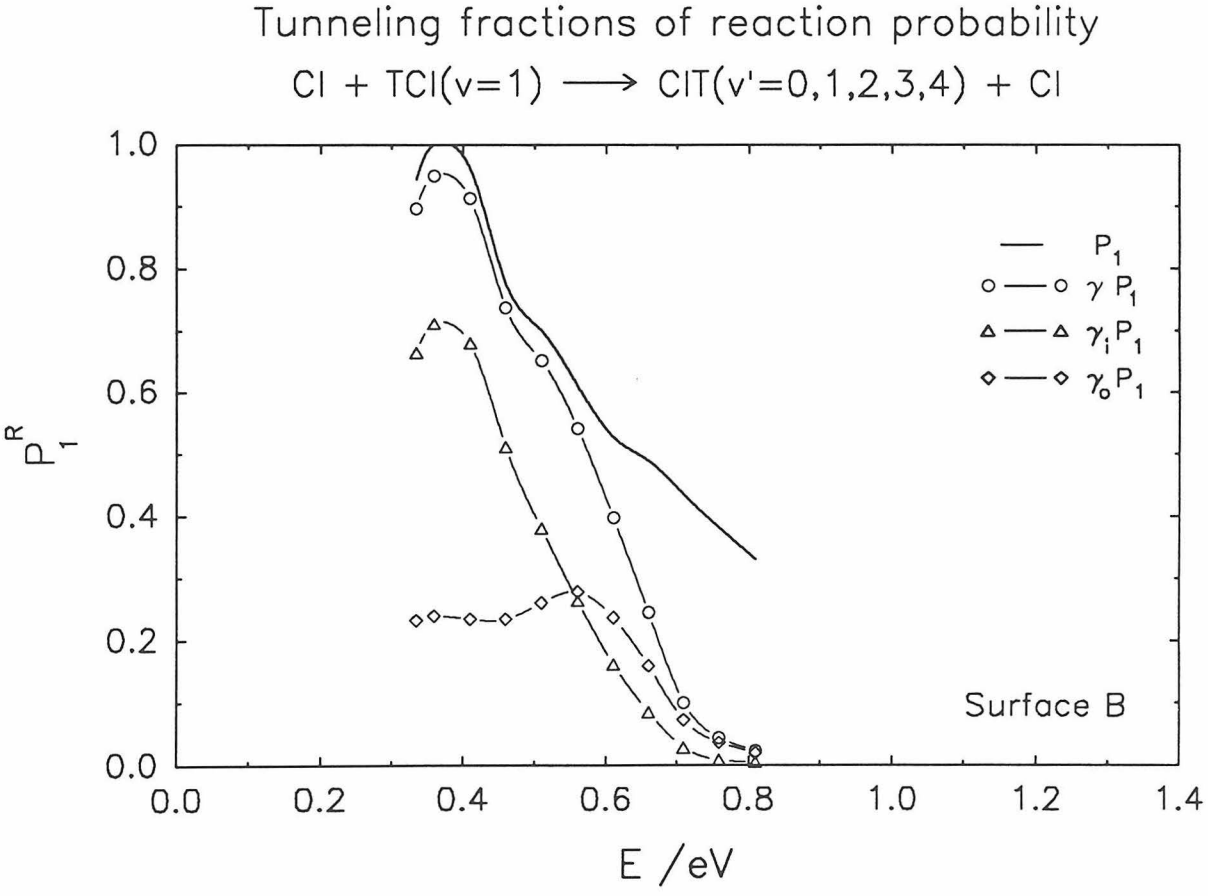
Tunneling fractions of reaction probability
Cl + TCl(v=1) ⟶ ClT(v'=0,1,2,3,4) + Cl
P_1^R
P_1
γP_1
$\gamma_i P_1$
$\gamma_o P_1$
Surface B
E /eV
1.0
0.8
0.6
0.4
0.2
0.0
0.0
0.2
0.4
0.6
0.8
1.0
1.2
1.4

Figure 61

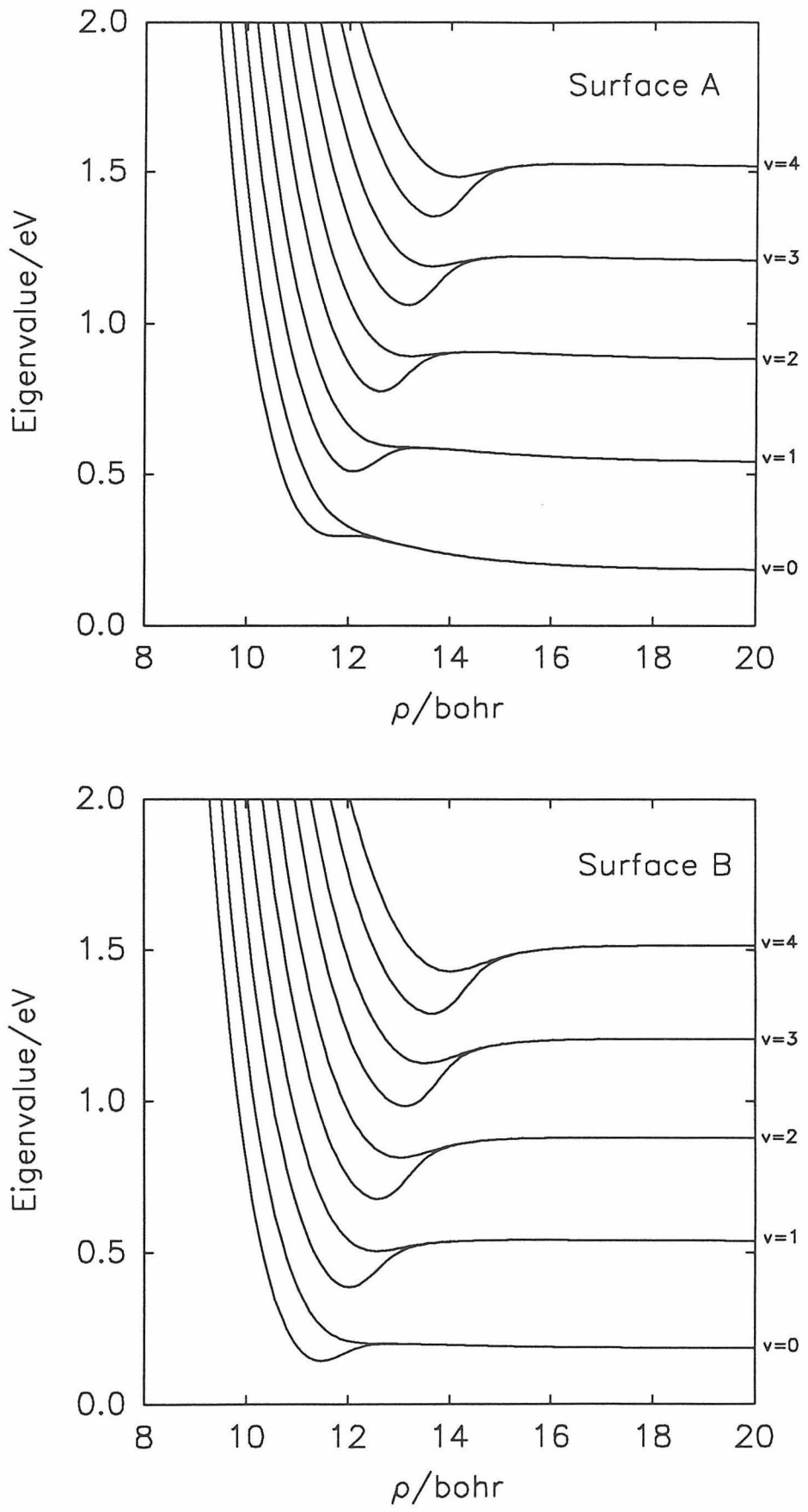
Cl + HCl
Surface A
Surface B
Eigenvalue/eV
ρ/bohr
2.0
1.5
1.0
0.5
0.0
8
10
12
14
16
18
20
v=4
v=3
v=2
v=1
v=0

Figure 62

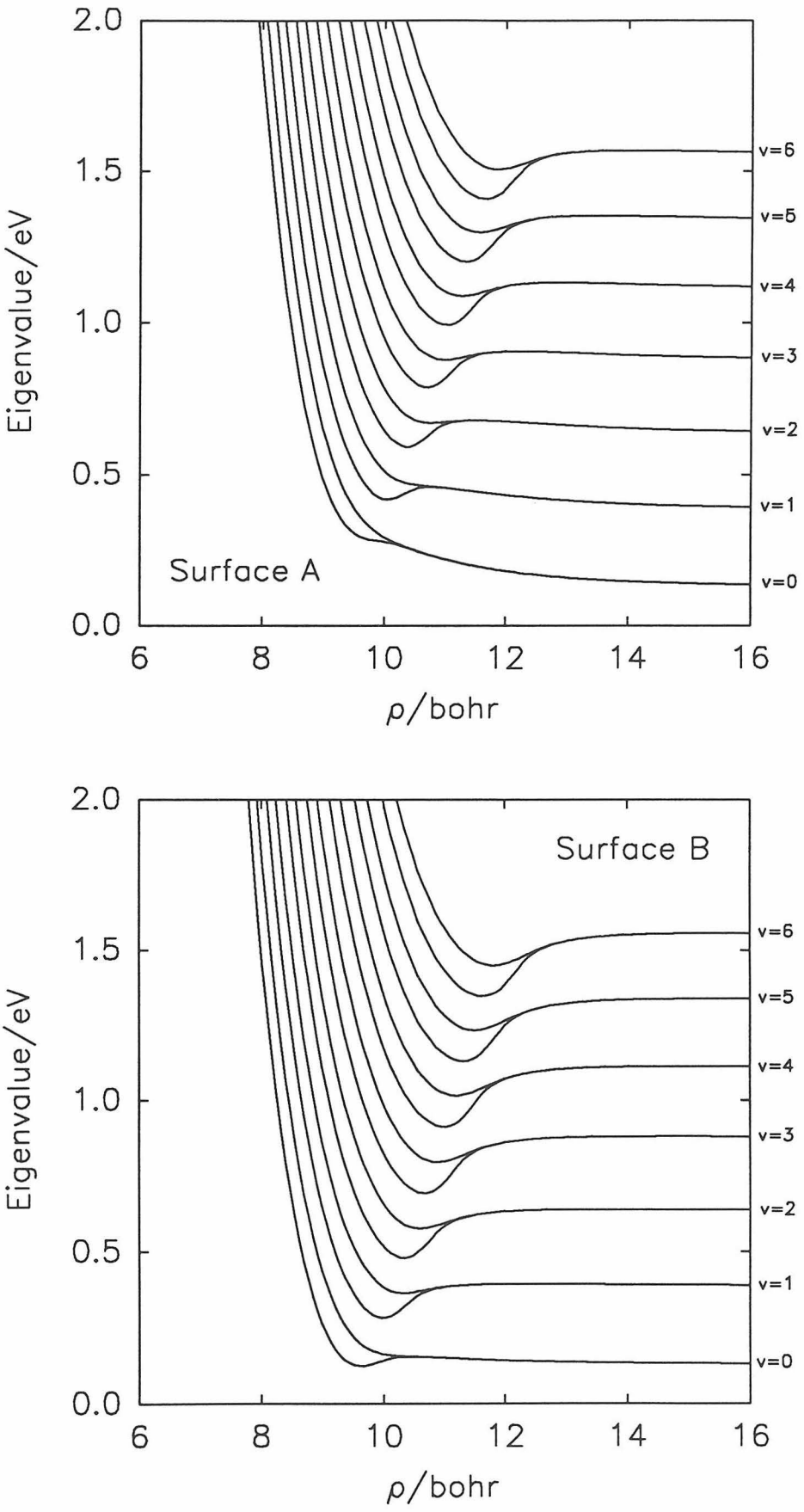
Cl + DCl
2.0
1.5
1.0
0.5
0.0
Eigenvalue/eV
v=6
v=5
v=4
v=3
v=2
v=1
v=0
Surface A
6
8
10
12
14
16
ρ/bohr
Surface B

Figure 63

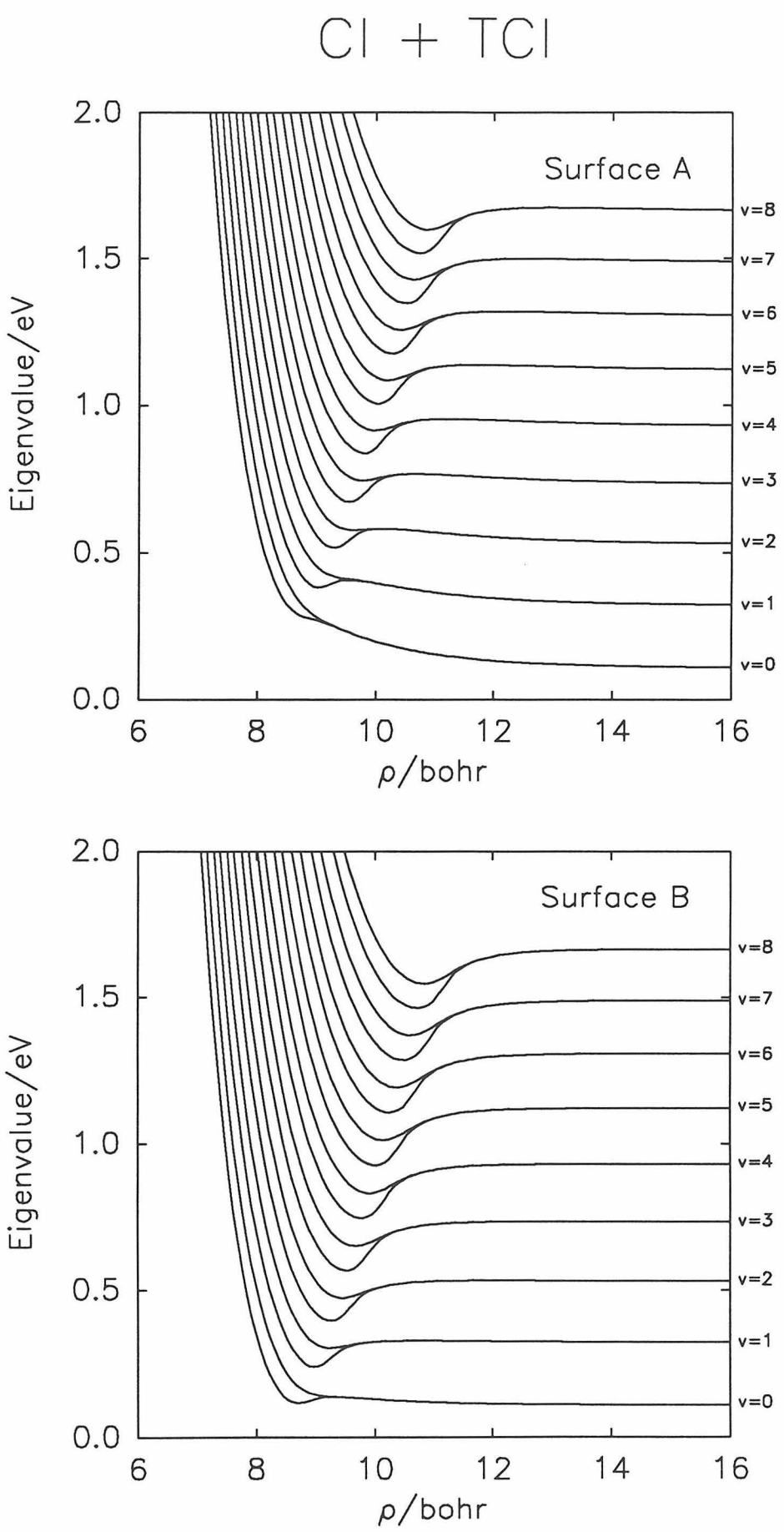
Cl + TCl
Surface A
Surface B
Eigenvalue/eV
ρ/bohr
2.0
1.5
1.0
0.5
0.0
6
8
10
12
14
16
v=8
v=7
v=6
v=5
v=4
v=3
v=2
v=1
v=0

Figure 64

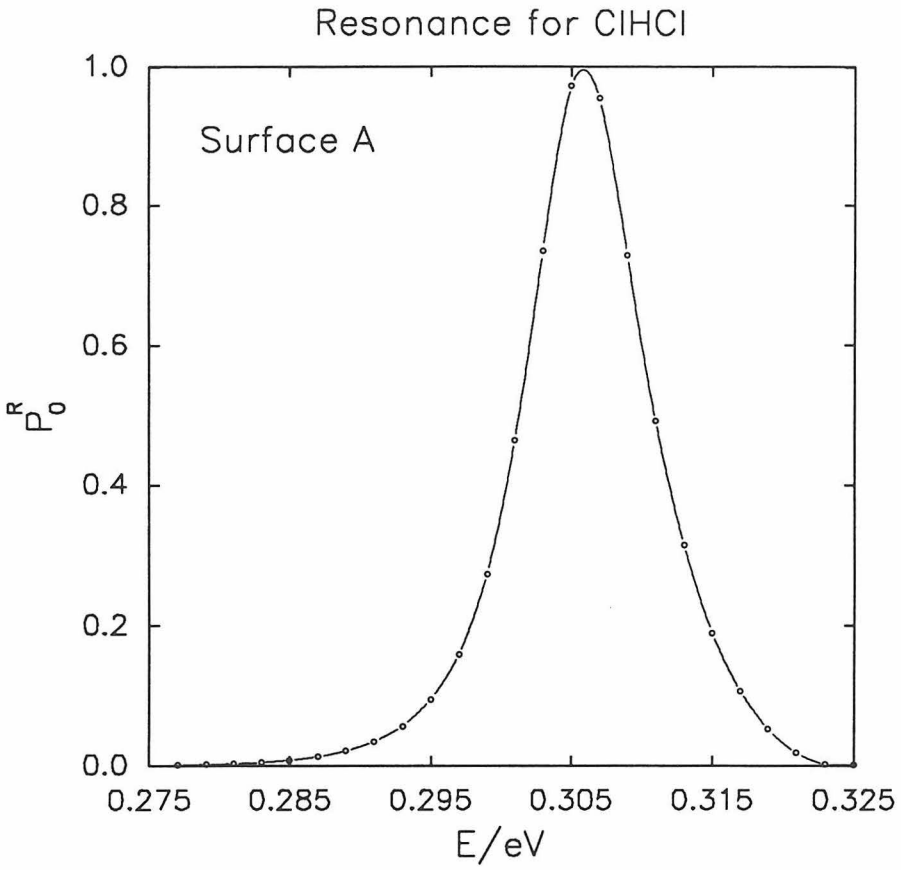
Resonance for ClHCl
Surface A
1.0
0.8
0.6
0.4
0.2
0.0
P_0^R
0.275
0.285
0.295
0.305
0.315
0.325
E/eV

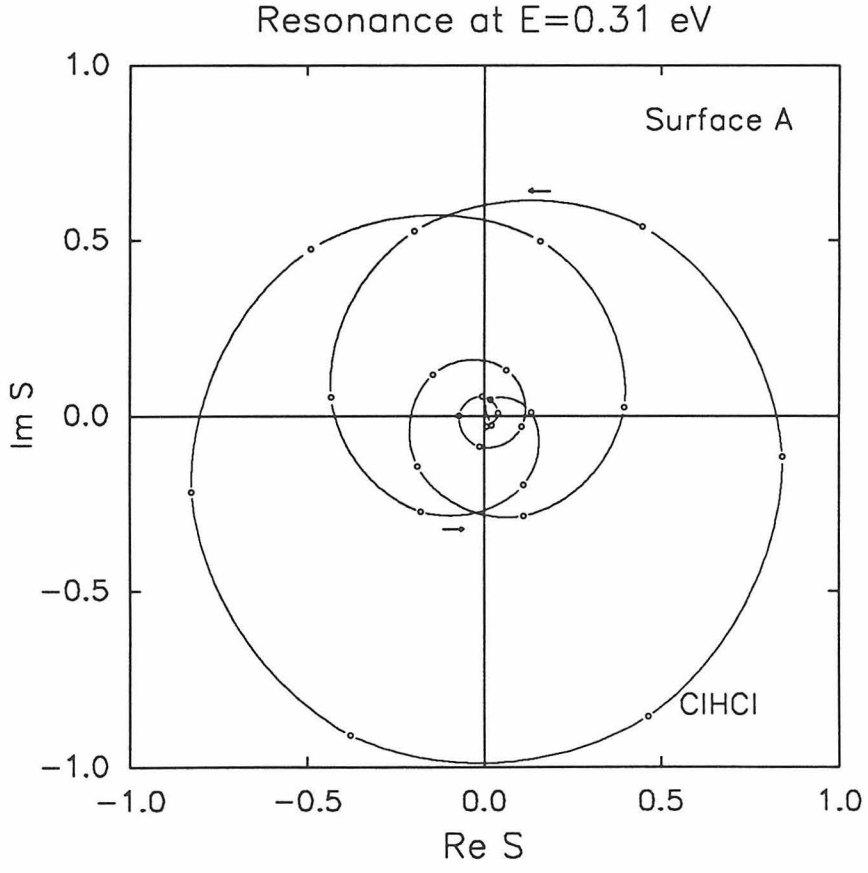
Resonance at E=0.31 eV
Surface A
ClHCl
1.0
0.5
0.0
−0.5
−1.0
Im S
−1.0
−0.5
0.0
0.5
1.0
Re S

Figure 65

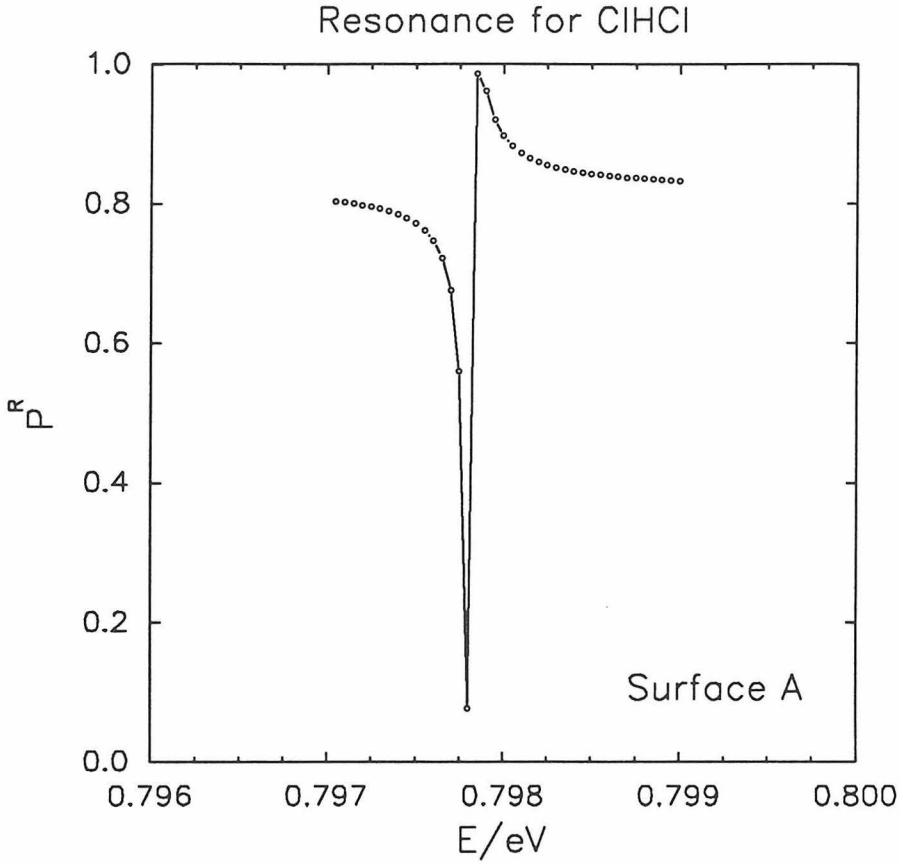
Resonance for ClHCl
1.0
0.8
0.6
0.4
0.2
0.0
P_R
0.796
0.797
0.798
0.799
0.800
E/eV
Surface A

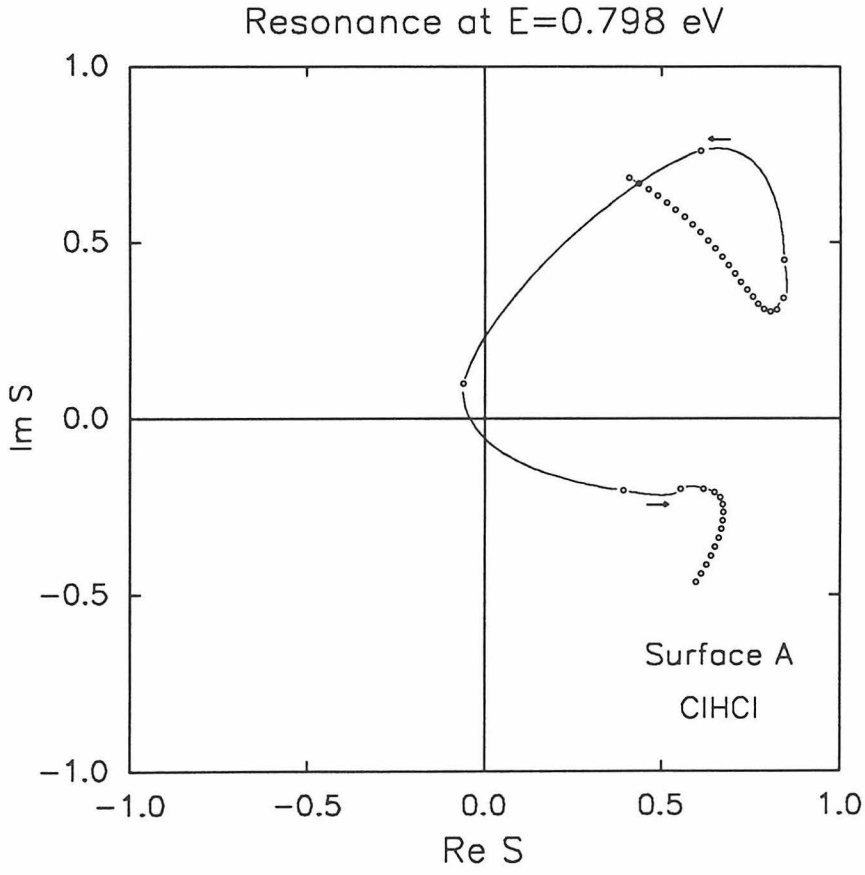
Resonance at E=0.798 eV
1.0
0.5
0.0
−0.5
−1.0
Im S
−1.0
−0.5
0.0
0.5
1.0
Re S
Surface A
ClHCl

Figure 66

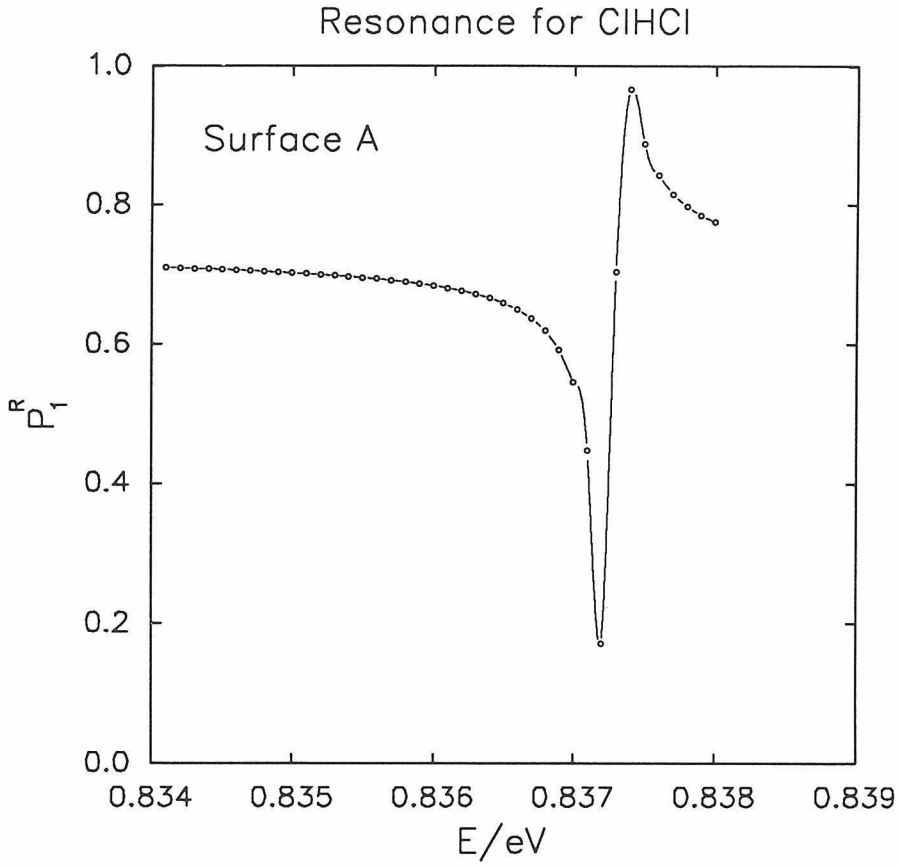
Resonance for ClHCl
Surface A
1.0
0.8
0.6
0.4
0.2
0.0
P_1^R
0.834
0.835
0.836
0.837
0.838
0.839
E/eV

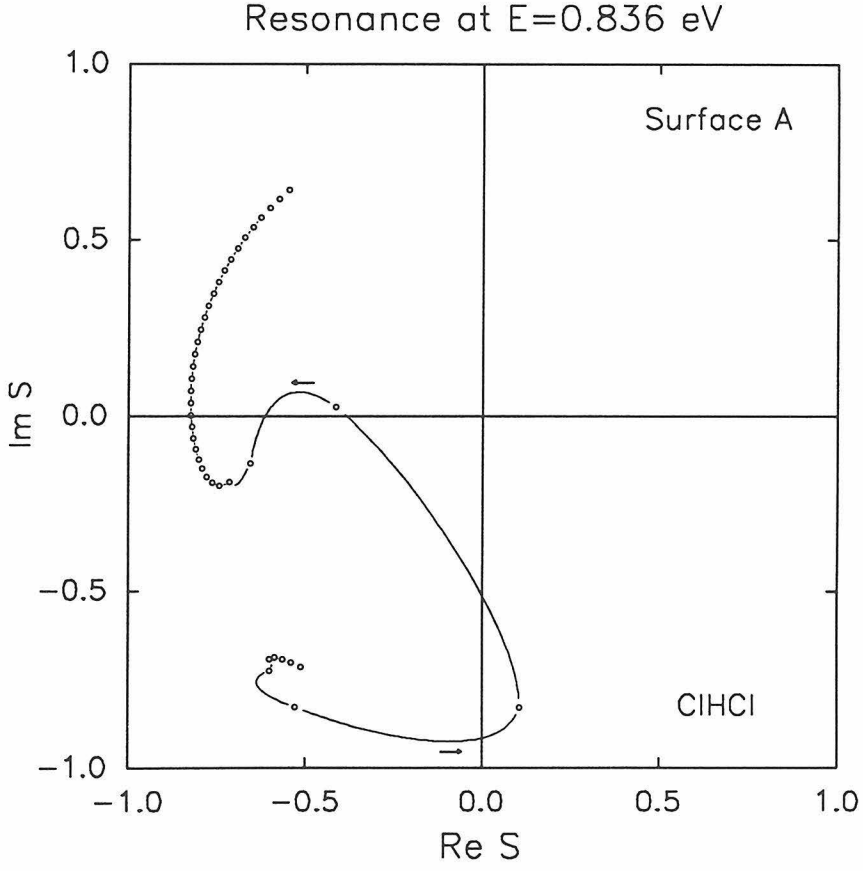
Resonance at E=0.836 eV
Surface A
ClHCl
1.0
0.5
0.0
−0.5
−1.0
Im S
−1.0
−0.5
0.0
0.5
1.0
Re S

Figure 67

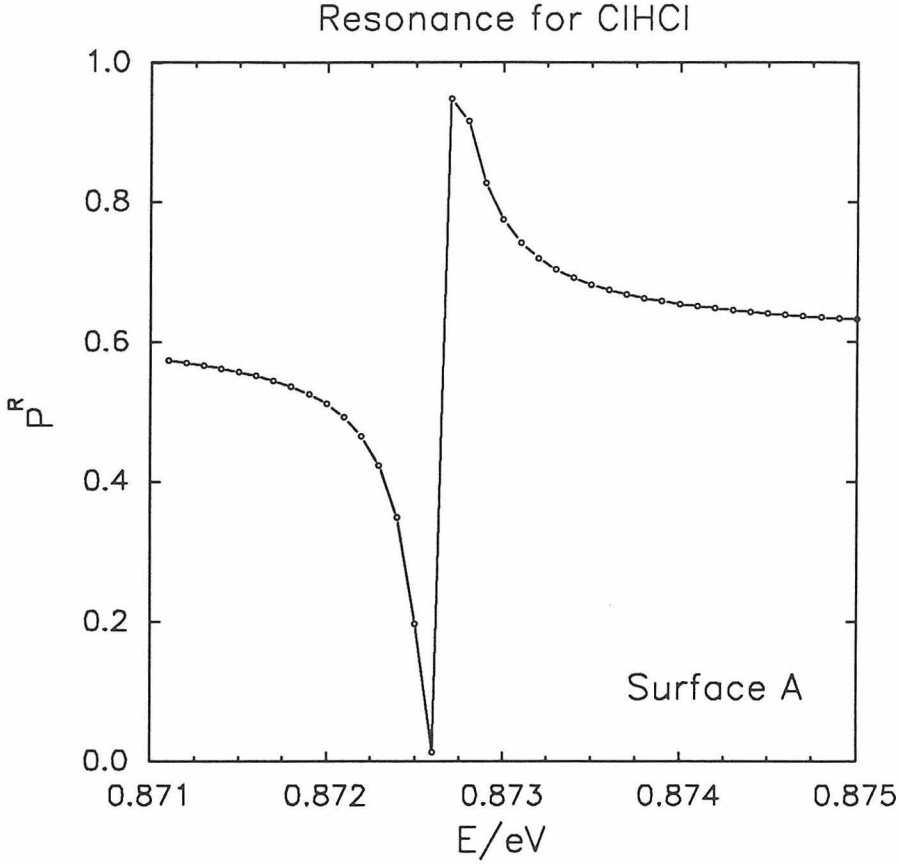
Resonance for ClHCl
1.0
0.8
0.6
0.4
0.2
0.0
P_R
0.871
0.872
0.873
0.874
0.875
E/eV
Surface A

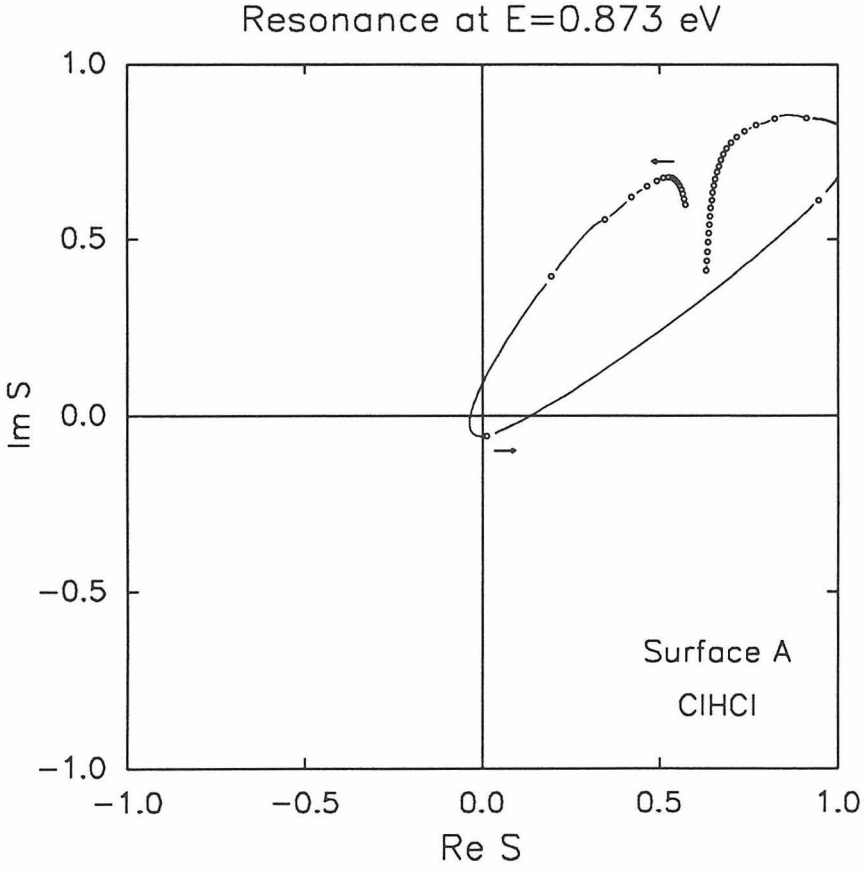
Resonance at E=0.873 eV
1.0
0.5
0.0
−0.5
−1.0
Im S
−1.0
−0.5
0.0
0.5
1.0
Re S
Surface A
ClHCl

Figure 68

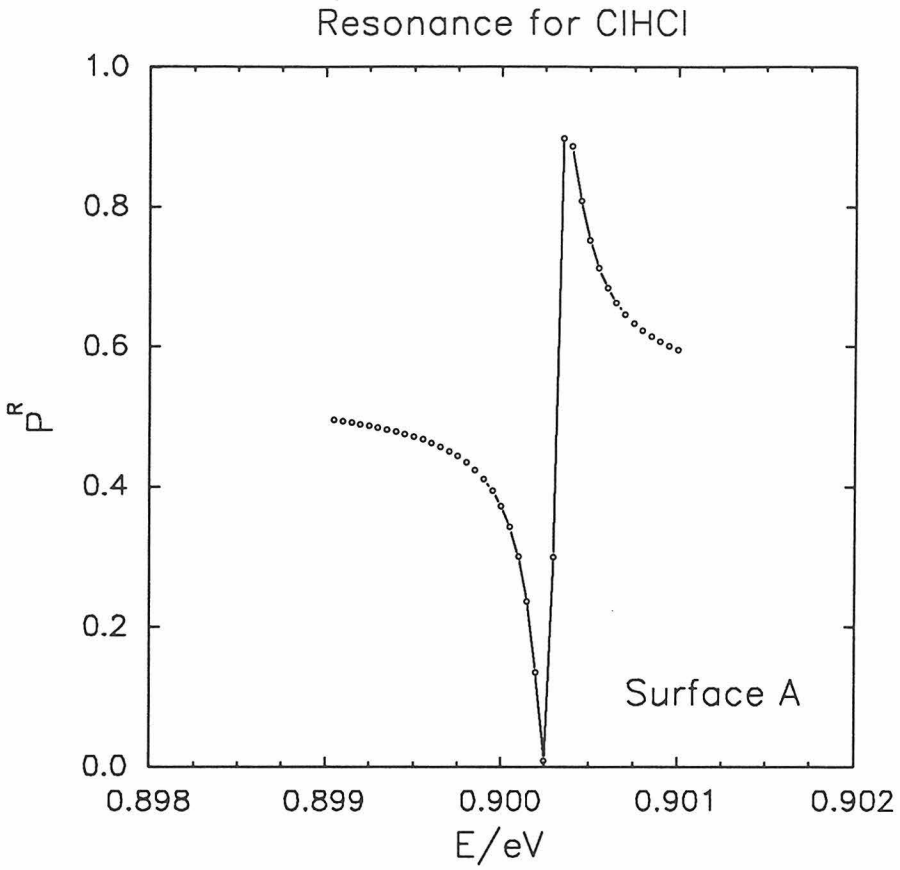
Resonance for ClHCl
1.0
0.8
0.6
0.4
0.2
0.0
P_R
Surface A
0.898
0.899
0.900
0.901
0.902
E/eV

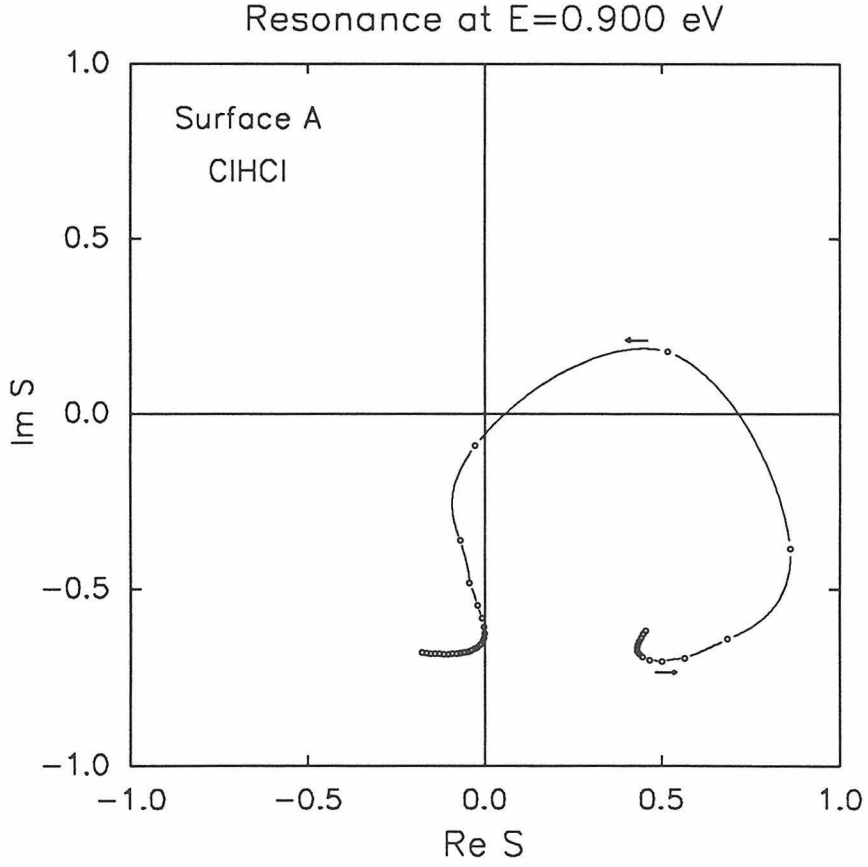
Resonance at E=0.900 eV
Surface A
ClHCl
1.0
0.5
0.0
−0.5
−1.0
Im S
−1.0
−0.5
0.0
0.5
1.0
Re S

Figure 69

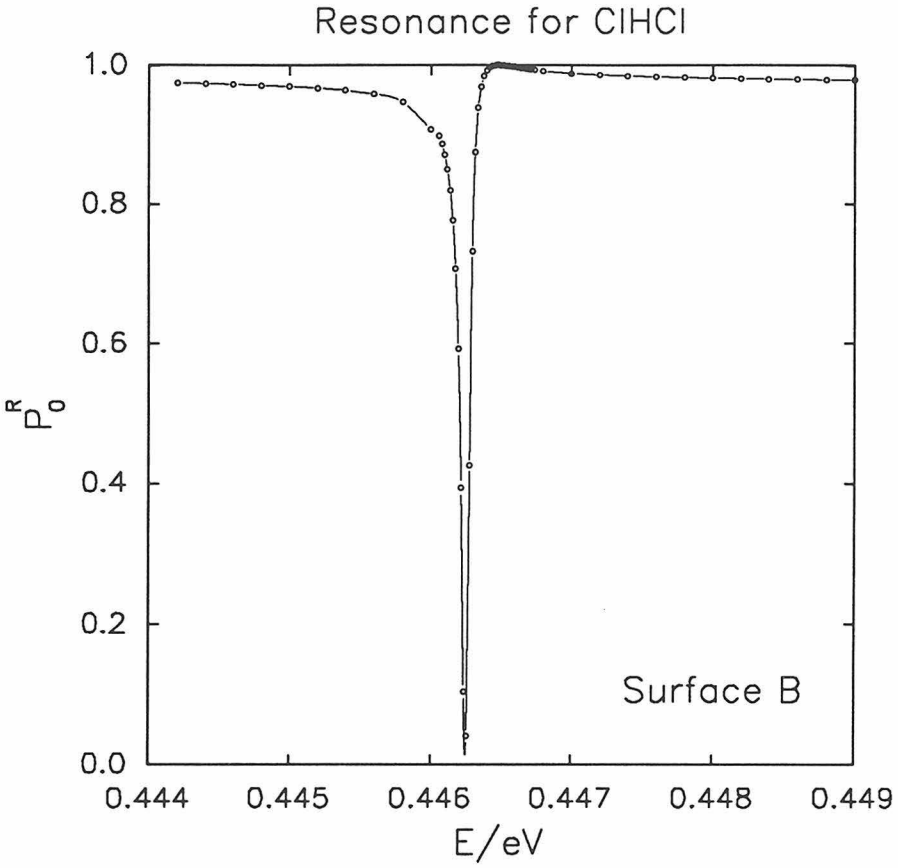
Resonance for ClHCl
1.0
0.8
0.6
0.4
0.2
0.0
P_0^R
Surface B
0.444
0.445
0.446
0.447
0.448
0.449
E/eV

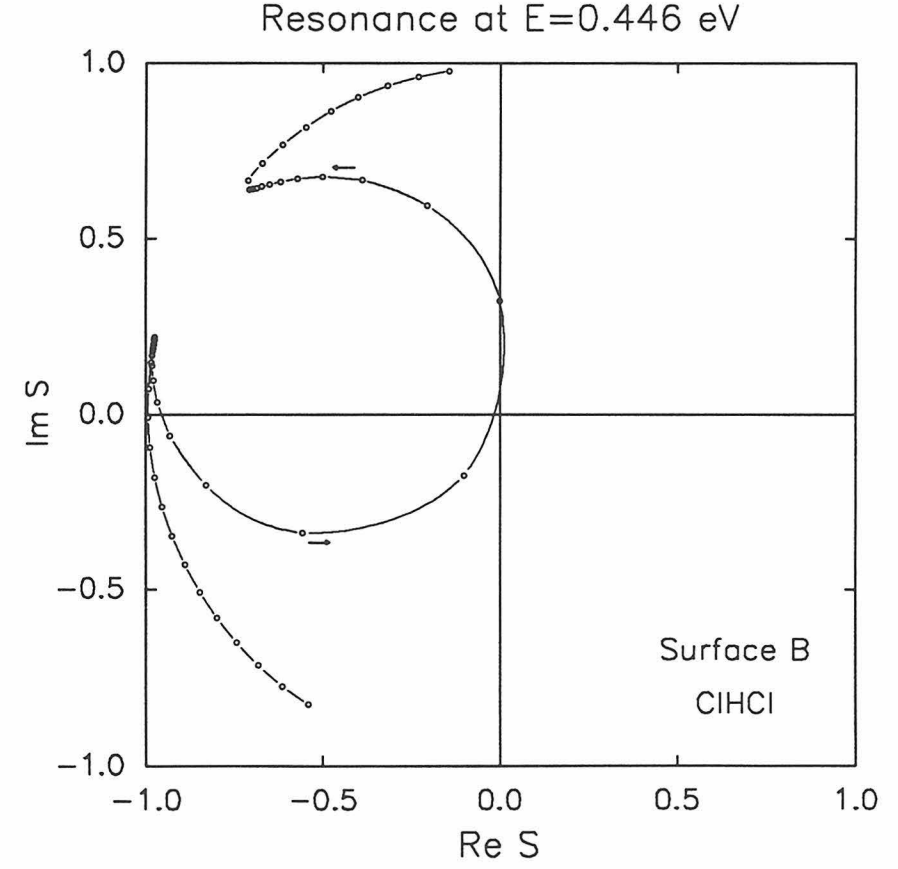
Resonance at E=0.446 eV
1.0
0.5
0.0
−0.5
−1.0
Im S
Surface B
ClHCl
−1.0
−0.5
0.0
0.5
1.0
Re S

Figure 70

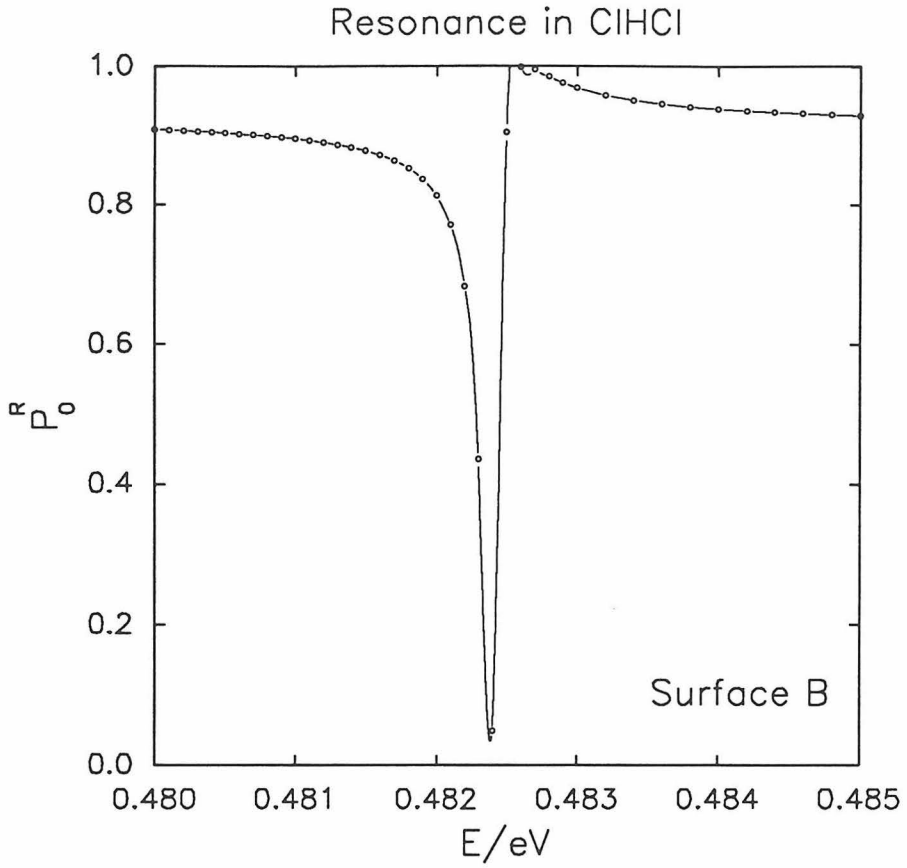
Resonance in ClHCl
1.0
0.8
0.6
0.4
0.2
0.0
P_0^R
Surface B
0.480
0.481
0.482
0.483
0.484
0.485
E/eV

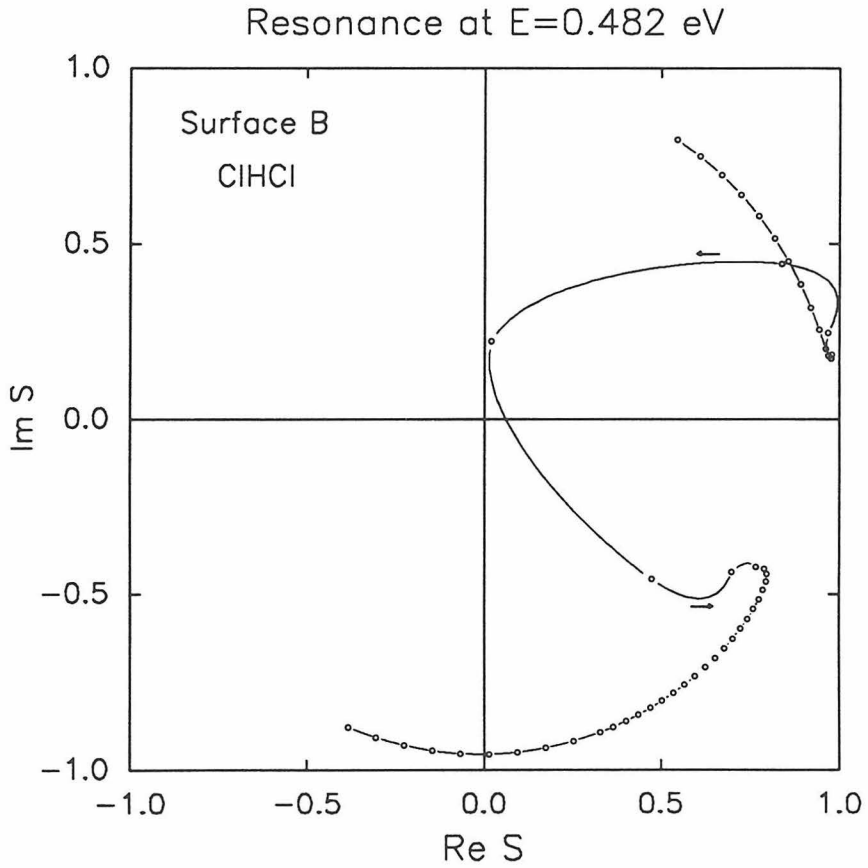
Resonance at E=0.482 eV
Surface B
ClHCl
1.0
0.5
0.0
−0.5
−1.0
Im S
−1.0
−0.5
0.0
0.5
1.0
Re S

Figure 71

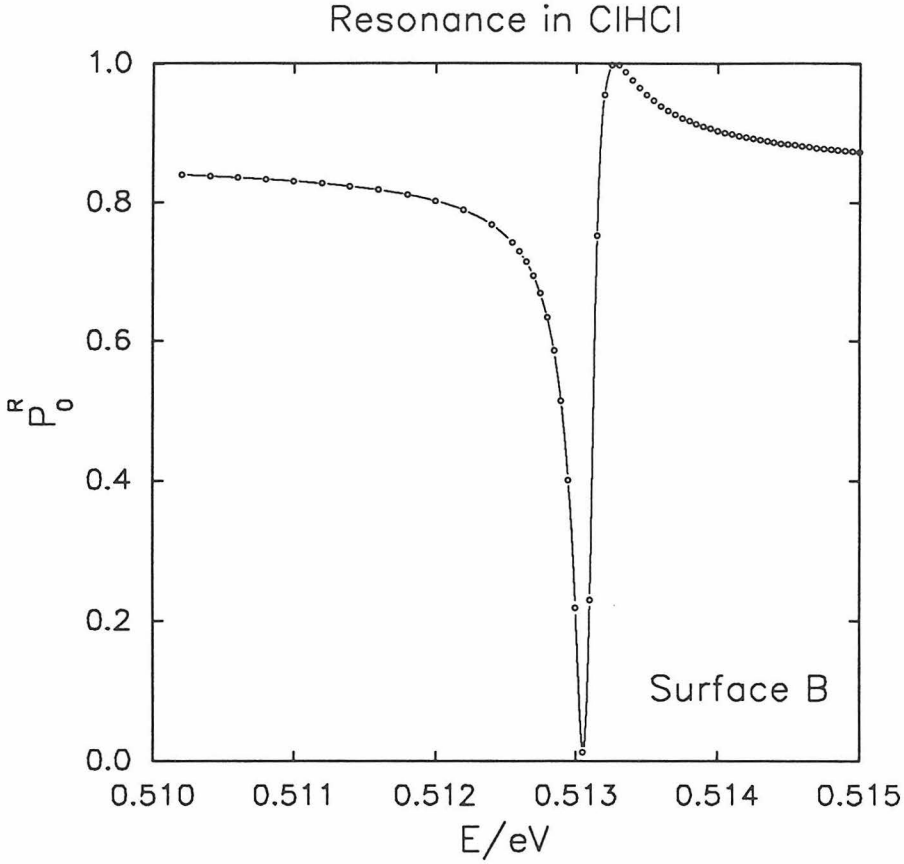
Resonance in ClHCl
1.0
0.8
0.6
0.4
0.2
0.0
P_0^R
Surface B
0.510
0.511
0.512
0.513
0.514
0.515
E/eV

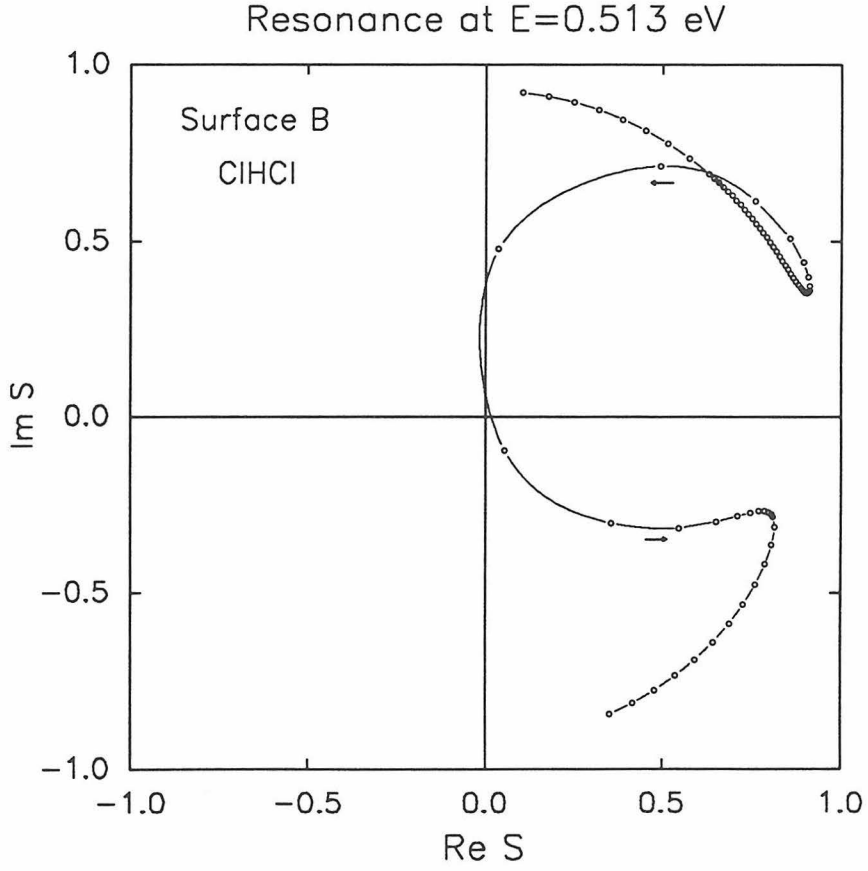
Resonance at E=0.513 eV
Surface B
ClHCl
1.0
0.5
0.0
−0.5
−1.0
Im S
−1.0
−0.5
0.0
0.5
1.0
Re S

Figure 72

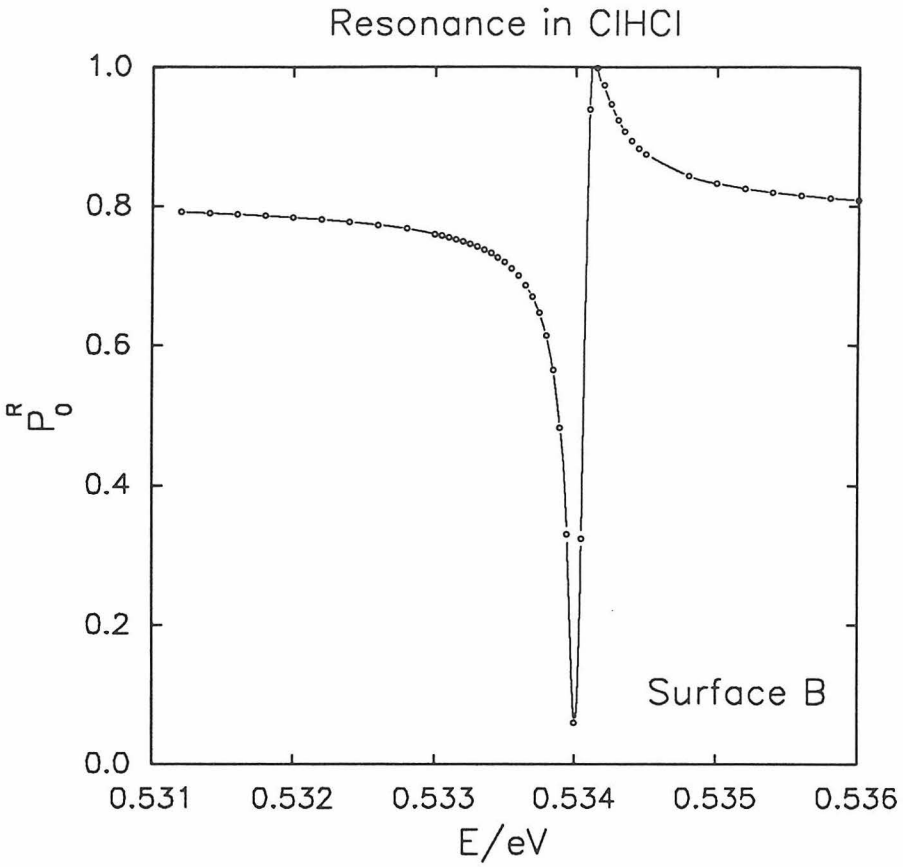
Resonance in ClHCl
1.0
0.8
0.6
0.4
0.2
0.0
P_0^R
0.531
0.532
0.533
0.534
0.535
0.536
E/eV
Surface B

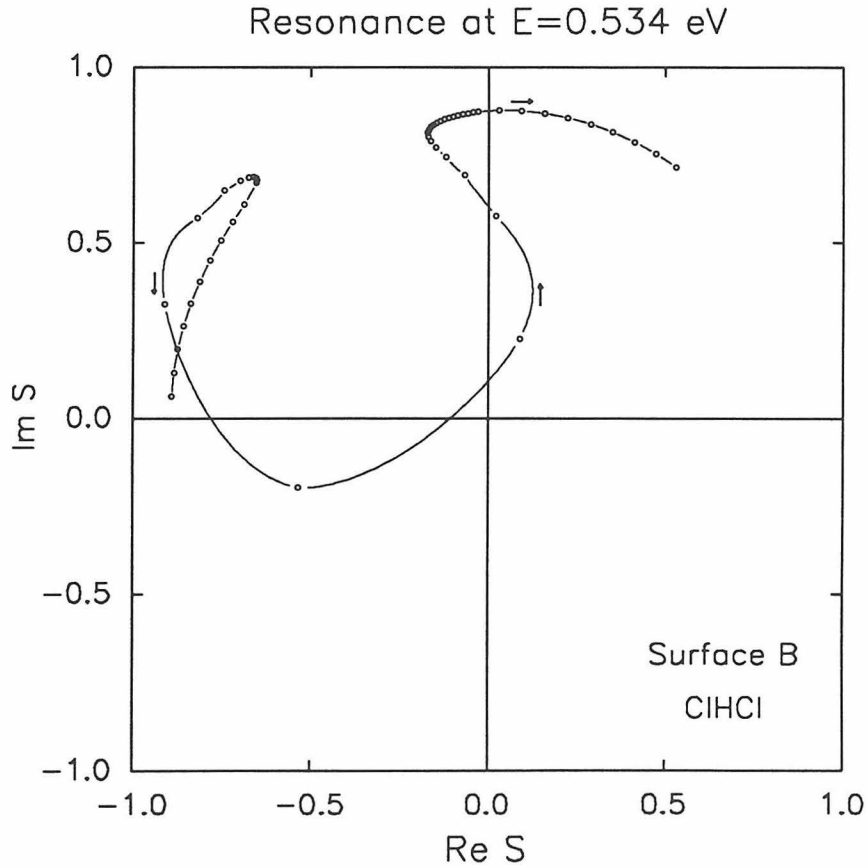
Resonance at E=0.534 eV
1.0
0.5
0.0
−0.5
−1.0
Im S
−1.0
−0.5
0.0
0.5
1.0
Re S
Surface B
ClHCl

Figure 73

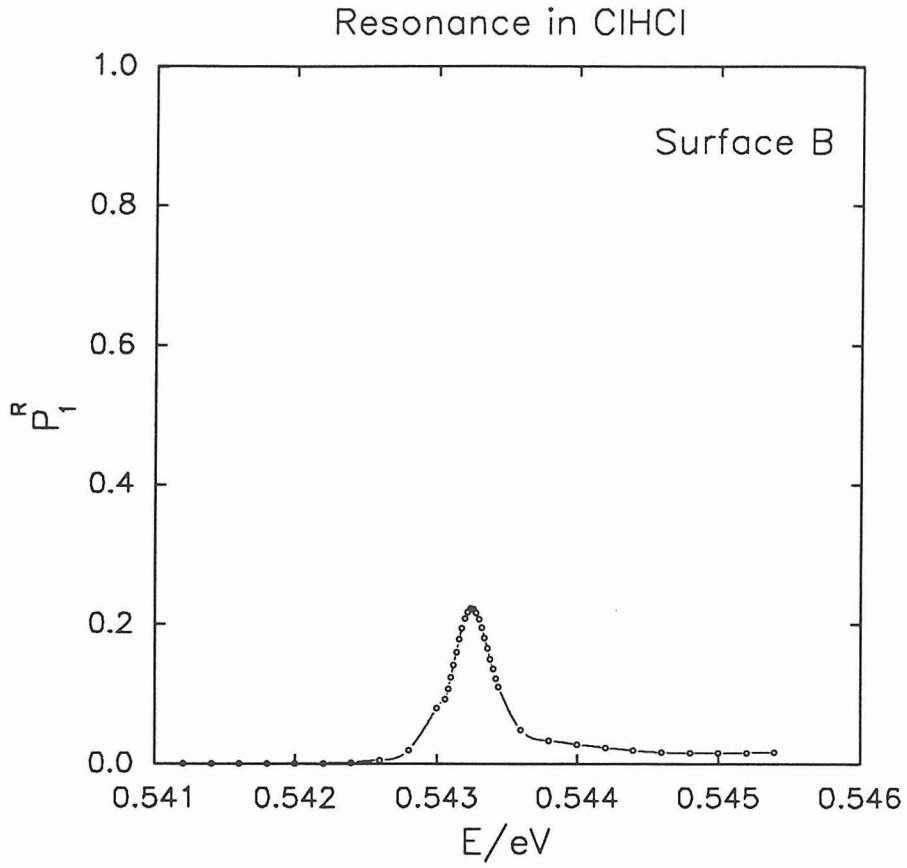
Resonance in ClHCl
Surface B
1.0
0.8
0.6
0.4
0.2
0.0
P_1^R
0.541
0.542
0.543
0.544
0.545
0.546
E/eV

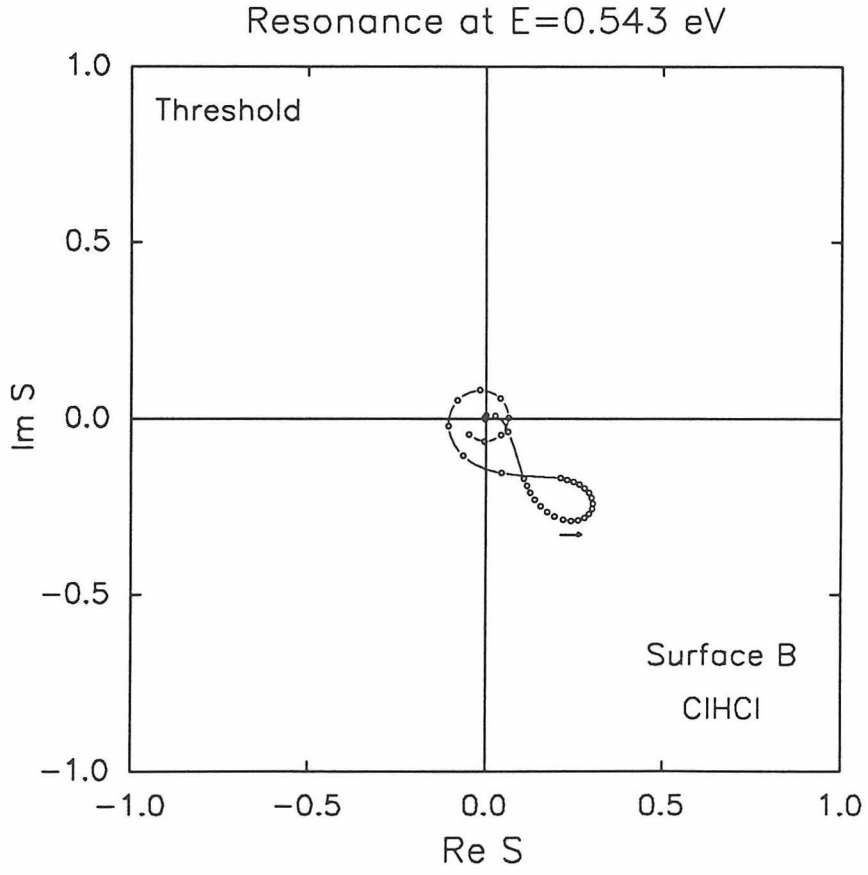
Resonance at E=0.543 eV
Threshold
1.0
0.5
0.0
−0.5
−1.0
Im S
Surface B
ClHCl
−1.0
−0.5
0.0
0.5
1.0
Re S

Figure 74

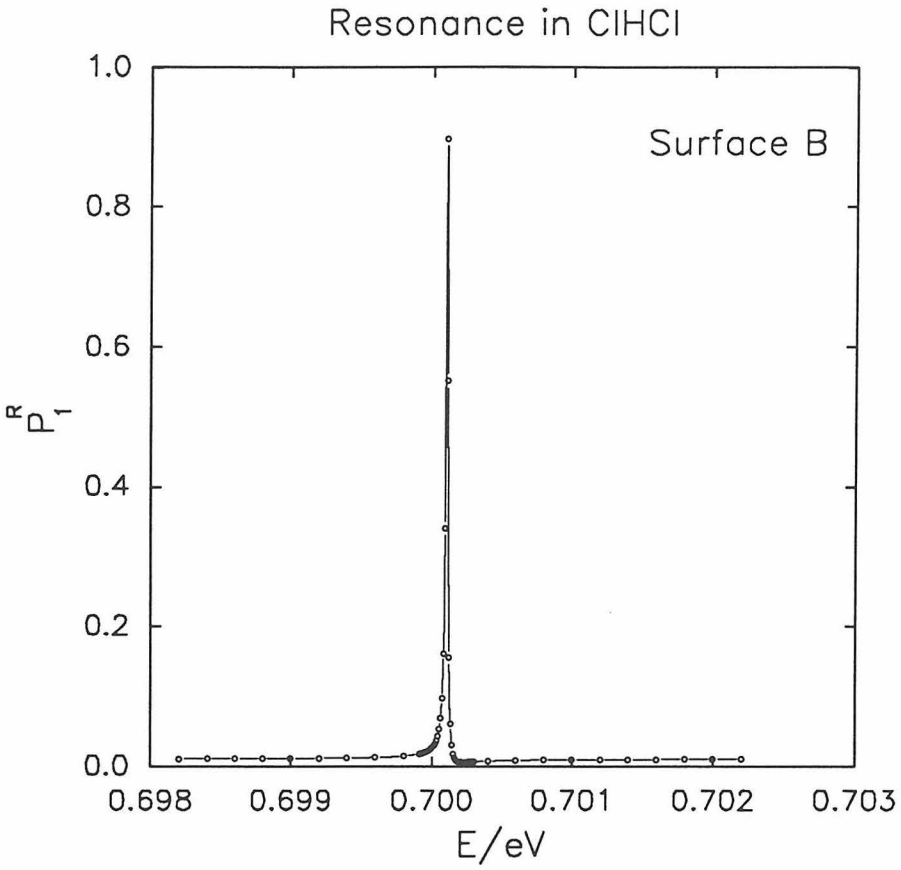
Resonance in ClHCl
Surface B
1.0
0.8
0.6
0.4
0.2
0.0
P_1^R
0.698
0.699
0.700
0.701
0.702
0.703
E/eV

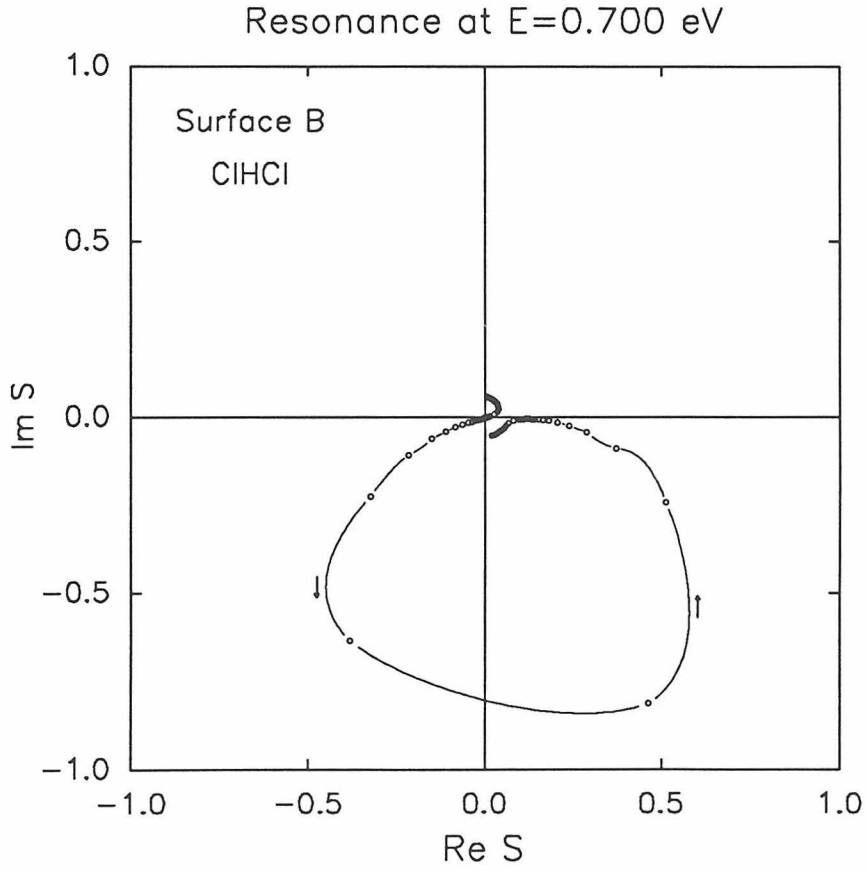
Resonance at E=0.700 eV
Surface B
ClHCl
1.0
0.5
0.0
−0.5
−1.0
Im S
−1.0
−0.5
0.0
0.5
1.0
Re S

Figure 75

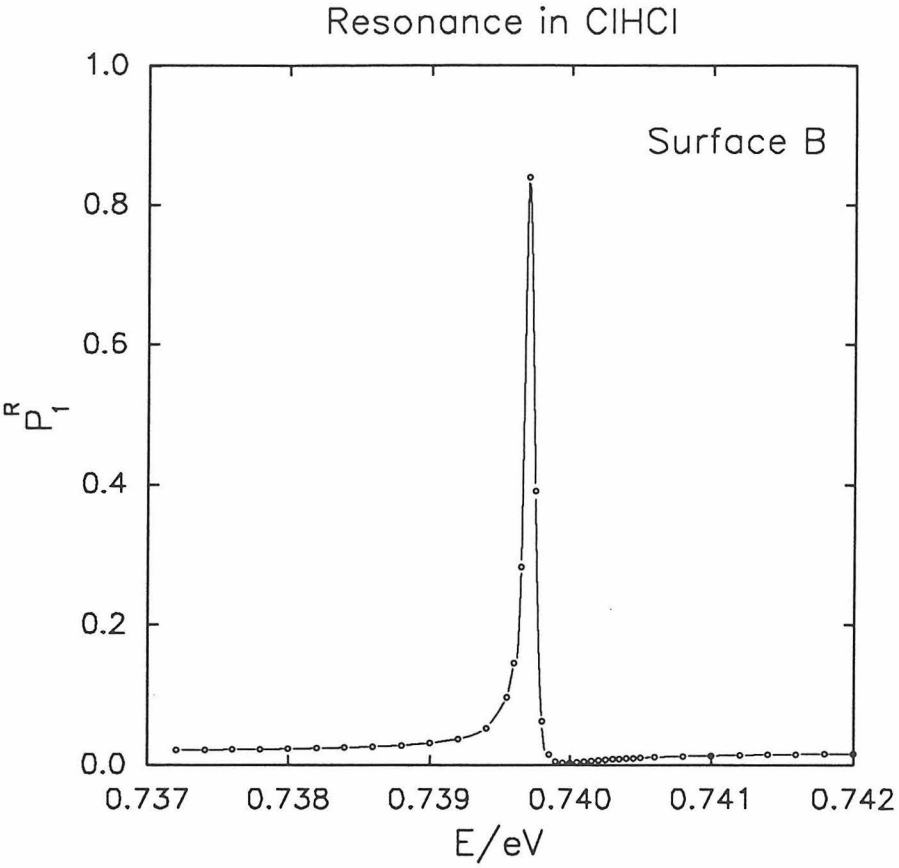
Resonance in ClHCl
Surface B
1.0
0.8
0.6
0.4
0.2
0.0
P_1^R
0.737
0.738
0.739
0.740
0.741
0.742
E/eV

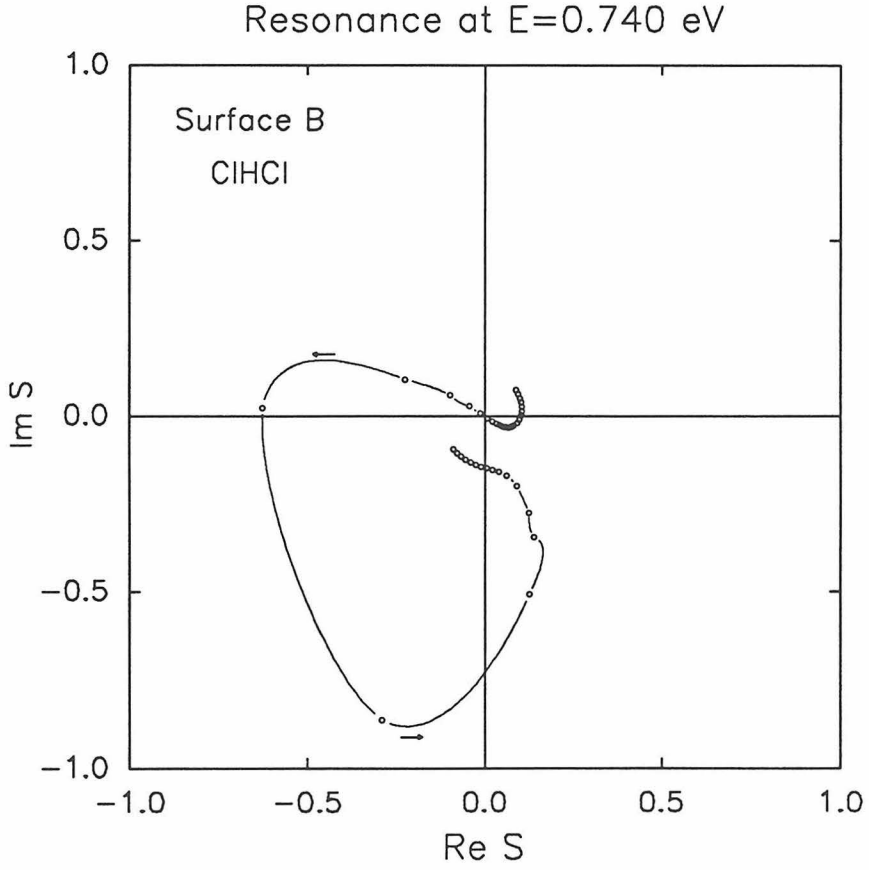
Resonance at E=0.740 eV
Surface B
ClHCl
1.0
0.5
0.0
−0.5
−1.0
Im S
−1.0
−0.5
0.0
0.5
1.0
Re S

Figure 76

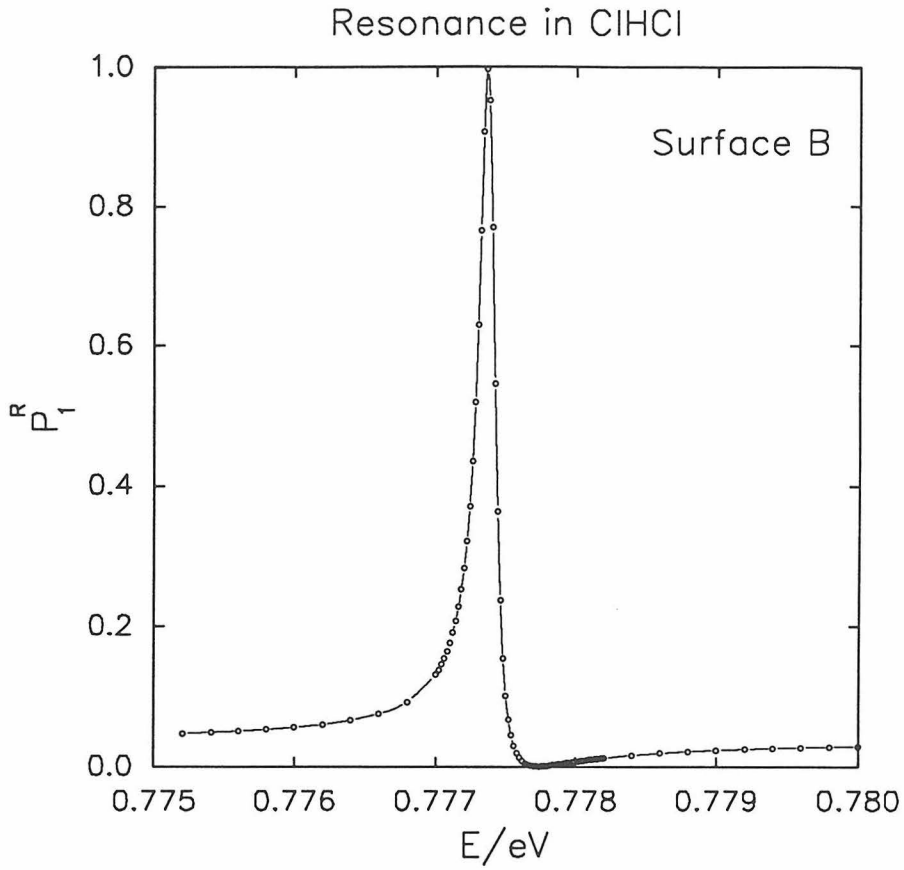
Resonance in ClHCl
Surface B
1.0
0.8
0.6
0.4
0.2
0.0
P_1^R
0.775
0.776
0.777
0.778
0.779
0.780
E/eV

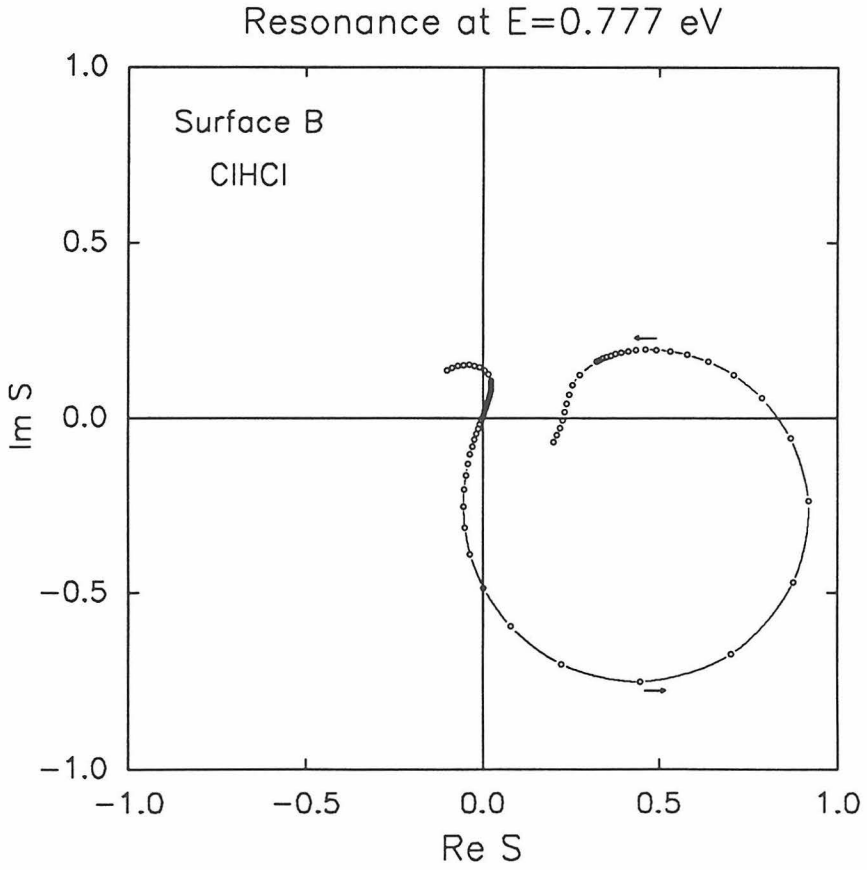
Resonance at E=0.777 eV
Surface B
ClHCl
1.0
0.5
0.0
−0.5
−1.0
Im S
−1.0
−0.5
0.0
0.5
1.0
Re S

Figure 77

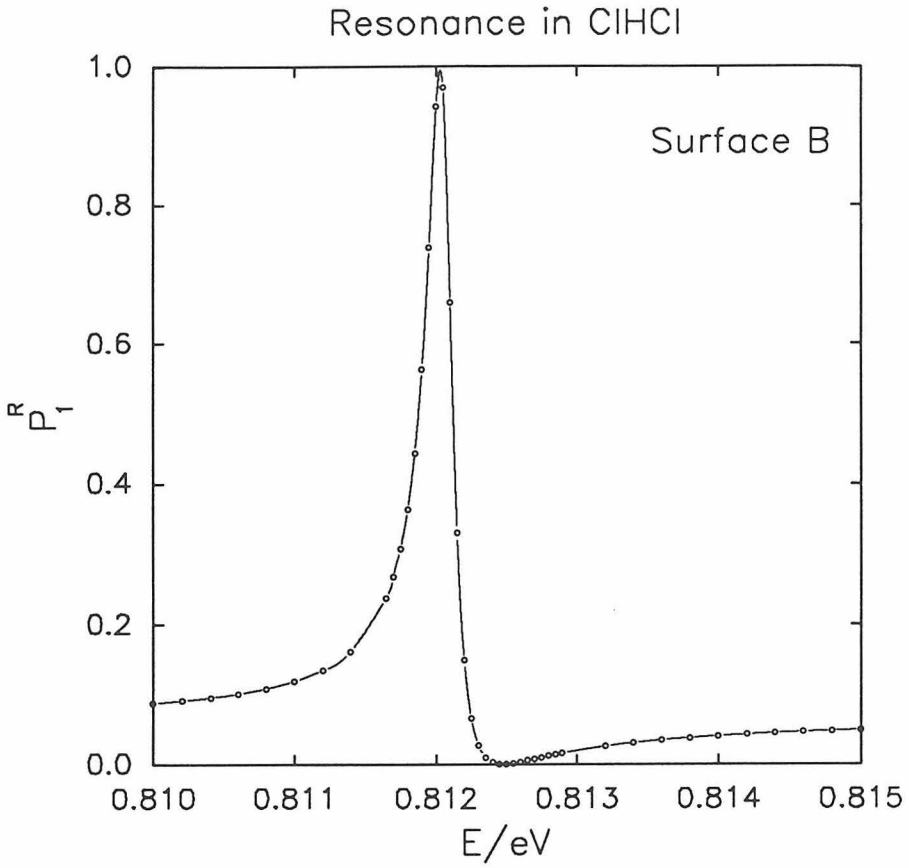
Resonance in ClHCl
Surface B
1.0
0.8
0.6
0.4
0.2
0.0
P_1^R
0.810
0.811
0.812
0.813
0.814
0.815
E/eV

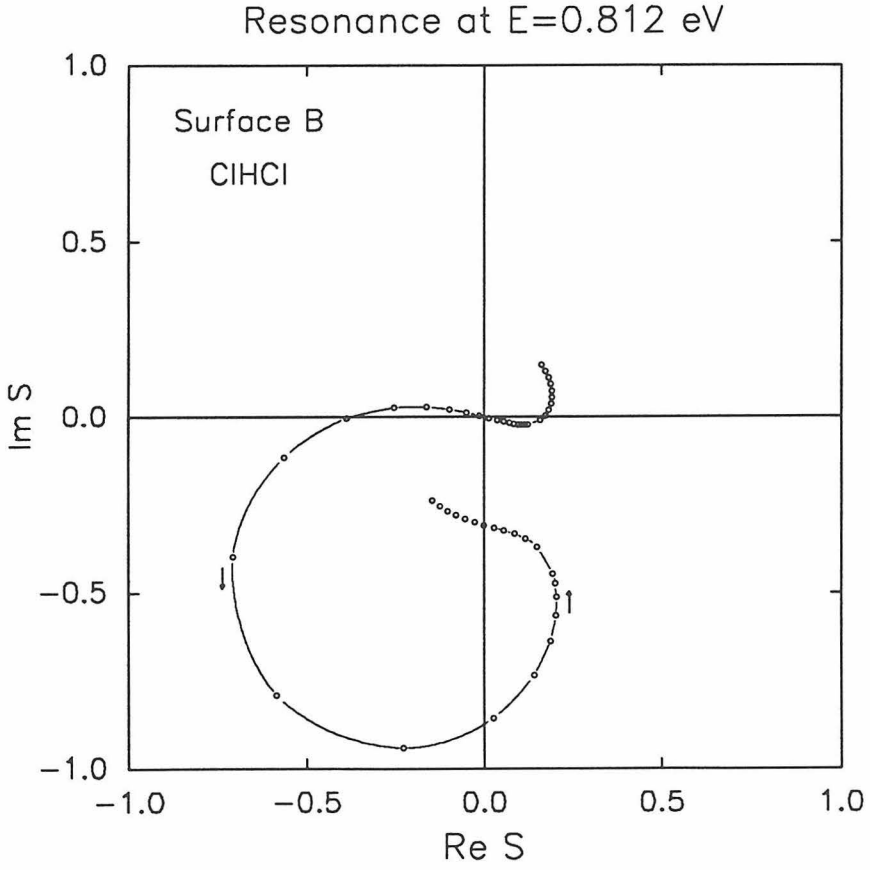
Resonance at E=0.812 eV
Surface B
ClHCl
1.0
0.5
0.0
−0.5
−1.0
Im S
−1.0
−0.5
0.0
0.5
1.0
Re S

Figure 78

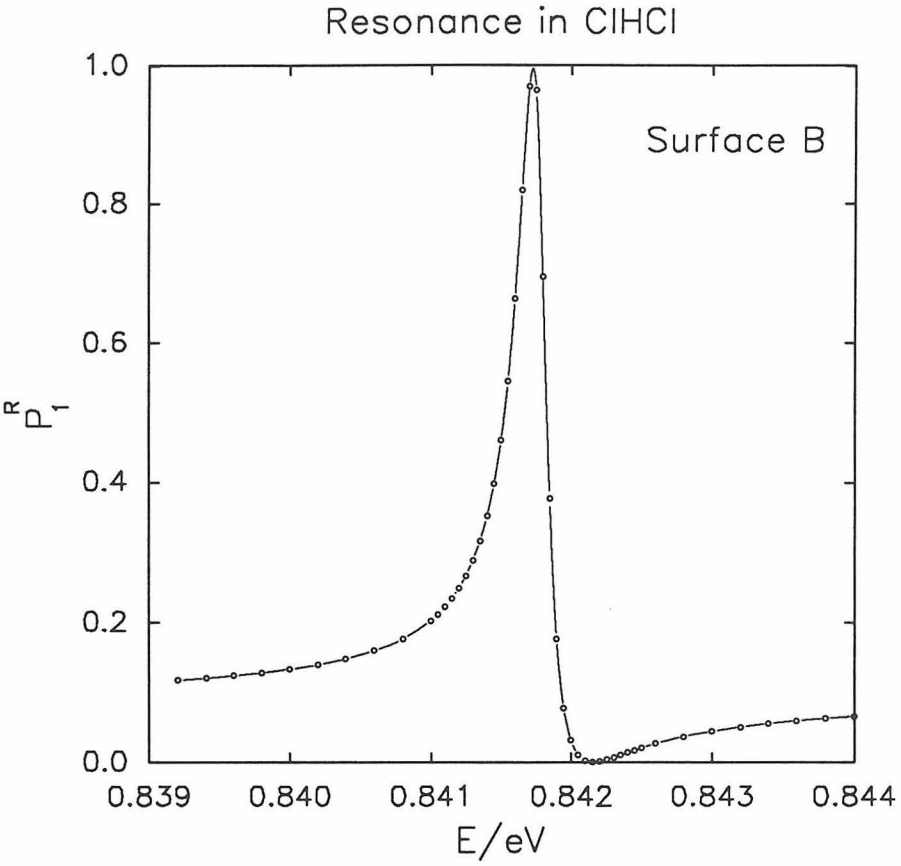
Resonance in ClHCl
Surface B
1.0
0.8
0.6
0.4
0.2
0.0
P_1^R
0.839
0.840
0.841
0.842
0.843
0.844
E/eV

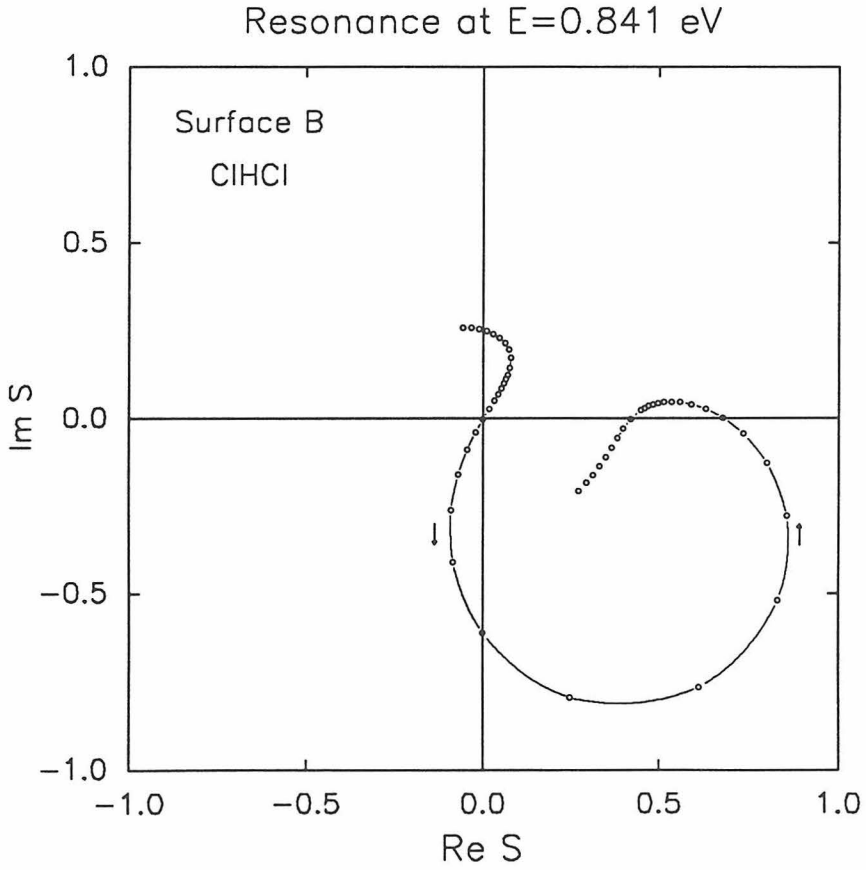
Resonance at E=0.841 eV
Surface B
ClHCl
1.0
0.5
0.0
−0.5
−1.0
Im S
−1.0
−0.5
0.0
0.5
1.0
Re S

Figure 79

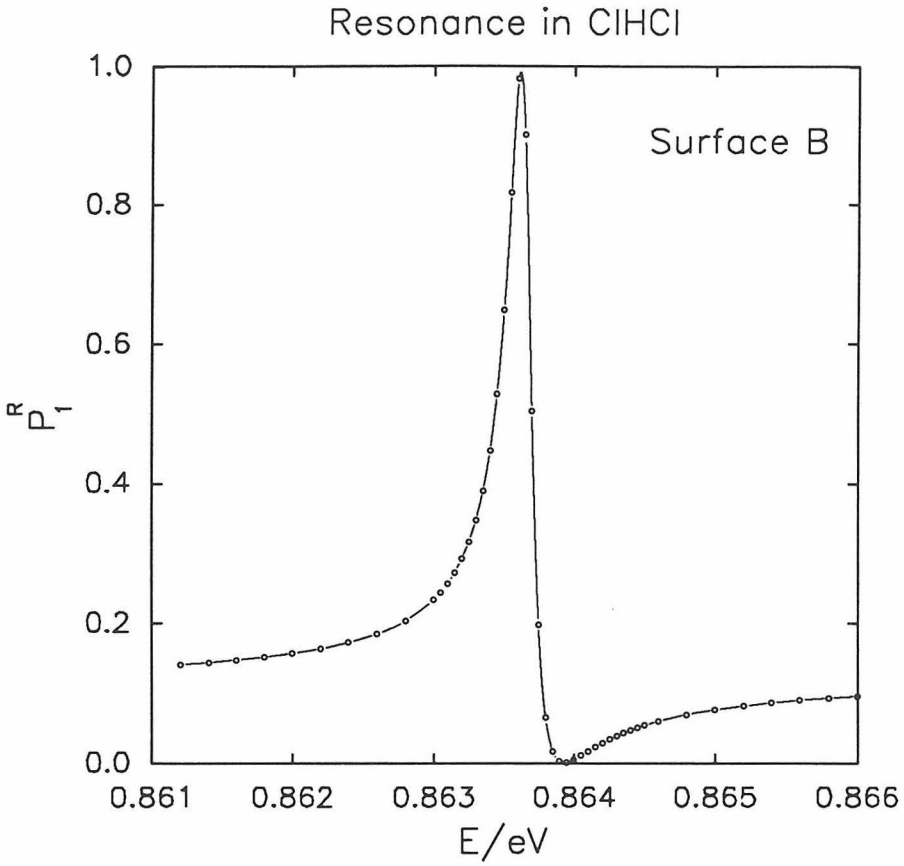
Resonance in ClHCl
Surface B
P_1^R
E/eV
1.0
0.8
0.6
0.4
0.2
0.0
0.861
0.862
0.863
0.864
0.865
0.866

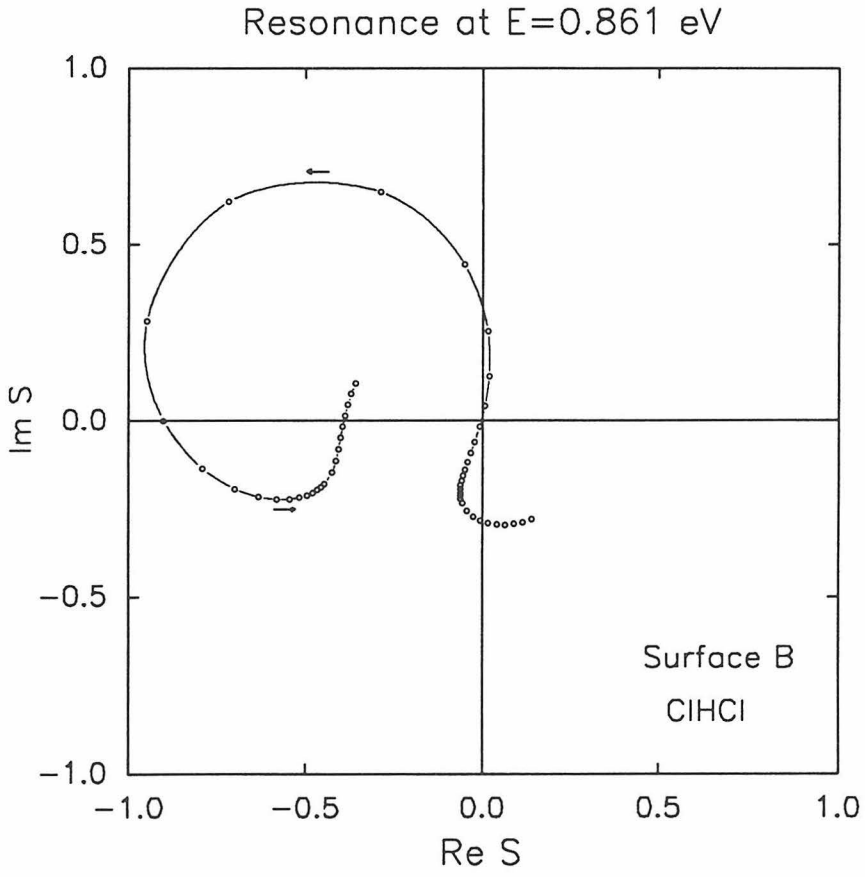
Resonance at E=0.861 eV
Im S
Re S
Surface B
ClHCl
1.0
0.5
0.0
−0.5
−1.0
−1.0
−0.5
0.0
0.5
1.0

Figure 80

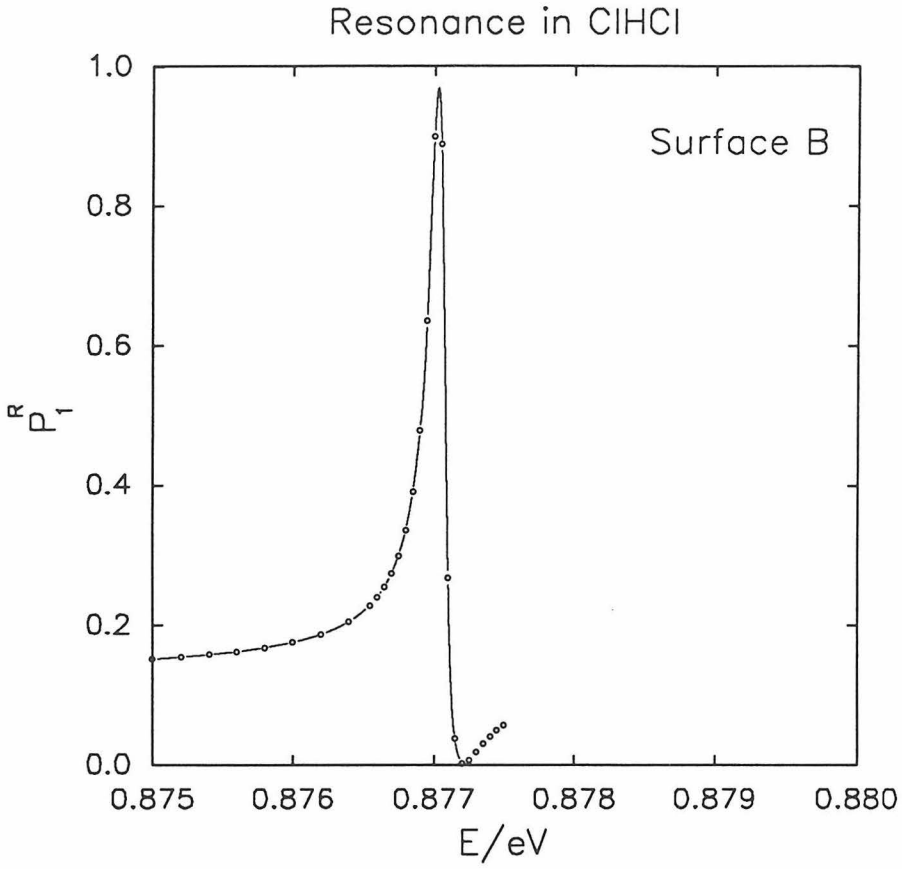
Resonance in ClHCl
Surface B
1.0
0.8
0.6
0.4
0.2
0.0
P_1^R
0.875
0.876
0.877
0.878
0.879
0.880
E/eV

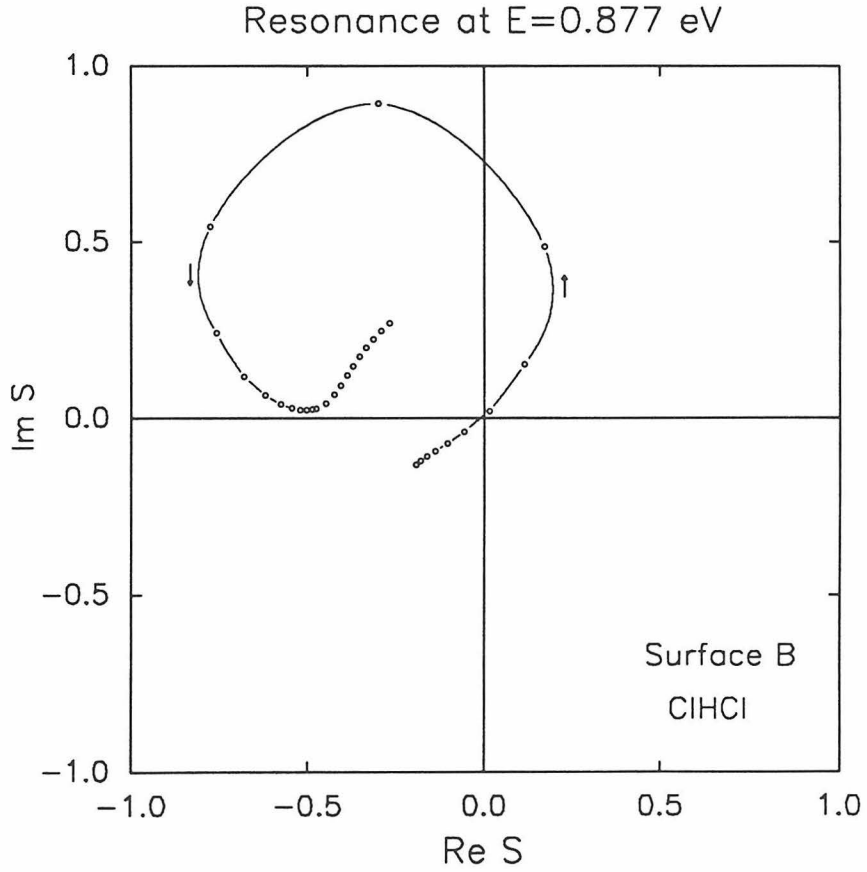
Resonance at E=0.877 eV
1.0
0.5
0.0
−0.5
−1.0
Im S
−1.0
−0.5
0.0
0.5
1.0
Re S
Surface B
ClHCl

Figure 81